Imperial College London
Department of Mechanical Engineering

The Development of Modelling Tools for Railway Switches and Crossings

Ian Coleman

April 2014

Thesis submitted for the Diploma of Imperial College (DIC)
PhD Degree of Imperial College London

I declare that the research presented is my own work and that the work of others is properly acknowledged and referenced.

Ian Coleman

Abstract

Network Rail records indicate that approximately 24% of the total track maintenance and renewal budgets are spent on railway switches and crossings (S&C), which account for only 5% of the total main line track mileage. S&C complexities also introduce a degree of risk, which must be adequately managed to ensure a safe and reliable network. In recent years, risk mitigation fell short, resulting in some high profile incidents at S&C. A recent derailment investigation uncovered knowledge gaps within the UK rail industry, including the understanding of S&C degradation. This PhD research project was therefore initiated to investigating modelling tools for S&C wheel-rail interaction and degradation.

A new wheel-rail contact detection routine has been developed and validated using existing software and a novel experimental technique using thermal imagery. Existing techniques were then integrated to enable the prediction of normal and tangential contact stresses whilst also simulating wear accumulation. To improve accuracy for long-term S&C damage, a combined tool for assessing non-Hertzian normal contact stresses and multiple modes of S&C degradation was sought. A novel 2.5D boundary element model capable of simulating wheel-rail contact detection, surface and sub-surface elastic and elastic-plastic stress analysis and dynamic material response is presented. Superior computational effort is also achieved, illustrating further the feasibility of such an approach.

To conclude, a three-dimensional dynamic finite element model of a railway wheel passing through a cast manganese crossing has also been developed. For the first time, a tool capable of simulating both dynamic contact forces and corresponding plastic material response has been used to discover flaws within existing designs of UK cast manganese crossings. This approach has enabled immediate recommendations for asset improvement to be provided to Network Rail and gives the UK rail industry more scientific insight into the optimal design of railway crossings.

Key words: S&C, contact, degradation, simulation

Acknowledgements

I would like to thank my supervisors at Imperial College London for their support and guidance throughout the duration of my PhD research. Firstly, thanks are given to Professor Roderick Smith for granting me the opportunity to undertake the PhD research and allowing me the freedom to flourish as an independent researcher. His constant enthusiasm, support and technical guidance have paved the way for the successful completion of this thesis. Next, I would like to thank Professor Elias Kassa (now of the Norwegian University of Science and Technology) for sharing his significant expertise in railway systems modelling when creating the PhD aims and objectives for this Network Rail and Imperial College London collaboration. I would also like to give special thanks to Dr Daniele Dini for supporting the PhD research after the departure of Professor Kassa from Imperial College London. His expert knowledge and enthusiasm enabled many of the advanced and novel modelling techniques to be realised. I am hugely indebted to each of my supervisors.

I am extremely grateful to Network Rail for supporting me, both financially and technically, through the PhD research process. Network Rail has given me the opportunity to develop as a professional engineer and researcher and I would therefore like to express my sincere gratitude and future commitment to the company. Within Network Rail, I would like to give special thanks to Mr Phil Winship for his expert industry knowledge, technical support and continued dedication to the project. Further thanks are given to Mr Ian Bostock for providing information on cast manganese crossings.

I would also like to acknowledge my good friend and colleague Mr Andrew Cornish for boosting morale when the pressure was on. It has been a pleasure working alongside Andrew and I am extremely thankful for our technical discussions when solving problems encountered during the PhD.

I am very grateful to Catherine Griffiths for taking the time to read through my thesis and providing excellent feedback to further improve the content and structure.

Finally, I would like to give special thanks to my darling wife, Louise, for her continued support and patience, to my beautiful daughter, Amelia, for keeping me smiling and to my parents for always believing in me.

Nomenclature

Symbol	**Units**	**Meaning**
2α	*rads*	Crossing dip angle
a	*mm (m/s^2)*	Longitudinal contact patch semi-axis and boundary element semi-length (*also denotes accelerations*)
A	*mm^2*	Contact area
$\boldsymbol{A}$	-	Combined stress / displacement boundary element influence function matrix
b	*mm*	Lateral contact patch semi-axis
$\boldsymbol{b}$	-	Boundary element boundary condition matrix
BF	*N*	Body force
C_{11}	-	Longitudinal contact patch stiffness coefficient
C_{22}	-	Lateral contact patch stiffness coefficient
C_{23}	-	Spin contact patch stiffness coefficient
$\boldsymbol{C}$	-	Boundary element stress influence function coefficient matrix
$\vec{d}$	-	Rail-wheel normal deformation vector
d_1	*mm*	Minimum distance from wheel to stock rail profile
d_2	*mm*	Minimum distance from wheel to switch rail profile
d_{horiz}	*mm*	Horizontal minimum distance vector
E	*MPa*	Young's modulus of elasticity
$\boldsymbol{E}$	-	Elliptic integral
f_w^f	-	Wheel flange profile function
f_w^t	-	Wheel tread profile function
F_X	*N*	Longitudinal linear creep force
F_y	*N*	Vertical wheel contact force
F_Y	*N*	Lateral linear creep force
F_T	*N*	Resultant linear creep force
g_0	*mm*	Track gauge
G	*MPa*	Material shear modulus
H	*mm*	Wheelset back-to-back dimension
H_w	*MPa*	Hardness of softer material within Archard's wear model
$\boldsymbol{I}$	-	Identity matrix
$\boldsymbol{J_2}$	-	Second deviatoric stress invariant
k^2	-	Modulus for elliptic integral

k_w	-	Wear coefficient
$\boldsymbol{K}$	-	Elliptic integral
K_p	-	Passenger vehicle bogie load and wear coefficient
K_f	-	Freight vehicle bogie load and wear coefficient
K_t	-	Track coefficient
L	*mm*	Sliding distance
$\overrightarrow{n_r}$	-	Rail surface normal vector
$\overrightarrow{t_w}$	-	Wheel surface tangent vector
m	- *(kg)*	Components of stress / displacement within BEM fundamental solution (also denotes mass)
M_u	*kg*	Unsprung mass per wheel
M_t	*kg*	Lumped track mass per rail
n	-	Direction component within BEM fundamental solution (also denotes normal coordinate system)
N	*N*	Normal contact load
$p_{(x,y)}$	*MPa*	Hertzian normal pressure distribution
p_a	*MPa*	Tangential traction excluding slip influence
p_s	*MPa*	Tangential traction limited by slip
P_0	*N*	Static contact force
P_2	*N*	Peak analytical dynamic contact / impact force
P_i	*MPa*	Boundary element normal traction component
Q	*mm*	Archard’s wear depth
Q_i	*MPa*	Boundary element tangential traction component
q	-	Slip factor
r_0	*mm*	Flange-back to nominal tread radius
r_{ij}	*mm*	Contact Radius (where *i = direction* and *j = contact body*).
R	*mm*	Wheel radius
S_{ij}	-	Boundary element solution matrix
S_p	-	Passenger vehicle speed coefficient
S_f	-	Freight vehicle speed coefficient
s	*m/s*	Slip velocity
$\boldsymbol{s}$	*MPa*	Deviatoric component of stress tensor
s_i	*mm*	Boundary element semi-length
s_x	*m/s*	Longitudinal slip velocity
s_y	*m/s*	Lateral slip velocity
T	- *(s)*	Tangential coordinate system (*also denotes time*)

T_p	*tonnes*	Tonnage of hauled passenger vehicle
T_f	*tonnes*	Tonnage of hauled freight vehicle
T_{tp}	*tonnes*	Tonnage of tractive passenger vehicle
T_{tf}	*tonnes*	Tonnage of tractive passenger vehicle
T_γ	-	Wear index
u_0	*mm*	Vertical displacement of top contact body
u_n	*mm*	Normal surface contact displacement
u_t	*mm*	Tangential surface contact displacement
u_w	*mm*	Lateral position along wheel profile
u_x	*mm*	Lateral displacement component
u_y	*mm*	Vertical displacement component
$\boldsymbol{u*}$	-	Boundary element displacement condition vector matrix
$\boldsymbol{U}$	-	Boundary element displacement influence function coefficient matrix
v	*m/s*	Velocity of wheel through contact patch (also denoted as V_c)
V	*m/s*	Velocity
w_i	-	Boundary element weight function
$\boldsymbol{w}$	-	Boundary element weight function matrix
x	*mm*	Longitudinal direction / coordinate
y	*mm*	Lateral direction / coordinate
y_{offset}	*mm*	Lateral wheelset offset
z	*mm*	Vertical direction / coordinate (also denotes boundary element field point)
$z_n^{Elliptic}$	*N*	Discrete contact force using an elliptic approximation
$z_n^{Parabolic}$	*N*	Discrete contact force using a parabolic approximation
Z_w	*mm*	Vertical position of wheel profile
Z_r	*mm*	Vertical position of rail profile
α	*rads*	Wheelset yaw angle
β	*rads*	Wheelset longitudinal rotation
γ_1	-	Longitudinal creepage
γ_2	-	Lateral creepage
$\boldsymbol{\Gamma}$	-	Boundary element domain
δ	*mm (rads)*	Wheel and rail profile penetration depth (*also denotes contact angle*)
ε	-	Strain
θ	*rads*	Rail inclination (also denotes boundary element stress rotation angle)
κ	-	Kolosov's constant

μ	-	Coefficient of friction
ν	-	Poisson's ratio
ξ	-	Boundary element source point
σ	*MPa*	Stress
σ_n	*MPa*	Normal surface contact stress
σ_t	*MPa*	Tangential surface contact stress
σ_y	*MPa*	Yield stress
$\boldsymbol{\sigma^*}$	-	Boundary element stress condition vector matrix
$\boldsymbol{\sigma}$	-	Boundary element fundamental solution for stress
σ_{xx}	*MPa*	Lateral stress component
$\boldsymbol{\sigma_{xx,x}}$	*MPa*	Lateral stress component due to lateral force component
$\boldsymbol{\sigma_{xx,y}}$	*MPa*	Lateral stress component due to vertical force component
σ_{yy}	*MPa*	Vertical stress component
σ_{xy}	*MPa*	Shear stress component
τ_y	*MPa*	Maximum material shear stress at yield
φ	*rads*	Track cant angle
$\Phi_{(\xi,z)}$	-	Complex potential for Kelvin's solution for a point force in a plane
ψ	*rads*	Wheelset roll
$\Psi_{(\xi,z)}$	-	Complex potential for Kelvin's solution for a point force in a plane
ω_3	-	Spin creepage
$\boldsymbol{\Omega}$	- $(\mathit{rad.s}^{-1})$	Contact body boundary (*also denotes wheelset angular velocity*)

Abbreviations

Abbreviation	**Meaning**
BEM	Boundary Element Method
BF	Body Force
BIE	Boundary Integral Equation
CAD	Computer Aided Design
CPU	Central Processing Unit
CTO	Consistent Tangent Operator
DBEM	Direct Boundary Element Method
DPRS	Distributed Point Reactive Spring
EMGTPA	Equivalent Million Gross Tonnes Per Annum
FEA	Finite Element Analysis
FPM	Freight Performance Measure
FRRC	Future Rail Research Centre
GB	Great Britain
HSE	Health & Safety Executive
HST	High-Speed Train
IBEM	Indirect Boundary Element Method
MBS	Multi-Body Simulation
NMT	New Measurement Train
NR	Network Rail
ORR	Office of Rail Regulation
PEEQ	Accumulated Equivalent Plastic Strain
PPM	Public Performance Measure
RAIB	Rail Accident & Investigation Branch
RCF	Rolling Contact Fatigue
RRA	Radial Return Algorithm
RRD	Rolling Radius Difference
S&C	Switches & Crossings
UIC	International Union of Railways
UK	United Kingdom
WLRM	Whole Life Rail Model

Contents

List of Figures

List of Tables

Chapter 1 : Introduction

This chapter explains the aims of the PhD and reasons for the research approach. Background information is given to discuss why this PhD research project was initiated, building from an overview of the rail industry under the management of Railtrack to how the railway is currently managed under Network Rail. An overview of railway switches and crossings (S&C), from a system perspective, is given to provide the reader with an immediate appreciation of terms used throughout this thesis report. Research aims are then described before providing a chapter-by-chapter overview.

1.1 Background

This research is part of a collaborative effort between Imperial College London and the UK rail infrastructure manager, Network Rail, with the aim to develop novel computational tools for predicting degradation at railway switches and crossings (S&C). A significant proportion of the UK rail infrastructure managers' budget is spent on S&C. In 2009/10, S&C expenditure stood at 24% and 23% of the total maintenance and renewals budgets, respectively. These figures are significant due to S&C occupying only 5% of the total UK main line track mileage. Within the same period, over 820,000 delay minutes were attributed to S&C, equating to just over 10% of the total delay minutes recorded for the entire network [1]. In parallel to the financial implications, high profile S&C derailments have invoked a reaction by UK rail infrastructure manager to develop a deeper understanding of its various modes of degradation. Financial and safety concerns surrounding S&C are not unique to the UK rail network. Internationally, S&C degradation has recently come to the forefront of railway research and from many different perspectives. Investigations using advanced railway vehicle dynamics simulations, detailed finite element models and novel, in-house tools for studying geometry optimisation, detailed wheel to S&C interaction and localised material degradation are just some to note. This PhD was initiated as a reaction to the high speed derailment at Grayrigg, Cumbria. Soon after the derailment, Network Rail recognised the necessity to develop a deeper understanding of the forces experienced at S&C and to exploit modern computational techniques for optimising the system.

There have been three high profile derailments in recent years, two of which were directly associated with S&C. The first derailment occurred on the 17th October 2000 at Hatfield, Hertfordshire, as the train struck a fractured rail, which subsequently fragmented into many other pieces. The primary cause of failure was due to extensive rolling contact fatigue (RCF) cracking [2]. At this time, the UK knowledge about RCF and its prediction, gained by British Rail Research, had been forgotten by Railtrack. A large scale rail grinding programme had also been abandoned by Railtrack due to not fully appreciating that the removal of small surface defects significantly reduces, or indeed removes, the likelihood of RCF crack growth. The revival of UK RCF knowledge and a further research push therefore followed Hatfield. Burstow el al. [3] went on to develop the whole life rail model (WLRM); an RCF prediction tool based on a damage index. The WLRM is described in more detail within *Chapter 2*. The first major incident associated with S&C occurred on the 10th May 2002 when a passenger train derailed whilst traversing the switch (also known as points) at Potters Bar. A full investigation by the Health and Safety Executive (HSE) reported that the mechanical failure of 2182A points initiated the derailment [4]. At that time, Railtrack plc owned and operated the UK rail network and was therefore responsible for all infrastructure maintenance. Further investigation revealed that the maintenance system fell far short of what was required to ensure safe operation of the rail network. This saw the demise of Railtrack, who were taken over by 'not for dividend' company, Network Rail Infrastructure Ltd, in October 2002. Network Rail was given a mandate by government to improve the safety, reliability and efficiency of the railway. On the 23rd February 2007, five years into NR's tenure, the second and most recent S&C related derailment occurred near Grayrigg, Cumbria. All nine vehicles of a Virgin Pendolino derailed with five overturning and eight falling down the adjacent embankment, as illustrated within Figure 1-1.

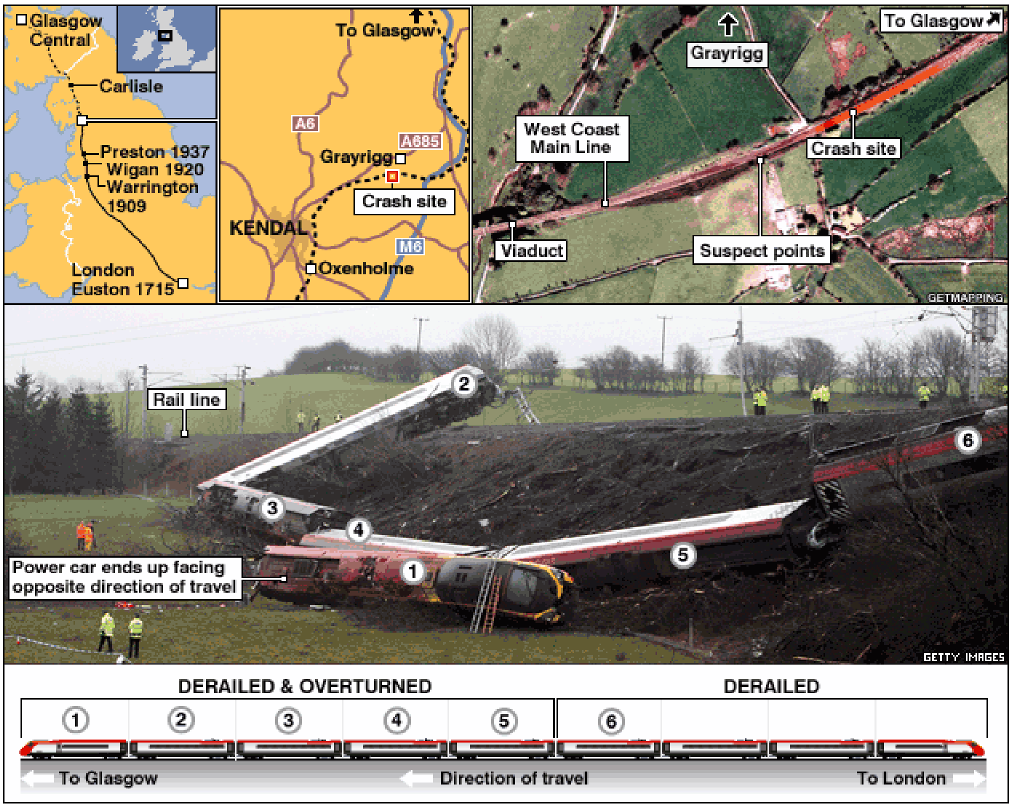

Figure 1-1: Overview of the derailment at Grayrigg [5].

Similar circumstances to those from Potters Bar surrounded the incident as mechanical failure of the points (known as Lambrigg 2B points) was the overriding cause of derailment. The Rail Accident Investigation Branch (RAIB) conducted the immediate investigation and issued a series of recommendations and comments to Network Rail [6]. One critical comment, which also proved to initiate this PhD research project, stated:

> *"It is concluded that Network Rail's incomplete understanding of the design and performance of S&C, and its inspection and maintenance requirements, was an underlying factor in the accident at Grayrigg"*

1.2 UK Railway Efficiency and Financial Obligations

Subsequent to the Grayrigg investigation, the ORR set a number of financial and operational targets, which Network Rail committed to delivering during control period 4 (2009/10 to 2013/14), including:

- Deliver £8bn worth of rail enhancement projects.
- Increase train punctuality to an average of 92.6 % of trains on time by 2014.
- Reduce disruption to passengers by 37%.
- Reduce costs by a further 21%.
- Improve safety by reducing the risk of death or serious injury from accidents on the railway for passengers and rail workers by 3%.

These targets were set with the condition that freight availability must not be adversely affected to compensate. Unprecedented growth saw a 49.6% increase in UK passenger numbers during Network Rail's management of the UK rail infrastructure, from 976 million during 2002/03 to 1.46 billion in 2011/12 [7]. Figure 1-2 also shows that, since the privatisation of British Rail, passenger kilometres have continued to climb, representing a 102.4% increase over a 19 year period. Figure 1-3 provides a historic overview of public performance measure (PPM), which measures the percentage of trains arriving at their destination within 5-10 minutes, depending on the type of service, of the national timetable. Moving annual averages are plotted to remove seasonal effects. From early 2001/02, PPM continuously improved year-on-year until reaching a plateau during 2010 just short of 92%. Freight performance measure (FPM) data was only available from 2005/06 but demonstrates a similar upwards trend until peaking at approximately 76%. With demand continuing to grow on an already close to capacity rail network, there becomes a need to more efficiently maintain, renew and redevelop the railway infrastructure using fewer resources and reduced track assess times. The problem of measuring and managing rail capacity was studied and published by Sameni [8], who defined capacity as "the ability of the infrastructure to generate added value by enabling passengers or freight to reach their destination as planned".

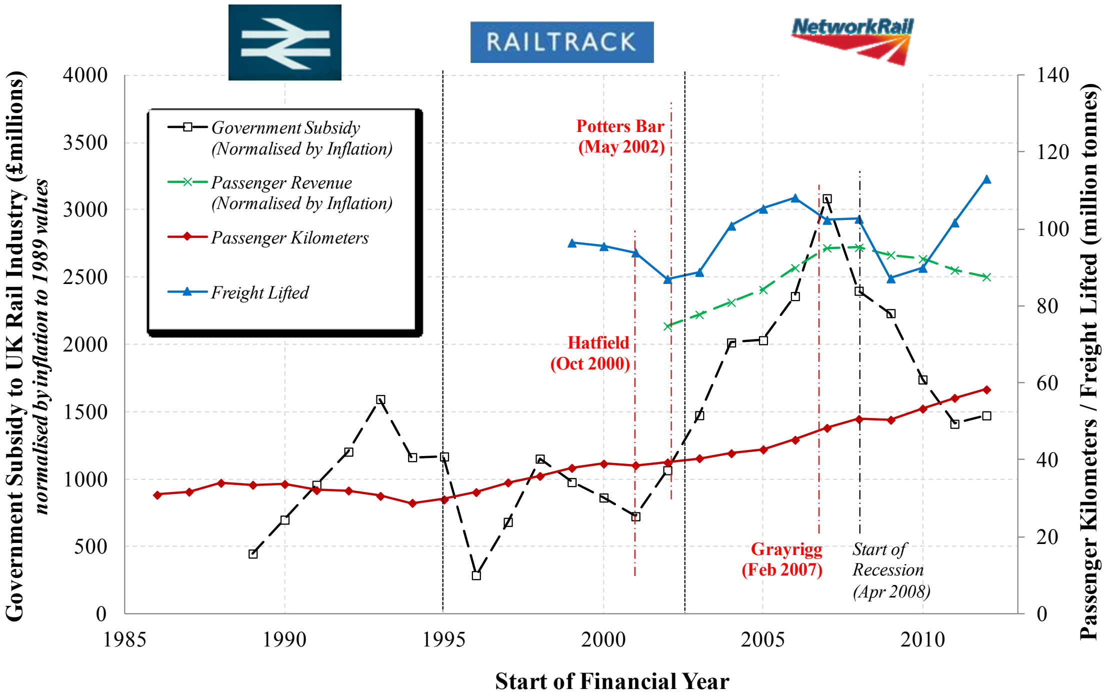

Figure 1-2: Government support to the rail industry and passenger kilometres travelled during the tenure of British Rail, Railtrack and Network Rail (1985-2011). Freight lifted is also presented but data is not available prior to financial year 1999/2000. All data was obtained from [9] and historical inflation rates from [10].

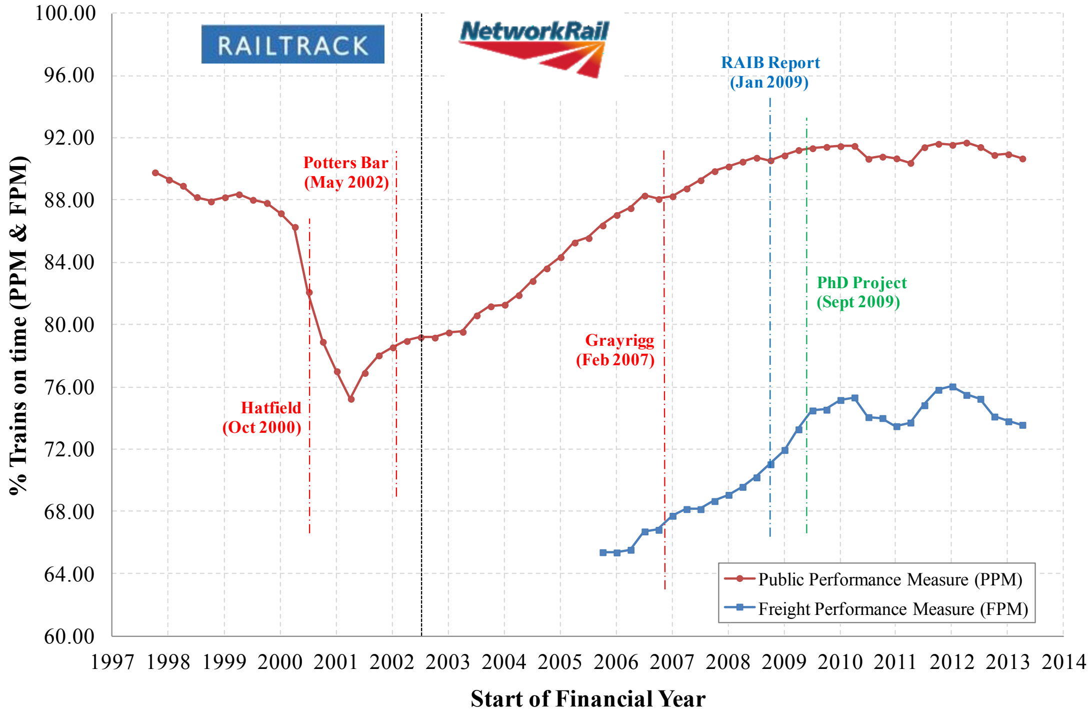

Figure 1-3: Public and Freight Performance Measures (FPM and PPM) moving annual average. Data obtained from [9].

Both the Potters Bar and Grayrigg derailments highlighted issues with regards to the design and maintenance of railway switches. During the financial year prior to the Grayrigg derailment, government subsidy to the rail industry had peaked at approximately £6.3billion, as illustrated within Figure 1-2. It was at this time that Sir Roy McNulty (Chair, Rail Value for Money Study), at a request from Government, commenced a comprehensive study into potential cost savings in GB rail [11]. McNulty identified industry savings of £50-100m in fiscal year 2013/14, with dramatically increased savings in the range of £600-1,000m by the end of 2018/19. Reporting from a 2008 periodic review commissioned by the Office of Rail Regulation (ORR), Network Rail's infrastructure maintenance and renewals efficiencies were benchmarked as between 34-40% less efficient than the top-performing European railways. The ORR commissioned a further study to better understand the reasons for the efficiency gap, which included contributions from premature asset renewals, use of sub-optimal life cycle cost models and inefficient maintenance and renewals strategies [12]. S&C failures, of which a comprehensive review was completed by Cornish et al. [13], make up a significant proportion of UK maintenance and renewals.

1.3 Switches and Crossings

Switches and crossings (S&C) provide the railway network with operational flexibility by enabling vehicles to be directed from one track (or line) to another. There are many different S&C layouts of which a comprehensive guide can be found in Cope and Ellis [14]. All layouts consist of at least one switch (allowing vehicles to 'switch' from one line to another), one crossing (allowing vehicles to 'cross' over adjacent lines) and a closure panel between the two. Figure 1-4 illustrates the most common type of S&C design, the railway turnout.

Current maintenance of UK railway S&C is based around track categories and inspection frequencies. The track category was originally derived as a means of assessing the duty on the track and hence the expected level of maintenance intervention required due to degradation. Figure 1-5 illustrates the track category matrix currently used by UK infrastructure maintainers, which has been extracted from the Network Rail Company Standard NR/L2/TRK/001 [15].

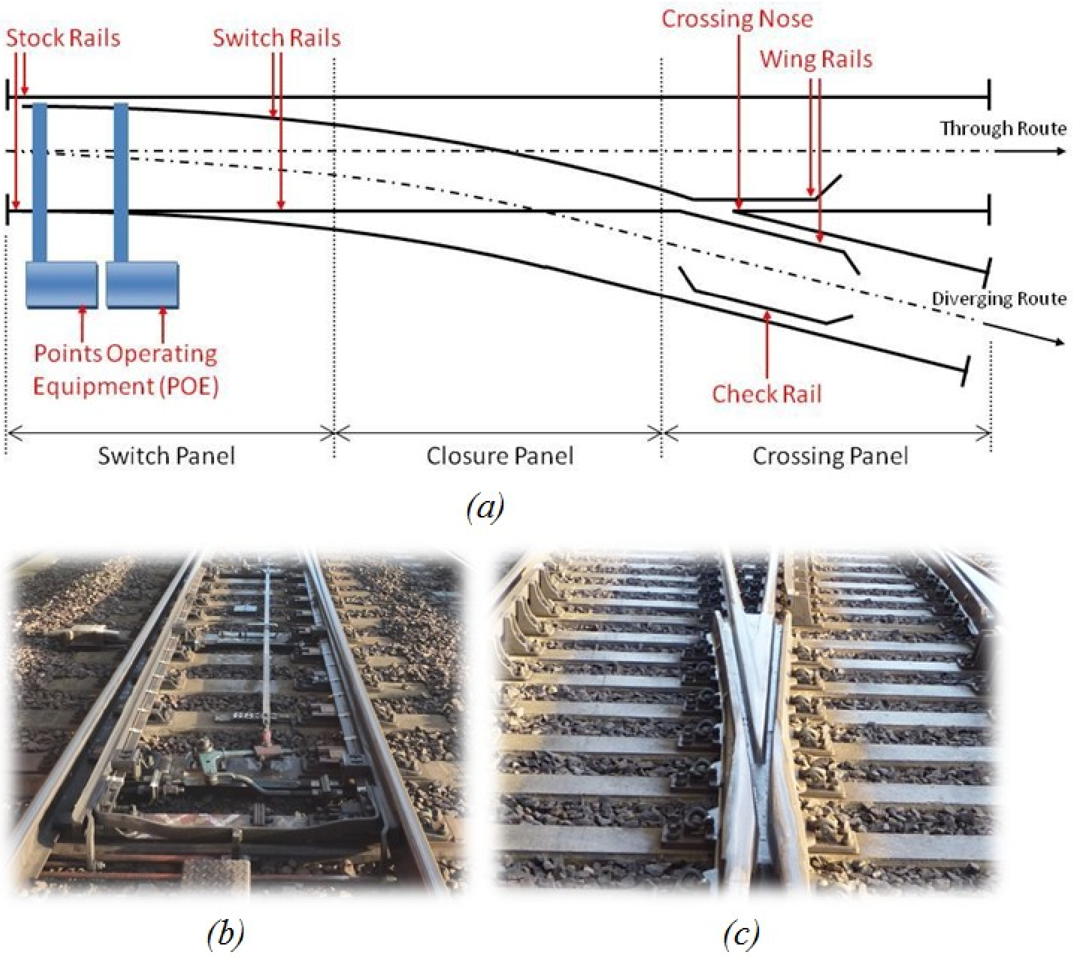

Figure 1-4: Diagram of a common railway turnout (b) consisting of a switch panel (a) and crossing panel (c)

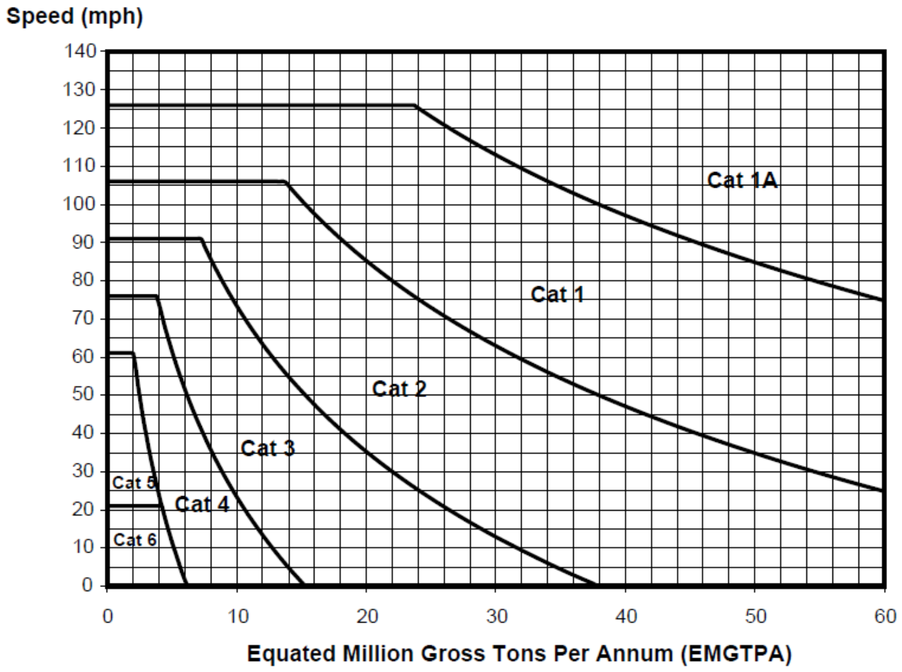

Figure 1-5: Track category matrix, adapted from [16].

The horizontal part of the track category boundary is defined by a combination of the physical asset (*i.e.* jointed track is limited to 90mph) and the maximum speeds of the principal traffic types. The curved boundaries were generated through experience of track damage caused by the Equivalent Million Gross Tons Per Annum (EMGTPA) seen by the route. EMGTPA combines the tonnage effects of both passenger and freight vehicle on the overall degradation of the track. A larger weighting is assigned to freight vehicles due to their greater impact on track degradation. The formula for generating the EMGTPA for a route is reproduced within Equation 1-1, which was developed in the 1990's by British Rail research [16]:

$$EMGTPA = S_p\left(K_pT_p + K_tT_{tp}\right) + S_f\left(K_fT_f + K_tT_{tf}\right) \qquad \text{1-1}$$

Where:

S_p and S_f are passenger and freight vehicle speed coefficients
K_p and K_f are passenger and freight vehicle bogie load and wear coefficients
K_t is a track coefficient
T_p and T_f are the tonnage of hauled passenger and freight vehicle
T_{tp} and T_{tf} are the tonnage of tractive passenger and freight vehicle

Upon determining the track category in which the S&C resides, the minimum inspection frequencies are then obtained through use of Figure 1-6, which is defined within the Network Rail Track Inspection Standard [17].

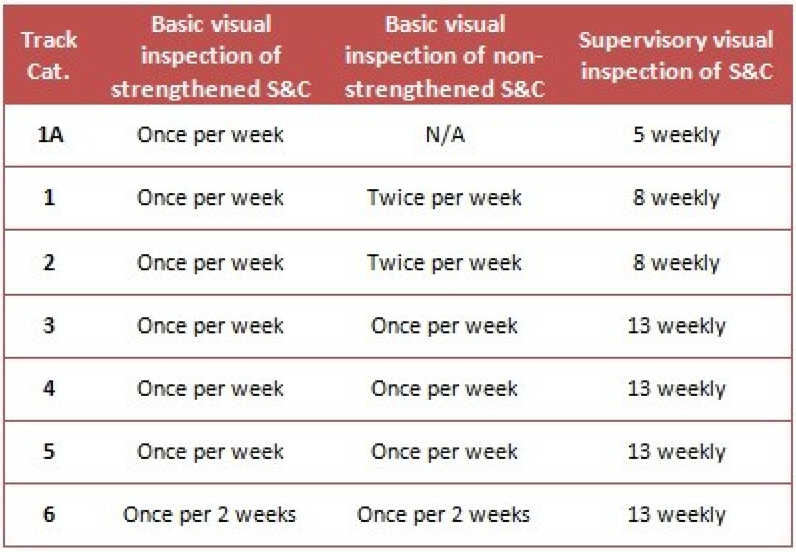

Track Cat.	Basic visual inspection of strengthened S&C	Basic visual inspection of non-strengthened S&C	Supervisory visual inspection of S&C
1A	Once per week	N/A	5 weekly
1	Once per week	Twice per week	8 weekly
2	Once per week	Twice per week	8 weekly
3	Once per week	Once per week	13 weekly
4	Once per week	Once per week	13 weekly
5	Once per week	Once per week	13 weekly
6	Once per 2 weeks	Once per 2 weeks	13 weekly

Figure 1-6: S&C inspection frequencies taken from [17].

Current industry practices therefore demonstrate a ‘find and fix’ infrastructure maintenance philosophy, reacting to failures as they occur rather than monitoring progressive degradation and/or predicting where and when asset maintenance should take place. Categorising all S&C inspection (and hence subsequent maintenance) in this manner also ignores the uniqueness of each individual S&C layout. In comparison to standard plain line track, S&C’s are complex infrastructure assets both in terms of their design and operation. Significant complexities, such as variation in rail cross-section, varying rail inclinations, sudden changes in track curvature and high impact forces, all contribute to a complex system with many different parameters affecting their rate of degradation. S&C units tend also to be located in and around busy junctions, increasing their frequency of operation and use. Combined with additional variables attributed to the rail vehicle, such as speed, axle-load, wheel profile, and the potential for multiple wheel-rail contact points, we soon realise that the S&C degradation is a highly complex, non-linear process. To improve the efficiency of S&C maintenance, there is an obvious need to move away from the current reactive ‘find and fix’ approach to a proactive ‘predict and prevent’ strategy. To achieve this goal, accurately modelling the S&C as a complex, non-linear system is essential.

In 2009, Network Rail approached the Future Rail Research Centre (FRRC) at Imperial College London to initiate a joint research project as a first step towards a this ‘predict and prevent’ maintenance philosophy. Two parallel PhD research projects were funded. The first project involved computational modelling of wheel-rail contact and material degradation whilst the second took an experimental approach through S&C instrumentation and data analysis. This thesis report is for the work completed under the first of these projects. By the end of the PhD research, the second projects had not reached a point where validation data could be used within this thesis. This will be identified within recommendations for further work.

1.4 Research Objectives

The complex nature of wheel to S&C interaction and how the degradation process adds up to the large maintenance requirement is not yet fully understood by the railway industry. The motivation of this project is to help Network Rail understand wheel-rail interaction at S&C and the degradation process due to dynamic loading from trains. The long term vision is to develop computational tools capable of providing guidance on inspection intervals and maintenance strategies whilst supporting track engineers and S&C designers on S&C acceptance and selection criteria with respect to geometry and material.

Whilst considering both the needs of Network Rail and the issues outlined within the subsequent sections of this chapter, the main aims of this thesis include:

1. Establishing current, international best practice with regards to computational modelling of S&C degradation whilst identifying existing limitations associated with long-term S&C damage predictions.

2. Addressing significant limitations and combining best practice to investigate and develop novel computational tools for material degradation, specifically at railway S&C.

3. Provide recommendations for potential asset performance improvement(s).

1.5 Approach

When considering degradation of a complex system, such as railway switches and crossings, it is important to clearly identify the boundaries of the system under analysis. If considering the entire S&C system, degradation of everything from the rail surface down to the underlying track foundation needs to be considered. Many different interfaces would be involved and at an individual component level, resulting in a very complex system of interactions. No two S&C units are the same as different designs contain a wide range of components, each of which will differ in condition depending on their age and frequency of use. Similar designs of S&C can also be specified in different lengths and are installed over a wide range of geographical locations, each containing their own set of unique environmental conditions and vehicle types operating on the route. It becomes evident that results from an investigation into complete S&C system degradation become very unique to the individual scenario used.

In this thesis, the problem has been reduced to that of wheel-rail interaction through S&C, with the system boundaries extending to the wheel and rail contacting bodies. This provides a clearly defined set of boundaries within which to realise the research aims. Reducing the problem to one of wheel-rail contact mechanics also enables a more realistic set of achievable objectives to be defined.

1.6 Thesis Outline

The general structure of this thesis is as follows:

Chapter 2 contains a literature review of existing wheel-rail contact models and serves to illustrate knowledge gaps when considering their application specifically at railway S&C. Common damage mechanisms are identified and existing modelling techniques discussed. A summary identifying where this thesis aims to contribute towards the identified knowledge gaps is provided.

Chapter 3 describes the development of an in-house computational tool for S&C interaction modelling by discussing contact point detection and a new algorithm developed specifically for wheel to S&C multipoint contact detection. Theoretical model validation for contact point detection is presented against a well established computational tool in parallel with a novel experimental technique utilising thermal imaging technology.

Simplified contact stress theories are then introduced within the tool with regards to normal and tangential contact traction prediction. This is described in detail within *Chapter 4* prior to discussing current model limitations with regards to accuracy and applicability. Further developments to simulate rail profile evolution due to wear damage accumulation is included and discussed.

Chapter 5 presents the novel integration of a 2D lateral boundary element method (BEM) model into the S&C contact interaction tool for improving the normal contact traction predictions. Accurate sub-surface stress predictions are also presented.

Chapter 6 then demonstrates a new routine for generating accurate 3D contact patch stress distributions (termed the 2.5D BEM model). Comparisons are made with the established FEA tool, Abaqus, and also the simplified contact theory of Hertz. Internal domain inertia is included to present a solution capable of simulating wheel-rail impacts, which is novel to wheel-rail contact models. Initial developments to include plastic-flow modelling are also discussed.

Chapter 7 introduces a novel application of the explicit finite element approach for assessing dynamic wheel-rail interaction through railway crossings. This study compliments the previous chapters by presenting a tool capable of predicting plastic deformation and dynamic impact loading throughout the crossing. A wide range of case studies are simulated and provide an in-depth assessment of the critical parameters effecting wheel-crossing contact performance. *Chapter 7* concludes by providing suggestions for potential asset improvements.

Chapter 8 reviews the thesis, summarises the main findings and discusses the implications of introducing novel tools for wheel-S&C interaction and degradation modelling. The major contributions to knowledge are then highlighted before recommending area for further work.

Chapter 2 : Review of Wheel to Rail Contact and Damage Prediction Modelling

The wheel to rail contact problem is introduced before describing each critical stage in detail. A review of wheel to rail contact detection techniques is provided prior to discussing both simplified and complex contact stress models. Common modes of material degradation, associated with railway switches and crossings (S&C), and existing computational models for their prediction are then considered. All of the models introduced within this literature review are discussed with regards to their applicability to S&C. Chapter 2 concludes by identifying current knowledge gaps, stating the subsequent aims of the PhD, discussing the approach to addressing the knowledge gaps and finally providing a high level summary of the thesis.

2.1 Review Structure

The primary aim of this thesis is to develop novel computational tools for modelling wheel to rail interaction phenomena specific to railway switches and crossings (S&C). This review therefore focuses on three major topics:

1. *Wheel-Rail Contact Mechanics*

   This sections aims to review existing computational tools capable of modelling rolling contact phenomena occurring at the wheel to rail interface. A particular focus is given to contact point detection techniques and both normal and tangential contact stress solutions.

2. *Common S&C Damage Mechanisms*

   The significant modes of material degradation associated with railway S&C's are introduced before reviewing existing computational models adopted to capture different damage mechanisms.

3. *State-of-the-art S&C Degradation Modelling*

   A critical review of existing and current state-of-the-art processes for combined damage accumulation modelling will complete *Chapter 2*.

This critical review will conclude by drawing upon both benefits and limitations of existing, state-of-the-art solutions for S&C damage prediction modelling before identifying knowledge gaps and opportunities.

2.2 Wheel-rail contact mechanics

Wheel-rail contact mechanics problems are generally divided into two distinct areas; (1) the geometric problem of contact point detection and (2) the evaluation of contact stresses and their analyses in the context of damage initiation and propagation. The geometric solution concentrates on assessing the contact geometry of the wheel-rail profile combination. Full parameterisation of the wheel-rail system is required in order to locate the wheel and rail profiles correctly in relation to each other. Parameters including the track gauge, cant angle and rail inclination, as well as the wheel nominal tread radius, wheelset back-to-back dimension and yaw angle, contribute to the kinematics and dynamic response of the system and the determination of the contact areas between the rail and the wheel. Deviations in wheel and rail profiles from the nominal (due to wear and deformation) also play a significant role within the wheel-rail contact geometry problem. The contact stress problem combines the geometric parameters local to the contact patch with external global parameters, such as axle-load, velocity and wheel/rail material properties, to evaluate what is happening within the contact interface (*i.e.* contact patch shape/size, pressure distributions, wheel-rail relative slip (creepage), etc).

The wheel-rail contact problem is very unique in comparison to many other engineering rolling contact problems. Most rolling contact problems can be classified as 'closed systems', in which the model operating assumptions can be pre-defined with confidence (*i.e.* contact geometry, loading and lubrication conditions of bearing and gear applications will experience minimal variation during the operational life of the component). The simulation of damage within such systems can be simplified as these model inputs become fixed internal parameters rather than external system variables. In comparison, wheel/rail interaction is a highly complex, non-linear 'open system' where many external factors have an impact on the final solution. Parameters associated with the dynamics of the vehicle, the system lubrication (*i.e.* dry, grease, water, etc.) and the geometry and condition of the track vary significantly and, therefore, must be continuously evaluated when modelling accurate contact forces and their associated modes of degradation [18].

Many different techniques for investigating the wheel to rail contact problem have been developed, each with their own benefits and limitations depending on the problem to which they are applied. Techniques used within the simulation of rail vehicle dynamics demand a fast and efficient solution, in order to maintain an acceptable degree of computational efficiency, and is often accompanied by simplifying assumptions. If the primary focus of study is material degradation, particularly when associated with the track, a more accurate solution becomes essential to ensure realistic inputs to damage models are obtained. The sections to follow describe existing and state-of-the-art techniques for solving different stages of the wheel-rail contact problem and are each reviewed with regards to their applicability to S&C material degradation modelling.

2.2.1 Multi-body Simulation for S&C Vehicle Dynamics

In recent years, multi-body simulation (MBS) packages have been used for the prediction of railway vehicle dynamics [19,20]; with the associated wheel-rail contact forces used as inputs to material degradation models [21,22]. In particular, S&C have become a focal point for such simulations due to their significant maintenance costs and the complexity of the problem. Due to the geometric discontinuities associated with S&C (*i.e.* irregular track geometries and rail profiles), it is common for complex wheel to rail interactions to occur. For S&C modelling, there are currently several commercial and in-house codes available. There are several codes that have been used previously for simulating the dynamic behaviour of a vehicle passing through S&C. Kassa et al. [23,24] used GENSYS to model the dynamic interaction between train and turnout and validated the results through full-scale field tests [25]. Kassa et al. [26] also developed the in-house code DIFF3D to include flexible track modes within the vehicle-S&C dynamic simulation. It was demonstrated that track modes with frequencies up to at least 200 Hz significantly influenced the dynamic wheel-rail contact forces. The software package SIMPACK has also been widely used to calculate the vehicle dynamic behaviours when passing through a turnout. Recent examples come from the INNOTRACK project by Manchester Metropolitan University [1] and Deutsche Bahn [27]. Sun et al. [28] from the Centre for Railway Engineering, Australia, used VAMPIRE to study wheel-rail contact issues through a fixed crossing. Table 2-1 lists and compares the available MBS software packages with respect to the contact model, number of detectible contacts points, the available track model and also agreement with measured contact forces.

Software	Wheel-rail contact model	Number of contact points	Track dynamics modelling	Comparison with field experiment
GENSYS	Pre calculated table	One or two-point contact	Simple track model	Good prediction of the general trend of the forces
SIMPACK	Online calculation / Pre calculated table	One or two-point contact	Simple track model and possibility to include track flexibility	Good prediction of the general trend of the forces
VAMPIRE	Pre calculated table	One point contact; two-point contact	Simple track model	-
NUCARS	Pre calculated table	One point contact; two-point contact	-	-
DIFF3D	Pre calculated table / online calculation	Pre-calculated two-point contact; online one point contact	Detailed modelling of the track dynamics, valid for a wide frequency range	Very good prediction of the magnitude of forces

Table 2-1: Existing software for S&C modelling benchmark

Each software package uses a contact detection algorithm that contains simplifying assumptions for efficient railway vehicle dynamics simulations. They are designed specifically for modelling dynamic interaction between the vehicle and the track (S&C) and are therefore not concerned with highly detailed contact patch predictions with regards to stress and adhesion distribution. They are also only capable of detecting a maximum of two points of contact, which presents an immediate limitation when accurate material degradation predictions at S&C are the primary focus.

2.2.2 Wheel-Rail Contact Point Detection

The geometrical problem of contact detection is the first step in assessing wheel-rail interaction. Both the wheel and rail profiles are represented mathematically before being positioned relative to one another. This becomes the starting point for many different contact detection techniques. In its simplest form, contact detection is represented by the minimum distance between wheel and rail profile curves. One such technique was described by Ayasse et al. [29] and enables to detect an initial, single point of contact. Common parameters are used to locate the wheel and rail profiles at their nominal positions before introducing a wheelset lateral shift. A single contact origin is then defined by the function $min(Z_w-Z_r)$, as illustrated by within Figure 2-1.

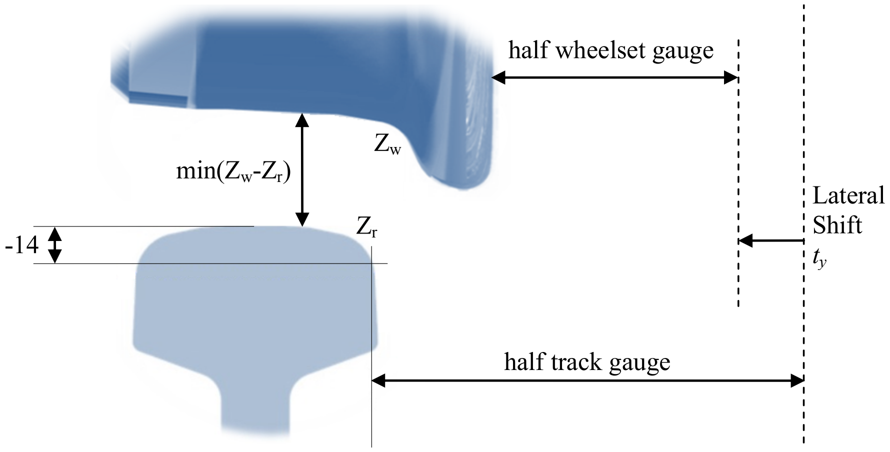

Figure 2-1: Minimum distance technique for wheel-rail contact detection, adapted from [29]

The complexity of the technique is increased by introducing the second wheel and rail profile pair to compute the wheelset roll angle associated with an applied lateral shift. Ren et al. [30] adapted the minimum distance technique for detecting two-point contact situations within railway switches. The assumption of a single point of contact between the wheel and rail was maintained but applied independently to the switch and stock rails. Equations 2-1 provide the relational definitions for single and two-point contact. Figure 2-2 shows that a maximum of two points of contact are possible; one on the stock rail and one on the switch rail. This is a significant limitation as it is common for multiple points of contact to occur on a single rail profile due to conforming wheel and rail profiles, large wheelset yaw angles and / or complex rail geometries, as found within S&C.

$$\begin{aligned}\text{Single contact point: } & |d_1 - d_2| \geq \delta \\ \text{Two contact points: } & |d_1 - d_2| < \delta\end{aligned} \tag{2-1}$$

where d_1 and d_2 are the minimum distances from wheel to stock and switch rails, respectively, and δ is the profile penetration depth.

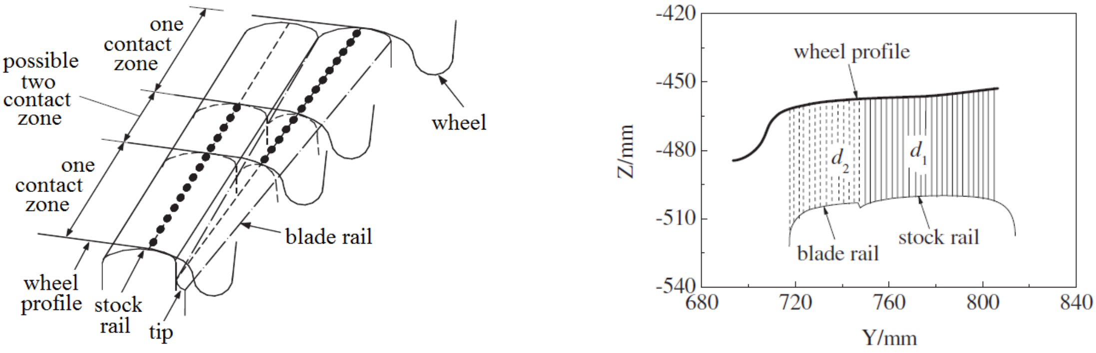

(a) *(b)*

Figure 2-2: Wheel-rail contact state for a closed switch scenario (a) and a minimum distance technique for two-point contact parameter calculation (b), illustrated from [30]

Schmid *el al.* [31] also considered contact behaviour by assessing a railway-bogie passing a switch. Figure 2-3 shows the four main wheel-rail contact configurations that were discussed, including one-point *(a)*, two-point *(b)*, transitional contact from stock to switch rail *(c)* and multi-point contact *(d)*. Schmid discussed that, due to only occurring at isolated locations along the switch, the transitional contacts could be excluded within railway vehicle dynamic simulations without impairing the final results. This assumption may hold true for the simulation of railway vehicle dynamics but is not acceptable when long-term S&C damage prediction is the primary focus of study. Wheel-rail transition regions are, in these cases, of significant interest. This is particularly important when assessing heavy freight lines with worn wheel and / or rail profiles, which would inevitably result in more conformal contact conditions and hence increase the likelihood of multiple points of contact occurring.

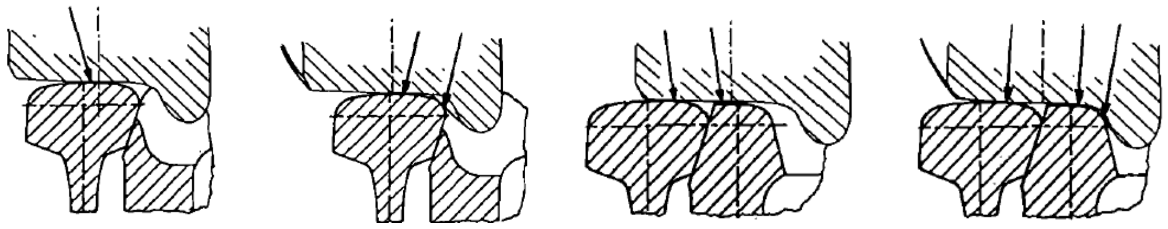

(a) *(b)* *(c)* *(d)*

Figure 2-3: Wheel-rail contact configurations at the switch interface as presented within [31].

The type of geometric model applied when studying wheel-rail damage applications is also an important consideration. Shabana and Rathod [32] compared the use of both two dimensional (planar) and three dimensional (spatial) contact theories within rail vehicle dynamics and material degradation simulations. Results demonstrated that the use of planar contact conditions lead to accurate prediction of rail vehicle dynamics. Shabana then went on to demonstrate limitations of the planar contact model when used within material degradation studies, which rely heavily on the prediction of accurate contact locations. Small errors in contact point location were observed. It was concluded that a three dimensional contact model is required when studying material degradation due to flange contact potentially occurring ahead of or behind the axle centre line during wheel-rail misalignment. Pombo [33] described a new computationally efficient technique capable of assessing any spatial wheel-rail configuration but shows how highly conformal contact invalidates the procedure due to the existence of multiple contact origins, as illustrated within Figure 2-4 *(c)*. This problem was eliminated by considering the wheel profile as two independent functions, f_w^f for the wheel flange and f_w^t for the wheel tread, demonstrated within Figure 2-4 *(a)*. Here, u_w relates to the lateral position along the wheel profile.

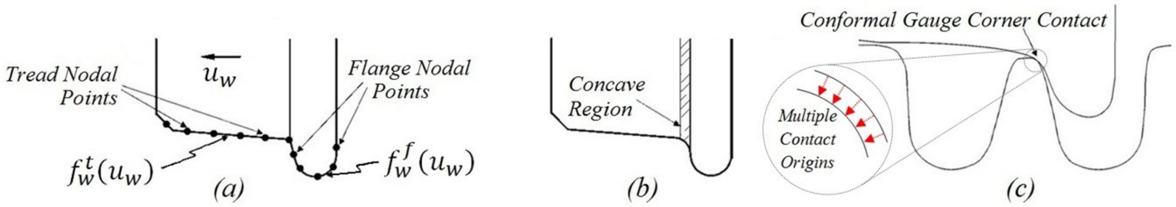

Figure 2-4: (a) Wheel profile approximation adapted from [33], (b) actual wheel profile showing concave region and (c) technique limitation when considering S&C contact point detection.

Simplifying the wheel profile in this manner would, however, create a new problem when considering contact through S&C. For example, Figure 2-4 *(c)* shows how highly conformal contact may occur as the wheel passes through a railway crossing. In this scenario, simplifying the wheel profile would exclude conformal gauge corner contact and move the contact origin(s) incorrectly to either the wing rail or the head and / or further down the gauge face of the crossing nose.

For long-term material degradation modelling throughout railway S&C's, prediction of accurate contact points and corresponding contact stresses is essential. Typically flange and gauge corner contact regions, within both the switch and crossing panels, experience high levels of wear due to large normal and tangential contact stresses. Therefore, a general wheel-rail contact detection method capable of detecting multiple contacts, including within the concave region of the wheel, is vital for predicting long-term material degradation throughout S&C.

2.2.3 Wheel-Rail Contact Stress Analysis

Subsequent to contact point detection, the normal and tangential contact stresses between wheel and rail must then be solved to provide traction and adhesion results required by material damage models. There are broadly two types of solution, the simplified Hertzian ellipse and more detailed, non-Hertzian models. Section 2.2.3 reviews in detail the commonly use theories along with some of the most advanced solutions currently available.

2.2.3.1 Hertzian model for normal contact

To provide grounds for advancing to non-Hertzian contact theories; an overview of Hertzian contact, with particular focus on wheel to rail application, is given here. In vehicle/track dynamic simulations, the normal contact stress problem is generally solved using the simplified theory of Hertzian elliptic contact. The theory was developed by Heinrich Hertz in 1882 [34] and is the most widely used normal contact theory in contact mechanics. Key assumptions are made to allow an efficient but approximate solution to be found, which is attractive for online vehicle to track dynamic simulations. A comprehensive description of Hertzian contact theory is given by Johnson [35], who summarised the four critical assumptions required for Hertzian elliptic contact theory to hold true:

1. *Small strain, linear elasticity*

   The contacting bodies are modelled as perfectly linear elastic solids. This assumption requires the strains to be sufficiently small to ensure the solution remains within the elastic region of the material response.

2. *Each body can be considered an elastic half-space*

   This assumption allows the highly localised contact stresses to be treated independently from the global body stresses. The surface contact area must be small in relation to the overall dimensions of the contacting bodies, which result in the limiting application of Hertzian theory to non-conformal contact geometries. Under load, the contact area should remain small in relation to the overall body dimensions and local contact radii, which is necessary to ensure that the strains are small enough to lie within the scope of the linear theory of elasticity.

3. *The contacting surfaces are continuous and non-conforming*

   The local contact surfaces are perfectly smooth (*i.e.* no surface irregularities) and can therefore be adequately described by quadratic functions.

4. *No friction*

   Friction is excluded to ensure that only normal pressure is transmitted between the contacting surfaces and there is no coupling between normal and tangential tractions.

Providing the above assumptions are met, Hertzian theory provides an accurate and efficient solution perfectly suited for efficient railway vehicle dynamics simulations. Despite this, it is common for these assumptions to be violated during wheel to rail interaction. Under certain configurations, highly conformal contact will occur, particularly at the wheel flange root and rail gauge corner. This issue is exemplified when considering S&C due to the relatively small contact radii associated with complex rail geometries. The true shape of the contact patch is also non-elliptical in nature, leading to irregular distributions of both normal and tangential contact stresses within it. This is particularly significant when considering S&C due to the continuously varying profiles along the length of the rail. Rail profile roughness and damage will also have a significant effect on the pressure distribution within the true contact patch. S&C interaction modelling therefore requires a normal contact solution not bound by the limiting assumption of Hertzian theory.

2.2.3.2 Non-Hertzian models for normal contact

When considering the development of an integrated tool for S&C material degradation, it is vital to consider suitable contact models for adequately coupling the vehicle dynamics with the tribology. Wu et al. [36] classified wheel to rail contact problems into four different categories; non-conformal Hertzian / non-Hertzian problems and conformal roller / non-Hertzian problems, as illustrated within Figure 2-5:

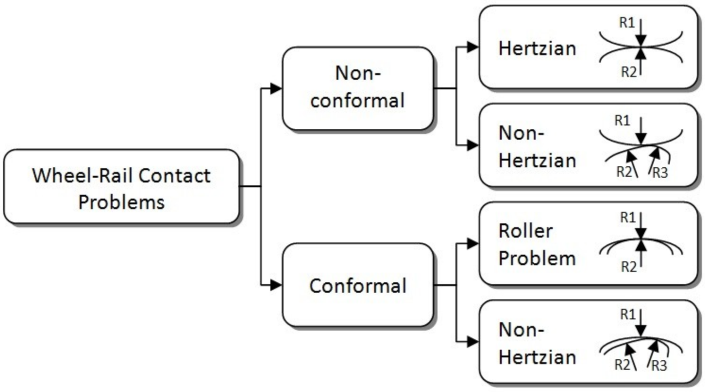

Figure 2-5: Wheel-rail contact problem categories recreated from Wu et al. [36].

Under the assumptions outlined within section 2.2.3.1, the Hertzian theory will give the exact solution for normal contact problems. Despite this, the Hertzian solution is only applicable within cases of non-conformal wheel/rail interaction, typically associated with tread contact on plain rail sections. Violation of the 'half-space' assumption is common within complex wheel to S&C interactions, whereby conformal contact leads to contact patches similar in magnitude to the characteristic dimensions of the contacting bodies. Many authors have studied the variation in contact results between simplified Hertzian and detailed non-Hertzian models in order to assess the validity of the Hertzian model under various contact conditions. Yan and Fischer [37] found that the Hertzian solution provided a surprisingly good match to finite element analysis for a case of conformal gauge corner contact between a UIC S1002 wheel and UIC60 rail profile. A similar case by Wu and Wang [36], however, demonstrated that significant errors arise when variations in contact radii occur within the vicinity of the contact patch. Here, the assumption of smooth-quadratic surfaces was violated, which resulted in errors of up to 72% between the normal contact pressure and contact patch area. Wiest [38] also demonstrated excellent agreement between the theory of Hertz, Kalker's CONTACT model and an elastic finite model for conformal contact on the nose of a cast Manganese crossing.

The results changed significantly when non-linear material properties were modelled, leading to a significantly larger contact area (+25% longitudinal and +75% lateral semi-axes) and an overall reduced normal contact pressure (-42% maximum pressure). Many of the Hertzian assumption are violated during complex wheel-S&C interaction, therefore Hertzian theory can only be assumed to be approximate. Non-Hertzian normal contact models must be studied when considering material degradation at S&C. There are five major types of non-Hertzian contact model:

1. Detailed boundary element methods
2. Finite element methods
3. Multi-Hertzian methods
4. Virtual-penetration methods
5. Winkler foundation methods

Probably the most well known boundary element method for non-Hertzian contact is Kalker's variational model, CONTACT [39]. Kalker's program is based on the principle of complementary virtual work, which minimises the elastic energy potential or maximises the complementary energy over the contact area. The model is built upon elastic half-space influence functions derived by Boussinesq and Cerruti (known as the Boussinesq-Cerruti integral equations) and is discussed in detail within [40]. CONTACT is an extremely flexible tool capable of identifying the shape and size of the contact patch, slip and adhesion regions, normal and tangential surface stresses (tractions), elastic displacements and internal domain stresses. Although widely used and recognised as the current state-of-the-art wheel-rail contact solution, CONTACT has a number of limitations with regards to long-term damage accumulation modelling. Knothe et al. [41] produced a comprehensive paper discussing the advantages and disadvantages of CONTACT. The most significant include:

1. Computation times associated with CONTACT are high therefore it is not yet possible to implement the solution directly within the vehicle system dynamics formulation. Recently, Vollebregt et al. [42] implemented CONTACT as a post-processing tool within the vehicle dynamics package SIMPACK. This has enabled more detailed contact studies to be completed within the multi-body framework and provides improved shear stress and micro-slip distributions for off-line wear simulations. On-line use of CONTACT within the dynamic simulation is still not fully realised.

2. CONTACT only considers the influence of the contacting surfaces when solving the boundary problem, therefore the calculation the sub-surface stresses becomes a post-processing step based on elastic surface stress results. This does not allow for the influence of internal body forces (inertia) on the overall solution.

3. CONTACT is based on the theory of linear-elasticity and is restricted to the half-space assumption. The use of CONTACT for degradation modelling is therefore limited to assessing surface defects only, such as wear and rolling contact fatigue (surface plasticity). Effects of internal material yielding on the overall performance of the contact domain are excluded, therefore excluding the potential for modelling gross plastic flow.

4. Inertial effects are also ignored and hence dynamic impacts, which are of particular interest when considering wheel-rail interaction at crossing noses, cannot be investigated.

A more recognised engineering tool capable of assessing in detail the interaction between two contacting bodies is the finite element (FE) method. Numerous authors have used FE analysis as a means to either validate new contact models or to study limitations within existing models (Wiest et al. [43,44]). FE models are undoubtedly one of the most flexible tools currently available as they are capable of predicting many physical attributes of wheel-rail interaction (*e.g.* temperature effects, non-linear material properties, wear and plastic deformation, highly irregular, conformal and non-conformal contact geometries, frictional effects, third-body interactions, etc...). Unfortunately, significant computation times have limited the use of FE analysis to detailed but isolated studies, pushing the use of multi-body simulation tools to the forefront of wheel-rail interaction research. Many approximate non-Hertzian contact models have been developed to provide an interim solution between simplified Hertzian theory and computationally expensive FE and BE solutions. These solutions provide a degree of accuracy improvement but still contain limiting assumptions with regards to predicting the true phenomena occurring within the contact patch. One such model is the multi-Hertzian technique, which was developed to improve contact modelling within commercial MBS packages. Pascal and Sauvage [45,46] introduced the concept of multiple Hertzian ellipses within a single contact patch upon detection of close contact “jumps”, which is described by a large lateral shift of the contact origin with regards to the overall lateral shift of the wheelset. Load distribution within the contact patch is then approximated using a Hertzian calculation and the known profile penetrations. A multi-Hertzian solution is then achieved by solving a Hertzian calculation at each known contact centre, as presented within Figure 2-6 and Figure 2-7. Although the general shape and size of the contact patch presents an improvement over the standard Hertzian model, the multi-Hertzian technique is still limited to operating within the assumptions for Hertzian contact.

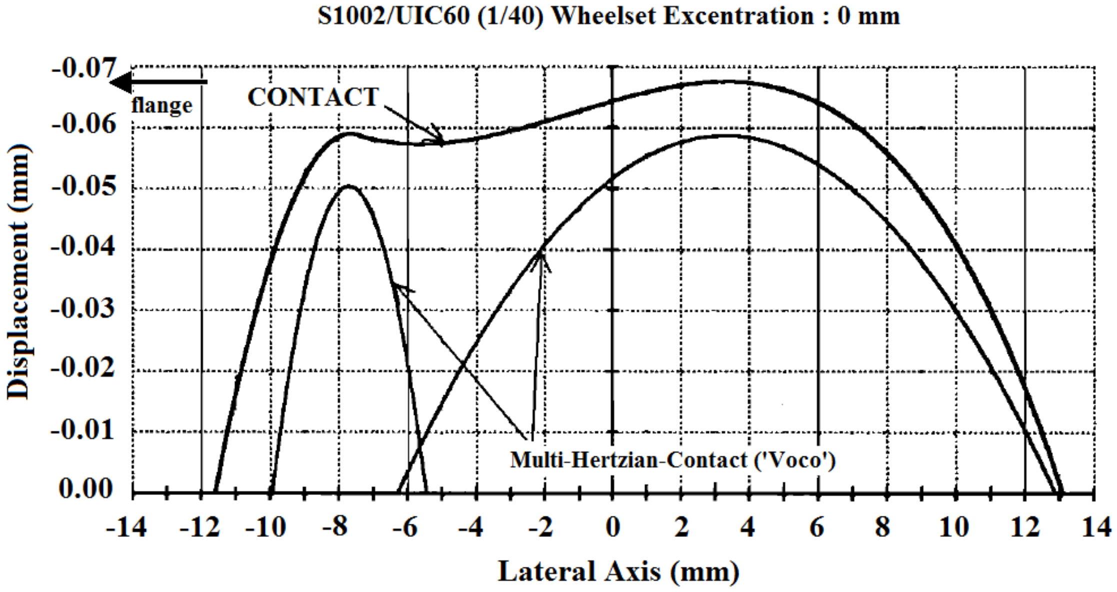

Figure 2-6: Comparisons of the un-deformed distances between profiles, with respect to Y (the wheel reference frame), between Kalker's CONTACT model and the Multi-Hertzian model by Pascal and Sauvage. Image adapted from [45].

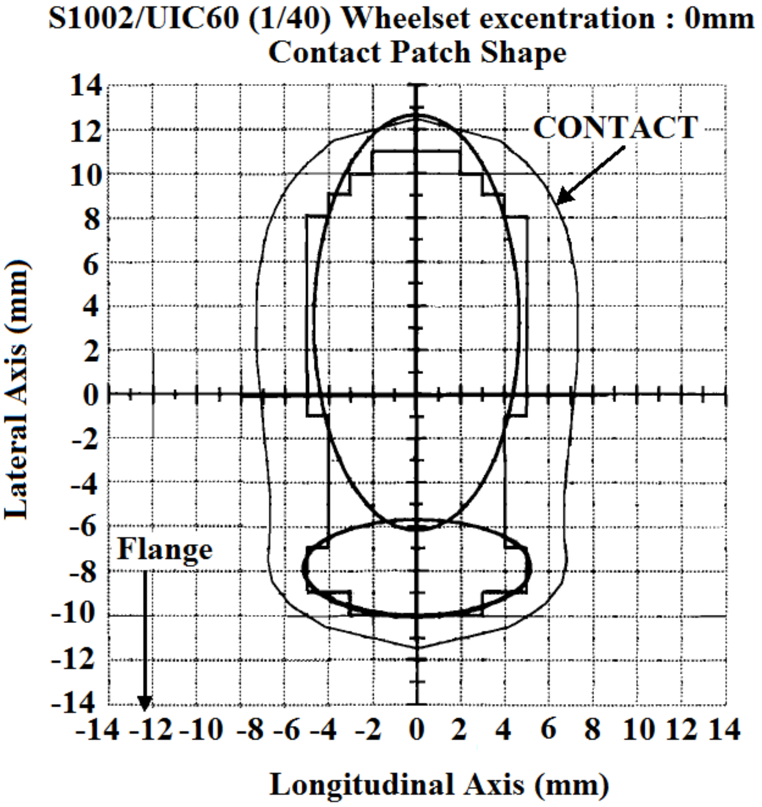

Figure 2-7: Comparison of contact patch shape between Kalker's CONTACT model and the Multi-Hertzian approach. Image adapted from [45].

The next approach considers virtual penetration to provide an estimate of the contact patch shape and size through rigid interpenetration of the wheel and rail profiles. Ayasse and Chollet [47] proposed the computer algorithm "STRIPES", dividing the contact patch into many interpenetrating strips in order to estimate the contact patch area. This "Semi-Hertzian" approach uses Hertzian theory to approximate laterally discrete elliptical normal stress distributions across the longitudinal axis of the contact patch, as illustrated within Figure 2-8. STRIPES provides a further improvement upon the multi-Hertzian approach but can only model longitudinally symmetric contact patches, rendering the technique unsuitable for S&C due to longitudinal variations in the rail profile.

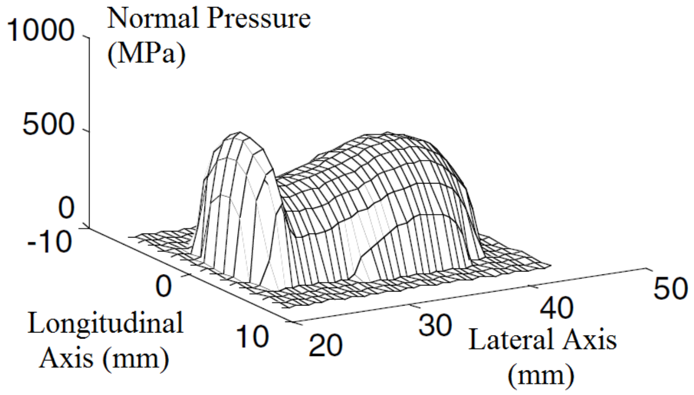

Figure 2-8: Semi-Hertzian contact result presented by Ayasse and Chollet. Image adapted from [29].

The final type of commonly used, non-Hertzian contact model is the Winker foundation, which segregate the contact patch into discrete elastic springs. They are generally found within models for predicting rolling noise due to wheel and rail surface roughness, where they are also referenced as distributed point reactive spring (DPRS) models. DPRS models were originally proposed for three-dimensional contacts by Remington and Webb [48], who concluded that such models were suitable for both low and high speed noise predictions. A somewhat simplified, two-dimensional model was later developed by Ford and Thompson [49], which was also recently implemented by Pieringer [50] for the analysis of noise due to short-wavelength contact irregularities.

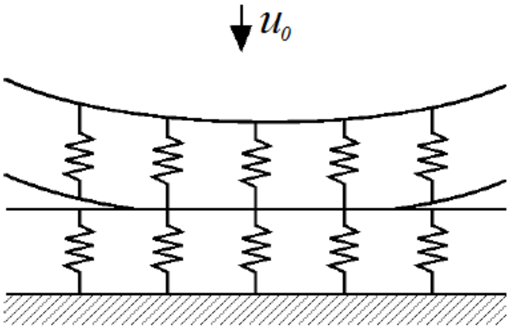

Figure 2-9: Point reacting springs on the running surface of the wheel and rail adapted from [48].

The Winkler foundation solution provides a technique capable of overcoming many of the Hertzian assumptions. These models are particularly good at introducing contact roughness whilst also coping well with both conformal and non-conformal geometries. One significant limitation to the approach comes from the inability model the internal domain and hence sub-surface displacements and stresses.

This review has highlighted that many different wheel-rail contact models exists but, to the authors' knowledge, not one solution alone is entirely suitable for the study of long-term damage accumulation at railway S&C. Hertzian type solutions (*i.e.* Hertzian, Multi-Hertzian and Semi-Hertzian) provide a computationally efficient means of calculating approximate contact pressures and normal forces, which are perfectly acceptable, and indeed desired, within rail vehicle dynamics simulations. On the other hand, such models generate unacceptable discrepancies, with regards to the contact patch shape, size and internal stress distributions, for the study of long-term damage at geometrically complex S&C rail profiles. Non-Hertzian type solutions begin to overcome some of these assumptions but are also constrained by their own limitations when applied to complex S&C interactions.

To realise accurate, long-term material degradation predictions at S&C, this thesis must overcome many of the limitations identified here, either by combining existing solutions or through development of a new, novel wheel-S&C contact model.

2.2.3.3 The Tangential Contact Problem

The normal contact solution alone does not provide enough information to enable the simulation of damage occurring at S&C. For example, wear damage requires both the normal pressure distribution and the relative slip between the wheel and rail, which is obtained through assessment of the tangential tractions, in order to predict wear depths and distributions. Within this section, the tangential effects occurring within the contact patch during the rolling contact process are discussed and their relevance to material degradation studies illustrated. Existing wheel to rail tangential rolling contact models are then reviewed in the context of railway S&C degradation studies.

Research into the tangential behaviour of rolling contact was first completed by Frederick William Carter. In the early 1900's, steam locomotives were being replaced with electric traction with the introduction of main-line electrification and the electric locomotive. It was the purpose of Carter's investigation in 1916 to discuss the 'motive power' of the electric locomotive [51]. As part of his study, Carter identified that the driver was now able to control the vehicle acceleration so that the applied traction was very close to the adhesion limit without exceeding it. Tractive resistance tests were soon conducted, using a New York Central locomotive, from which Carter introduced the concept of 'creepage', the relative slip between the wheel and the rail. Longitudinal creepage values in the order of 1x10^{-6} are associated with normal, dry rolling contact between plain line rail and nominal wheel profiles.

In 1926, Carter went on to develop the first theory of rolling contact. He assessed two-dimensional wheel to rail rolling contact problems by assuming two cylinders with parallel axes in rolling contact, both of like materials and radii but opposite rotational torques [52]. Figure 2-10 *(a)* illustrates the tangential traction distribution limited by the traction bound (μp_z). A no-slip condition is assumed with adhesion at the leading edge of the contact and slip only initiating once the tangential traction ($|p_t|$) locally violates the friction bounds associated to Coulomb's law. Figure 2-10 *(b)* describes the relationship between creepage and vertical contact force.

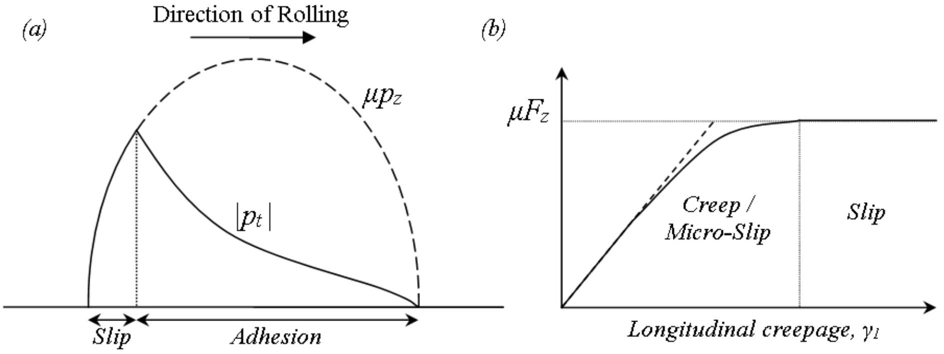

Figure 2-10: Two-dimensional rolling contact as described by Carter: (a) Traction bound μp_z and tangential traction $|p_t|$ (b) Longitudinal creepage γ_l limited by vertical force F_z.

Kalker extended the two-dimensional theory of Carter by including both the lateral and spin creepage, whose values during normal rolling contact are in the order of 1x10^{-3} and 1x10^{-1}, respectively. Using experimental data, Kalker developed a linear creep force theory using contact stiffness coefficients (C_{ij}), which depend purely on the contact patch shape [39,53]. Under the assumptions of Hertzian elliptical contact, the associated linear creep forces, denoted F_X, F_Y and F_T, are obtained by:

$$F_X = -ab\gamma_1 G C_{11} \tag{2-2}$$

$$F_Y = -ab\gamma_2 G C_{22} - (ab)^{1.5}\omega_3 G C_{23} \tag{2-3}$$

$$F_T = \sqrt{{F_X}^2 + {F_Y}^2} \tag{2-4}$$

where a and b are the contact patch longitudinal and lateral semi-axes, γ_1, γ_2 and ω_3 are the longitudinal, lateral and spin creepages and G is the material shear modulus.

This linear theory is still extensively used within railway vehicle dynamics simulation software due to excellent computational efficiency. The next significant contribution by Kalker was his complete theory for three-dimensional rolling contact. Kalker's complete theory was not bound by the Hertzian elliptic contact patch limitation, although the bodies of contact were still described as elastic half-spaces. The complete theory was implemented within his program CONTACT [54], which is still classed as one of the state-of-the-art solutions for rolling contact problems. Despite this, significant computation times have prevented CONTACT from being implemented within rail vehicle dynamics simulations. In 1982, Kalker presented his third significant contribution with his simplified theory for non-linear, three-dimensional rolling contact. This theory was implemented within the algorithm FASTSIM [39], which solved the simplified theory of rolling contact through use of the normal contact pressure distribution and the complete kinematic conditions of the wheelset. Shear tractions, p, and wheel-rail slip conditions, w, are calculated for both lateral and longitudinal directions within a defined contact patch. The longitudinal creepage (γ_1) is used to describe the rotational and absolute wheelset velocities, lateral creepage (γ_2) is adopted to characterise the wheel-rail nonalignment, and the wheel spin (ω_3) considers the conicity of the wheel. Coulomb's Law is introduced to couple traction and slip within the defined contact patch. Polach proposed an alternative approach to Kalker for improving the computational efficiency of the solution [55]. He then introduced modifications to allow for non-linearity of the creep force function by including two reduction factors, k_A and k_S, for the tangential stiffness in the adhesion and slip areas, respectively, as well as a creep-dependent friction model [56]. Contacts experiencing particularly large creepage values, such as in situations common to S&C, do not follow a linear relationship. In these situations, non-linear creep force calculations are required to accurately predict the tangential forces occurring during contact. More recently, Fletcher and Lewis [57] presented a new technique for creep curve measurement using an advanced twin-disc test rig [58]. For very low levels of creep (0 to 1%), results demonstrated a clear dependence of the creep and friction coefficients on the contact conditions (*i.e.* dry or lubricated). Fletcher [59] then went on to develop a new two-dimensional model of rolling-sliding contact creep curves based on experimental results for a range of lubricated contact conditions. Tomberger et al. [60] also published a model for calculating the frictional forces as outputs for online use within vehicle dynamics simulations. In contrast to the conventional approach of defining a constant level of friction, this enabled variable friction to be used throughout the MBS simulation. An overview of the friction model is given within Figure 2-11.

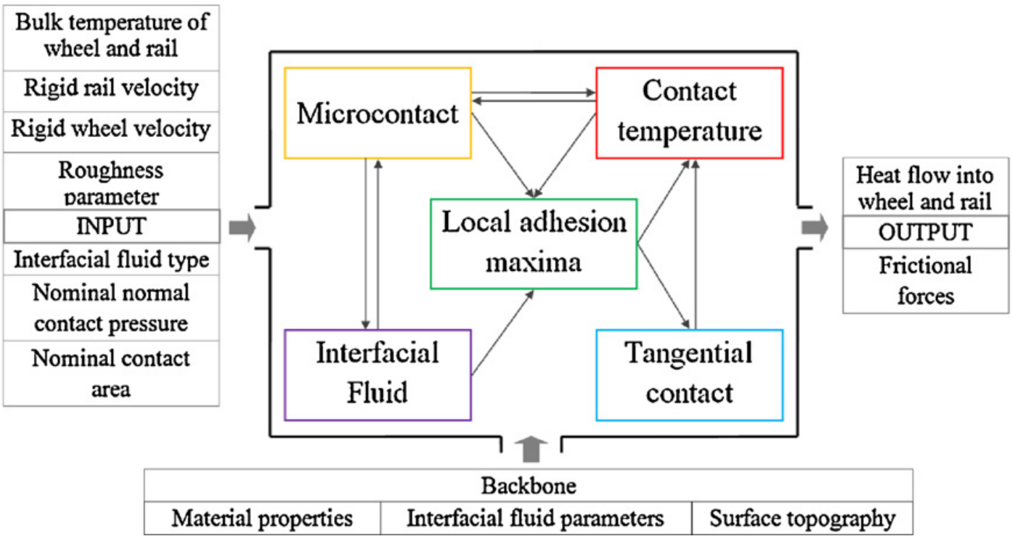

Figure 2-11: Friction model developed by Tomberger [60] as part of the Virtual Vehicle initiative.

The operating conditions found at S&Cs are highly variable, resulting from not only external environmental conditions but also from different types and positions of applied lubrication throughout the system. The ability to implement variable creep curves and hence model accurate frictional forces, based on realistic experimental data, should be considered during the development of a combined tool for long-term damage accumulation at S&C.

2.3 Common S&C Damage Mechanisms

There are a number of different deterioration modes associated with wheel to rail interaction. Sawley [61] categorised these into two distinct categories:

- Category 1 Deterioration Mechanisms:
    - Wear of wheel and rail surfaces;
    - Rolling contact fatigue (RCF);
    - Profile deterioration (by wear and plastic deformation);
    - Thermal damage.
- Category 2 Deterioration Mechanisms:
    - Metal fatigue remote from the contact patch;
    - Brittle fracture.

In the context of UK S&C deterioration, Cornish et al. [13] identified three major Category 1 type deterioration mechanisms, including wear, plastic deformation and RCF, as illustrated by Figure 2-12 *(a)*, *(b)* and *(c)-(d),* respectively. Category 2 type failure modes exist due to more global system conditions, such as track quality (*i.e.* foundation support), manufacturing defects and abnormal loading (*e.g.* impacts). A typical example is cracking at the foot cast crossings, as illustrated within Figure 2-13. Discussions with senior Network Rail engineers has identified that a combination of type 1 and type 2 failure modes within cast Manganese crossing is an area of current significant interest within the UK rail industry, although no published literature studying the problem has been found.

The following sections of *Chapter 2* reviews existing degradation models associated with wear, RCF and plastic deformation along with their applicability to railway switches and crossings.

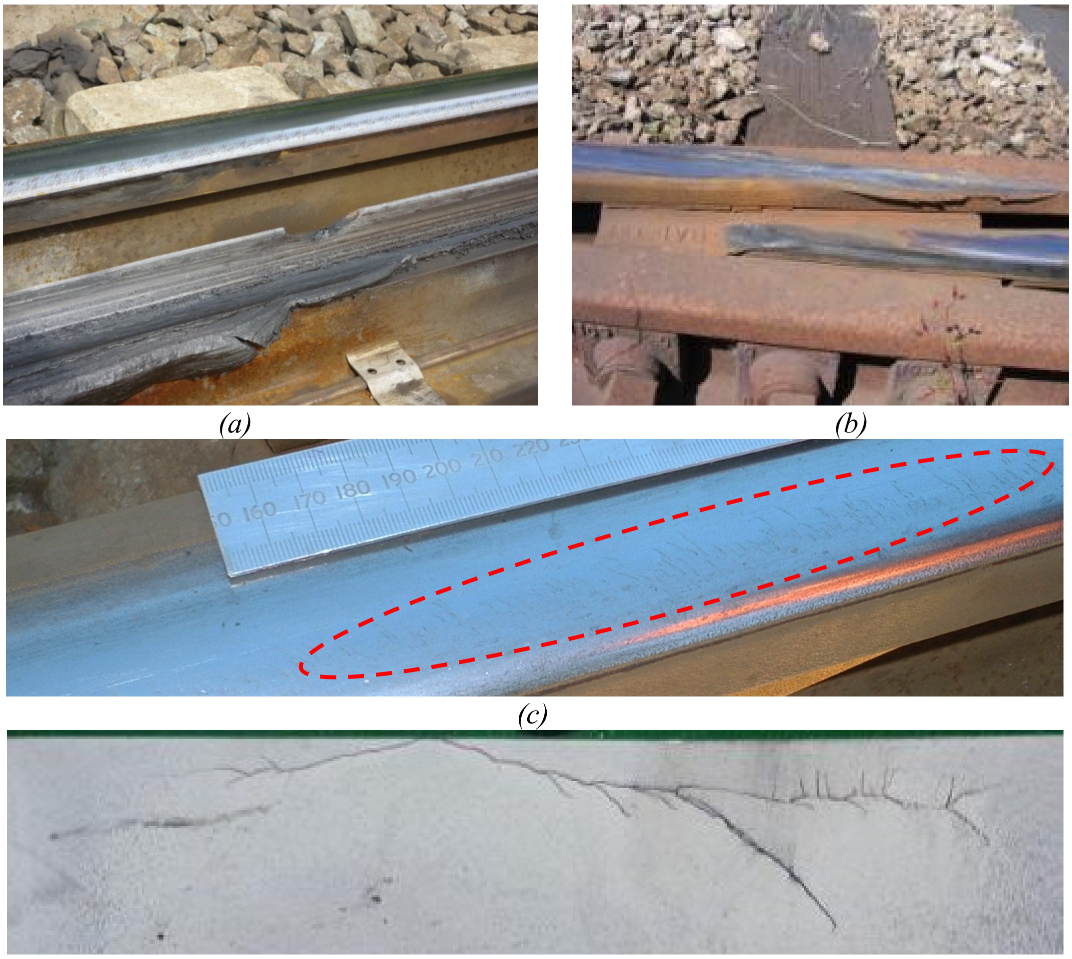

(a) *(b)*

(c)

(d)

Figure 2-12: Common damage mechanisms associated with railway S&C: switch rail damage resulting from excessive wear (a), gross plastic flow observed within a wing rail to crossing nose transition region (b), rolling contact fatigue (RCF) cracks visible from the rail surface (c) and internal RCF branching (d).

Figure 2-13: Cracked cast Manganese crossing.

2.3.1 Wear

The academic field of wear prediction has enjoyed significant research effort over several decades. Meng and Ludema [62] completed a comprehensive survey of over 5400 papers relating to wear models and equations, from which they discovered over 300 different equations covering many different types of wear. From these, three general forms of wear model were perceived, including:

1. ***Empirical equations*** – derived from test data where few test conditions are varied. Empirical equations, such as those presented by Rhee [63], are generally far more accurate within the range of the tests carried out to construct the formula but fall short when applied generally.

2. ***Contact-mechanics-based equations*** – generated as models of a system where the local contact geometries are taken into consideration and general material properties are considered important to the wear process. The most common and widely used example of this type came from the contribution of Archard [64,65]. Archard's wear model evolved from studying the severity of sliding occurring between the teeth of gears. *Equation 4-4* presents the general form of Archard's wear approximation where external parameters (*i.e.* the sliding distance (L) and applied load (N)) are combined with material properties (*i.e.* hardness of the wearing material (H_w)) and a constant (k_w) describing the probability of asperities coming into contact and generating wear particles. Otherwise known as the wear coefficient, k_w is obtained through experiment and varies depending on external factors such as system lubrication.

$$Q = \frac{k_w N L}{H_w} \tag{2-5}$$

An alternative to the Archard wear model is the energy wear approach whereby the wear material removal is related to the friction energy dissipated through the contact interface. The relationship is shown in Figure 2-14 and a recent example is presented by Fouvry et al. [66].

3. ***Equations based on material failure mechanisms*** – these forms of wear approximation are generally more complex and recognise that the resistance to wear is not just a combination of basic material properties and external influencing factors. They also consider factors such as plastic deformation, fracture toughness and fracture strain to model directly the physical behaviour of the contact interface. Some examples include delamination theory, asperity deformation models and oxidation (corrosion) wear models. Due to the highly complex nature of material failure mechanism equations, no examples have been reproduced here.

Wear is the most common form of degradation occurring at the wheel to rail interface and has therefore been the focus of many previous studies. Of these, the most common research area is that of wheel wear accumulation. This is due to having available entire data sets of wheel contact results from single vehicle dynamic simulations that are many kilometres in length. In contrast, predicting damage at discrete locations on the track would require many thousands of simulations to build a load history of rail contact results, adding to the computational effort and complexity of the overall problem. This can be amplified further if degradation of a complete stretch of track (or S&C unit) is required. Pearce et al. [67] first implemented a simplified wear accumulation model based on energy dissipated within the contact patch. The calculation related the wear index ($T\gamma$) with material volume loss from the profile radius. A simulation of wheel wear on a high mileage P11 profile was made, using a route no longer than 1100km for computational efficiency purposes. Good qualitative agreement between measurements and predictions were achieved. More recently, Braghin et al. [68] published a methodology incorporating the Hertzian normal contact solution coupled with Fastsim to obtain a discrete wear distribution. A wear law was developed based on experimental twin disc tests, which was implemented within an overall routine for wheel profile evolution. The wear depth profile is then summed at each time step before updating the wheel profile at a frequency related to a maximum accumulated wear depth threshold.

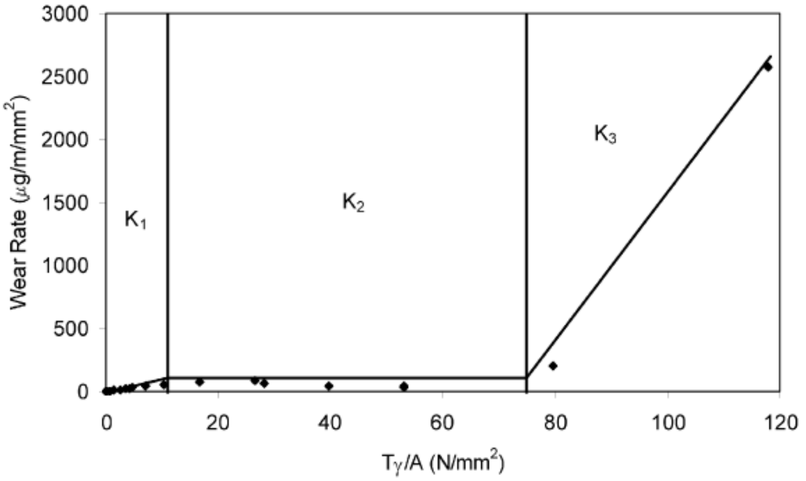

Figure 2-14: Wear rate law based on energy dissipated (Tγ/A) within the contact patch adapted from [68].

Fries et al [69], and more recently Li [70,71], associated wheel and rail wear with four main categories, each related to contact patch parameters; load history, contact geometry, material properties and environmental conditions. Each of these parameter categories has an effect on the prediction of wear and must therefore be considered within any chosen model for wheel to rail degradation studies. The load history considers variations in the normal and tangential contact forces within the contact patch as a result of vehicle parameters, such as axle-load and velocity, in conjunction with the geometry of contact, determined through parameters associated with the wheel and rail profiles. Load history and contact geometry are therefore coupled during the wear simulation process. Material properties and environmental conditions, in most applications, are considered constant during many wear modelling processes. Different rail steels and lubrication conditions (*i.e.* water, oil, grease, dry, etc...) present within S&C require a computational tool capable of taking both material properties and environmental conditions (*e.g.* friction) as input variables.

Telliskivi presented a methodology for predicting wear using a Winkler foundation formulation for a cylindrical roller case [72], which was validated against well known dry wear disc-on-disc testing. This simple model was subsequently modified the account for railway wheel to rail contact [73]. Archard’s sliding wear law was implemented through the calculation of the slip distance using elastic contact displacements and rigid body motions.

2.3.2 Plastic Deformation

Despite being one of the most prominent mechanisms to causing shape degradation of the rail profile, there seems to be very few publications with regards to simulating gross plastic flow within S&C. Large wheel-rail interaction forces, especially those associated with S&C, can lead to situations where both the surface and domain stresses exceed the elastic limit of the rail material. These high values of stress generally result from large axle loads, unconventional contact patches (*i.e.* due to irregular local contact geometries) and the amplification of contact loads due to dynamic effects, such as impacts occurring at rail joints and crossing noses. Repeated loading above the material elastic limit is often assumed to result in elastic-shakedown, whereby, after only a few load cycles, a build-up of 'protective' residual stresses and strain hardening enable the material to support loads in excess of the material yield strength [74]. Increasing contact loads can then enter the plastic-shakedown region where cyclic plastic strains occur over a hysteretic cycle without any strain accumulation. Finally, as loading increases further, the material enters the 'ratchetting' region where plastic strains accumulate during each load cycle (wheel pass). The four material responses to cyclic stresses were discussed by Mazzu [75] and are illustrated within Figure 2-15.

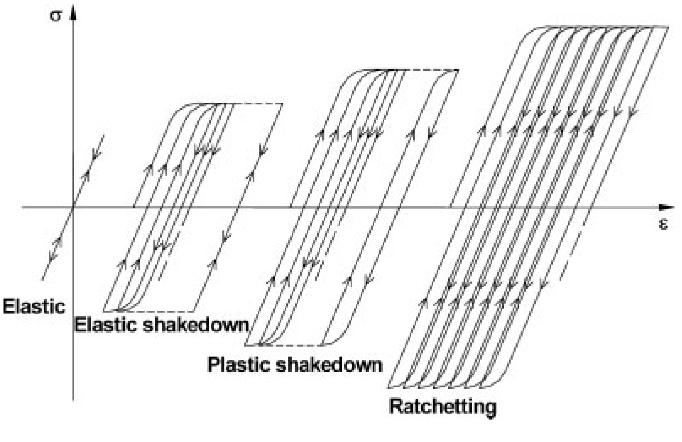

Figure 2-15: Material shakedown curves within elastic and plastic regions [75].

Almost all publications concerning gross plastic flow and material hardening of railway rails discuss the use finite element simulations, with a large proportion studying damage associate with plain line railhead sections. Although focussing on RCF; Ringsberg [76,77] used an FE approach to simulate residual stress and plastic strain fields within railheads. The material model implemented allowed for the prediction of shakedown limits and strain rate estimations. Kapoor et al. [78] presented a validated model of plastic strain accumulation in rail steel under repeated wheel–rail contact. Plastic-shakedown was investigated with regards to contributing towards both wear and RCF crack growth mechanisms. The model was based on a ratchetting law derived from experimental twin-disc tests and was capable of simulating tens of thousands of ratchetting cycles and the associated material strain hardening with reasonable computational efficiency. Typical simplifications were assumed, including a 2D approximation, Hertzian normal contact pressure and non-varying, single point of contact. Several material models were investigated and compared against experimental results for strain accumulation and strain hardening. It was concluded that for accurate simulation of the material response to ratchetting behaviour, a well defined stress-strain curve generated under high hydrostatic pressure (*i.e.* from compression testing as opposed to tensile testing) is the key to successfully modelling plasticity effects associated with wheel-rail contact. Busquet et al. [79] developed a three-dimensional elasto-plastic FE model of rolling contact along the head of a UIC60 rail type. Plastic deformations within the near-surface layer were computed as a function of the traction coefficient and were qualitatively correlated to micro-structural observations of plastic flows within real railheads and existing theoretical studies. The entire procedure for the simulation of stress and strain within the railhead was discussed within [80]. Wen et al. [81] used an FE approach for simulating plastic flow on the crown of a section of plain line rail. The aim of Wen's study was to investigate the influence of partial slip conditions and used Kalker's CONTACT model to provide the true contact patch shape and the magnitudes of tangential tractions within it. Brouzoulis [82] recently developed a 2D elasto-plastic FE analysis in conjunction with a 3D local contact analysis using the commercial package Abaqus. The technique enabled the simulation of plastic ratchetting and hence the prediction of material relocation at the lower gauge corner of plain line rail (also known as lipping).

Very few authors have tackled the plasticity problem whilst considering S&C rail profiles due to the complexity of the problem and the computational effort required. Foletti et al. [83] presented a numerical 3D model specifically for the study of ratchetting damage of a tramcar line. The vehicle dynamics software MO.N.S.TRAM (developed specifically for modelling tramway vehicle dynamics) was used to provide inputs to Kalker's CONTACT model. The stress field within the contact region was then used as input to an in-house ratchetting model. One significant limitation of the process comes from the restrictions associated with the CONTACT model, whereby the contact stress inputs to the damage model are generally overestimated due to considering elastic material behaviour. More specific to railway crossings; Wiest et al. [44,84] presented a simplified FE model for wheel to crossing nose interaction. To aid computational efficiency, the model geometry was reduced to a single crossing nose cross-section, 500 mm in length, containing an artificial 'dip' in order to simulate an equivalent dynamic impact. This model studied the effect of material properties and track foundation stiffness on the impact loading and the cyclic material response (ratchetting) at the crossing nose. Pletz et al. [85,86] recently published developments regarding an explicit finite element model for assessing dynamic wheel-rail impacts on a crossing nose. The model consisted of a short section of a 1:15 UIC60 type crossing (*i.e.* ±1.5 m either side of the crossing nose), a single UIC S1002 type wheel and focussed on the dynamic interactions within the wing rail to crossing nose transition region. Further discussion regarding the benefits and limitations of the model by Pletz can be found within *Chapter 7* of this thesis.

Despite the contributions of the aforementioned authors, significant non-linearity and small mesh sizes (*i.e.* many hundreds of thousand elements) result in excessive computation times associated with the FE approach, which, due to current computational power, restricts its use to very specific track locations. Model simplifications are therefore common, limiting many procedures to very specific contact conditions. Many of the solutions discussed also require an interface between various numerical tools to obtain sufficiently detailed predictions of wheel-rail interaction phenomena. The influence of co-existing modes of degradation, such as wear and RCF on plastic deformation (and vice versa), are also excluded from existing modelling techniques due to the focus of study being limited to individual modes of degradation.

2.3.3 RCF Modelling

RCF crack growth modelling does not fall within the scope of this PhD thesis but the associated, advanced contact modelling tools indeed do. A review of existing computational tools for RCF prediction is therefore included within *Chapter 2* for completion. The review will also investigate whether existing techniques for RCF prediction can be adapted for modelling lateral rail damage.

RCF is not a phenomenon unique to wheel-rail contact and many authors have investigated RCF modelling outside the railway application. For the purpose of this review, a range of models developed specifically for railway wheel-rail contact modelling are discussed. There are two main types of RCF model; theoretical and empirical. Theoretical models are those that attempt to predict the magnitude of an event, such as RCF crack growth models. On the other hand, empirical models are based upon relating modelling outputs to experimental measurements in an attempt to predict the likelihood of the event occurring. Both of these approaches have advantages and disadvantages depending on how and to what problems they are applied to. The most well known and industrially accepted empirical model for RCF prediction is the Whole Life Rail Model (WLRM), which was developed by Burstow et al. in 2003 [3]. The study compared a variety of parameters obtained from rail vehicle dynamics simulations of two sites with known RCF problems; Acton and Ruscombe. Results indicated that a parameter derived from the wear number, $T\gamma$, gave the best correlation between RCF damage simulation and crack location. Figure 2-16 illustrates the bi-linear RCF damage function as proposed by Burstow [87]. In summary, a $T\gamma$ value <15 results in no damage, 15>75 equates to RCF only, 75>175 indicates the transition from RCF to wear whilst values >175 result in severe wear, removing all surface cracks before RCF can initiate.

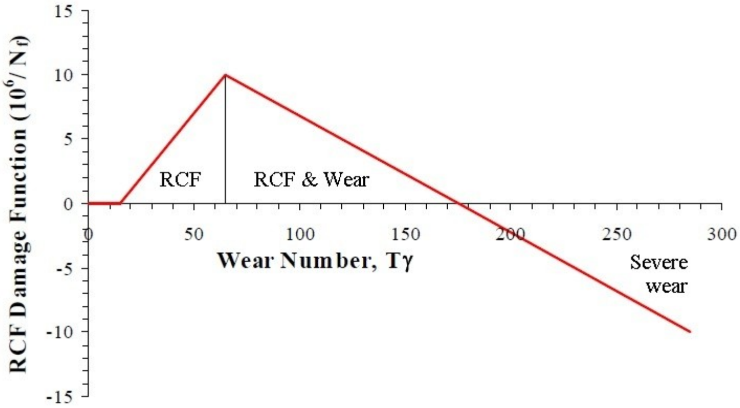

Figure 2-16: Bi-linear RCF Damage Function for 220 Grade Rail Steel. Image recreated from [87].

The WLRM deals with an empirical approximation to the likelihood of RCF and / or wear occurring. Other modelling techniques make the assumption that RCF cracks already exist and therefore model the rate of crack growth under various loading conditions. Figure 2-17 demonstrates the different mechanisms of RCF crack growth, including shear driven, hydraulic pressure transmission, fluid entrapment and squeeze film fluid action. A detailed description of each mechanism can be found within [88].

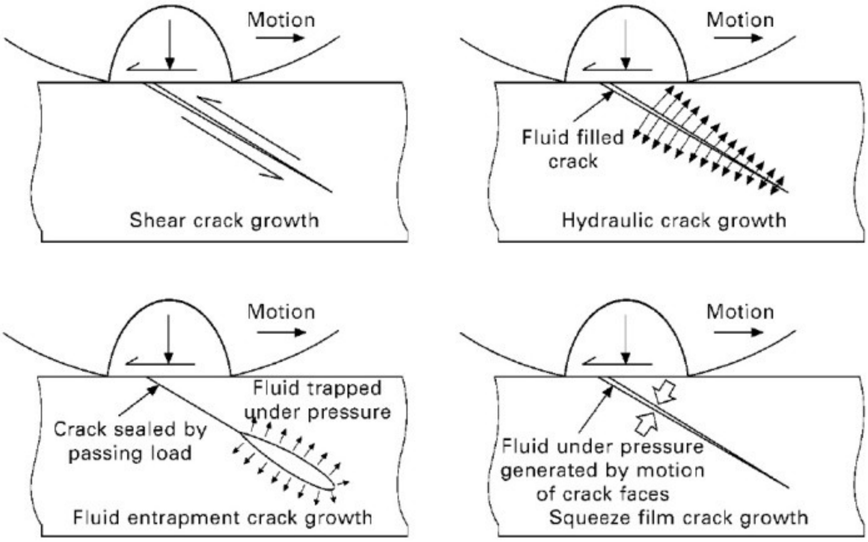

Figure 2-17: RCF crack growth mechanisms [88].

Balcombe et al. [89-92] developed a novel method for coupling fluid pressure and crack deformation for modelling the rolling contact fatigue behaviour of fluidised cracks. The technique, as illustrated within Figure 2-18, utilised the boundary element method with coupled fluid and solid solvers. A detailed description of this state-of-the-art solution can be found within [92]. Lubrication conditions within wheel-rail interaction problems are synonymous to boundary fluid films therefore, due to currently simulating a full fluid film, using such a model for wheel-rail interaction should be carefully considered.

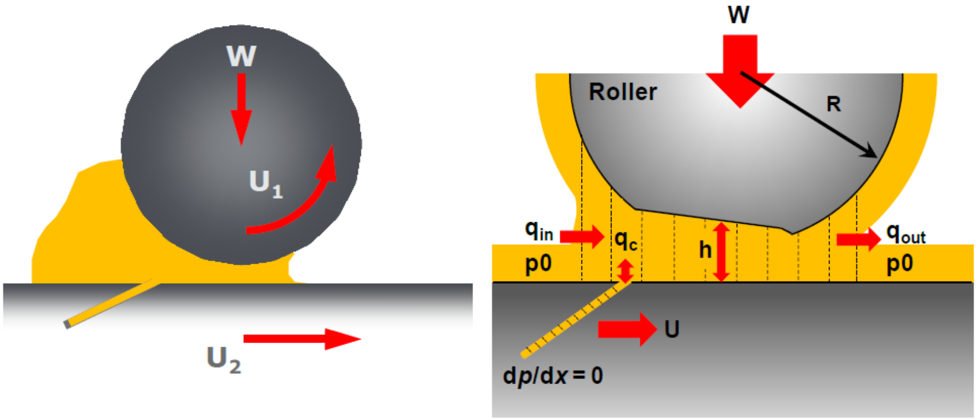

Figure 2-18: Schematic of the Elastohydrodynamic Lubrication (EHL) model [92]

A significant contribution to the understanding of mechanisms associated with rolling contact fatigue came from the University of Sheffield. In 1999, Fletcher and Beynon [93] presented a simple method for predicting stress intensity factors at fluid-pressurized inclined surface cracks, synonymous with rolling contacts. Fletcher and Beynon subsequently published developments associated with an advanced twin-disc test rig for investigating the physical processes taking place during rolling contact fatigue [58]. A series of rolling contact experiments soon followed, including the effects of contact pressure variation [94], un-lubricated rolling-sliding [95] and the effects of intermittent lubrication [96], to name just a few. The developments of numerical models, validated against the results from the twin-disc test rig, were presented throughout the following decade. Frolish et al. [97] discussed a new model for predicting the growth and branching of RCF cracks. Good quantitative agreements were achieved with test samples examined under optical, scanning-electron and back-scatter-electron microscopy. Kapoor and Franklin [98] developed and presented a technique for estimating the wear rate of a ductile material subject to cyclic rolling/sliding contact. The model divided the rail domain into thin, sub-surface layers that accumulated plastic shear deformation. Wear of the top layer would occur when critical values of plastic strain were reached, causing wear debris through ratcheting failure. The computer program 'Dynarat', also known as the 'brick' model, was first published by Franklin [99], who further discretised the 'layer' model by including an array of sub-surface elements to enable isolated failures to occur (as opposed to entire surface layers). Plastic accumulation could now occur within individual elements, allowing the effects of microstructure on ratchetting failure to be investigated. The integrity of each element is assessed against the magnitude of the plastic accumulation, with weakened elements representing a finite crack or region susceptible to crack initiation, as illustrated within Figure 2-19. Fletcher et al. [100] went on to publish work concerning a ratchetting based computer simulation for the simultaneous investigation of wear, crack initiation and early crack propagation. The next stage in development converted the model into a '2.5D' model, considering a 3D Hertzian stress distribution traversing the underlying 2D model. Fletcher and Kapoor [101] presented the model and discussed benefits such as the ability to model a contact patch running alongside a crack rather than directly across it, which is synonymous to interactions concerning newly turned wheels or ground rails.

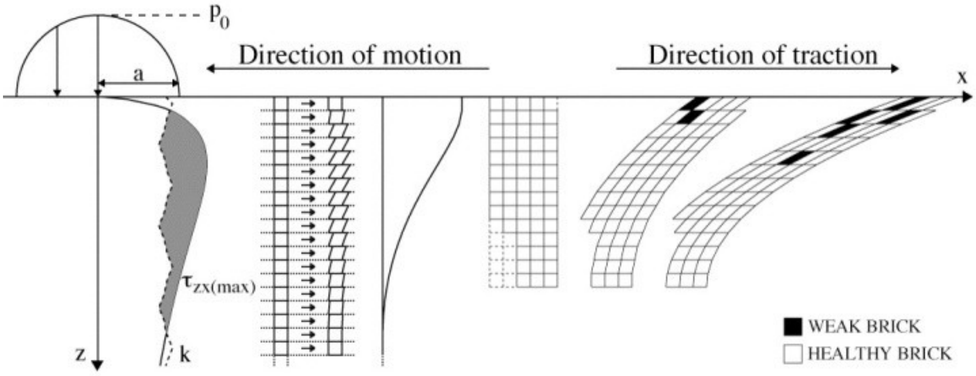

Figure 2-19: RCF predictions using the 'brick' model [102].

Fletcher et al. [103] validated the ‘2.5D’ model using a full 3D FEA and BEM model with very good agreement being found. An alternative model for RCF crack growth simulation was also presented by Fletcher et al. [104], which used the already established boundary element software package FRANC3D for modelling three close proximity cracks within the rail head, as illustrated within Figure 2-20. Results demonstrated that the proximity of the cracks (10 mm radius crack separated by 10 mm) had a profound effect on the mode I and II stress intensity factors during rail bending.

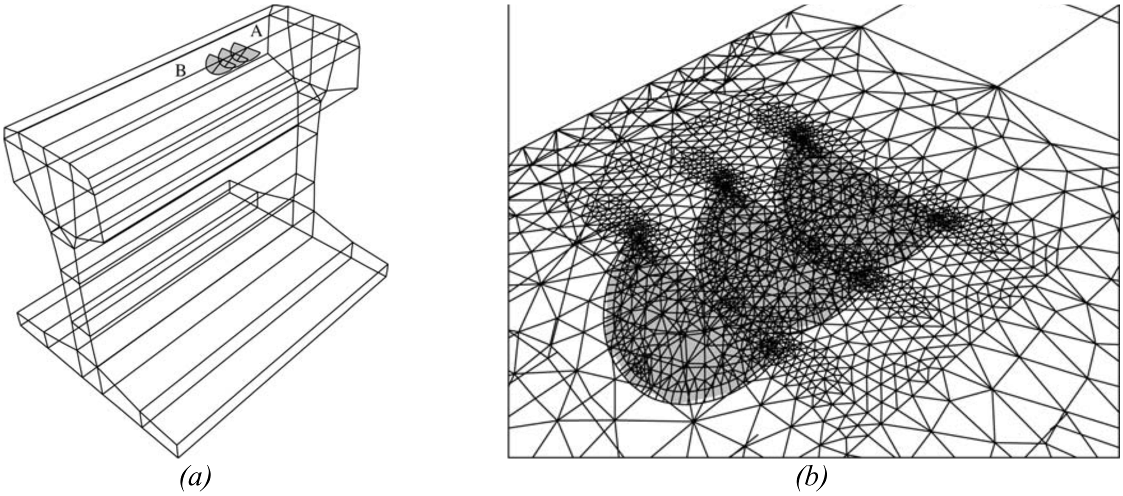

Figure 2-20: Rail geometry modelled by Fletcher et al. [104] illustrating three rail head cracks (a) within the boundary element software FRANC3D (b).

Despite the exclusion of RCF crack growth modelling within this PhD thesis; the successful application of various computational models relating to complex wheel-rail interaction gives confidence that a combined solution for modelling lateral rail damage (*i.e.* wear and gross plastic flow) at S&C is indeed a feasible concept.

2.4 State-of-the-art S&C Damage Simulation

Expenditure on track infrastructure is the major costs for railway infrastructure managers, which has not seen any significant change over the past 30 years [105]. With continuous demand for a more cost effective railway, innovative research to solutions for many track related problems is becoming more prominent. In September 2006, a joint European research project for innovative track technologies, named 'INNOTRACK', was initiated to help drive down significant investments and maintenance related infrastructure costs within the rail industry. The project was divided into a matrix structure, as illustrated within Figure 2-21, and an executive summary of the entire project can be found within [105]. Sub-project 3 (SP3) is of significant interest to this thesis because many state-of-the-art solutions for addressing performance issues at S&C were developed. Some examples include the use of railway vehicle dynamics simulations to redesign the S&C layout, improve foundation support and to optimise component geometries. Investigations into novel S&C materials were also ongoing at the time of writing this thesis.

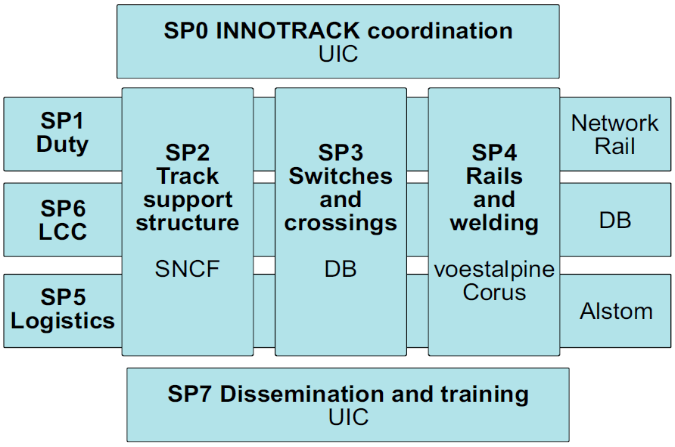

Figure 2-21: Structure of the INNOTRACK project [105].

From all of the technologies emerging from the INNOTRACK project, the development of a combined vehicle dynamics and rail material damage simulation process is of significant interested to the aims of this thesis. Modelling the degradation of railway wheels and rails during service is an area of research that has become more prominent. Technological advances in computer hardware, such as multiple-processing and the availability of large amounts of memory, have now enabled large and complex simulations to be run with acceptable levels of computational efficiency. The simulation of damage occurring at the wheel to rail interface consists of three sub-systems; a vehicle to track dynamics model, a wheel to rail contact model and a material degradation model. As part of INNOTRACK SP3, Nicklisch et al. [21] developed a methodology that incorporated several independent tools for assessing each of these sub-systems. Figure 2-22 illustrates the overall simulation procedure, which was demonstrated through investigating rail profile degradation at the crossing nose of a turnout in Haste, Germany. Predictions of wear and plastic deformation were compared with measurements taken for a 5 week period of mixed traffic. Results demonstrated a good agreement between the simulated and measured profiles.

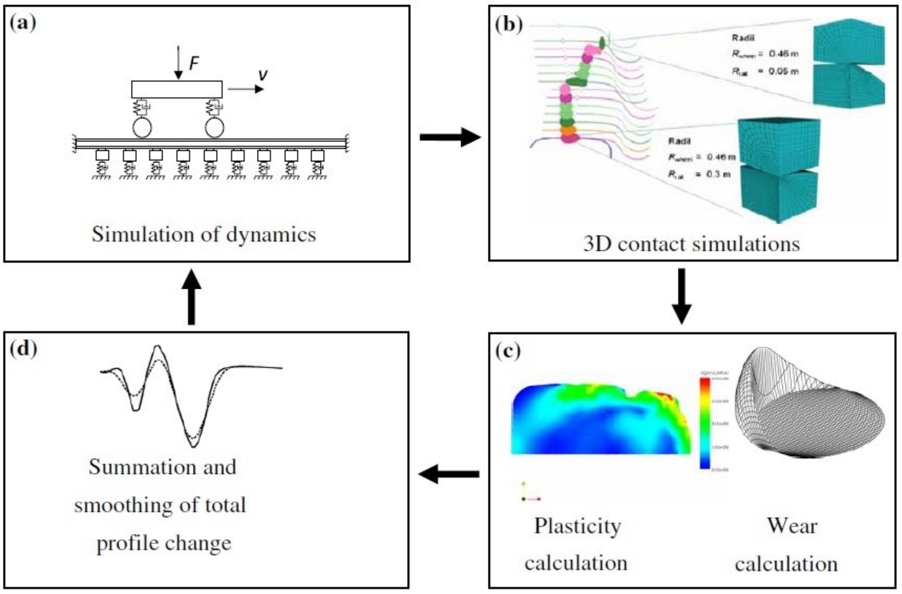

Figure 2-22: Rail damage simulation as implemented within the INNOTRACK project by Nicklisch et al. [106].

The methodology combines the use of two independent ABAQUS non-linear finite element models during simulation steps (b) and (c), a combined FASTSIM and Archard's wear model for wear simulation during step (c) and another separate routine for updating the total rail profile change during step (d). Four different tools are therefore required to achieve total damage accumulation, resulting in a sophisticated yet complex process with many interventions required by the user. As described by Nicklisch, the methodology provides a powerful tool for simulating the effects of vehicle type, track design and material on the expected life of the rail. For such a methodology to be of practical use to rail maintenance managers and track maintenance engineers, it is the authors' view that a solution combining stages (b) to (d) should be investigated. This will:

- Improve wheel to rail contact point detection by removing the reliance on simplified MBS detection routines.

- Reduce the number of manual interfaces between critical modelling stages and hence improve the overall computational efficiency and ease of use. This will also remove the possibility of errors being introduced during data conversion between different modelling tools.

- Provide a tool capable of combining the effects of numerous modes of degradation on the overall change in rail profile. The current state-of-the-art solution simulates individual modes of degradation separately, only combining the effects of each mode after a defined number of load cycles. A combined tool will enable interrelated modes to be investigated.

2.5 Discussion

2.5.1 Brief Overview of the Literature

The problem concerning wheel-rail interaction has enjoyed many years of research effort, which has inevitably resulting a variety of modelling tools and techniques being developed. Many are accompanied by simplifying assumptions that are justified by the nature of their application. This literature review has explored each stages of the problem, from contact point detection to material degradation simulations, and critically examines their limitations when applied to railway switches and crossings.

Contact point detection routines are used within railway vehicle dynamics simulations and therefore contain simplifications to ensure computational efficiency. Many of these simplifications have an adverse effect on the true detection of contact within complex S&C geometries, leading to inaccurate or false points of contact being identified.

There are two major types of normal contact stress solution, simplified Hertzian and more detailed non-Hertzian, each with their own benefits and limitations depending on their intended application. Hertzian solutions are very efficient and provide acceptable results in circumstances where each of the theoretical assumptions is satisfied. Unfortunately, these assumptions are commonly violated at S&C due to irregular and constantly varying rail profiles. Non-Hertzian models provide an increase in accuracy by overcoming one or more of the simplifying assumptions of Hertz, usually at a computational cost. It has been shown that, although five major types of non-Hertzian solution exist, none fully satisfy the requirements for accurate long-term simulation of S&C rail damage.

There are three critical modes of degradation associated with S&C, including wear, plastic deformation and rolling contact fatigue. A wide range of computational tools exist for predicting individual damage modes but none capable of simulating multiple and hence the influence of interrelated modes.

2.5.2 Knowledge Gaps and Opportunities

From a comprehensive review of existing literature, several key knowledge gaps have been identified:

- Existing, state-of-the-art S&C studies rely heavily on MBS tools, although the representation of wheel-rail contact in such models is not sufficiently accurate for S&C analysis. There is an opportunity to develop a novel contact detection model that overcomes significant limitations, such as detecting accurate contact locations during circumstances of conformal contact.

- Whilst significant effort has been put into assessing the validity of different wheel-rail contact models for contact detection, stress analysis and material degradation, a single tool combining all of these critical modelling stages is yet to be developed. More significantly, a large proportion of existing tools contain simplifying assumptions, resulting in unacceptable limitations when applied within long-term S&C degradation studies. There is an opportunity to develop a combined tool to provide an integrated solution suitable for S&C modelling.

- Perhaps due to the complexity of the problem, both plastic deformation and inertial effects (impact) are neglected from existing wheel to rail contact models. However, frequent and large wheel-rail contact forces lead to both of these effects occurring throughout the S&C. Existing models used for predicting rail damage accommodate only one major type of damage mechanism, commonly a wear model, for simulating rail profile evolution. This has led to the use of independent tools, usually incorporating commercially available yet computationally expensive FE analyses, within current state-of-the-art studies. There is an opportunity to develop a new modelling approach capable of combining wear, plastic deformation and the effects of impact on long-term S&C degradation.

- A combined tool catering for all critical modes of degradation at S&C would present a further opportunity to investigate the interrelationships between modes.

- Degradation of cast manganese crossings is of worldwide interest to railway infrastructure maintenance managers. An assessment of the contact performance of cast manganese crossings with regards to contact geometry, impact forces and material performance does not exist.

2.5.3 Next steps

Whilst several opportunities have been identified within this critical review, it is not deemed possible to address them all within this thesis alone. This thesis therefore aims to bridge the following knowledge gaps:

1. ***Remove limitations associated with existing wheel-rail contact models*** by developing an integrated routine for wheel-rail interaction and material degradation. Known limitations with existing tools, with regards to complex S&C problems, will be addressed. This will provide a base model for tackling subsequent knowledge gaps.

2. ***Develop a novel wheel-rail contact model specifically designed for S&C interaction studies.*** The model should be capable of simulating complex, non-Hertzian contact patches whilst also accommodating numerous modes of degradation associated with S&C.

3. ***Study in detail the interaction between railway wheels and cast manganese crossings*** to acquire new knowledge on contact trajectory, impact loading and material performance. This will provide a parallel study, focusing on detailed wheel-rail interaction through UK crossings, during the development of items (1) and (2), above.

Chapter 3 : S&C Contact Point Detection

Chapter 3 initiates the development of an integrated routine for wheel-rail interaction and material degradation by first considering the geometric problem of contact point detection. A novel algorithm for multi-point contact, with particular attention to railway switches and crossing, is presented. A description of each stage of the process is given whilst discussing how current limitations within existing contact detection routines are addressed. Both theoretical and a novel experimental validation process is given before presenting theoretical examples to demonstrate the achieved benefits.

3.1 Background

This chapter focuses the geometric problem of wheel-rail contact point detection by demonstrating a new algorithm suitable for use at the wheel-S&C interface. This is a vital step in the developing a combined tool for wheel-S&C interaction due to the existing limitations residing within commercially available MBS software (*i.e.* limitations discussed in detail within *Chapter 2*). Investigation of this problem provides an advanced in-house contact detection tool that is capable of detecting multiple (*i.e.* more than two) contact locations between the wheel and complex S&C rail profiles. This in turn will provide a sufficiently accurate platform for integrating subsequent critical stages in the S&C rail profile degradation process. Implementing a mixture of both analytical and numerical techniques, the algorithm demonstrates the capability of accurately detecting multiple contact points (including tread, flange and flange-back contact) for both conformal and non-conformal contact conditions. Figure 3-1 illustrates the overall pseudo-code, which has been implemented within a MATLAB code [107].

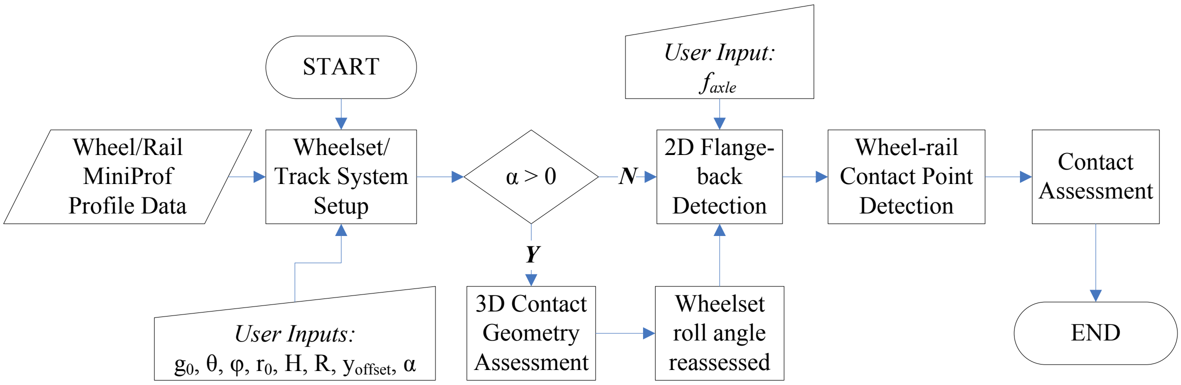

Figure 3-1: Wheel-rail contact detection algorithm flowchart.

3.2 Wheelset/track system setup

The wheelset/track system setup stage of the algorithm represents a simple pre-processing step, capable of taking any measured wheel and rail profile and automatically detecting a common datum point prior to positioning the profile pairs relative to each other. Figure 3-2 illustrates the parameterisation of the wheelset/track system, allowing 6 degrees of freedom (x, y, z, ψ, β, α) manipulation of the wheelset and 3 degrees of freedom (y, θ, ϕ) positioning of the rails. The datum points used for positioning the wheel relative to the rail include the UK rail gauge point, located 14 mm below the crown of the rail, and the nominal rolling radius of the wheel, located 70 mm from the wheel flange-back. These parameters, along with additional geometric constraints, are used to translate the raw profile data into a common track coordinate system through use of transformation matrices and translation vectors. For a comprehensive description of the process, see the work of Pombo [33].

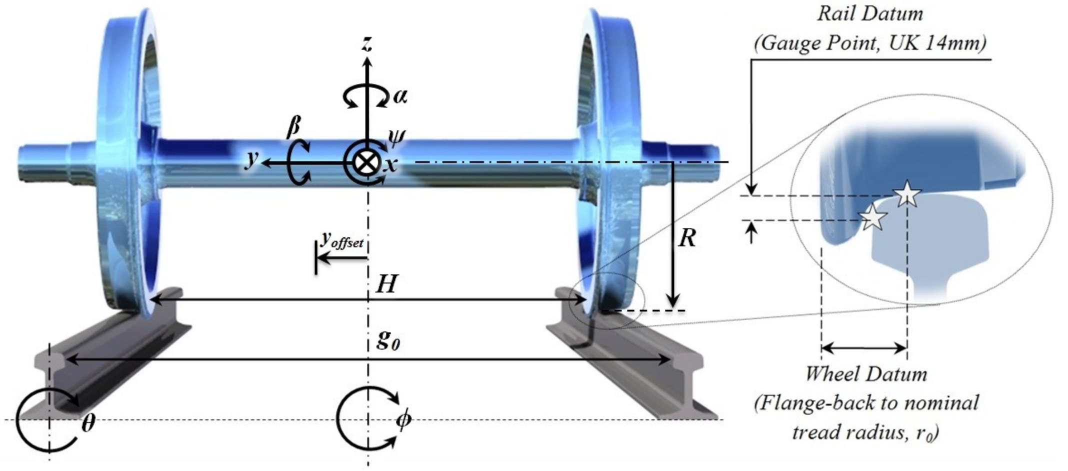

Figure 3-2: Wheelset and track degrees of freedom including wheel and rail common datum points.

3.3 Three-dimensional analysis

To account for a general state of a wheelset, including effects of wheelset yaw (α), on the location of contact, a three-dimensional rail geometry analysis has been developed. Upon existence of a wheelset yaw angle, a three-dimensional rail surface is constructed for both the left and right rails. This is achieved by importing preceding and succeeding rail profiles and positioning them within the track coordinate system relative to the original central rail profile. A regular grid spanning the length and width of the profiles is generated and used to create a surface profile matrix. Since real measured profiles are adopted in this investigation, the quality of the surface fit has been significantly improved by (a) dividing each rail profile into common segments with a common number of lateral data points to avoid linear interpolation irregularities, and (b) generating intermediate data points longitudinally between profiles through weighted linear interpolation, which assigns an incrementally increasing influence of the approaching rail profiles shape during the interpolation process. Once the rail surface has been constructed, the original wheel profile (broken line in Figure 3-3) is included and yawed about the origin of the wheelset coordinate system.

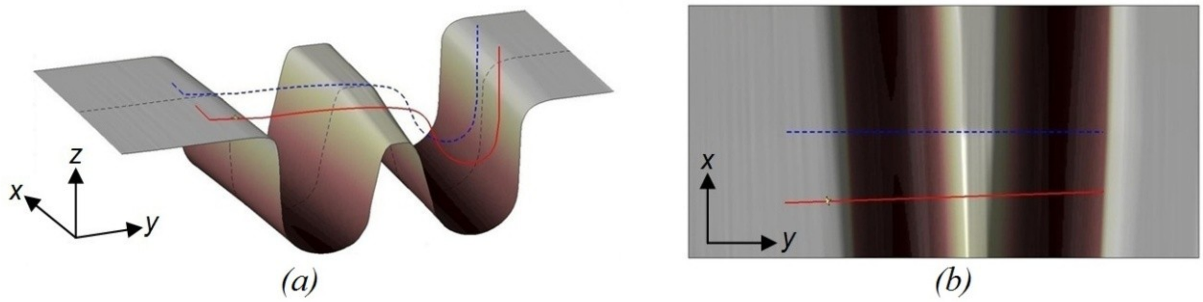

Figure 3-3: 3D rail surface profile showing original (broken line) and yawed (solid line) wheel profiles (a) isometric view (b) top view.

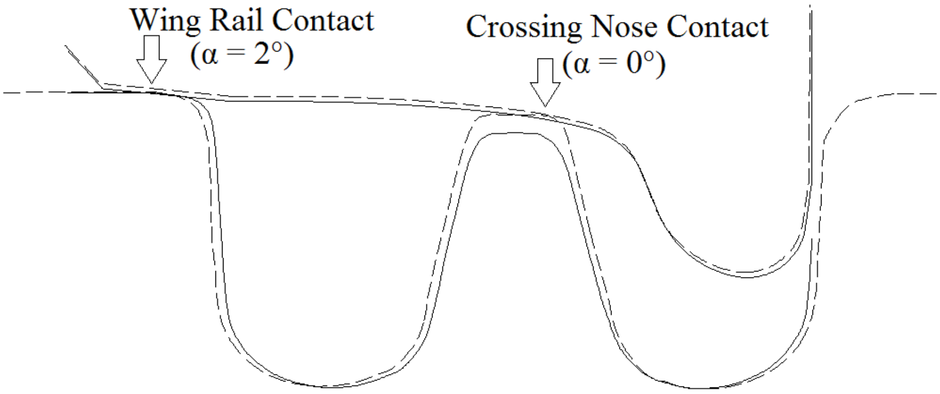

Figure 3-4: Original (dashed) and yawed (solid) left wheel/rail profile pairs.

The three dimensional problem is subsequently simplified into a two dimensional wheel-rail contact problem by slicing through the rail profile along the yawed wheel. For a given state (position and orientation) of the wheelset, a surface interpolation technique is used to generate a new two-dimensional rail profile from the x-y data points of the yawed wheel profile. After the new wheel-rail profile pairs have been constructed, the wheelset roll angle and flange-back contact are reassessed prior to initiating contact detection. Figure 3-4 demonstrates how a two-dimensional wheel-rail contact solution, excluding the wheelset yaw angle, would have a significant impact on the location of contacts. For example, a yaw angle of 0° results in contact on the crossing nose, whereas a 2° yaw angle shows that the true point of contact is on the left hand wing rail.

3.4 Flange-back detection

As the wheelset traverses the crossing panel, the wheel flange-back may come into contact with the crossing wing/check rail. Failure to account for such contact situations would result in the incorrect lateral offset of the wheelset, incorrect roll angle and false detection of contact points, as illustrated in Figure 3-5 for an example configuration.

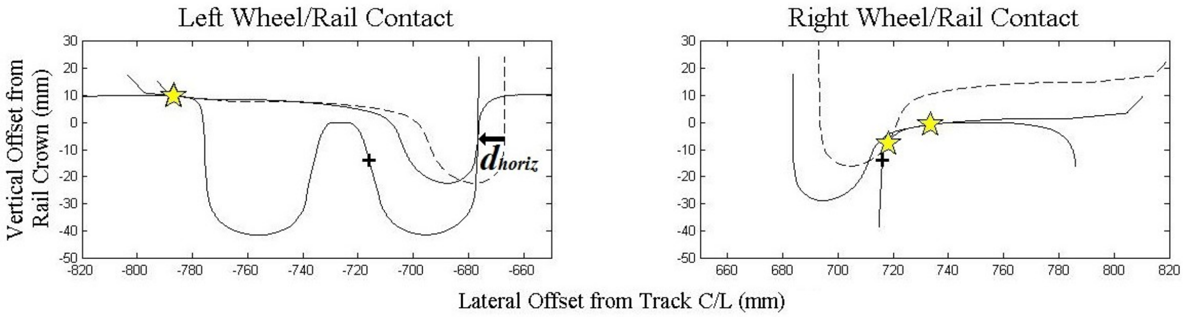

Figure 3-5: Wheel-rail contact with (solid) and without (dashed) flange back detection included.

The wheel profile is divided into a general contact region and a flange-back region. A horizontal minimum distance vector ($\boldsymbol{d_{horiz}}$, Figure 3-5) is used to check for contact between the flange-back profile and associated rail profile. To assess if flange-back contact exists on the left wheel, the following conditions are implemented:

$$\boldsymbol{d_{horiz}} \leq 0 : Contact \quad \boldsymbol{d_{horiz}} > 0 : No\ contact$$

If flange-back contact is detected, the wheelset is repositioned by adjusting the lateral offset iteratively and recalculating the roll angle, which is essential to avoid excessive profile penetration or the flange-back coming out of contact with the rail. The developed technique models a rigid bump stop at the onset of flange-back contact, therefore assuming that any small lateral deformations are negligible with regards to affecting the final wheel-rail contact location(s). This process therefore enforces a constraint to the maximum allowable lateral displacement of the wheelset.

3.5 Contact Point Detection

The methodology implemented within the main contact detection algorithm is illustrated within Figure 3-6 and explained, step-by-step, below:

1. Using the given state of wheelset and rail profile data, initial minimum distance contact point estimation between the wheel and rail profiles is made.

2. Local curve fitting is applied to the wheel and rail profiles enabling the lateral contact radii to be calculated.

3. Using Hertzian elastic contact theory, the local elastic deformation (penetration depth, $\boldsymbol{\delta}$) within the initial contact region is found by applying the normal wheel load, **N**, which is obtained through vehicle system dynamics. A contact geometry parameter, as discussed in detail within *Chapter 4*, is used to calculate the local elastic contact deformation.

4. The initial deformation is then used to vertically shift the wheelset, placing the wheel and rail profiles into a state of penetration.

5. The rail surface normal vectors and wheel surface tangent vectors are then used to obtain a non-linear expression for the first contact condition:

$$\overrightarrow{\boldsymbol{n_r}} \cdot \overrightarrow{\boldsymbol{t_w}} = 0$$

6. For a point on the rail to potentially be in contact with the wheel, the rail surface normal vector $(\overrightarrow{\boldsymbol{n_r}})$ must be perpendicular to its equivalent wheel surface tangent vector $\left(\overrightarrow{\boldsymbol{t_w}}\right)$. This expression is solved using a modified Newton-Raphson iteration scheme, which identifies all potential candidates for contact.

7. The rail-wheel normal deformation vectors $\left(\vec{\boldsymbol{d}}\right)$ are found.

8. A surface penetration condition is enforced to filter out all contact candidates that fall outside of profile penetration:

$$\vec{\boldsymbol{d}} \leq 0 : \text{Contact}$$

9. The quantity of individual contact regions are then determined by assessing the profile penetration limits.

10. Within each region, the maximum normal deformation vector is then defined as the initial point of contact.

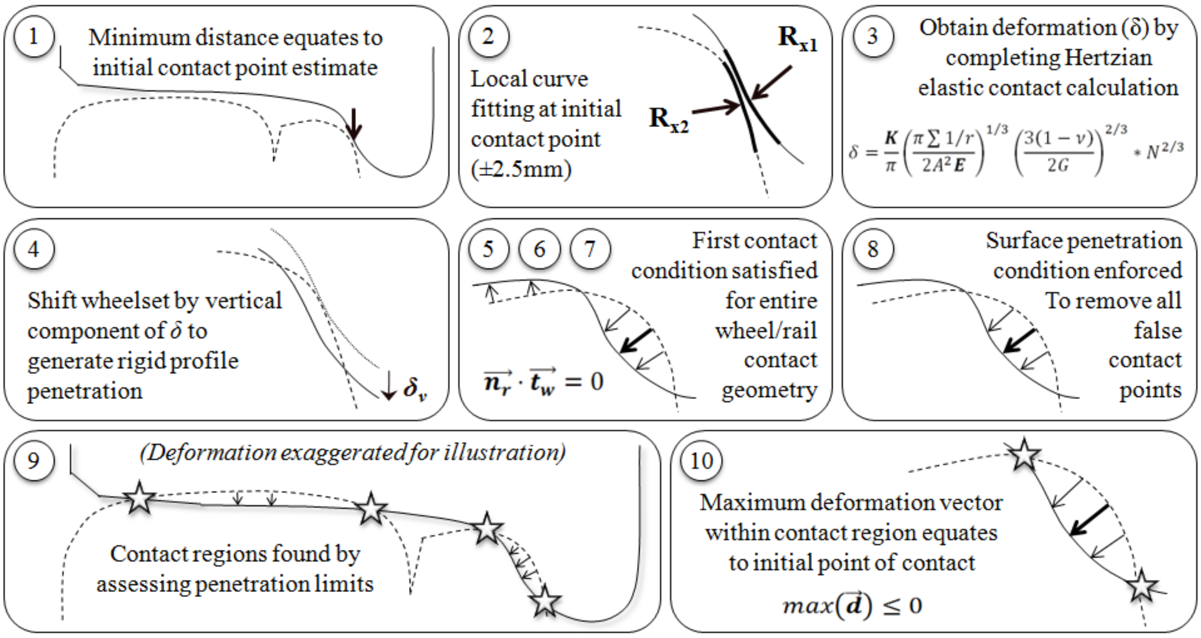

Figure 3-6: Illustration of computation steps implemented within the new contact detection algorithm.

3.6 Contact Force Equilibrium

Using the Hertzian normal deformation at the initial point of contact assumes that the entire wheel-load acts over a single contact area. Once multi-point contact is detected, this load becomes shared between all contact patches. To account for this, a numerical procedure is introduced to manipulate the vertical position of the wheel iteratively until the sum of the resultant forces at each contact patch equates to the load that was initially applied. A convergence tolerance of 0.5% deviation from the applied wheel load is used. If the initial contact angle is large (*i.e.* flange contact) the vertical shift, calculated from the normal deformation, could be significantly larger than necessary. Force equilibrium is therefore essential not only to provide accurate contact forces for multi-point contact but to also avoid additional contact points being incorrectly detected.

3.7 Theoretical validation

Numerical validation of the new contact detection has been completed through comparison with the already established railway vehicle dynamics software package Vampire. Three key parameters were chosen based on their influence on both vehicle dynamics and the resulting contact stress solutions.

Figure 3-7 shows a rolling radius difference (RRD) chart for a nominal UK P8 wheel profile, BS113A rail profile and a wheelset lateral displacement of ±12 mm. Comparison is made using both Vampire's contact data generation tool and the new algorithm. The rail and wheel parameters used are presented within Table 3-1. RRD contributes to the steering ability of the wheelset and hence the vehicles critical speed [108]. To ensure that the required inputs for future tangential stress calculations are correct, the contact angle at the wheel-rail interface was also assessed as demonstrated in Figure 3-8. The contact angle combined with the rolling radius can be used to describe the relative slip between a rolling wheel and a stationary rail. The contact location is checked within Figure 3-9 by plotting the wheelset lateral shift against the contact location on the rail head. All three parameters compared very well with only small discrepancies at large lateral offsets. These minor differences are due to Vampire linearly interpolating between fairly coarse data points to obtain approximate results based on the lateral offset of the wheel. In comparison, the new algorithm calculates an exact solution each time from significantly more data points. This provides a smoother and more realistic prediction of contact results when minor shifts in contact location are present. Wheel and rail contact geometries are also generally non-linear, therefore small shifts in contact location, such as those experienced at the field side of the opposite wheel during flange contact, will not follow a linear relationship. This is captured by the new algorithm and is clearly visible between 4 mm and 12 mm on Figure 3-9. The effects of modelling accurate geometric changes during small shifts in contact location are less noticeable within Figure 3-8 because the contact angle difference is dominated by the significant contact angles arising during flange contact, occurring at approximately ±9 mm lateral offsets.

Rail (BS113A)			***Wheel (P8)***		
Gauge	*Gauge Point*	*Rail Inclination*	*Flange back spacing*	*Wheel diameter*	*Axle load*
mm	*mm*	-	*mm*	*mm*	*kN*
1435	14	1:20	1360	850	98.15

Table 3-1: Wheel / rail contact setup parameters

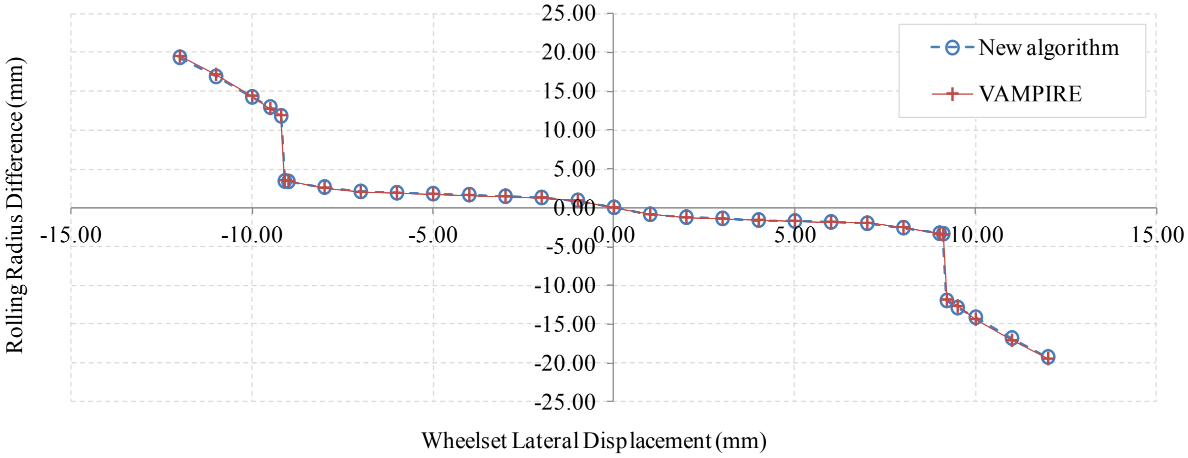

Figure 3-7: Rolling radius difference comparison between VAMPIRE and new algorithm.

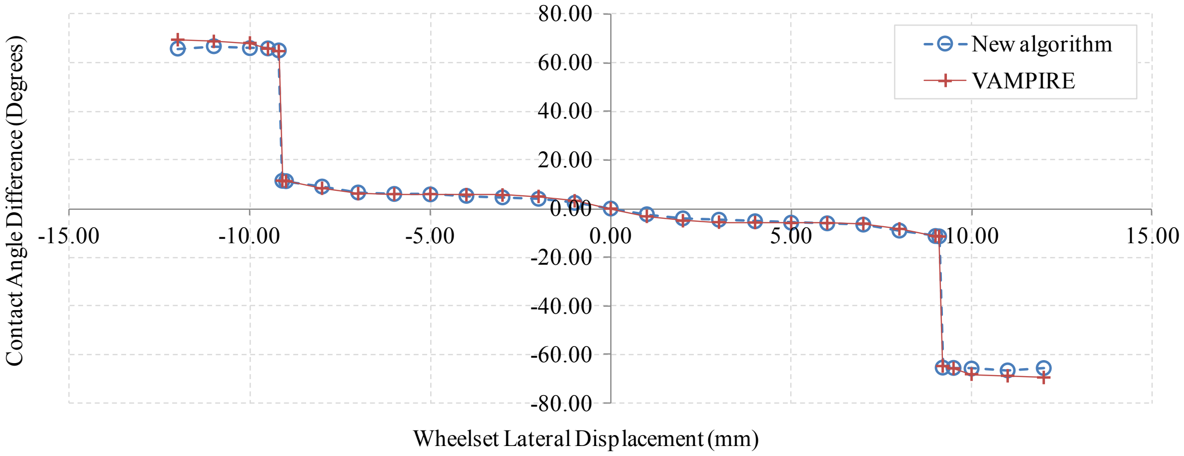

Figure 3-8: Contact angle difference comparison between VAMPIRE and new algorithm.

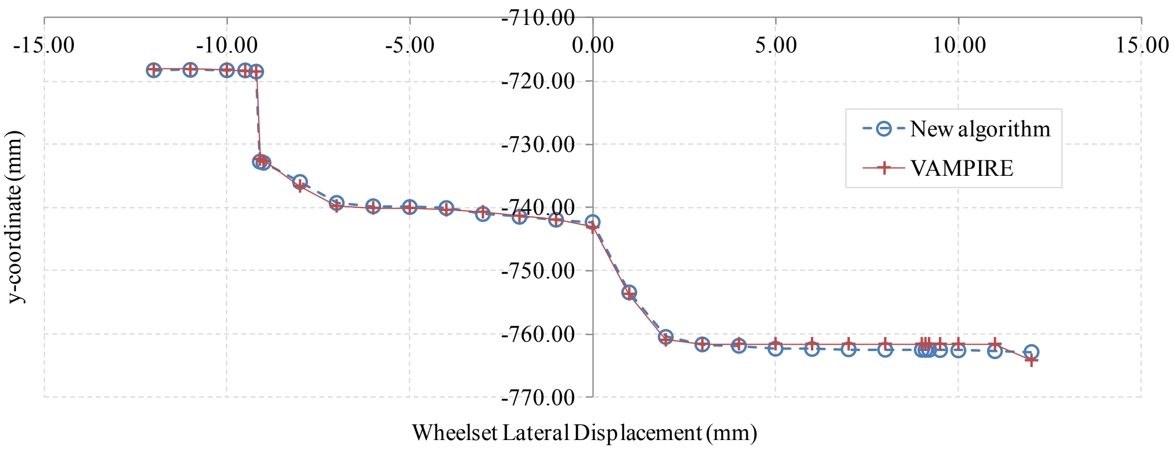

Figure 3-9: Left contact location comparison between VAMPIRE and new algorithm

3.8 Experimental validation

To further validate the contact locations generated from the new S&C contact detection algorithm, a new means of assessing wheel-rail contact was utilised. Burstow et al [109] recently presented a new experimental technique for assessing the heat trace generated by the frictional work within the contact patch. Direct observation of the local rise in rail temperature passing through the contact patch was made and measured using a thermal imaging system mounted to Network Rail's New Measurement Train (NMT).

Within this study, wheel-rail contact locations were compared at six plain line track features, each selected from track quality data obtained by the NMT during the experimental run. Measurements of the actual rail profiles, including both the S&C and plain line track sections, were not required during the original scope of the Barstow's work therefore none were available for use within this study, hence the decision to use significant plain line track features during this study. Due to the overall length of the experimental run and for the purpose of this preliminary study, it was deemed unnecessary and impractical to include measured rail profiles along the extent of the simulation, which totalled over 3 km of track. A vehicle to track dynamics model, containing nominal BS113A rail profiles, P8 wheel profiles measured from the NMT and the measured track quality data, was provided by Burstow and used within this study to obtain key parameters required by the new contact detection algorithm. Figure 3-10 illustrates the NMT track quality data, where the cross-level irregularity describes the change in rail cant, ϕ, the curvature irregularity describes the lateral curvature of track, the lateral alignment irregularity describes the lateral shift, y, in track centre line from the nominal track design and the gauge variation describes the variation in nominal track gauge, g_0, of 1435 mm. Table 3-2 contains the parameters from each of the six selected track location. For each case study and at the associated longitudinal track distance; the variation in track gauge, alignment, cross-level and curvature are taken for positioning the track whilst vehicle velocity, wheelset lateral offsets, wheelset yaw angles and dynamic wheel loads are obtained for positioning the wheels relative to their equivalent rails.

This study only considers the accuracy of contact point detection as more detailed contact parameters, such as contact patch geometry, normal and tangential pressure distributions and hence parameters relating to material damage predictions, would require a more accurate description of the local contact geometries (*i.e.* rail profiles measured immediately prior to the experimental run for the entire track mileage).

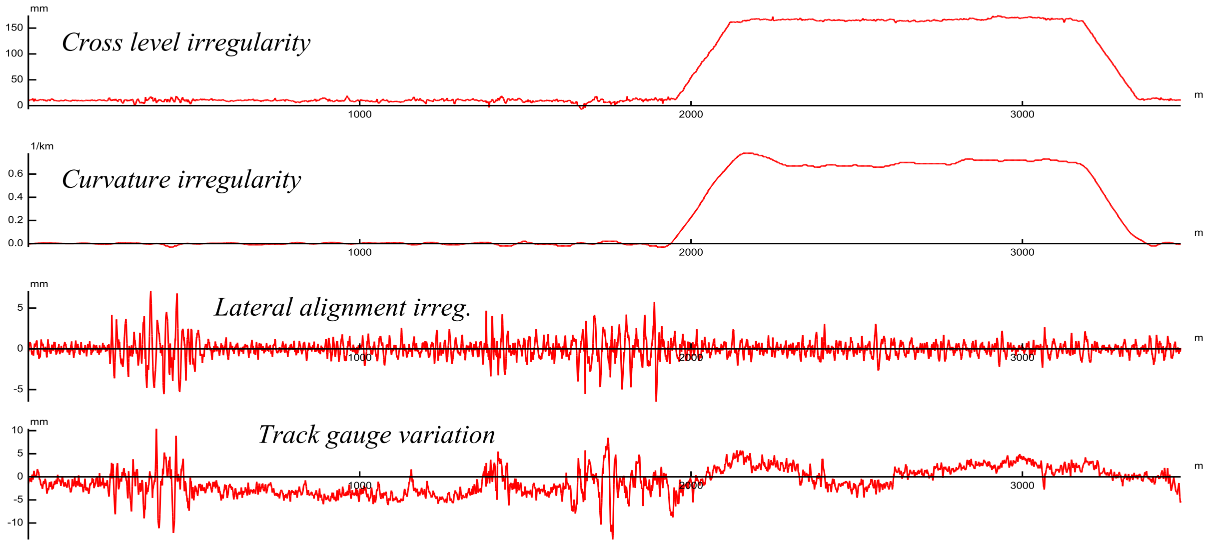

Figure 3-10: Track geometry data measured by the Network Rail NMT

Parameter	units	*(a)*	*(b)*	*(c)*	*(d)*	*(e)*	*(f)*
Track Distance	*m*	193.00	281.34	288.40	386.60	1967.00	2700.00
Left vertical load irreg.	*N*	265.70	434.80	-870.66	-150.33	305.55	-10593.60
Right vertical load irreg.	*N*	-6216.71	-2439.78	-8634.52	9253.05	-1244.38	12731.42
Track Gauge	*mm*	1435.00	1435.00	1435.00	1435.00	1435.00	1435.00
Gauge variation	*mm*	-0.36	-1.00	1.79	10.40	-1.19	0.45
Track Alignment Irreg.	*mm*	-0.29	-1.61	0.00	0.22	0.58	0.02
Cross Level Irreg.	*mm*	10.82	11.46	7.48	5.62	24.75	163.10
Curve Radius	*m*	INF	143000	125000	1000000	10000	1449
Curve Radius Irreg.	*m*	0.00	0.00	0.00	0.00	0.00	0.00
Vehicle Velocity	*m/s*	48.57	48.71	48.70	48.85	49.47	48.83
Wheelset Lateral Offset	*mm*	0.39	-0.11	3.00	-2.50	-0.27	-4.72
Wheelset Yaw Angle	*deg*	-0.02	0.02	-0.06	0.16	0.01	0.07

Table 3-2: System parameters obtained using VAMPIRE for 6 plain line track features

Despite the assumptions made with regards to the wheel and rail profiles, Figure 3-11 *(a)* through to *(f)* clearly show a general agreement between the computational and measured contact locations. The smooth, 'polished' surfaces of the wheel and rail result in reflected heat radiation, which proves to distort the overall thermal image. Green isobars have been used to highlight the increase in temperature due to the frictional work between the wheel and the rail pair under investigation. Although the exact shape of the rail head is difficult to judge, observing the changes in the contact position on the wheel demonstrates excellent agreement with the predictions obtained using the proposed algorithm.

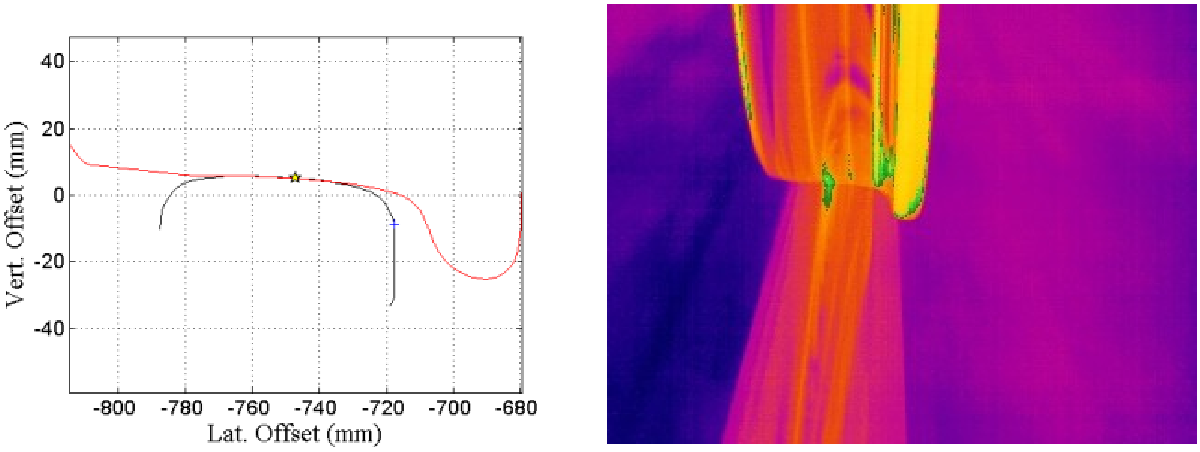
40
20
0
-20
-40
Vert. Offset (mm)
-800
-780
-760
-740
-720
-700
-680
Lat. Offset (mm)

(a)

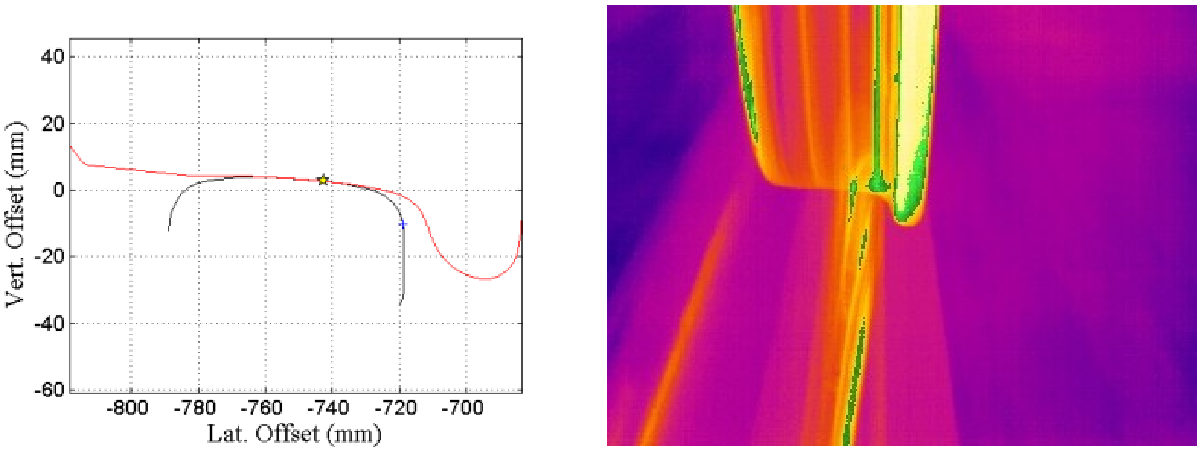
40
20
0
-20
-40
-60
Vert. Offset (mm)
-800
-780
-760
-740
-720
-700
Lat. Offset (mm)

(b)

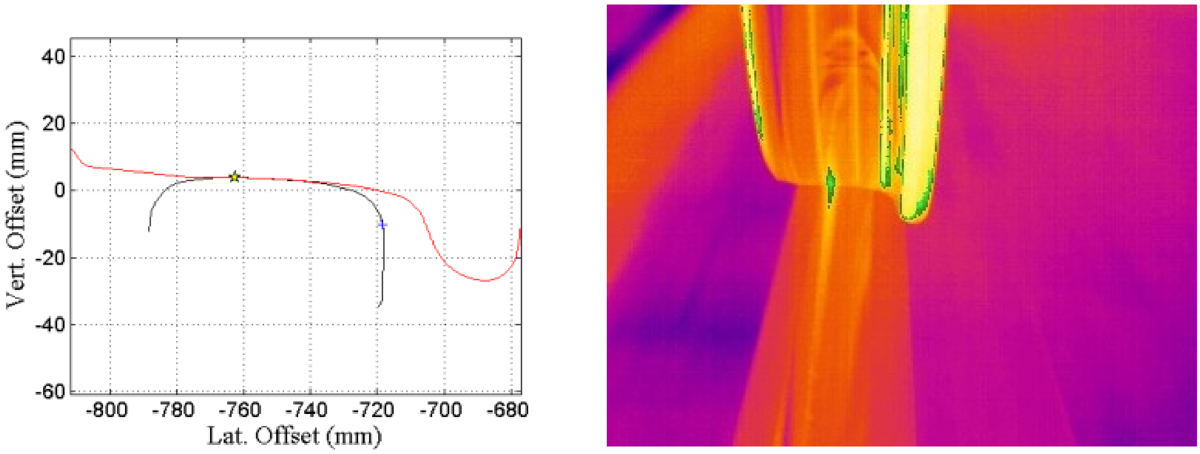
40
20
0
-20
-40
-60
Vert. Offset (mm)
-800
-780
-760
-740
-720
-700
-680
Lat. Offset (mm)

(c)

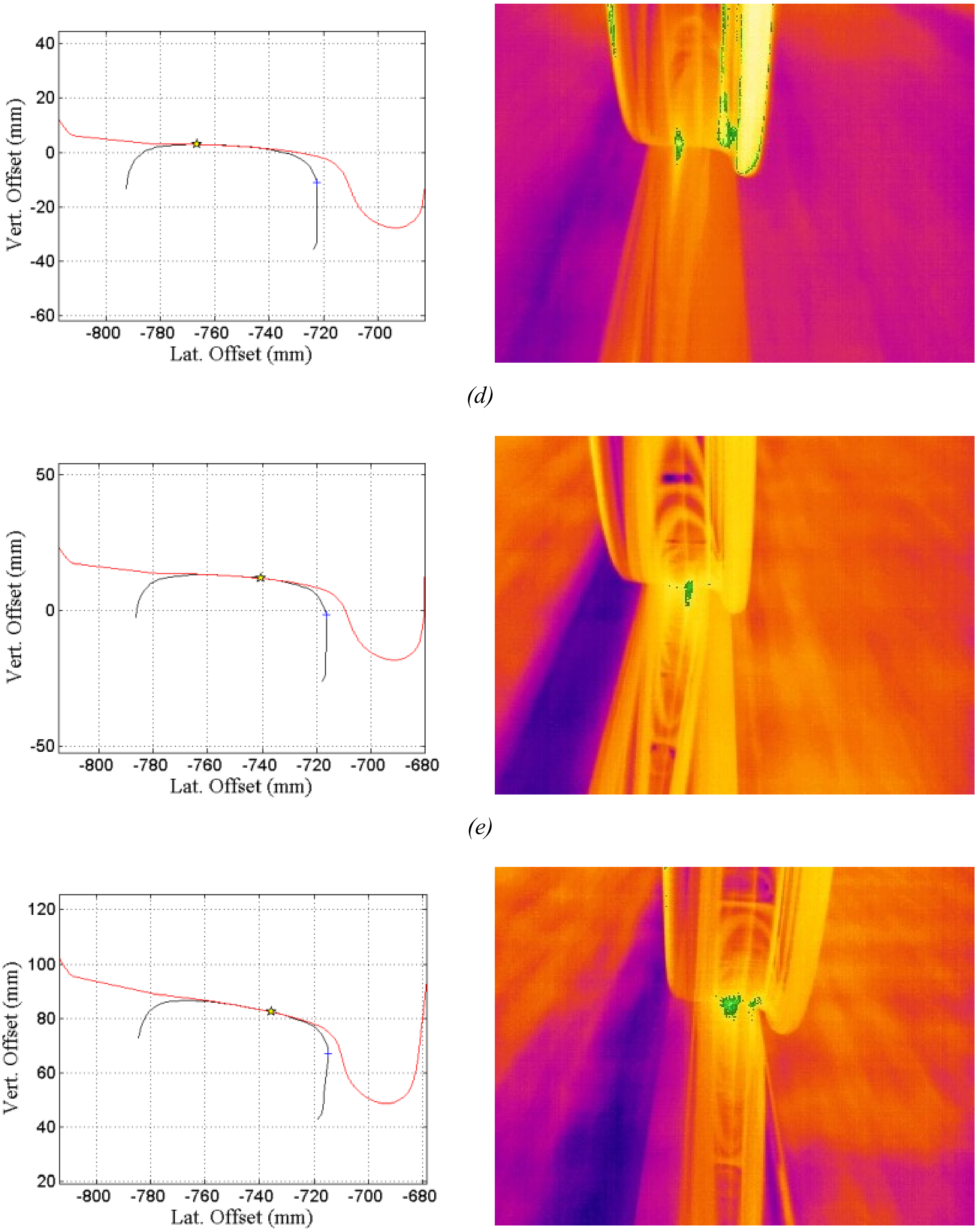

(d)

(e)

(f)

Figure 3-11: Contact location during plain line running (a), after the switch toe (b), at a wide gauge feature (c), at a significant plain line gauge widening feature (d), on the transition to a 1400m curve (e) and during a 1400m curve (f)

It must also be noted that Figure 3-11 *(f)* seems to demonstrate a two point contact situation with the first point on the head of the rail and a second closer to the gauge corner. Observing the green isobars carefully, the apparent rise in temperature at the gauge corner occurs in isolation on the wheel profile only. All other contact points, as illustrated within Figure 3-11 *(a)* to *(e)*, contain a matching rise in temperature present on the rail profile. This leads the author to conclude that the second contact point is actually a result of reflected heat radiation. Figure 3-11 *(a)* to *(d)* also demonstrate this phenomenon from within the same region of the wheel profile.

To add a further level of scientific context and clarification to the experimental analysis, Table 3-3 presents the theoretical and experimental contact locations as measured and percentage offsets from a common datum point, the wheel flange-back. Test sites *(b)* to *(e)* present excellent comparisons with a maximum variation within the sub-millimetre range. Discrepancies are observed at test sites *(a)* and *(f)*, which are believed to be a direct result of not using the exact rail profiles present at the time of the experimental run. This is very difficult to confirm as a complete survey of the test track would be required prior to obtaining a second set of thermal imaging results. Errors associated with test site *(f)* are amplified somewhat due to the change in field of view of the thermal imaging camera as the vehicle tilts whilst travelling around the curve.

Test Site	*Theoretical offset from flange-back*		*Experimental offset from flange-back*		*Difference*	
	mm	*%*	*mm*	*%*	*mm*	*%*
(a)	70.00	52	78.28	58	-8.28	-6
(b)	61.67	44	62.16	47	-0.49	-3
(c)	87.50	64	87.49	64	0.01	0
(d)	86.67	63	87.49	63	-0.82	0
(e)	60.83	45	59.86	44	0.97	1
(f)	55.83	42	73.67	54	-17.84	-12

Note: All measurements have been taken from the wheel flange back face. Percentages are in terms of the total wheel width and 'Difference %' is presented as 'Experimental %' minus 'Theoretical %' to demonstrate the variation in contact point position along the total wheel width.

Table 3-3: Theoretical and experimental contact point comparison.

3.9 Switch contact example

To demonstrate the algorithm, a simple contact scenario has been modelled. An independent railway vehicle dynamics analysis was used to provide realistic wheelset lateral offsets (0 mm to -8.2 mm) and yaw angles (0 mrad to -8.55 mrad) for a 200 kN axle-load vehicle passing through a railway turnout (290 m curve radii) at 10 m/s. These results were then used to perform numerous static wheel-rail contact detection analyses.

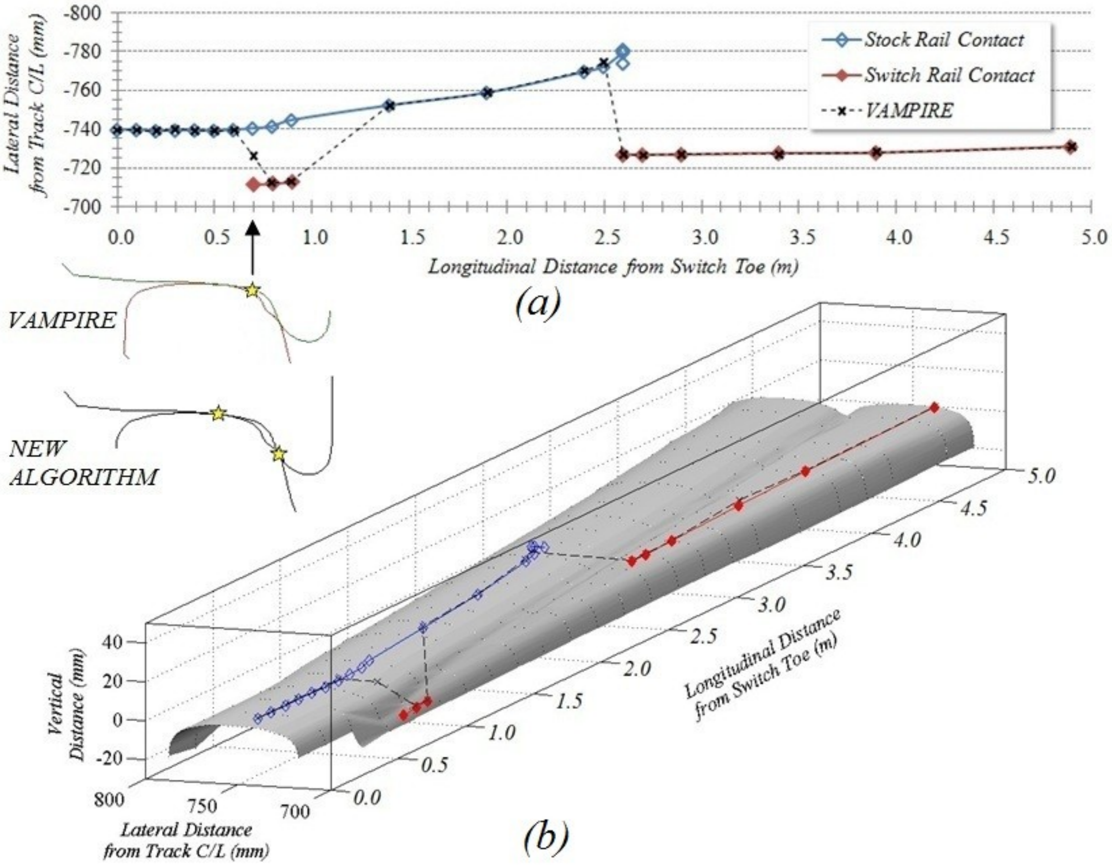

Figure 3-12 - Wheel-rail contact points along a switch rail (a) top view (b) 3D view [axes not to scale].

Figure 3-12 demonstrates the benefits and improvements available due to implementing the new algorithm when compared with the commercially available railway vehicle dynamics package VAMPIRE. Figure 3-12 *(a)* illustrates the static contact points and hence contact paths predicted by both Vampire's contact data generation tool and the new algorithm. Figure 3-12 *(b)* presents the same results overlaid onto a three-dimensional representation of the stock and switch rails (for visualisation purposes). A static analysis is completed every 100 mm until the initial contact on the switch tip is lost. 500 mm intervals have then been modelled until the wheel reaches the stock to switch rail transition region, where 100 mm intervals are resumed until the end of multi-point contact.

Four points of contact have been detected using the new algorithm at a longitudinal distance of 2.6 m in comparison with a single point of contact found by VAMPIRE (see Figure 3-12). Three of the contact origins reside on the stock rail and are close enough to be regarded as being within a single contact patch, which would be non-Hertzian in nature. This becomes significant when considering subsequent material degradation modelling as accurate contact pressure distributions will highly depend on the initial distribution of the wheel-rail contact forces. Another significant benefit to the new algorithm can be seen at a longitudinal distance of 0.7 m. With the wheelset lateral displacement set to -5.95 mm, VAMPIRE predicts a physically implausible point of contact towards the gauge corner of the stock profile. This is due to VAMPIRE obtaining its contact location from linearly interpolating results, from within its contact data table, between -5.9 mm and -6.0 mm. At this wheelset position, the new algorithm has detected two correct points of contact, one on the head of the stock rail and the other at the gauge corner of the switch rail.

3.9.1 Concluding remarks

A new wheel-rail contact detection technique, suitable for complex S&C rail geometries and subsequent material degradation modelling, has been developed and demonstrated. The algorithm is capable of detecting multiple points of contact (up to four within this study) for any general wheel and rail combination in addition to wheel flange-back detection. The ability to detect contact origins within highly conformal regions is included, which is essential for the accuracy of future long-term material degradation predictions.

The methodology is validated through a comparison with the commercially available railway vehicle dynamics package VAMPIRE. For a standard wheel-rail combination, with single contact point situation, both the new algorithm and VAMPIRE compare extremely well with regards to contact locations, contact angles and rolling radius difference for a wide range of wheelset displacements. A novel experimental technique, using thermal imaging of wheel-rail interaction, has also been used for validating the new S&C wheel-rail contact detection algorithm. The heat trace remaining from frictional work between the wheel and rail was compared to the predicted points of contact and successful qualitative comparison was achieved. Significant benefits of the new algorithm have also been demonstrated, such as accurate multi-point contact detection and the ability to model accurate contact parameters, such as contact angle, for any lateral shift in wheelset position (*i.e.* avoiding the linear interpolation as required by Vampire).

The new algorithm accounts for a general three-dimensional state of a wheelset and rail, including effects of wheelset yaw and roll angles, on detecting the location of contact points. It has been demonstrated that excluding the wheelset yaw angle using a two-dimensional wheel-rail contact solution will lead to an incorrect location of contacts, which have a significant impact on the prediction of material degradation.

Chapter 4 : Simplified Contact Stress Modelling

Chapter 4 describes in detail the work completed within the author's publication [110] with respect to the integration of simplified contact theories within a novel wheel-S&C contact detection and degradation tool. Normal and tangential contact tractions are simulated automatically for up to four points of contact with subsequent wear depth predictions made. An iteration scheme has also been devised to enable wear accumulation due to multiple load cycles. Results demonstrating successful rail profile evolution due to wear are presented and current model limitations are discussed.

4.1 Background

Chapter 3 introduced a novel wheel-rail contact detection routine for complex interactions at S&C. The next stage of the damage modelling process uses local contact patch parameters to simulate phenomena such as normal and tangential contact pressures and areas of slip (creepage) and adhesion within the contact patch. Wheel and rail damage simulation is an ongoing area of interest and many different approaches have been adopted, such as the finite element method [111], mathematical models such as the Winkler foundation [72], simplified Hertzian and Fastsim approximations [68] and Kalker's variational model for three-dimensional rolling contact [112]. Despite proving adequate for use within railway vehicle dynamics software, the question to whether or not simplified contact theories are suitable for S&C material degradation studies has not been completely answered. For this reason, Hertzian normal and Fastsim tangential contact models have been implemented. This represents a simple and computationally efficient solution for comparison with a more detailed non-Hertzian model, as described within *Chapter 5*.

4.2 Modelling strategy overview

The modelling strategy implemented within this study is illustrated within Figure 4-1. Wheel to rail contact point detection, as described within *Chapter 3*, initiates the degradation model by accurately locating each of the wheel to rail contact patch origins. Local contact information is then extracted from each origin to provide the necessary inputs to the Hertzian normal contact solution and then subsequently the Fastsim tangential solution. The resulting contact forces are then balanced against the applied wheel load before being used within the Archard wear model (see §2.3.2 and §4.4.1) for damage approximation.

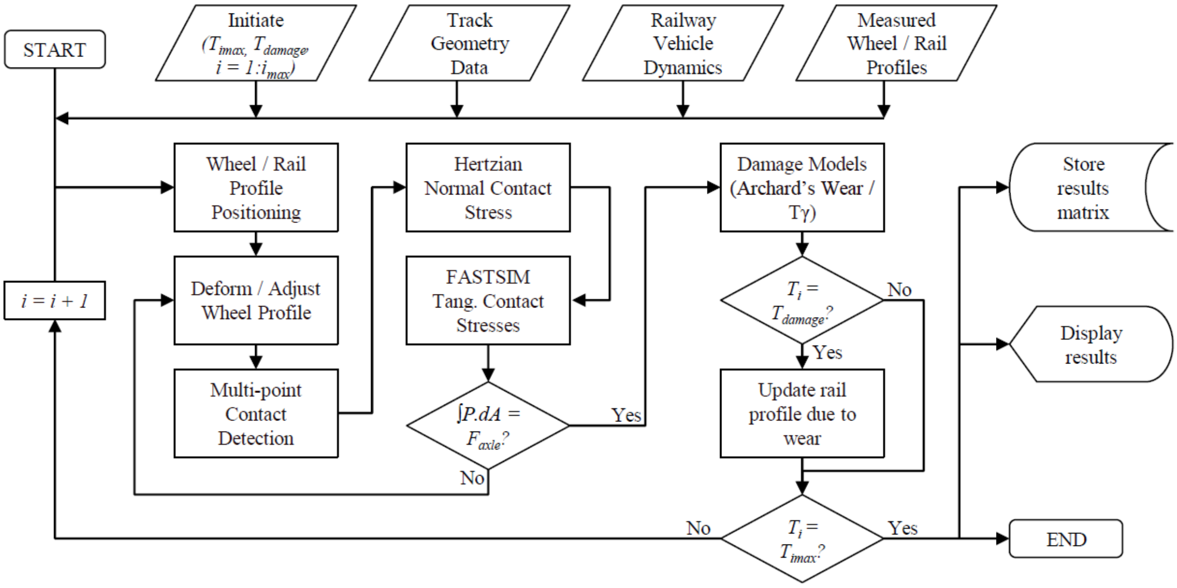

Figure 4-1: Simplified degradation model applicable to railway switches and crossings.

This process is assigned to an iteration loop in order to simulate numerous load steps and hence the accumulation of rail degradation due to wear.

4.3 Contact stress modelling

The central steps within this novel S&C damage accumulation model require the calculation of both normal and tangential contact stresses. To provide a simple case for comparison, a computationally efficient process is first developed using the Hertzian and Fastsim solutions.

4.3.1 Hertzian normal contact model

The Hertzian normal contact theory, as introduced within *Chapter 2*, has been implemented to solve for simplified normal contact pressures. Hertzian theory assumes that the contact pressure (traction bound) is described by an ellipsoidal distribution using the following equation:

$$p(x,y) = \frac{3N}{2\pi ab}\sqrt{1-\left(\frac{x}{a}\right)^2-\left(\frac{y}{b}\right)^2} \qquad 4\text{-}1$$

where N is the contact load. Equation 4-1 requires the contact patch longitudinal and lateral semi-axes, a and b respectively, to be approximated. Lundberg and Sjövall [113] proposed a method whereby the contact geometry is defined by the parameter Θ, which is given in Equation 4-3 as a function of the contact radii, r_{ij}, and angle of contact patch misalignment (yaw angle), α. The elliptic integrals, $\boldsymbol{E}$ and $\boldsymbol{K}$ within Equation 4-2, are first solved using modulus $k^2 = 1 - A^{-2}$ and the Newton-Raphson iteration, where A is ratio of contact patch semi-axes, a/b. The contact ellipse semi-axes and the elastic penetration depth, δ, are then ascertained from Equations 4-5, 4-6 and 4-7.

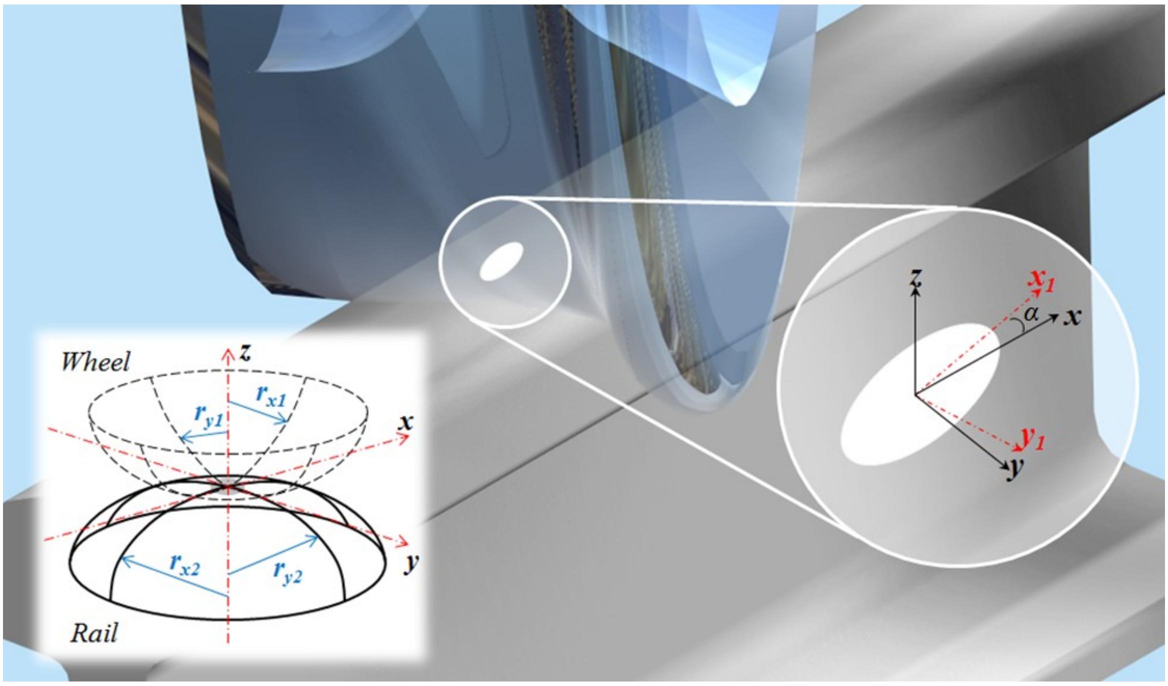

Figure 4-2: Contact patch misalignment (φ) and an illustration of wheel and rail contact radii (r_{ij}).

$$\Theta = \frac{(A^2+1)\boldsymbol{E}-2\boldsymbol{K}}{(A^2-1)\boldsymbol{E}} \qquad 4\text{-}2$$

$$\Theta\sum\frac{1}{\mathrm{r}} = \sqrt{\left(\frac{1}{\mathrm{r_{x1}}}-\frac{1}{\mathrm{r_{y1}}}\right)^2+\left(\frac{1}{\mathrm{r_{x2}}}-\frac{1}{\mathrm{r_{y2}}}\right)^2+2\left(\frac{1}{\mathrm{r_{x1}}}-\frac{1}{\mathrm{r_{y1}}}\right)\left(\frac{1}{\mathrm{r_{x2}}}-\frac{1}{\mathrm{r_{y2}}}\right)\cos 2\alpha} \qquad 4\text{-}3$$

$$\sum\frac{1}{r} = \frac{1}{\mathrm{r_{x1}}}+\frac{1}{\mathrm{r_{y1}}}+\frac{1}{\mathrm{r_{x2}}}+\frac{1}{\mathrm{r_{y2}}} \qquad 4\text{-}4$$

$$a = \left(\frac{3A^2\boldsymbol{E}(1-\nu)}{\pi G \sum 1/r}\right)^{1/3} * N^{1/3} \qquad 4\text{-}5$$

$$b = \left(\frac{3\boldsymbol{E}(1-\nu)}{\pi A G \sum 1/r}\right)^{1/3} * N^{1/3} \qquad 4\text{-}6$$

$$\delta = \frac{\boldsymbol{K}}{\pi}\left(\frac{\pi \sum 1/r}{2A^2\boldsymbol{E}}\right)^{1/3}\left(\frac{3(1-\nu)}{2G}\right)^{2/3} * N^{2/3} \qquad 4\text{-}7$$

The formulation described above has been automated within this study to obtain ellipsoidal normal contact pressure distributions at each contact location.

4.3.2 Fastsim tangential contact model

The tangential contact model implemented within this work is based on Kalker's frictional rolling contact model, Fastsim, as introduced within *Chapter 2*. Assuming a constant friction coefficient throughout the computation; Coulomb's law is implemented in conjunction with the normal and tangential pressure distributions to determine if or when friction is exceeded and locate slip and stick zones within a discretised contact patch.

The Fastsim algorithm, which is described in greater detail by Kalker [39], works under the assumption that the tangential surface deformations are linearly related to the discretised local surface tractions by a flexibility constant, L. This flexibility parameter is used in conjunction with the global creepage values to obtain tangential tractions within a discretised contact patch. To achieve maximum accuracy, the contact patch is discretised with an equal number of divisions in both the x and y direction. The contact patch cells are therefore divided equally in the lateral direction (Δy) whereas they become a function of the contact patch width in the longitudinal direction (Δx). This is illustrated within Figure 4-3. Upon discretisation of the contact patch and working backwards through the contact patch from the leading edge, the magnitude of tangential traction without slip is computed. Coulomb's law is then introduced to check whether or not the computed tangential traction exceeds friction and hence generates slip within the cell. A slip factor (q) is calculated to determine how close the tangential traction is to the chosen value of the coefficient of friction:

$$q = \frac{p_{x,y}}{N_{x,y} * \mu}$$
$$q \leq 1 : adhesion \qquad \text{4-8}$$
$$q > 1 : slip$$

If $q \leq 1$, the cell is assumed to be within the adhesion zone and the tangential traction is set to:

$$p_a(x, y) = p(x - \Delta x, y) - w\left(\frac{\Delta x}{L}\right) \qquad \text{4-9}$$

In this case, $x - \Delta x$ is the coordinate of the preceding cell and w is the rigid slip described by the pre-calculated creepage values. If $q > 1$, the tangential traction is assumed to fall within the slip region and its magnitude is limited by friction. The slip velocity is then determined within each cell apportioned to the slip region:

$$p_s(x, y) = N(x, y)\frac{p_a(x, y)}{|p_a(x, y)|} \qquad \text{4-10}$$

$$s(x, y) = \frac{Lv}{\Delta x}[p_s(x, y) - p_a(x, y)] \qquad \text{4-11}$$

Here, s is the discretised slip velocity due to the Fastsim model, v is the velocity of the wheel through the contact patch, p_s is the tangential traction vector limited by slip whilst p_a is the traction vector excluding slip. This slip velocity becomes the significant output used within the subsequent wear accumulation model.

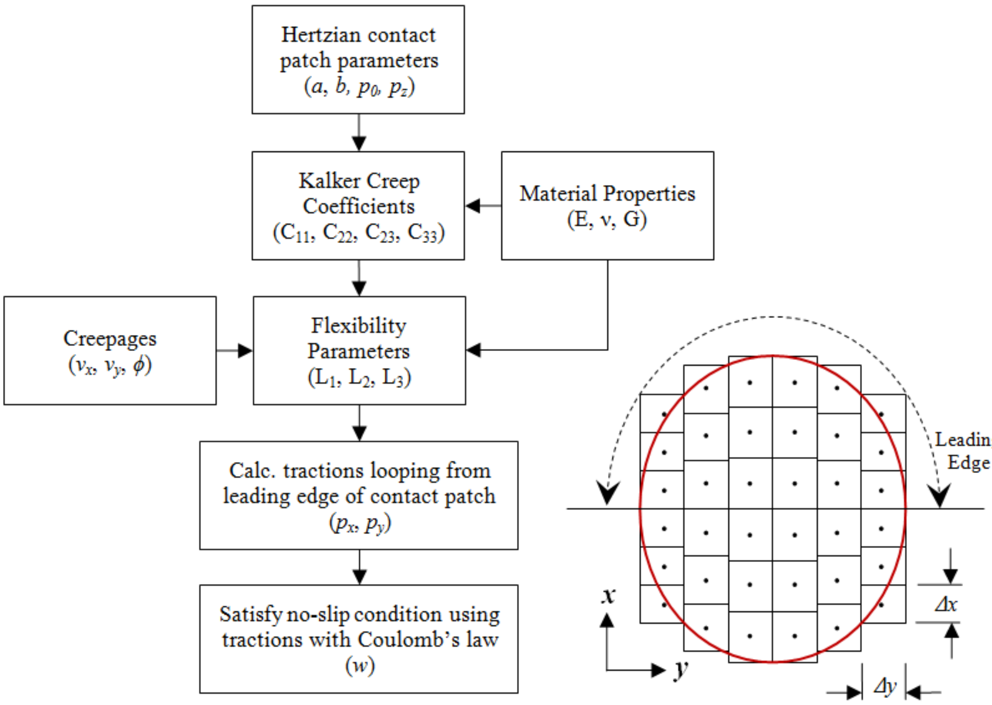

Figure 4-3: Kalker's 'Fastsim' algorithm for solving the simplified theory of rolling contact. Also illustrated is the method of contact patch discretisation.

4.4 Wear simulation

A process for simulating accumulated wear damage on a 2D rail profile is presented. As discussed within *Chapter 2*, wear damage associated with wheel to rail interaction is dependent on the load history, contact geometry, material properties and environmental conditions. The loading, contact geometry and, to some extent, material properties are all accounted for within *Section 4.3* of this chapter, therefore a wear law capable of introducing additional material properties and environmental conditions was sought. Due to the various combinations of wheel and rail material properties coupled with external environmental conditions such as weather, humidity and lubrication, it would be extremely difficult to implement an empirical wear model suitable for all conditions without first obtaining a significant number of test data sets. It was also deemed impractical to develop a detailed microscopic failure mechanism model, such as asperity deformation, as this type of model would not provide the computational efficiency required for long-term S&C wear accumulation predictions. The Archard wear law was therefore chosen as it offered excellent computational efficiency, the inputs aligned with the readily available, discrete outputs from both the Hertzian normal and Fastsim tangential contact models and it also provided a platform for developing a more complex wear model, if required, should a comprehensive set of wheel-rail wear measurement test data become available.

4.4.1 Archard wear depth approximation

The simulation of wear damage has been implemented within this novel S&C degradation tool through adapting the Archard wear law to accept outputs from both the Hertzian and Fastsim models. The total wear depth (Q) is achieved by combining the material wear coefficient (k_w), normal contact force (N), slip distance (L) and the hardness of the material under analysis (H_w). These parameters are all available as either general material properties or from results obtained during earlier computational steps. Equation 4-12 is the standard form of Archard's wear law whilst Equation 4-13 illustrates the adapted version as implemented within this study.

$$Q = \frac{k_w N L}{H_w} \tag{4-12}$$

$$Q = \frac{k_w}{H_w}\frac{3N}{2\pi ab}\sqrt{\left(1-\left(\frac{x}{a}\right)^2-\left(\frac{y}{b}\right)^2\right)}\sqrt{s_x^2+s_y^2}\,\frac{dx}{V_c} \tag{4-13}$$

When considering multi-point contact through S&C, it is important to assess the wear coefficient for each contact patch independently as each will contain different contact pressures and slip velocities. Jendel [114] developed a wear chart from experimental data relating wear coefficients to contact pressure and sliding velocity. More recently, Lewis et al. [115] demonstrated that the wear coefficient varies significantly between tread and flange contacts, resulting in the need for different wear coefficients within the same wheel-rail contact simulation. Figure 4-4 shows examples of typical wear maps for wheel and rail steels.

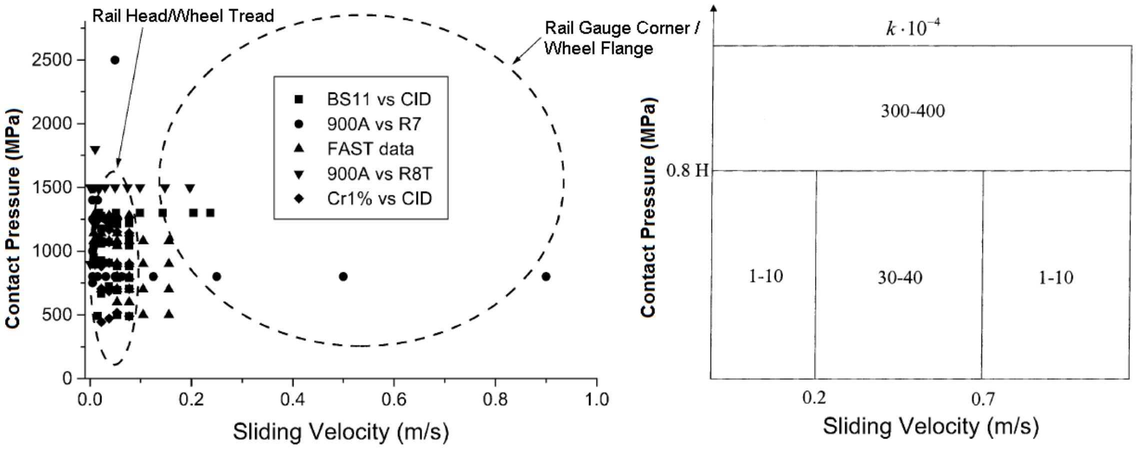

(a) *(b)*

Figure 4-4: Typical wear maps from (a) Lewis [115] and (b) Jendel [114].

To account for varying wear coefficients within this novel S&C degradation tool, an automated check on the maximum contact pressure and sliding distance is made. A unique wear coefficient is then assigned for each contact patch, during the wear prediction process, based on maximum values from Jendel's wear map. This represents a crude application of the wear coefficient due to the rather vague data set presented by Jendel. Despite this and to the author's knowledge, no other damage prediction tool varies the wear coefficient in this manner as static values are generally assigned for the duration of the simulation. Additional wear coefficient data can easily be integrated into the novel S&C degradation tool when made available.

4.4.2 Rail profile evolution due to accumulated wear

To simulate rail profile evolution, a technique for permanently deforming a 2D rail profile using a 3D wear depth distribution was required. This has been achieved by summing the predicted, discrete wear depths along each lateral strip of the contact patch. For example, a 50x50 grid would generate a 2D wear depth plot consisting of 50 lateral data points. Figure 4-5 *(a)* provides an example of an accumulated 2D wear depth distribution generated from the 3D wear plot, which is illustrated within Figure 4-5 *(b)*. An assumption has been made that the entire 3D wear distribution traverses the 2D rail profile in its entirety. To provide a certain degree of computational efficiency, the 2D wear profiles are accumulated over a total of 200 load cycles before the rail profile is updated.

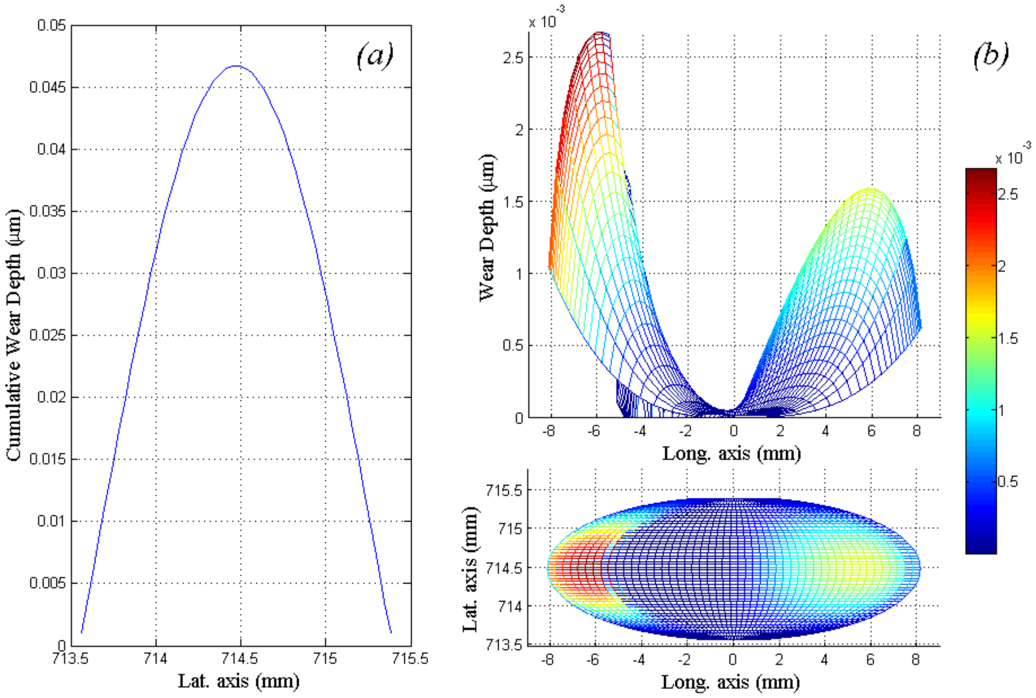

Figure 4-5: An example of a 2D cumulative wear depth profile (a) obtained from a 3D wear distribution (b).

4.5 Application of the S&C damage model

To demonstrate application of the damage accumulation process, an example involving wheel to rail contact on a common UK switch profile is given. At this stage, no direct link with rail vehicle dynamics has been made, therefore only a theoretical example is given to demonstrate model capabilities. A ±1.25 mm sinusoidal oscillation is applied around an initial -8.22 mm wheelset lateral offset to simulate the left flange of a nominal P8 wheel profile coming continuously in and out of flange contact with a measured switch rail profile. The switch profile was taken 1 m from the switch toes of 682B points at Barnwood Junction. To accelerate the damage process, a typical freight vehicle is assumed with an axle load of 25 t and velocity of 15 m/s. A grid of 50x50 elements was used within the Fastsim algorithm. The results presented subsequently are those extracted from the contact situation presented within Figure 4-6, which illustrates a multi-point contact result simulated at the onset of flange contact.

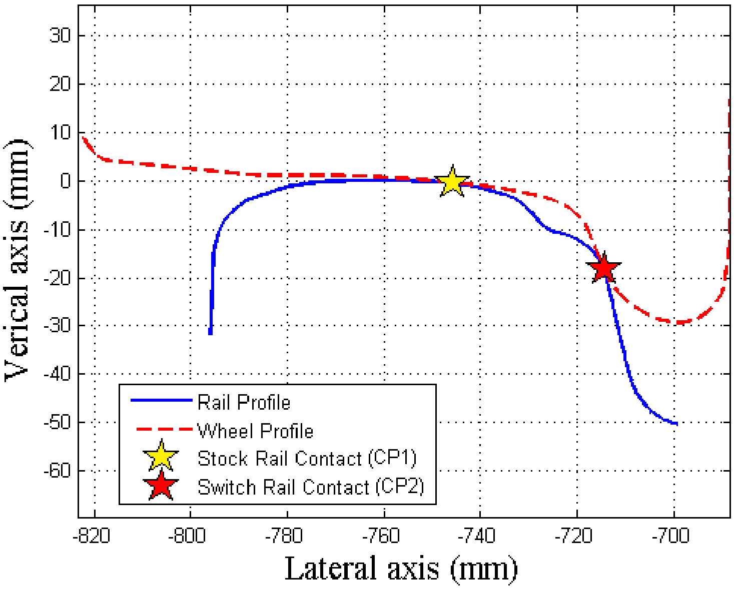

Figure 4-6: Two-point contact simulated between a nominal P8 wheel profile and a measured switch rail profile taken 1 m past the switch tips of 682B points at Barnwood Junction.

The stock and switch rail Hertzian normal contact pressures, Fastsim tangential tractions and Archard wear depth distributions for a single load cycle (wheel pass) are presented within Figure 4-7 *(a-b)*, *(c-d)* and *(e-f)* respectively. For this specific configuration, a $T\gamma$ damage index of 5.43 is predicted for the stock rail contact whilst the switch rail contact generates an index of 210.17. These values indicate that rolling contact fatigue is unlikely to occur, although the switch rail is indeed prone to severe wear. This is also observed through comparison of Figure 4-7 *(e)* and *(f)* with approximately eighteen times the maximum wear depth at the gauge corner of the switch rail when compared to the head of the stock rail. Large lateral and spin creepages present within the switch rail contact patch lead to significant sliding distances and hence increased wear depth predictions within the Archard wear model. These predictions correlate well with the wear damage experienced on site with majority of the damage occurring along the switch rail. In practice, this causes thinning of the switch rail and, in severe cases, can lead to eventual fatigue failure along the top surface, as previously illustrated within *Chapter 2*, Figure 2-13 *(a)*.

To demonstrate damage accumulation, a total of 2000 load cycles were then simulated, with profile evolution occurring after every 200 cycles. Figure 4-8 *(a)* and *(b)* illustrates the wear accumulation, prior to the first rail profile update, on the stock and switch rails respectively. Representing only 500 wagons, 2000 load cycles resulted in a relatively small change in overall rail profile, as illustrated within Figure 4-9 *(a)*. Profile evolution due to wear is shown by the solid lines within Figure 4-9 *(b)*, *(c)* and *(d)*, where it can be seen that majority of the damage is occurring at the switch rail.

The new S&C contact detection and degradation tool has not yet been integrated within a railway vehicle dynamics package therefore it is not yet possible to validate the rail profile evolution against field measurements. Alternatively, a theoretical simulation has been completed whereby the wear is accelerated by enforcing an amplified wear coefficient of 0.1. All of the other input parameters remain unchanged from the previous example. The purpose of this case study is to see if an approximate but similar wear pattern can be achieved on a switch rail profile experiencing continuous flange contact, which is common within switches set for the diverging route. A profile measurement was taken from a switch rail just outside of Waterloo Station, which was predominantly set for the diverging route and hence experienced a significant amount of flange contact. The switch was known by Network Rail to experience accelerated degradation through wear and was due for replacement.

Figure 4-10 illustrates the wear simulated on an as new switch rail after 2000 load cycles. The same sinusoidal loading cycle was applied, as described above, to bring the wheel continuously in and out of flange contact. The onset of a wear groove is observed within Figure 4-10 *(b)* and compares well with the location of a wear groove present on the measured profile, illustrated within Figure 4-10 *(c)*. It should also be noted that no prevalent wear is observed on the head of the rail within both the simulated and measured stock rail profiles, demonstrating the prediction of realistic wear depth magnitudes at the correct locations along the stock and switch rail profiles. Plastic deformation at the edges of the switch rail wear groove is also observed on Figure 4-10 *(c)*, which is not yet accounted for within the current modelling strategy.

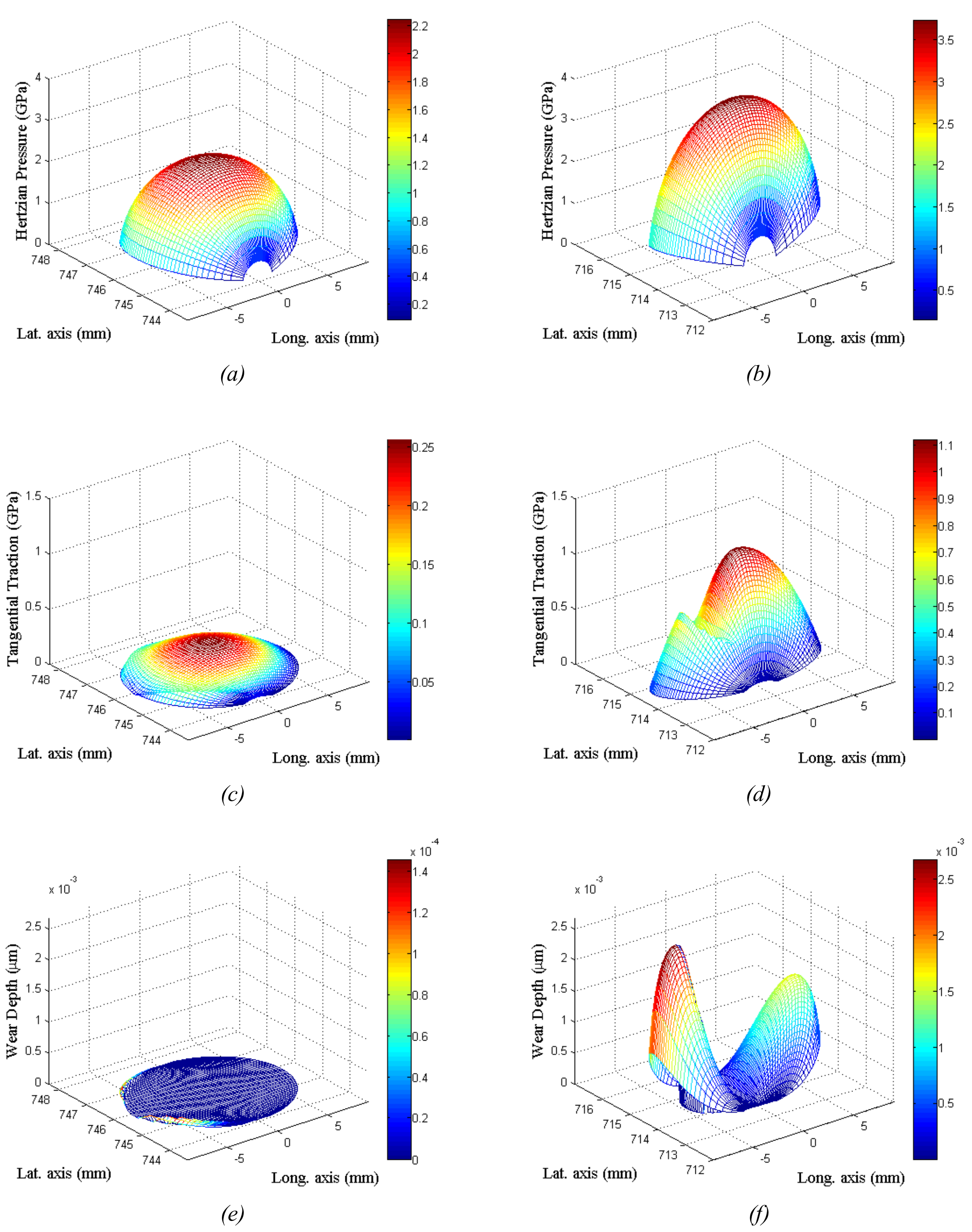

(a) *(b)*

(c) *(d)*

(e) *(f)*

Figure 4-7: Hertzian normal pressure for the stock rail (a) and switch rail (b), Fastsim tangential traction distributions for the stock rail (c) and switch rail (d) and associated Archard wear depth distributions for the stock rail (e) and switch rail (f).

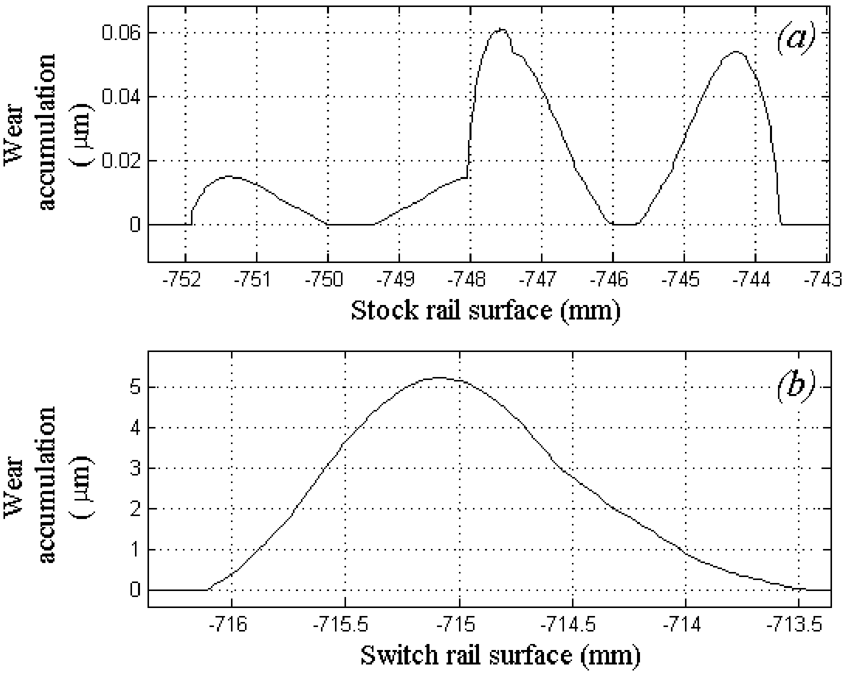

Figure 4-8: Wear accumulation after 200 load cycles on the stock rail (a) and switch rail (b) profiles.

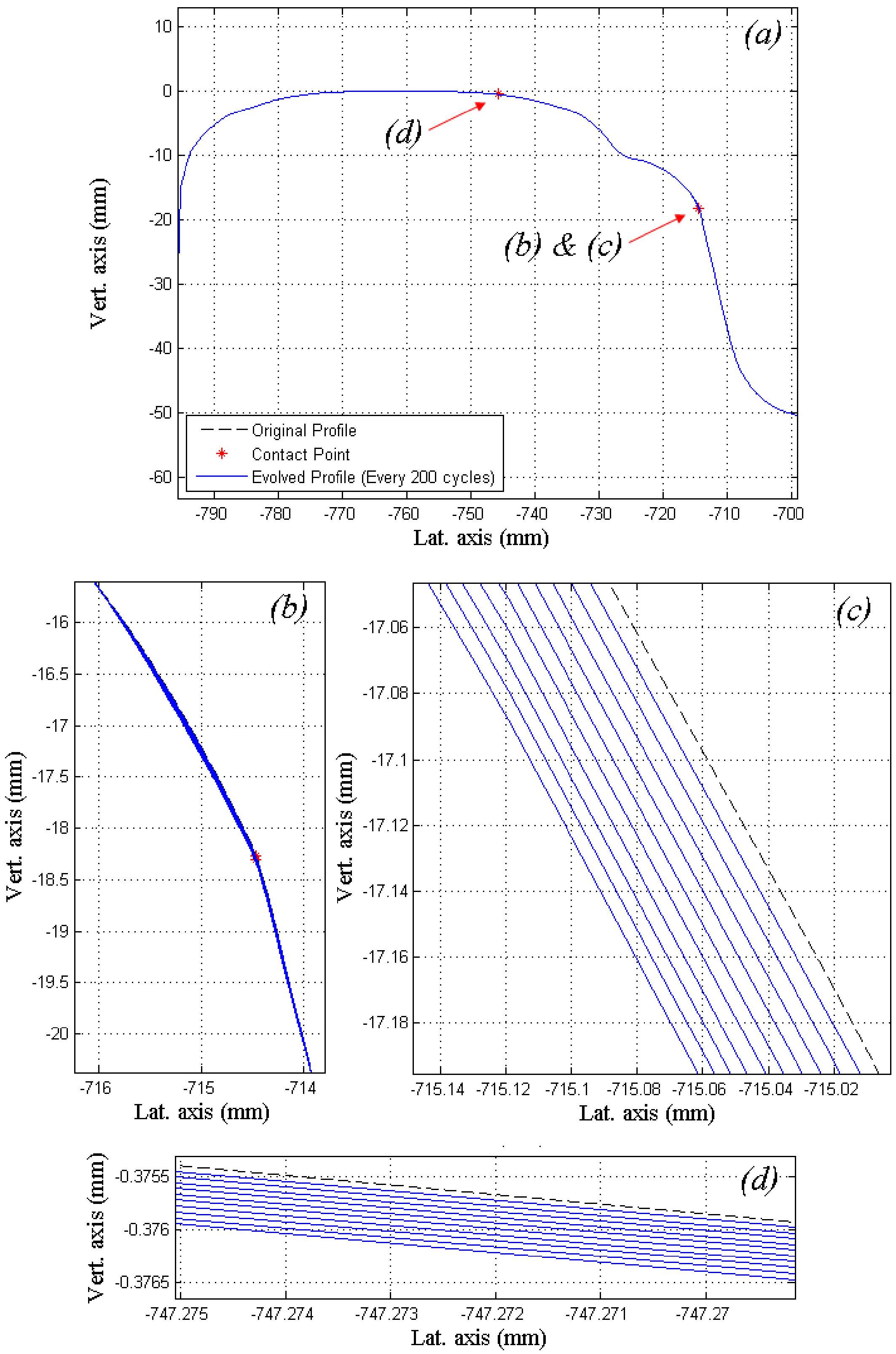

Figure 4-9: Measured rail profile 1m from toes of 682B points (a), switch rail profile evolution (b), switch damage magnified (c) and stock rail profile evolution (d). Note the difference in scales between the stock and switch rail results.

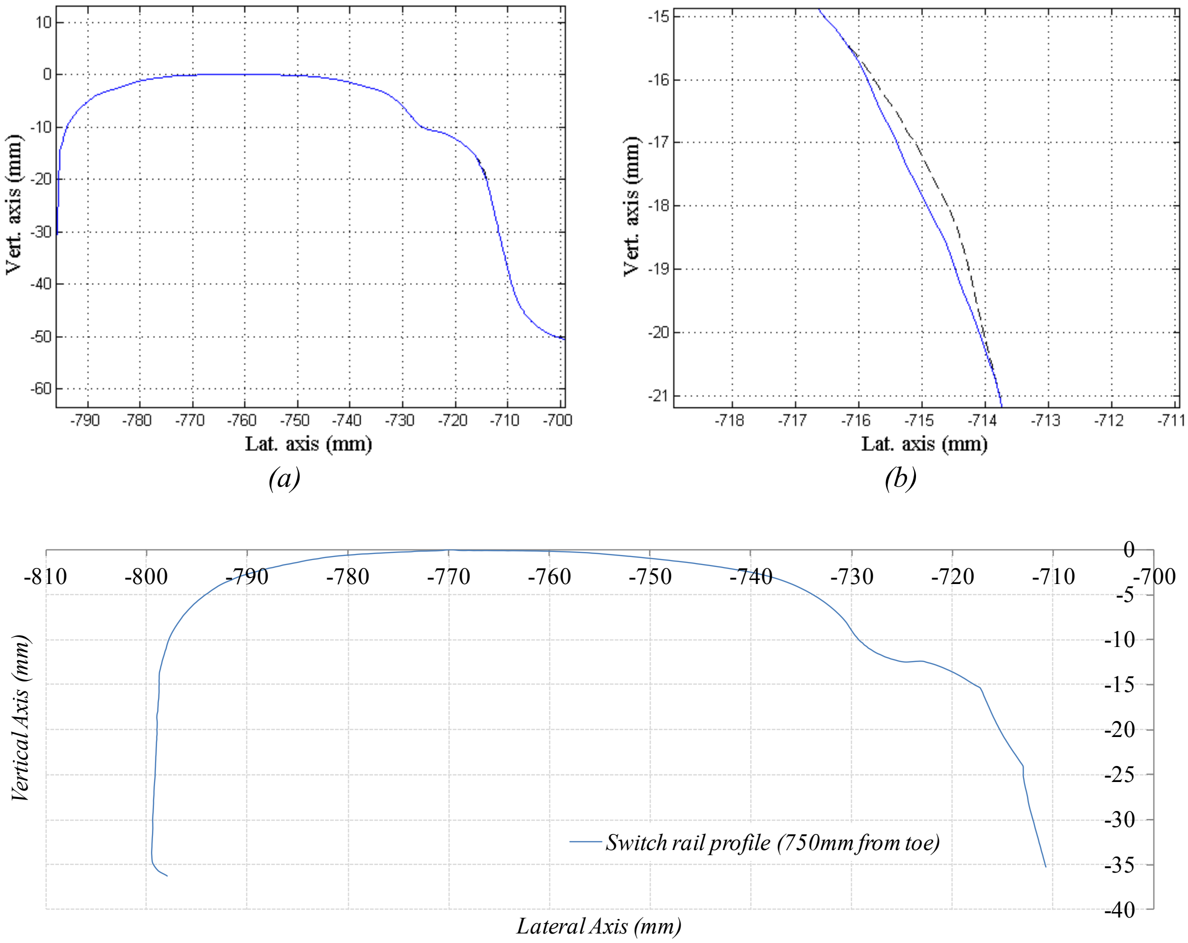

(a) *(b)*

(c)

Figure 4-10: Accelerated wear simulated on a switch rail profile 1 m from the switch tips (a), magnified profile evolution within the vicinity of the simulated wear groove (b) and an equivalent switch profile experiencing severe flange contact, measured from 1507 points at Waterloo (c).

4.6 Conclusion

A modelling strategy for simulating wear accumulation damage associated with railway switches and crossings is presented. Simplified contact stress theories have been integrated within a novel S&C wheel-rail multi-point contact detection tool to provide surface contact results, such as normal and tangential tractions and slip displacements. A wear model, based on Archard's law, is subsequently implemented to provide 3D wear depth approximations at up to 4 individual points of contact. To conclude the modelling strategy, a combined 2D accumulated wear depth profile is generated, over 200 load cycles, through summing the discrete wear approximations along each lateral element of every wear depth approximation. The rail profile is then deformed normal to the contact surface by the magnitude of the 2D accumulated wear depth profile.

The methodology has been demonstrated by simulating continuous wheel-rail flange contact interaction with a new switch rail profile taken 1 m from the switch tip of 628B points at Barnwood Junction. Results regarding the contact detection, normal (Hertzian) and tangential (Fastsim) tractions and associated wear depths (Archard) have been presented at a load cycle representing multi-point, stock and switch rail contact. An interface with railway vehicle dynamics is yet to be established therefore damage accumulation has been demonstrated through implementing a sinusoidal lateral shift of the wheelset, bringing the wheel into and out of flange contact with the switch rail profile. Although realistic vehicle dynamics were not simulated, a comparison with a similar switch rail experiencing severe flange contact demonstrates that the devised methodology is indeed viable approach to simulating S&C damage.

The methodology presented allows for further developments to overcome many of the limiting assumptions associated with simplified contact theories. The following areas of potential further work have been identified:

1. Simplified contact stresses will result in significant errors that are carried through from the contact traction stage of the modelling strategy. A solution not bound by the significant limitations of Hertzian normal contact modelling should be sought to improve damage approximations for long term S&C damage accumulation.

2. Investigate a more realistic problem by integrating the novel S&C damage accumulation tool within a vehicle dynamics package. This might also be achieved by using vehicle dynamics simulation outputs as inputs to the S&C damage accumulation tool, resulting in a parallel processing methodology.

3. This modelling strategy considers only wear damage and is not yet capable of predicting the secondary degradation effect of plastic deformation. The ability to include internal body stresses for future wear and plastic deformation modelling should be investigated.

4. As discussed within *Chapter 2,* empirical models for damage prediction bring uncertainty due to their validation against data obtained under very specific experimental conditions. For this reason, further validation of the empirical $T\gamma$ model against UK S&C site data should be completed prior to accepting it as a suitable tool for accurate S&C RCF prediction. To predict the true severity of RCF at S&C, alternative RCF predictive techniques, capable of simulating crack initiation and growth, should also be investigated and implemented within the tool.

Addressing some of these existing limitations will enable significant improvements to be made with regards to the accuracy of long term S&C degradation predictions. Such developments are next presented within *Chapter 5* with the novel implementation of a lateral, 2D boundary element solution.

Chapter 5 : Wheel-Rail Boundary Element Modelling

This chapter introduces the boundary element method (BEM) and its application to wheel-rail contact problems. The structure of an existing BEM model is presented before describing how the code has been adapted for automatically assessing elastic wheel-rail contact problems. The advantages of developing a novel BEM tool for improving both the normal surface contact stress distribution and internal domain results are presented and validated against finite element analysis. Further novel benefits associated with the lateral BEM model, that are directly applicable to S&C interaction, are then discussed.

5.1 Introduction

Chapter 3 and *Chapter 4* describe the basis for a computational tool capable of predicting wear damage at the wheel-S&C interface. The theories applied require a number of significant limiting assumptions, such as smooth, elliptical contact patches conforming to half-space assumptions and similar material properties (for further description, see *section 2.2.2*), which contribute to limiting the solution accuracy. Both switches and crossing are designed to have considerable operational lives and hence long-term damage accumulation generally requires a significant number of loading cycles. The limiting assumptions present within simplified contact theories will inevitably lead to an accumulation of error and inaccuracies in the simulated degraded state of the asset. To further improve the wheel-rail contact solution and remove a number of limitations from the simplified theory, a non-Hertzian contact model is investigated.

The major objectives within *Chapter 5* are therefore to:

1. Demonstrate the novel application of a two-dimensional lateral boundary element model (BEM) for solving complex wheel-rail contact problems. Although the boundary element technique is not fundamentally new, the implementation of a lateral BE model for solving complex wheel-S&C contact problems has not been previously published.

2. Investigate the feasibility of replacing existing FEA techniques, as used within current state-of-the-art S&C studies, with a novel implementation of a BEM model for wheel-rail interaction.

5.2 The Boundary Element Method

5.2.1 Background

Numerical methods are widely used in engineering for stress analysis of complex geometric problems. By far the most common and understood technique is the finite element (FE) method where the domain under analysis is represented by non-infinitesimal (*i.e.* finite) elements of material. Each element reproduces approximately the physical behaviour of a small region of the domain by simulating physical laws assigned to them (*i.e.* Material properties, Newton's / Hooke's laws, etc...). In the early 1950's, the FE method began to be recognised as a powerful tool for the simulation of physical systems and since has enjoyed many years of development and optimisation [116]. Despite this, the technique remains computationally expensive for large, non-linear systems due to discretisation of the entire domain under analysis. It is not uncommon to see many thousands of elements being used within a single analysis. This is demonstrated by Wiest [38], who studied a small section of a wheel to crossing nose interaction problem using over 130,000 elements. Figure 5-1 illustrates the small extent of the model with respect to the significantly large number of elements required.

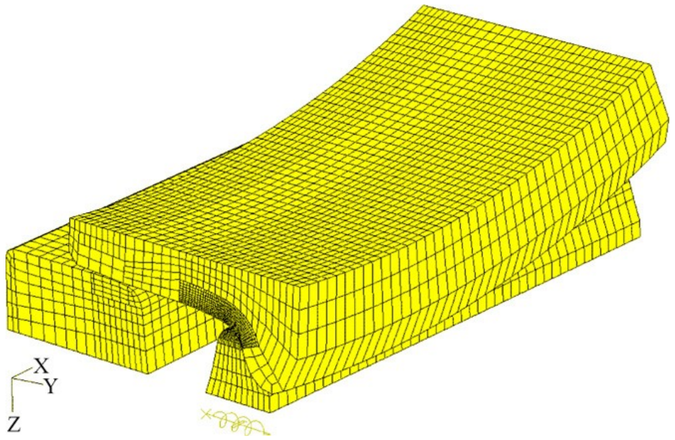

Figure 5-1: Finite Element model requiring over 130,000 elements (Example taken from Wiest [38])

It may be argued that, from a numerical point of view, wheel-rail interaction problems are boundary contact problems and a boundary solution, rather than domain type, would be more suitable. With this in mind; an alternative and undoubtedly less common approach to the FE method is the boundary integral equation (BIE) technique, commonly known as the boundary element method (BEM). There are two main types of BEM formulation, namely the direct (DBEM) and indirect (IBEM) boundary element solutions. Most modern codes utilise the direct formulation, which is derived from the

Maxwell-Betti reciprocal theorem. A more detailed description of the direct formulation is given by Brebbia [117]. The indirect formulation, which is the technique adopted within this study, is based on the principle of superposition. Here, the body of interest is modelled within an infinite plane through discretisation of the boundary into finite surface elements. Directional stresses and displacements, both at the surface and within the internal domain at a field point (z) due to point loading (P,Q) on the surface (ξ), can be easily calculated using integral equations, also known as fundamental solutions (denoted $\boldsymbol{\sigma}$ for stress and $\boldsymbol{U}$ for displacement). Total stress and displacement solutions can then be obtain through superposition. For example, the lateral stress component is given by:

$$\sigma_{xx} = \int_{\Omega} \left[\boldsymbol{\sigma}_{xx,x} w_x d\xi + \boldsymbol{\sigma}_{xx,y} w_y d\xi\right]$$

Similar expressions are derived for the vertical (σ_{yy}) and shear (σ_{xy}) stress components and vertical (u_y) and lateral (u_x) displacements.

The BEM code implemented within this study was originally developed for studying general contact problems for simple, smooth geometries [118]. This meant that, without significant manual effort, the available meshing routine only enabled automated mesh generation for basic straight or curved boundaries. Several code modifications were therefore required to enable accurate and automatic contact analysis of real, measured wheel and rail profiles. These modifications are discussed within *section 5.3*. The remainder of *section 5.2* describes in detail the theory and structure of the Indirect BEM code.

5.2.2 Indirect BEM Formulation

The adapted BEM code is based on an indirect boundary element formulation with displacement and stress fields expressed in the form:

$$u_{(z)} = \int_{\Omega} \boldsymbol{U}_{(\xi,z)} w_{(\xi)} d\xi \qquad 5\text{-}1$$

$$\sigma_{(z)} = \int_{\Omega} \boldsymbol{\sigma}_{(\xi,z)} w_{(\xi)} d\xi \qquad 5\text{-}2$$

Here, ξ and z represent the source and field points respectively, as illustrated within Figure 5-2. The fundamental solutions for displacement and stress are given by $\boldsymbol{U}_{(\xi,z)}$ and $\boldsymbol{\sigma}_{(\xi,z)}$ whilst $w_{(\xi)}$ is the vector of unknown weight functions, which describes the fictitious distributions of normal and shear tractions. $\boldsymbol{U}_{(\xi,z)}$ and $\boldsymbol{\sigma}_{(\xi,z)}$ are m by n matrices containing m components of displacement / stress at the defined field points (z) due to a unit point load applied at each available source point (ξ). Matrix component n stores the direction component, therefore $n = 2$ (x and y components) for two-dimensional problems.

5.2.3 Discrete form

To implement the above indirect boundary element solution into a computational code, a discrete form of equations 5-1 and 5-2 is required. Figure 5-2 illustrates the general BEM domain (***Γ***) and its boundary (***Ω***), which is divided into N segments, each consisting of length s_i and semi-length a. A source point, $\xi_{(x_0,y_0)}$, is defined at the centre of each segment and is defined within its own local coordinate system (n,t). Finally, w_i is the unknown magnitude of the triangular weight function (i.e. weighting of the traction component, P_i or Q_i depending on the applied boundary condition).

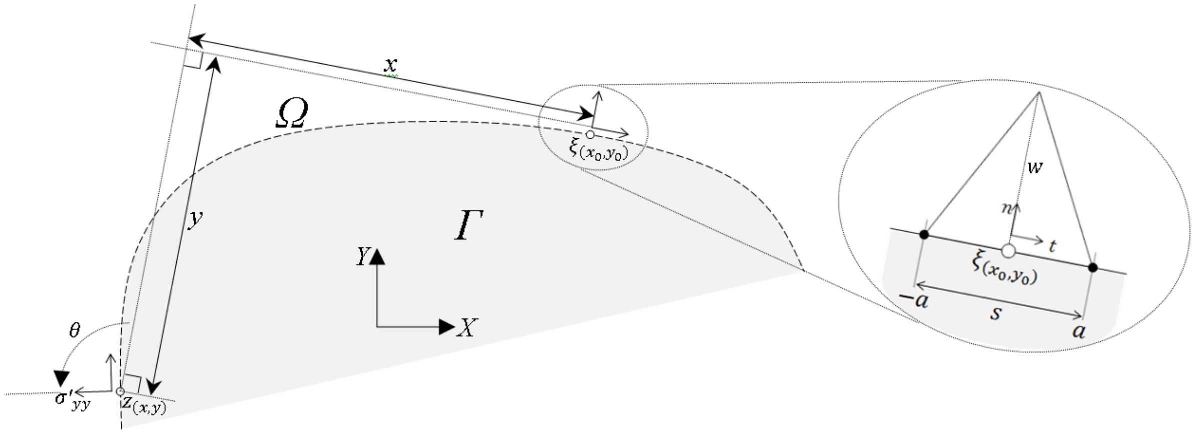

Figure 5-2: BEM schematic: triangular shape function over a straight boundary element.

Equations 5-1 and 5-2 are then represented in the discrete form as:

$$u_{(z)} = \sum_{i=1}^{N} \int_{s_i} \boldsymbol{U}_{(\xi,z)} w_{(\xi)} d\xi \qquad 5\text{-}3$$

$$\sigma_{(z)} = \sum_{i=1}^{N} \int_{s_i} \boldsymbol{\sigma}_{(\xi,z)} w_{(\xi)} d\xi \qquad 5\text{-}4$$

The integration is now solved over the length of each element and not the entire surface.

The adopted BEM code uses a piecewise linear discretisation scheme with overlapping triangular shape functions for evaluating the unknown weight functions. This is expressed as:

$$w_{(\xi)} = w_i \left(1 - \left|\frac{\xi}{a}\right|\right) \qquad 5\text{-}5$$

Inserting Equation 5-5 into Equation 5-3 gives:

$$u_{(z)} = \sum_{i=1}^{N} \int_{s_i} \boldsymbol{U}_{(\xi,z)} \left(1 - \left|\frac{\xi}{a}\right|\right) d\xi \cdot w_i \qquad 5\text{-}6$$

The same process can be followed to obtain a similar expression for the stress solution:

$$\sigma_{(z)} = \sum_{i=1}^{N} \int_{s_i} \boldsymbol{\sigma}_{(\xi,z)} \left(1 - \left|\frac{\xi}{a}\right|\right) d\xi \cdot w_i \qquad 5\text{-}7$$

Equations 5-6 and 5-7 can then be computed analytically and are expressed in matrix form by:

$$\boldsymbol{u}^* = \boldsymbol{U} \cdot \boldsymbol{w} \qquad 5\text{-}8$$

$$\boldsymbol{\sigma}^* = \boldsymbol{C} \cdot \boldsymbol{w} \qquad 5\text{-}9$$

Here, $\boldsymbol{u}^*$ and $\boldsymbol{\sigma}^*$ are the displacement and stress boundary condition vectors, respectively. $\boldsymbol{U}$ and $\boldsymbol{C}$ are the displacement and stress influence function coefficient matrices, respectively, and contain the integrals as defined within Equations 5-6 and 5-7. By reordering and combining Equations 5-8 and 5-9, a single linear system is achieved:

$$\boldsymbol{A} \cdot \boldsymbol{w} = \boldsymbol{b} \qquad 5\text{-}10$$

where $\boldsymbol{A}$ contains elements of either $\boldsymbol{U}$ or $\boldsymbol{C}$, depending on the type of prescribed boundary condition within $\boldsymbol{b}$, which contains elements of $\boldsymbol{u}^*$ or $\boldsymbol{\sigma}^*$. Equation 5-10 therefore solves for the unknown nodal densities of the weight functions, **w**, which are subsequently used within Equations 5-6 and 5-7 to obtain nodal solutions for displacement and stress.

5.2.4 Influence function coefficient matrices

The influence function coefficients (Green's functions [119]) are evaluated between each source (ξ) and field (z) point combination and used to populate the **U** and **C** matrices. The shape of the boundary elements will also have an influence on the fundamental solution required to populate the **U** and **C** matrices. Within the adopted BEM model, both straight and curved boundary elements are available although only straight elements have been used within this study.

The complex form of Kelvin's solution for a point force in a plane [119] is implemented and is given in terms of two complex potentials:

$$\Phi_{(\xi,z)} = -\frac{Q+iP}{2\pi(1+\kappa)}\frac{1}{z-\xi} \qquad 5\text{-}11$$

$$\Psi_{(\xi,z)} = \kappa\frac{Q-iP}{2\pi(1+\kappa)}\frac{1}{z-\xi} - \frac{Q+iP}{2\pi(1+\kappa)}\frac{\bar{\xi}}{(z-\xi)^2} \qquad 5\text{-}12$$

where $z = x + iy$.

These complex potentials can then be used within Equations 5-16 to 5-18 to ascertain the displacements and stresses at z due to point loading at ξ:

$$\sigma^{xx}_{(\xi,z)} + \sigma^{yy}_{(\xi,z)} = 4\,Re\left[\Phi_{(\xi,z)}\right] \qquad 5\text{-}13$$

$$\sigma^{yy}_{(\xi,z)} - \sigma^{xx}_{(\xi,z)} + 2i\tau^{xy}_{(\xi,z)} = 2\left(\bar{z}\Phi'_{(\xi,z)} + \Psi_{(\xi,z)}\right) \qquad 5\text{-}14$$

$$2G\mathrm{u}_{(\xi,z)} = \kappa\varphi_{(\xi,z)} - z\overline{\varphi'_{(\xi,z)}} - \overline{\psi_{(\xi,z)}} \qquad 5\text{-}15$$

Here, prime indicates differentiation with respect to z ($\Phi_{(\xi,z)} = \varphi'_{(\xi,z)}$ and $\Psi_{(\xi,z)} = \psi'_{(\xi,z)}$) and bar denotes the complex conjugate.

Assessing the influence function over a straight element places the source point entirely on the real axis. This simplifies the integration over the element as ξ can be defined as:

$$\xi = x_0 + iy_0 \Rightarrow \ \xi = x_0 \qquad \text{5-16}$$

Substituting Equation 5-19 into Equation 5-5 provides a description of the triangular shape function over the linear boundary element:

$$w_{(x_0)} = w_i \left(1 - \left|\frac{x_0}{a}\right|\right) \qquad \text{5-17}$$

The integration within Equation 5-6 can then be performed over the boundary element upon obtaining $\boldsymbol{U}_{(x_0,x,y)}$:

$$u_{(x,y)}^{tri} = \int_{x_0} \boldsymbol{U}_{(x_0,x,y)} \left(1 - \left|\frac{x_0}{a}\right|\right) dx_0 \qquad \text{5-18}$$

Subdividing the integral in two parts, we obtain the following solution:

$$u_{(x,y)}^{tri} = \int_{-a}^{0} \boldsymbol{U}_{(x_0,x,y)} \left(1 + \left|\frac{x_0}{a}\right|\right) dx_0 + \int_{0}^{a} \boldsymbol{U}_{(x_0,x,y)} \left(1 - \left|\frac{x_0}{a}\right|\right) dx_0 \qquad \text{5-19}$$

The above integration has been completed using the Symbolic Toolbox within the software package MATLAB. Closed form expressions have been obtained and are provided within *Appendix A1*. For the stress solution, this process is performed within a local (*n, t*) coordinate system, as illustrated previously within Figure 5-2; therefore, an appropriate rotation of the stress tensor is required. This is achieved through use of transformation matrices incorporating Mohr's relationship of stress transformation:

$$\tilde{\sigma}_{xx} = \cos^2\theta\sigma_{xx} + \sin^2\theta\sigma_{yy} + 2\sin\theta\cos\theta\,\sigma_{xy} \qquad \text{5-20}$$

$$\tilde{\sigma}_{yy} = \sin^2\theta\sigma_{xx} + \cos^2\theta\sigma_{yy} - 2\sin\theta\cos\theta\,\sigma_{xy} \qquad 5\text{-}21$$

$$\tilde{\sigma}_{xy} = -\sin\theta\cos\theta\,\sigma_{xx} + \sin\theta\cos\theta\,\sigma_{yy} + (\cos^2\theta - \sin^2\theta)\sigma_{xy} \qquad 5\text{-}22$$

Here, θ is the rotation angle between the global and local element coordinate systems.

The final solution then becomes the sum of all closed form displacement and stress contributions. Equations 5-6 and 5-7 are re-written as:

$$u_{(x,y)} = \sum_{i=1}^{N} u_{(x,y)}^{tri} \cdot w_i \qquad 5\text{-}23$$

$$\sigma_{(x,y)} = \sum_{i=1}^{N} \sigma_{(x,y)}^{tri} \cdot w_i \qquad 5\text{-}24$$

5.2.5 Contact problems

Within the adapted 2D BEM model, an incremental algorithm for the solution of frictional contact problems is implemented. The solution considers two elastic bodies in contact by firstly ensuring compatibility of the tractions and normal displacements at the contact interface.

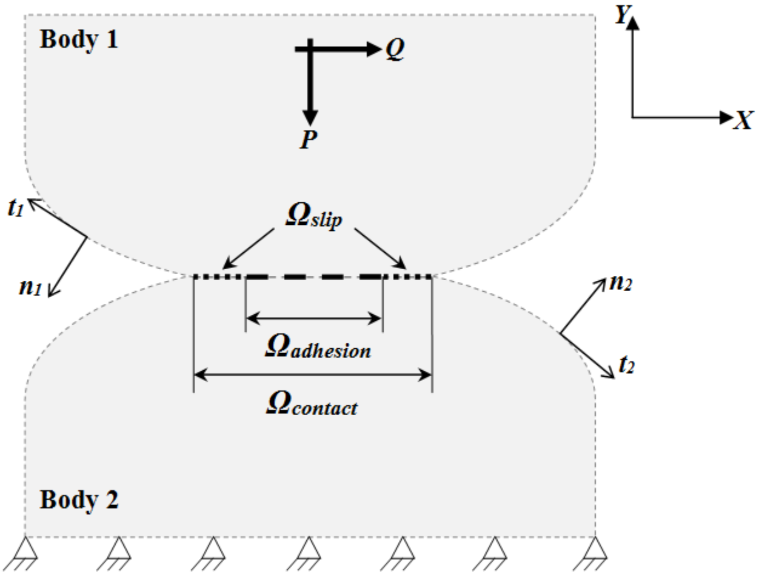

Figure 5-3: BEM Contact Schematic.

For each node residing within the contact interface (*Ω*$\Omega_{contact}$, see Figure 5-3):

$$\sigma_n^1 - \sigma_n^2 = 0 \tag{5-25}$$

$$\sigma_t^1 - \sigma_t^2 = 0 \tag{5-26}$$

$$u_n^1 - u_n^2 = h \tag{5-27}$$

$$\sigma_n^1 ,\ \sigma_n^2 \leq 0 \tag{5-28}$$

where σ_n^1 and σ_n^2 are the normal tractions for bodies 1 and 2 respectively. σ_t^1, σ_t^2 and u_n^1, u_n^2 represent tangential tractions and normal displacements with respect to the contact surface, $\Omega_{contact}$, respectively. h is the original separation between the two contacting bodies. Equations 5-25 to 5-27 ensure that system compatibility is maintained whilst Equation 5-28 demonstrates that only compressive contact stresses are allowed.

Adhesion ($\Omega_{adhesion}$) and slip (Ω_{slip}) conditions are modelled in the same fashion as previously implemented within the Fastsim algorithm (see Section 4.3.2). In summary, Coulomb's law is used to enforce a no slip (adhesion) condition through:

$$|\sigma_t| < \mu \cdot |\sigma_n| \tag{5-29}$$

$$u_t^1 - u_t^2 = 0 \tag{5-30}$$

Equation 5-29 states that to exceed friction, the magnitude of the tangential traction must exceed the magnitude of the normal traction multiplied by the coefficient of friction, μ. Equation 5-30 enforces the compatibility of tangential displacements of nodes residing within the adhesion zone.

Nodes residing within the slip zone will satisfy the following conditions:

$$|\sigma_t| = \mu \cdot |\sigma_n| \tag{5-31}$$

$$u_t^1 - u_t^2 \neq 0 \tag{5-32}$$

$$(u_t^m - u_t^n) \cdot \sigma_t^m \leq 0 \tag{5-33}$$

Upon detection of slip within the contact surface, the magnitude of the tangential traction is saturated to the traction bound through Equation 5-31. Tangential displacements between opposing nodes in the slip zone will become none-zero, which is illustrated by Equation 5-32. Finally, the direction of the tangential traction is defined by Equation 5-33.

Equilibrium of forces must also be satisfied and is implemented through:

$$\int_{\Omega_{contact}} \sigma_n ds - P = 0 \tag{5-34}$$

$$\int_{\Omega_{contact}} \sigma_t ds - Q = 0 \tag{5-35}$$

The discrete form of the BEM contact solution follows the same format as discussed previously within Section 5.2.3. Discrete expressions are combined to build relationships for the contact conditions as described above. To illustrate this, the discrete forms of Equations 5-30 and 5-31 are:

$$u_t^{1,i} - u_t^{2,i} = \boldsymbol{U}_t^{1,i}\boldsymbol{w}^1 - \boldsymbol{U}_t^{2,i}\boldsymbol{w}^2 = 0 \qquad \forall i \in \Omega_{adhesion} \tag{5-36}$$

$$\left|\sigma_t^{1,i}\right| = \mu \cdot \left|\sigma_n^{1,i}\right| \rightarrow \boldsymbol{C}_t^{1,i}\boldsymbol{w}^1 \pm \mu \cdot \boldsymbol{C}_n^{1,i}\boldsymbol{w}^1 = 0 \qquad \forall i \in \Omega_{slip} \tag{5-37}$$

5.3 BEM adaptation to Wheel-Rail Contact Problems

The purpose of implementing a boundary element solution within the already established wheel-rail contact and damage algorithm is to improve the solution accuracy, robustness and versatility through:

- eliminating the multi-point contact and force equilibrium routines (the BEM model deals with these stages automatically during the incremental solution procedure)

- replacing the simplified Hertzian normal contact model with the non-Hertzian BEM approximation, therefore eliminating some of the limiting assumptions and allowing:

    - dissimilar material properties within each contact body
    - conformal contact modelling
    - non-elliptical (non-Hertzian) pressure distributions

- enabling accurate evaluation of stress and displacements everywhere within the bodies in contact.

Figure 5-4 shows where the BEM implementation fits within the overall S&C degradation modelling process. For successful integration, the following code modifications were required:

- Automatic meshing of problem external boundaries and internal domain (when required)
- Automatic initial contact limits estimation

The following sub-sections of *section 5.3* describe these modifications and their implementation within the complete S&C damage tool.

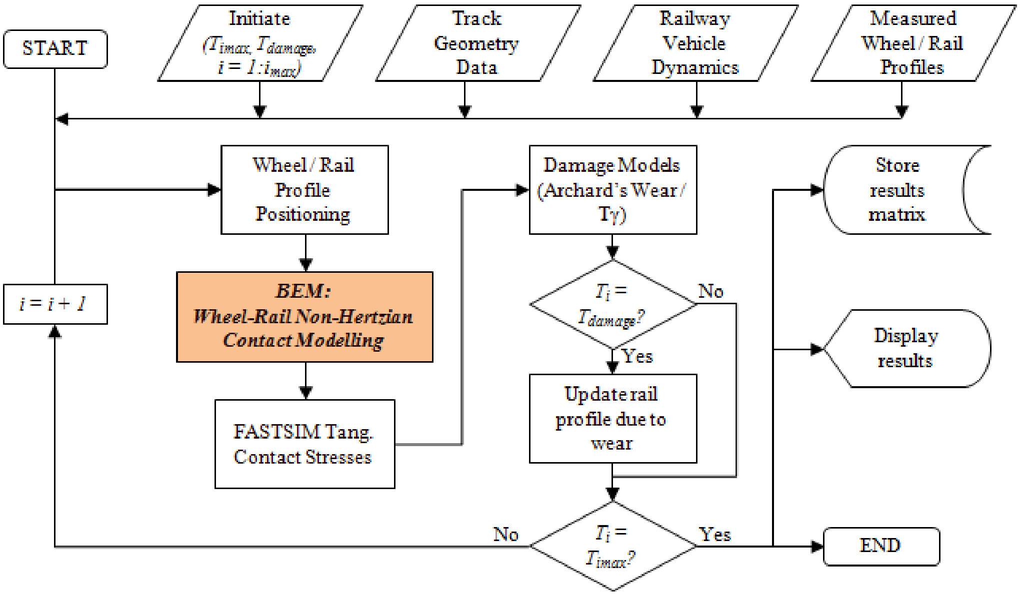

Figure 5-4: Modified version of Figure 4-1 to include BEM within the S&C degradation process

5.3.1 Automated initial contact zone estimation

Operation of the BEM code requires an initial, manual estimation of the contact zone size, which must be larger than the actual size of contact to fully capture all of the contact tractions. The initial contact size estimation needed to be automated in order to use the BEM code within a fully contained wheel-rail contact model. Within the benchmark tests (see §5.4), this is achieved by defining the initial contact search to ±10mm either side of the initial point of contact, which is acceptable when considering simple case studies where the initial contact zone is easily identifiable. For more complex wheel-rail problems, where contact could potentially exist anywhere between the wheel and rail, the initial search range is defined to be the maximum overlapping region of the two contact faces. Figure 5-5 provides an example of the two possible scenarios and also demonstrates that the upper contact body limits (wheel, ★) are defined slightly wider than those for the lower contact body (rail, ★). This is due to the nodes on the upper surface being used during the interpolation process when assessing the contact gap.

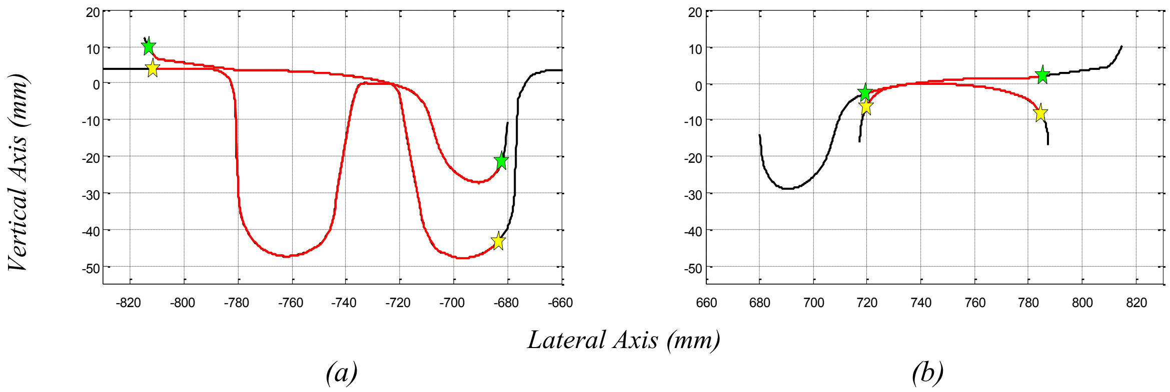

Figure 5-5: Profile search range for left wheel to crossing (a) and right wheel to plain line rail (b) interaction.

An automatic mesh optimisation process has also been included to further improve the solution efficiency. Once the extent of the initial contact zone has been estimated, the mesh size within any region on the contact surface falling outside of the initial contact zone is increased. Only mesh sizes <0.25 mm are coarsened to ensure that the general form of the overall boundary remains accurate. It is also demonstrated within *section 5.4.1* that mesh sizes down to approximately 0.25 mm have minimal effect on the overall computational efficiency of the BEM solution.

5.3.2 Automatic meshing

The post processing step of the original BEM code required a manually generated input file for describing the basic geometric outline of the elastic body under analysis. An example of the manual input file format is given within Table 5-1. Unless significant effort was exerted in generating sufficiently detailed input files, this meshing routine limited the availability of the BEM model to very basic geometries consisting of straight lines and continuous curves, illustrated by Figure 5-6. An automated routine for geometry discretisation and mesh file generation then followed. A section from an example mesh file is presented within Table 5-2. Columns 1 and 2 provide the nodal coordinates within the global coordinate system, columns 3 and 4 are respectively the shape function triangular semi-length (a) and the element normal vector (n), which are used to define element size and the local surface coordinate system. Finally, columns 5, 6 and 7 are used to define the boundary element radius, element type and whether or not the element belongs to the internal domain, respectively.

Key Point 1 (kp1)		Key Point 2 (kp2)		Elements between kp1 and kp2	Radii of segment	Element Type
x_{kp1}-coordinate	y_{kp1}-coordinate	x_{kp2}-coordinate	y_{kp2}-coordinate			
-1.5	2.0	1.5	2.0	50	0	0
1.5	2.0	1.5	0.0	20	0	0
1.5	0.0	-1.5	0.0	500	70	-1
-1.5	0.0	-1.5	2.0	20	0	0

Table 5-1: Example mesh input file (simple block with a 70mm radius cylindrical contact face)

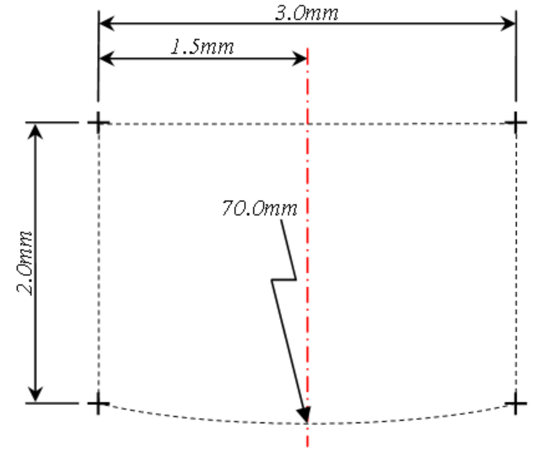

Figure 5-6: Simple contact geometry generated from input file provided within Table 5-1

1	2	3	4	5	6	7
x-coordinate	y-coordinate	Triangular semi-length	Normal vector	Element radius	Element type marker	Internal node marker
1.500	0.00000	0.006	-3.1202	0	0	0
1.494	-0.00013	0.006	-3.1202	0	0	0
1.488	-0.00026	0.006	-3.1203	0	0	0
1.482	-0.00038	0.006	-3.1204	0	0	0

Table 5-2: Example mesh data format (first 4 nodes of lower contact face)

Adapting the BEM model for railway wheel-rail applications therefore required the development of a completely automated meshing routine that enabled the discretisation of real, measured wheel and rail profiles. Figure 5-7 demonstrates the complete procedure required for automating the BEM mesh generation. The nodal xy-coordinates of the measured contact profile are imported from the initial wheel / rail profile positioning routine, as described within *Chapter 3*. The contact surface is then discretised further using a MATLAB shape preserving function to create the required quantity of nodes along the surface profile. This is an important step in automating the mesh procedure due to the requirement of the slave surface (wheel) having a more refined mesh than the master surface (rail).

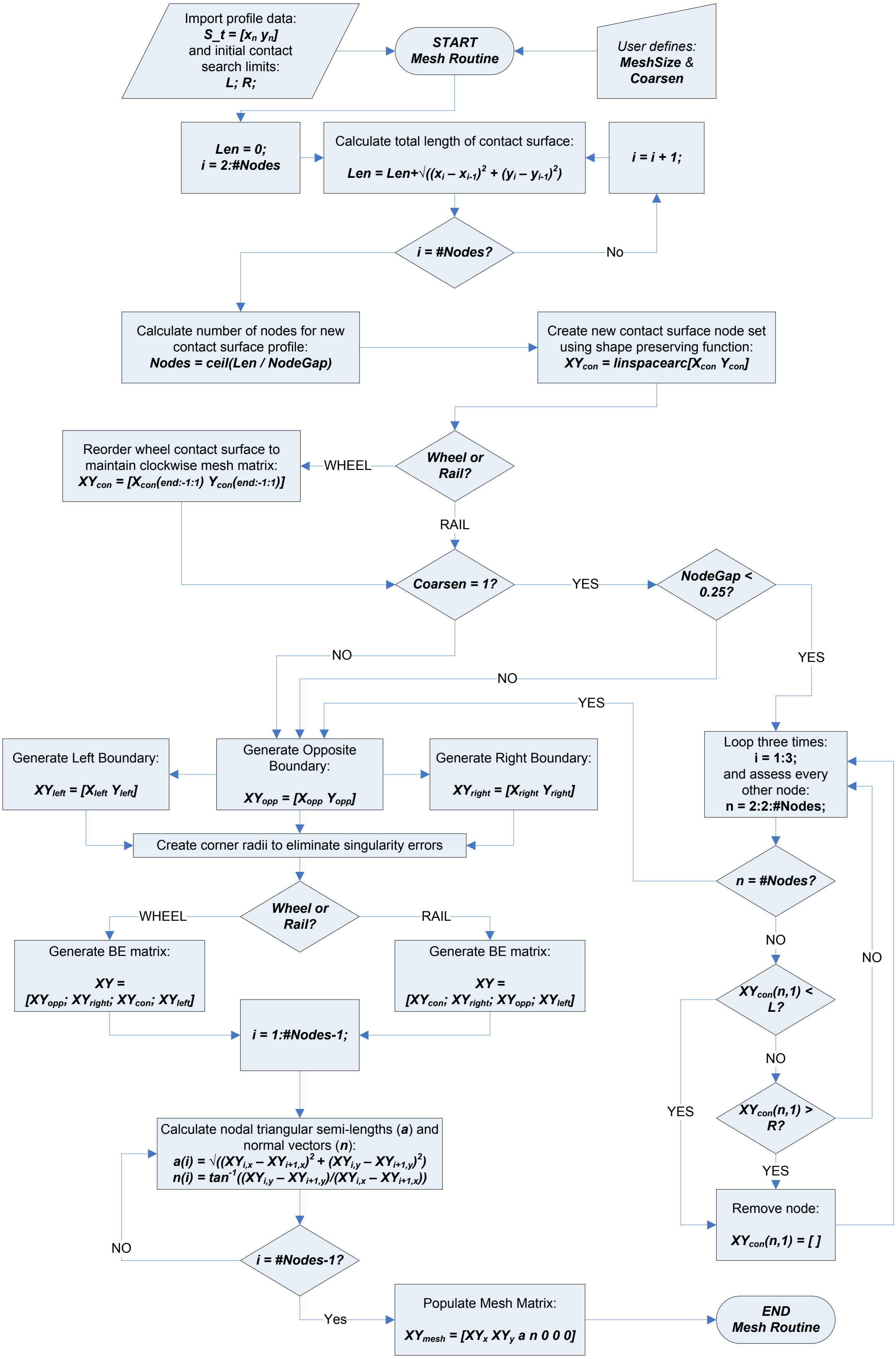

Figure 5-7: New BEM meshing routine for automated wheel-rail contact modelling.

5.3.2.1 Internal nodes for domain results

As can be seen within *section 5.4.2*, *Table 5-4*, the BEM solution becomes less efficient when evaluating the internal domain results. To ensure maximum solution efficiency, a switch is included to enable the user to turn off the internal results, prior to submitting the analysis, if only the boundary tractions and displacements are of interest. Within case studies 1 – 3 (see *section 5.4*), the total depth of the internal mesh is set to 15 mm into the contact body with a width of ±10 mm either side of the contact origin. This is easily defined within the benchmark tests due to the relatively simple and symmetric geometries associated with each problem. More complex geometries, such as those applicable to wheel-rail interaction, require a more flexible solution for capturing all of the internal domain results. The total internal mesh depth is again set to 15mm but the total width is automatically defined to cover the entire lower contact body (i.e. the rail). The total number of nodes in the x and y directions are defined by the substrate width, x_{nodes}, and the quantity of nodes required to achieve the desired mesh size within the prescribed mesh depth, y_{nodes}. The internal domain is then divided equally into x_{nodes} columns, which are then subsequently divided equally into y_{nodes} rows between the upper contact surface and prescribed internal mesh depth. Figure 5-8 demonstrates a resulting internal mesh for a BS113A rail profile.

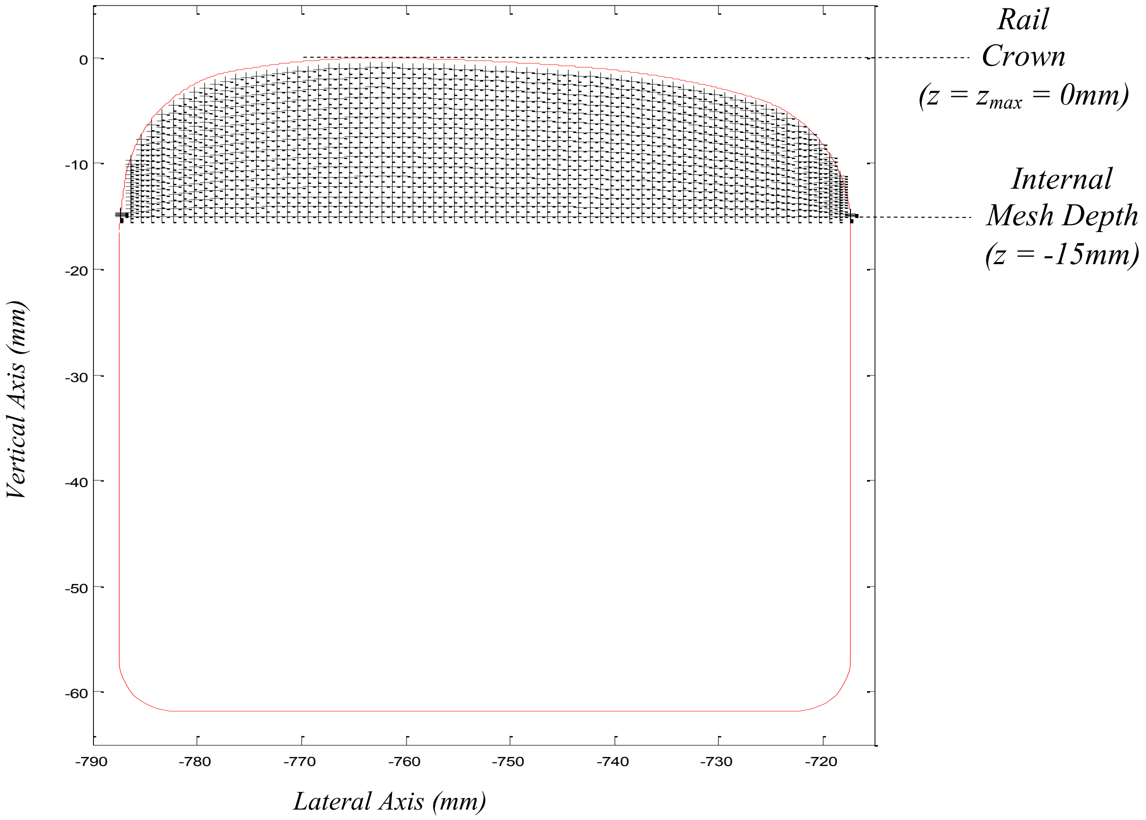

Figure 5-8: Internal meshing on a BS113A rail profile (1mm mesh used for illustration)

5.4 Benchmark tests

To demonstrate the applicability of the BE model to typical wheel-rail contact scenarios, three initial test cases have been completed. These include non-conformal, conformal and multi-point contact problem as illustrated in Figure 5-9. Each test case contains identical elastic material properties of $E = 210GPa$ and $v = 0.3$. The applied boundary conditions are also consistent between cases, with the top face of body 1 and bottom face of body 2 rigidly fixed in both x and y directions. The BEM model operates by iteratively distributing the applied loads (*P*, *Q*) over the contacting surfaces through evaluating the separation between the contacting faces, hence the requirement for also fixing the top surface of body 1. A total normal load of $P = 50kN$ is applied.

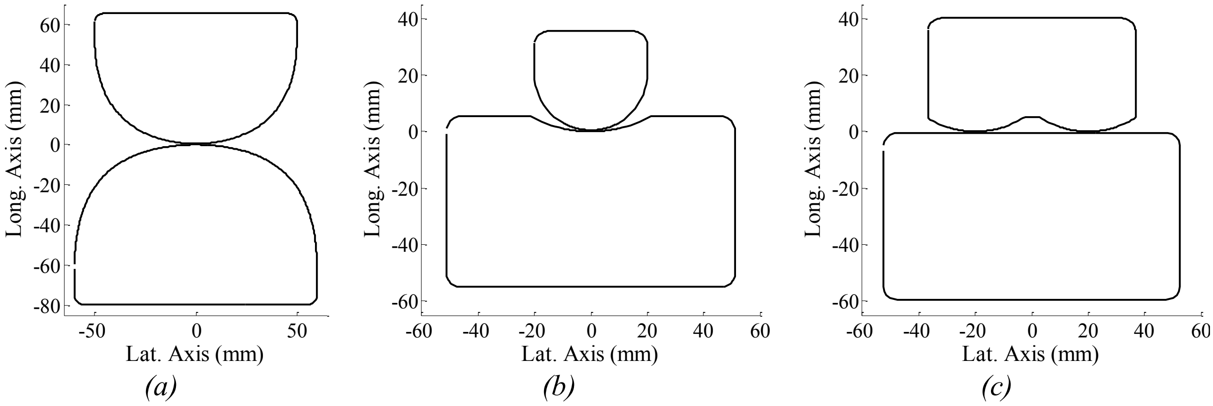

Figure 5-9: Case study geometries: (a) non-conformal (b) conformal and (c) multi-point contact.

5.4.1 Mesh Convergence

Before each test case is validated against the well established finite element methodology, a mesh convergence study has been completed. Within this study, each test case is used to demonstrate an optimal mesh size when implementing the BEM model for wheel-rail applications. Whilst holding mesh within the non-contacting faces constant, the mesh size on each contact face is slowly reduced (from 1mm – 0.01mm) until an acceptable level of accuracy is obtained for both the normal contact pressure and displacement of the contact face. These variables were chosen due to being the results of significant interest within this study. Figure 5-10 *(a)*, Figure 5-12 *(a)* and Figure 5-14 *(a)* all indicate that a mesh size of approximately 0.2 mm provides the best compromise between computational efficiency (automatic meshing and solution time) and solution accuracy. As the mesh is reduced to values smaller than 0.1 mm, a significant reduction in computational efficiency begins to develop, illustrated by the sharp increase in both the meshing and solution time curves. The percentage change in results is calculated using:

$$\%_{CHANGE} = \left|\frac{\sigma_n - \sigma_{n-1}}{\sigma_{n-1}}\right| \times 100 \qquad 5\text{-}38$$

The next convergence test was for the internal domain mesh. Here, the boundary mesh was held at the optimum value (0.2mm) whilst the internal domain mesh was slowly reduced from 1mm to 0.05mm. Again, the solution time increases significantly with reducing mesh size below approximately 0.1mm. Although the internal mesh time follows a similar relationship, the magnitude of the meshing times is significantly small to ignore this as a criterion when choosing the optimum internal mesh size. Figure 5-10 *(b)*, Figure 5-12 *(b)* and Figure 5-14 *(b)* all illustrate that an internal mesh within the region of 0.2mm provides the best compromise between computational efficiency and accuracy of solution.

To further increase the computational efficiency of the solution, an automatic mesh coarsening procedure is introduced to remove nodes evenly from outside of the estimated contact region on the contact face. This procedure is only invoked upon detection of meshes <0.25 mm due to mesh sizes greater than or equal to 0.25 mm having minimal effect on the computational efficiency of the solution. The final, optimised mesh for each case study can be seen within Figure 5-11, Figure 5-13 and Figure 5-15.

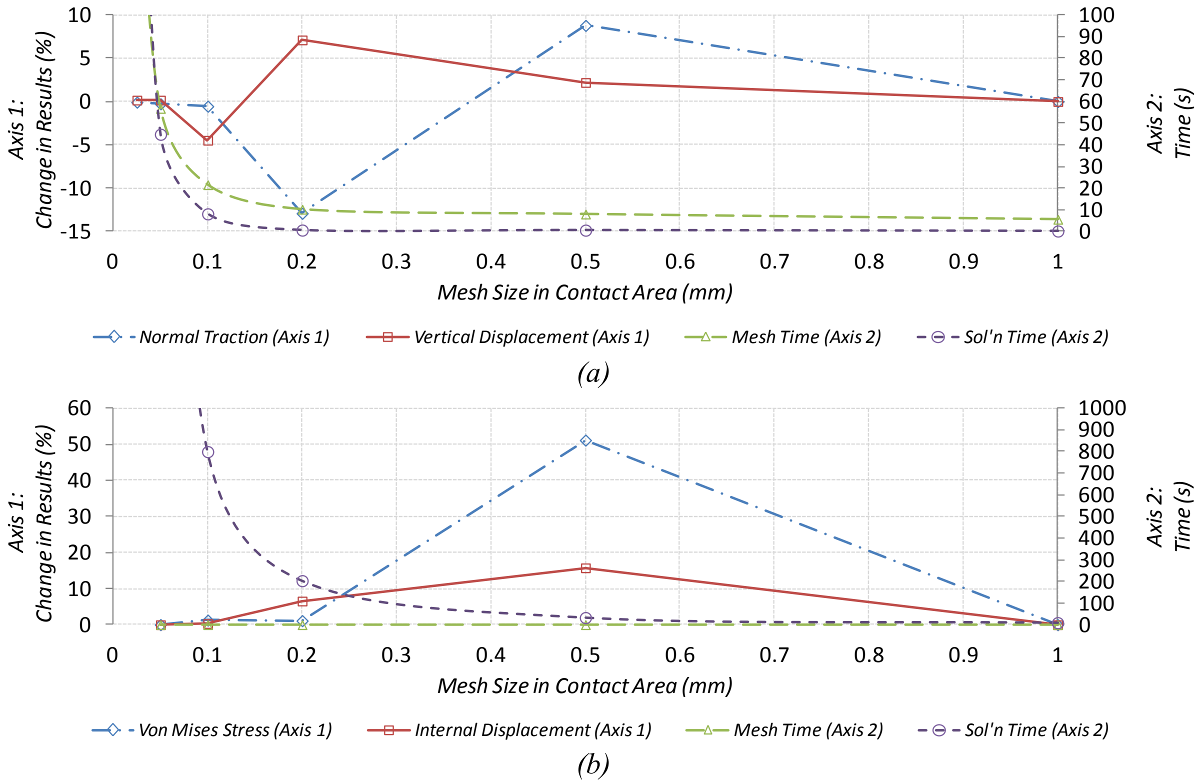

(a)

(b)

Figure 5-10: Case study 1 convergence charts for (a) boundary mesh and (b) internal mesh

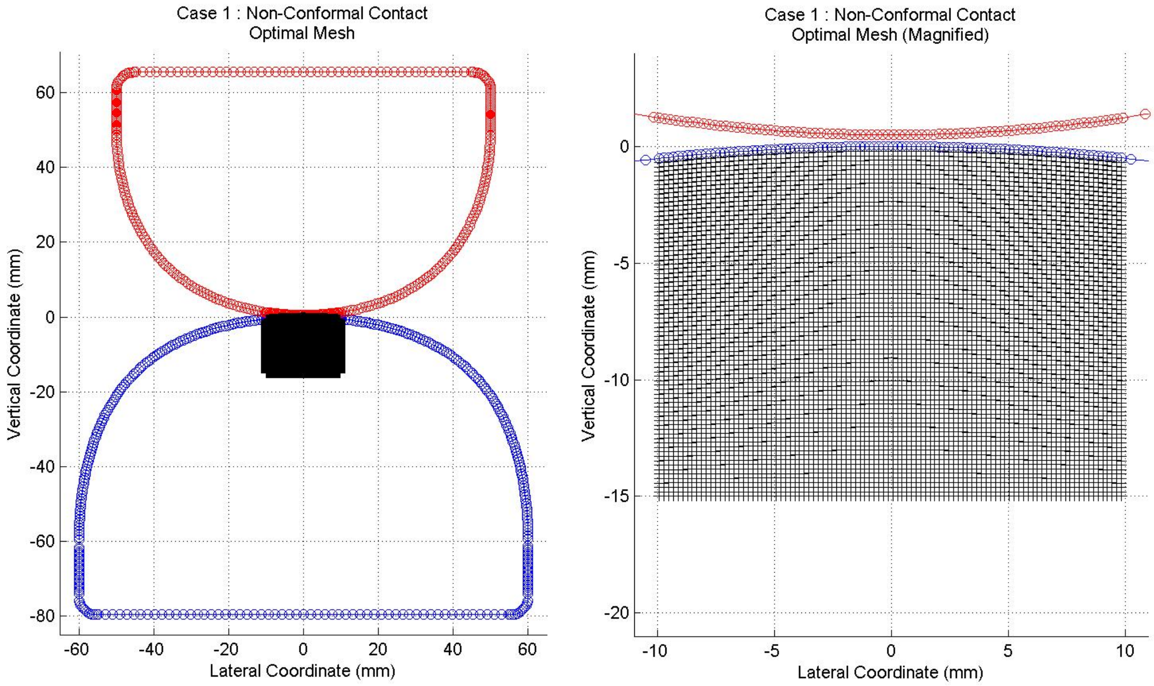

Figure 5-11: Case study 1 optimal mesh (Boundary and internal mesh size = 0.2mm)

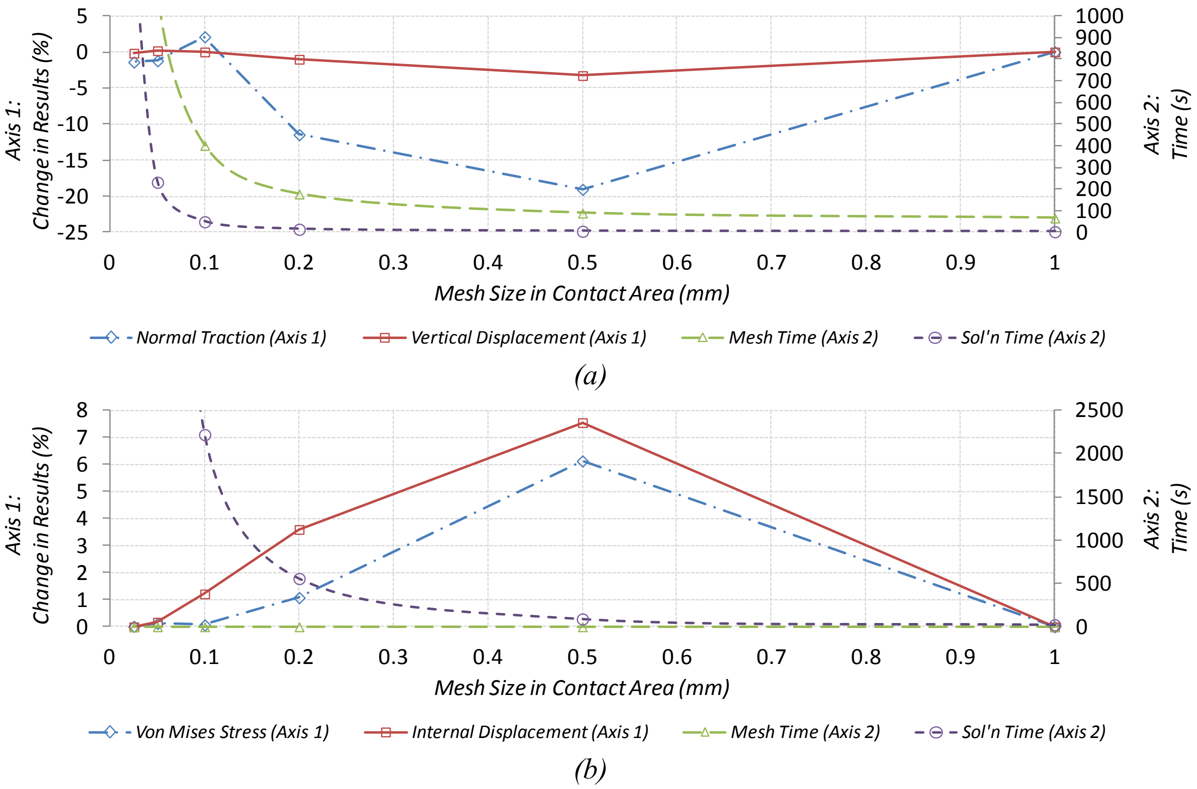

Figure 5-12: Case study 2 convergence charts for (a) boundary mesh and (b) internal mesh

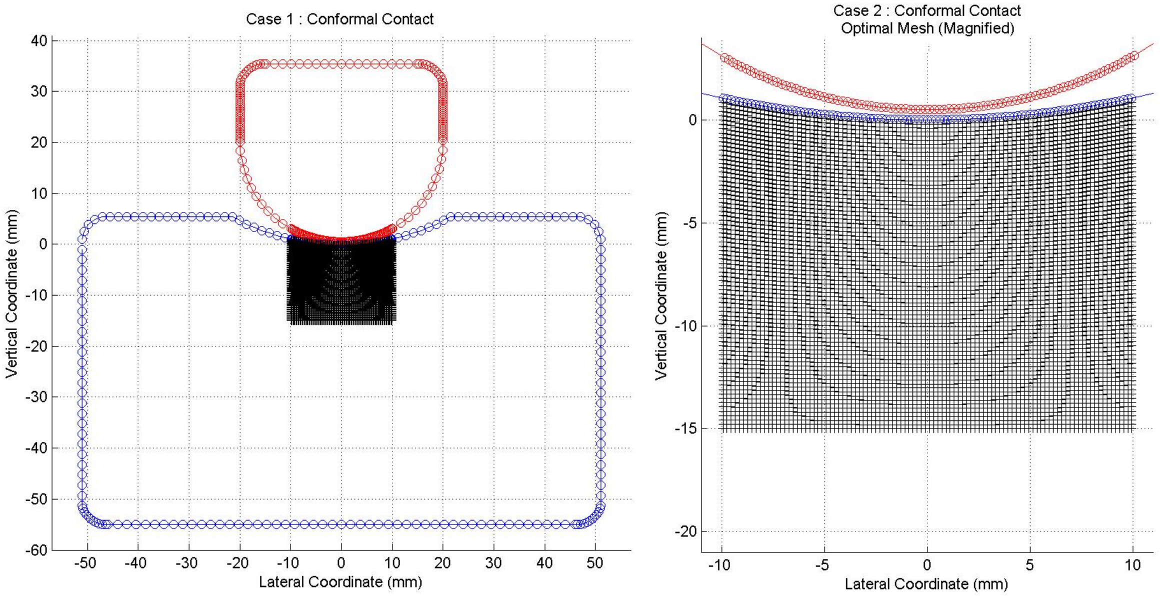

Figure 5-13: Case study 2 optimal mesh (Boundary and internal mesh size = 0.2mm)

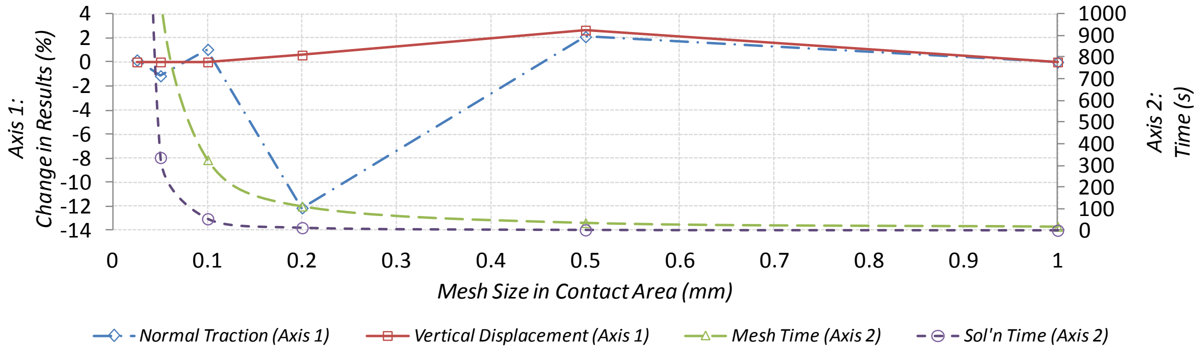

(a)

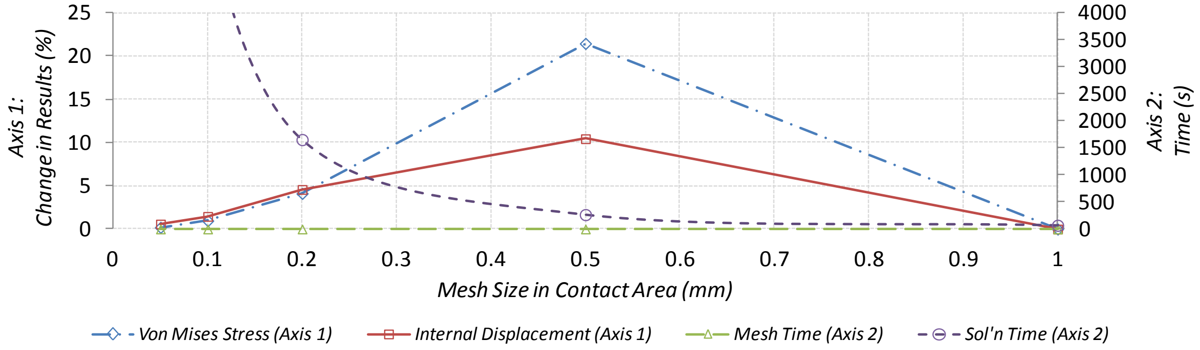

(b)

Figure 5-14: Case study 3 convergence charts for (a) boundary mesh and (b) internal mesh

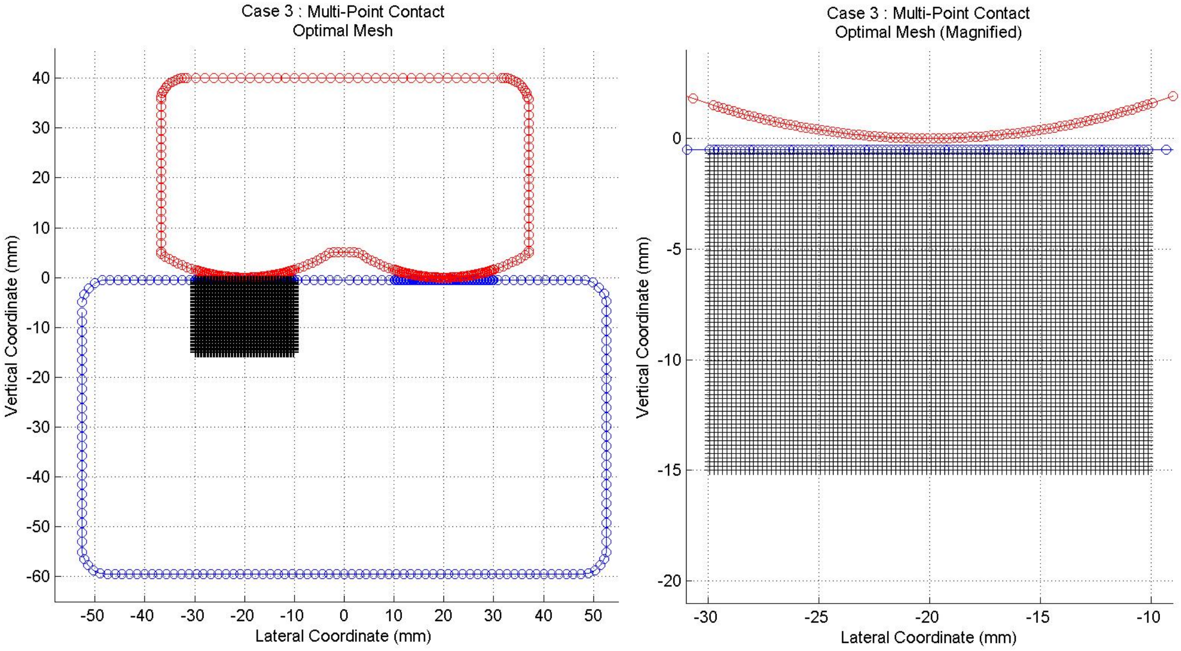

Figure 5-15: Case study 3 optimal mesh (Boundary and internal mesh size = 0.2mm)

5.4.2 Validation against finite element analysis (FEA)

For validation, an FEA replica of each case study has been generated. Before choosing the appropriate mesh size for comparison, a mesh convergence study was completed for each case study using FEA. A mesh size of 0.2mm provided an acceptable level of accuracy and was therefore chosen for the FEA vs. BEM comparison. To ensure that a direct comparison was made, a script file was developed to import the exact BEM mesh into the FEA software package Abaqus. Table 5-3 provides a summary of the normal pressure, vertical displacement and von Mises stress results, which were each extracted from Figure 5-16, Figure 5-17 and Figure 5-18. Table 5-4 provides a comparison of computational effort (CPU times). The percentage error between BEM and FEM is calculated using:

$$\%_{ERROR} = \left|\frac{\sigma_{BEM} - \sigma_{FEM}}{\sigma_{FEM}}\right| \times 100 \qquad 5\text{-}39$$

The first and most important comparison to be made between the BEM and FEA solutions is the accuracy of results. Table 5-3 provides a summary of the key results extracted from identical BEM and FEA solutions for each case study. Figure 5-16, Figure 5-17 and Figure 5-18 present visually the surface normal contact pressures *(a)* and displacements *(b)* and internal domain von Mises stress *(c)* and *(d)* and internal body vertical displacements *(e)*. All of these results, with regards to both the overall solution and maximum values, compare extremely well with a maximum deviation across all three case studies of only 2.61%. In all cases, for equivalent mesh sizes, the BEM solution marginally over-estimates in comparison to the FEA results. These small variations were indeed expected due to accepting a slight compromise on mesh size for improved computational efficiency. Despite excellent accuracy of results, to assess completely the feasibility of this novel BEM application to wheel-S&C interaction, a comparison of computational efficiency must also be included.

		BEM	FEA	$\%_{ERROR}$*
		Case Study 1: Non-Conformal Contact		
Max. Contact Pressure	*MPa*	2132.90	2110.00	1.09
Max. Vertical Deformation	*mm*	-0.0653	-0.0651	0.31
Max. von Mises Stress	*MPa*	1209.40	1186.00	1.94
		Case Study 2: Conformal Contact		
Max. Contact Pressure	*MPa*	2268.80	2211.00	2.61
Max. Vertical Deformation	*mm*	-0.0599	-0.05984	1.62
Max. von Mises Stress	*MPa*	1296.70	1276.00	0.10
		Case Study 3: Multi-Point Contact		
Max. Contact Pressure	*MPa*	1666.10	1662.00	0.25
Max. Vertical Deformation	*mm*	-0.0352	-0.0351	0.28
Max. von Mises Stress	*MPa*	951.22	941.10	1.08

* %ERROR correct to 2 decimal places.

Table 5-3: BEM vs. FEA key results comparison.

Table 5-4 presents the CPU times for each of the main stages in both the BEM and FEA processes. For a direct comparison with the BEM meshing process, the FEA meshing time is the average time taken to manually prepare the model for submission. This includes preparing the script file, importing the geometries, defining material properties, defining contact regions and generating the mesh. It should also be mentioned that this time is based on the authors experience with regards to setting up the FEA case studies and would therefore be significantly higher if completed by a first time user.

		BEM	FEA	$^{\text{FEA}}/_{\text{BEM}}$
		Case Study 1: Non-Conformal Contact		
Mesh Time	*s*	53.44*	706.60	13.22
Internal Mesh Time	*s*	0.0038	-	-
Solution Time	*s*	13.11	14.00	1.07
Internal Post-Processing	*s*	573.67	-	-
TOTAL TIME	***s***	***640.22***	***720.60***	***1.13***
		Case Study 2: Conformal Contact		
Mesh Time	*s*	38.34*	706.60	18.43
Internal Mesh Time	*s*	0.0038	-	-
Solution Time	*s*	5.78	8.20	1.42
Internal Post-Processing	*s*	359.64	-	-
TOTAL TIME	***s***	***403.76***	***714.80***	***1.77***
		Case Study 3: Multi-Point Contact		
Mesh Time	*s*	58.01*	706.60	12.18
Internal Mesh	*s*	0.02	-	-
Solution Time	*s*	22.06	8.40	0.38
Internal Post-Processing	*s*	469.02	-	-
TOTAL TIME	***s***	***549.11***	***715.00***	***1.30***

** BEM meshing times also include generation of the required influence functions*

Table 5-4: BEM vs. FEA computation (CPU) time comparison.

It can be seen that the un-optimised BEM solution times are already consistently faster than those achieved with the state-of-the-art FEA solution, which has already enjoyed many years of optimisation for solution computational efficiency. Other factors that support the use of BEM as opposed to FEA include:

1. An un-optimised mesh has been used within the internal BEM domain therefore solution times can also be improved without code optimisation.

2. Should only surface contact results be of interest, the internal domain meshing and post processing can be excluded. This would significantly improve further the BEM solution efficiency due to majority the CPU time being related to post-processing the internal domain results.

3. Manual meshing within FEA software can lead the introduction of human error and can take many hours to complete.

These results are all very promising with regards to the feasibility of using an in-house BEM code to replace existing state-of-the-art analysis tools. Further improvements can be made through code optimisation techniques to make the BEM solution even more suited towards integration within railway vehicle dynamics simulations.

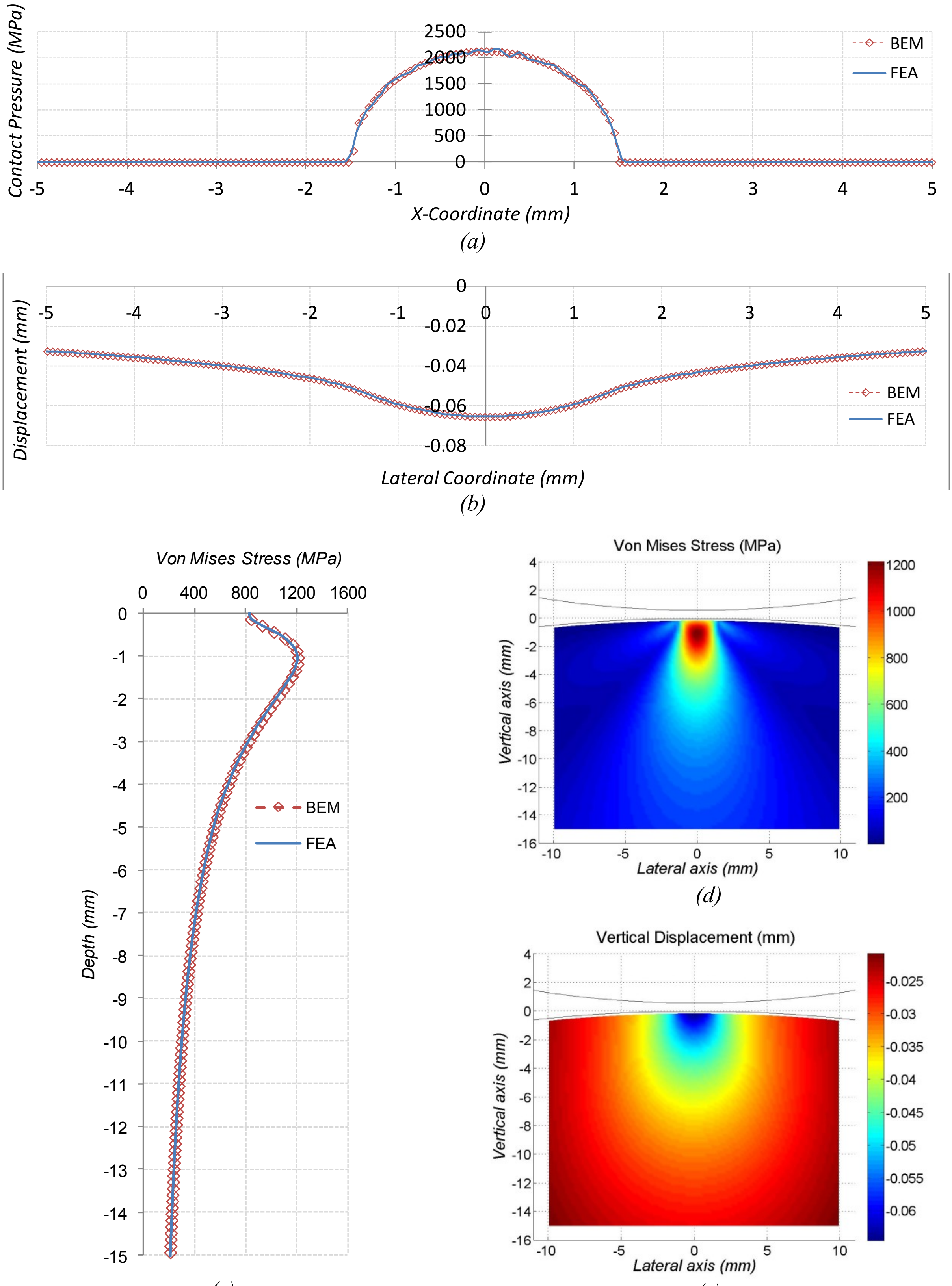

(a)

(b)

(c)

(d)

(e)

Figure 5-16: Case study 1 (non-conformal contact) normal contact pressure (a), vertical displacement (b), internal von Mises stress below initial point of contact (c), internal domain von Mises stress distribution (d) and internal domain vertical displacement distribution (e)

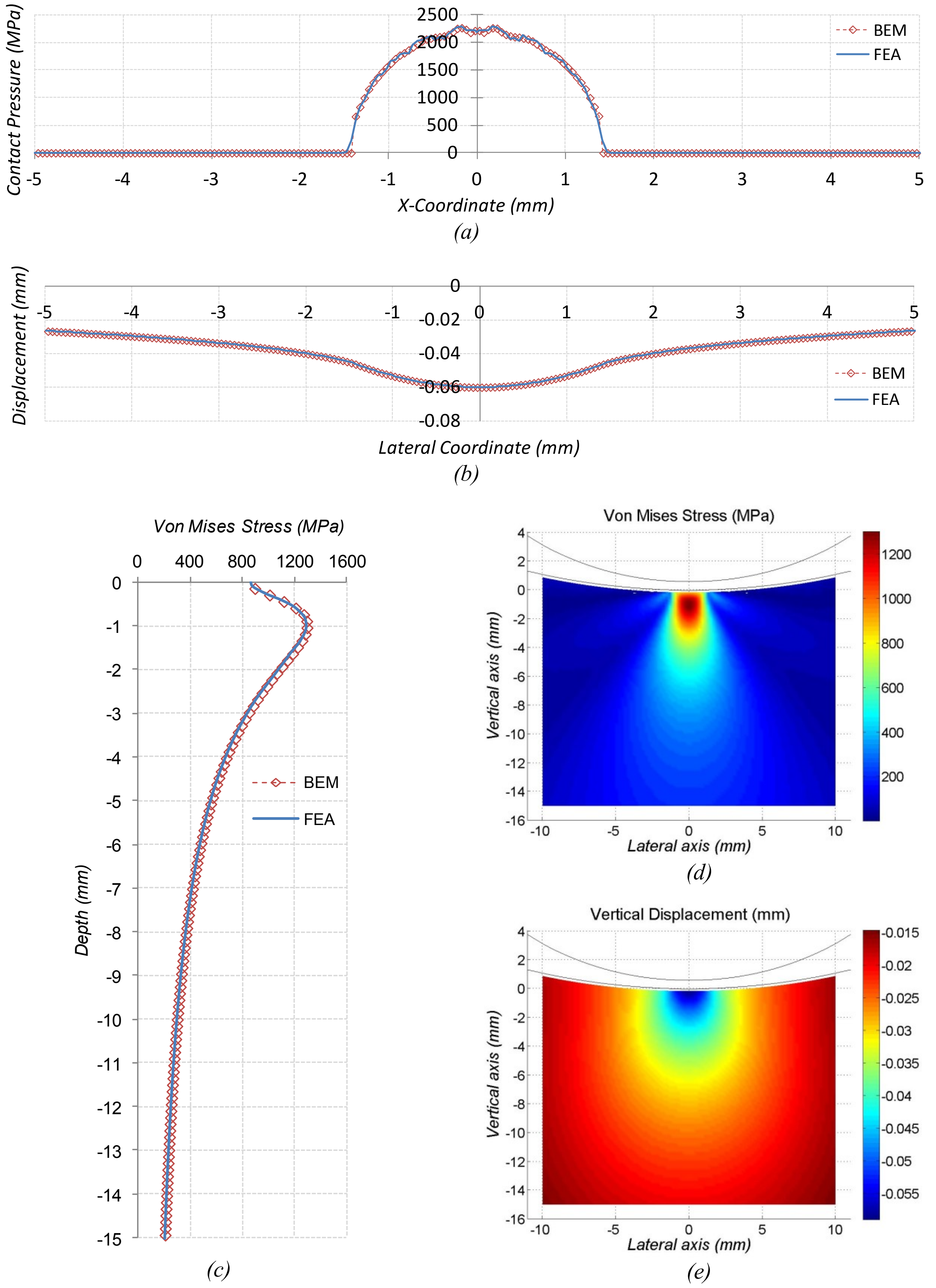

Figure 5-17: Case study 2 (conformal contact) normal contact pressure (a), vertical displacement (b), internal von Mises stress below initial point of contact (c), internal domain von Mises stress distribution (d) and internal domain vertical displacement distribution (e)

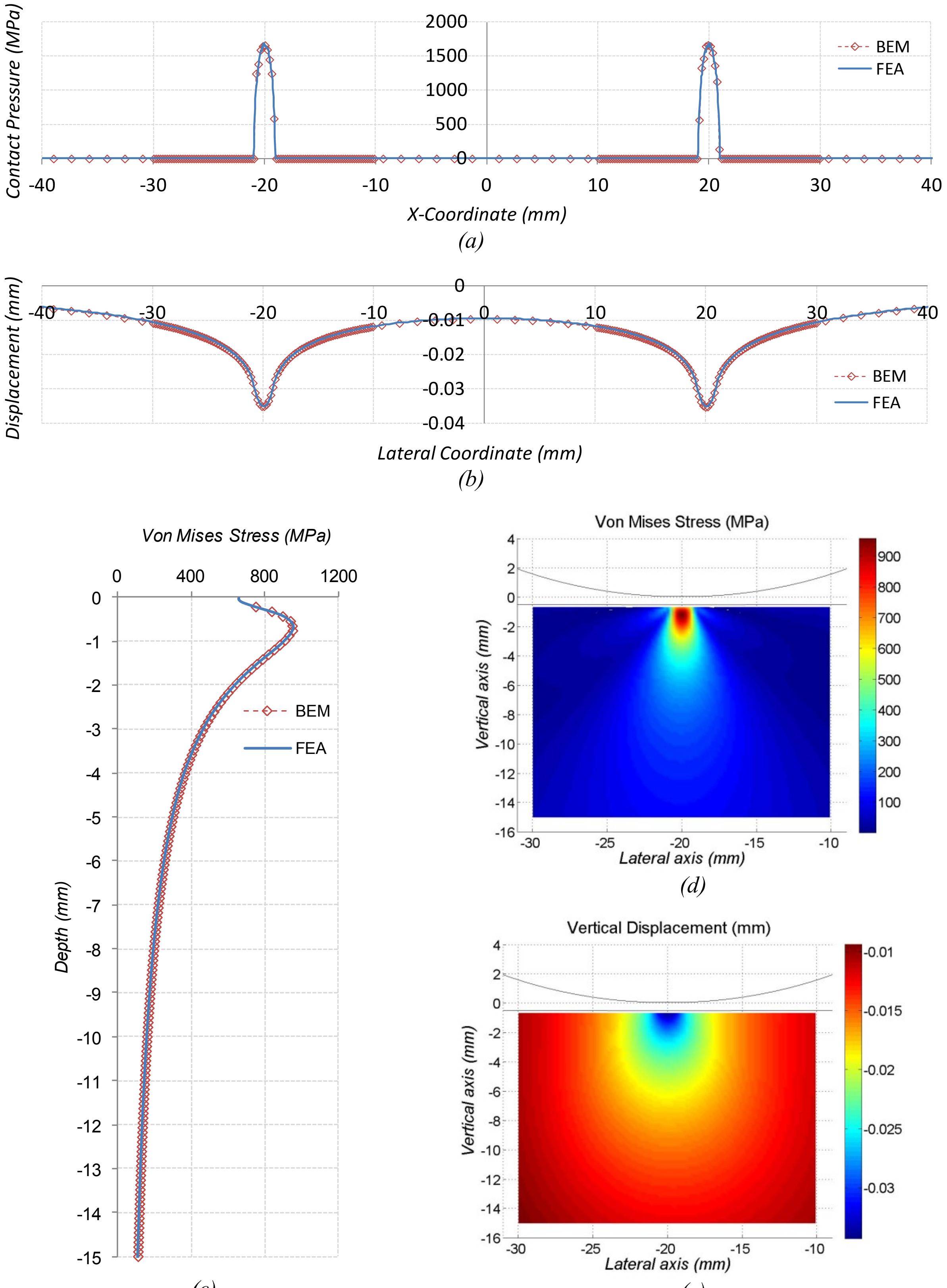

(a)

(b)

(c)

(d)

(e)

Figure 5-18: Case study 3 (multi-point contact) normal contact pressure (a), vertical displacement (b), internal von Mises stress below initial point of left contact (c), internal domain von Mises stress distribution below left contact patch (d) and internal domain vertical displacement distribution below left contact patch (e)

5.4.3 Wheel-Rail Application

To conclude the application of the BEM model to wheel-rail applications, a generic P8 wheel profile on a nominal BS113A rail profile is simulated. The elastic properties of both the wheel and rail are set to $E = 210GPa$ and $v = 0.3$. Figure 5-19 illustrates the general setup of the wheel to rail BEM problem. The rail surface profile has been taken from a 1:20 inclined BS113A rail and is positioned nominally using a track gauge of 1435mm. A new P8 wheel profile is used and positioned centrally with respect to the track centre line and a flange back-to-back measurement of 1360mm.

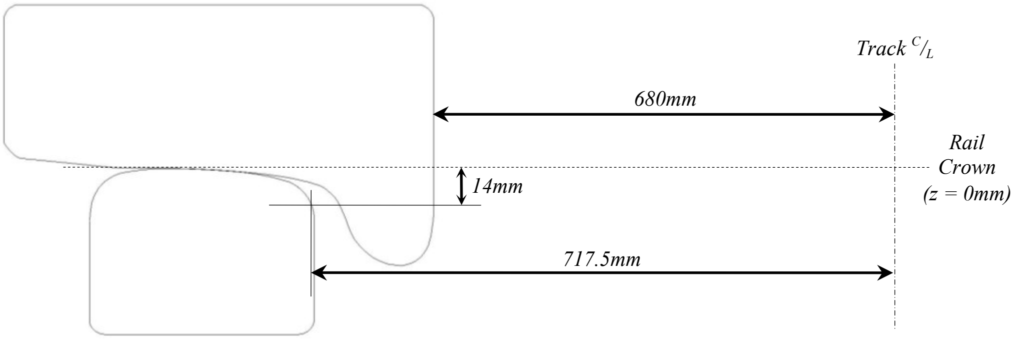

Figure 5-19: Positioning of BEM wheel and rail profiles

In Figure 5-20, the results of a mesh convergence study are plotted. A 0.2mm mesh, for both the boundary and internal domain, gave an optimal setup with regards to accuracy and computational efficiency and is demonstrated within Figure 5-21. Subsequent results are presented within Figure 5-22 and are compared against an identical FEA solution. The normal contact pressure, von Mises stress and vertical displacement results all demonstrate excellent agreement between BEM and FEA. Careful examination of Figure 5-22 *(a)* also shows that the BEM solution provides a much smoother contact pressure distribution. Due to the non-symmetrical nature of the problem, Figure 5-22 *(b) & (c)* and *(d) & (e)* provide a direct comparison of the BEM and FEA internal domain von Mises stress and vertical displacements respectively. The BEM and FEA internal distributions each match extremely well after taking careful consideration of the slight differences between the BEM and FEA colour spectrums.

A second simulation using the same geometry was then completed to demonstrate the ability to model different material properties. The wheel material was held constant whilst the rail Young's modulus was altered to $E = 190GPa$, representing similar material properties to those found within cast Manganese crossings. A summary of key results are provided within Table 5-5.

	$E_{wheel} = E_{rail} = 210GPa, v = 0.3$			$E_{wheel} = 210GPa, E_{rail} = 190GPa, v = 0.3$		
	BEM	FEA	$\%_{\text{Variance}}$	BEM	FEA	$\%_{\text{Variance}}$
σ_{N_Max}	740.43	728.23	1.68	718.93	706.82	1.71
σ_{VMS_Max}	390.35	383.69	1.74	378.31	373.43	1.31
U_{2_Max}	-0.0400	-0.0410	2.44	-0.0435	-0.0444	2.03

Table 5-5: Wheel to rail contact results summary

The percentage errors for each of the key results closely reflect those achieved during the conformal and non-conformal case studies. Very small differences between BEM and FEA exist, with the BEM solution again moderately over estimating the maximum normal pressure (σ_{N_Max}) and von Mises stress (σ_{VMS_Max}). Table 5-5 also demonstrates the ability to accurately model different elastic material properties between the two contacting bodies.

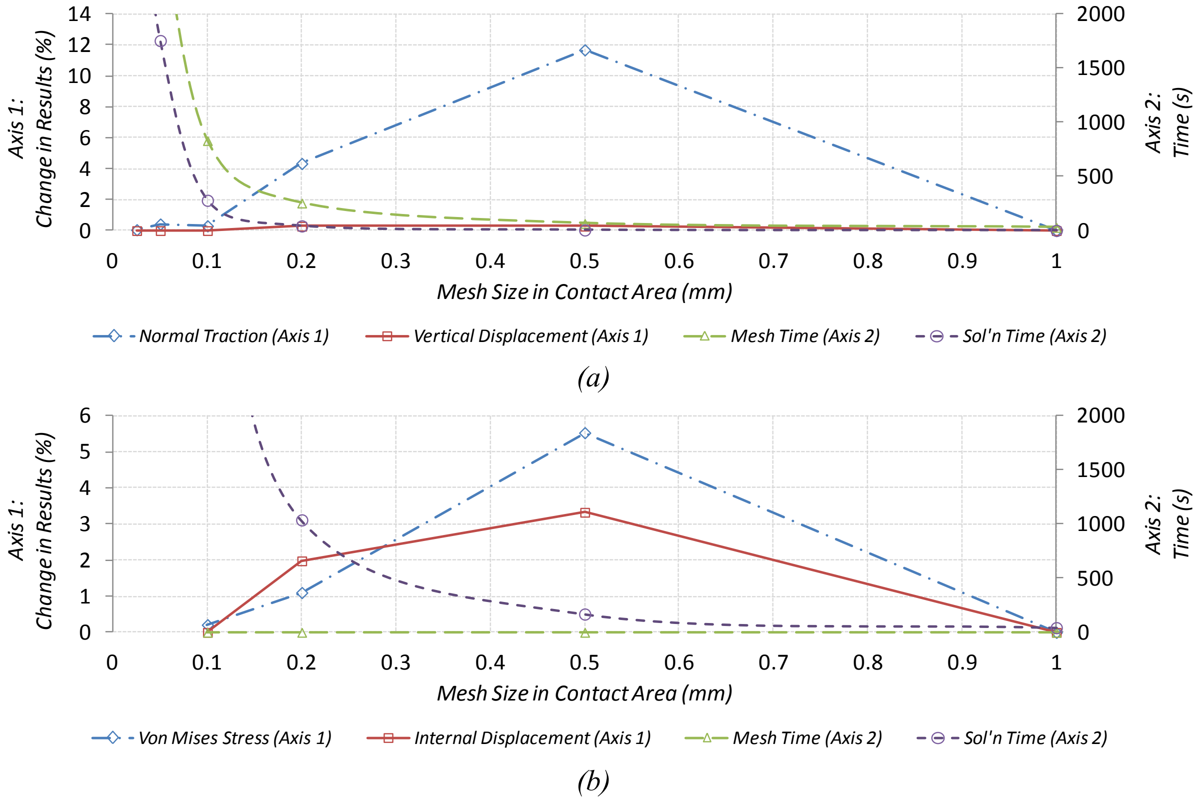

Figure 5-20: Case study 4 convergence charts for (a) boundary mesh and (b) internal mesh

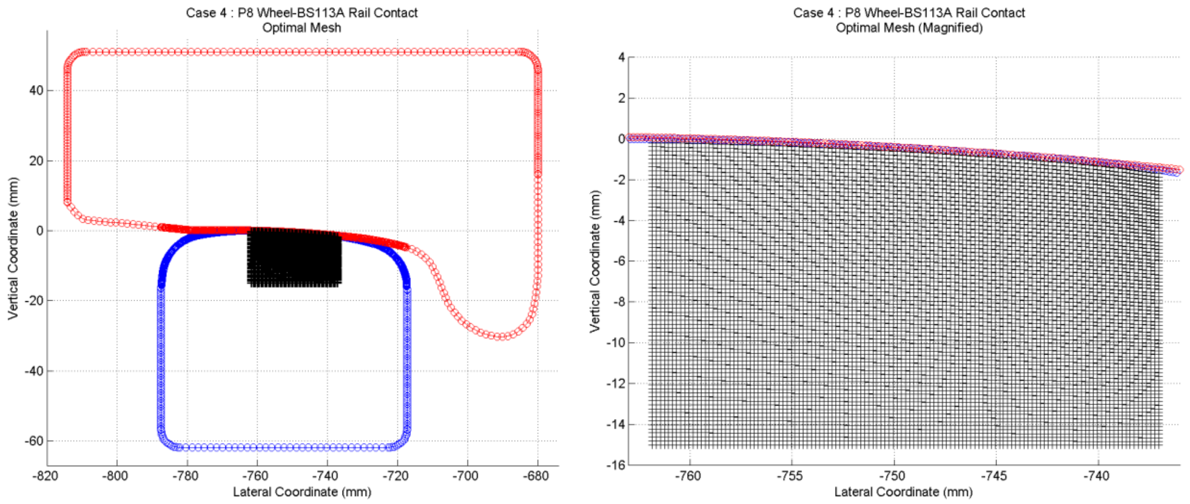

Figure 5-21: Wheel-rail case study optimal mesh (Boundary and internal mesh size = 0.2mm)

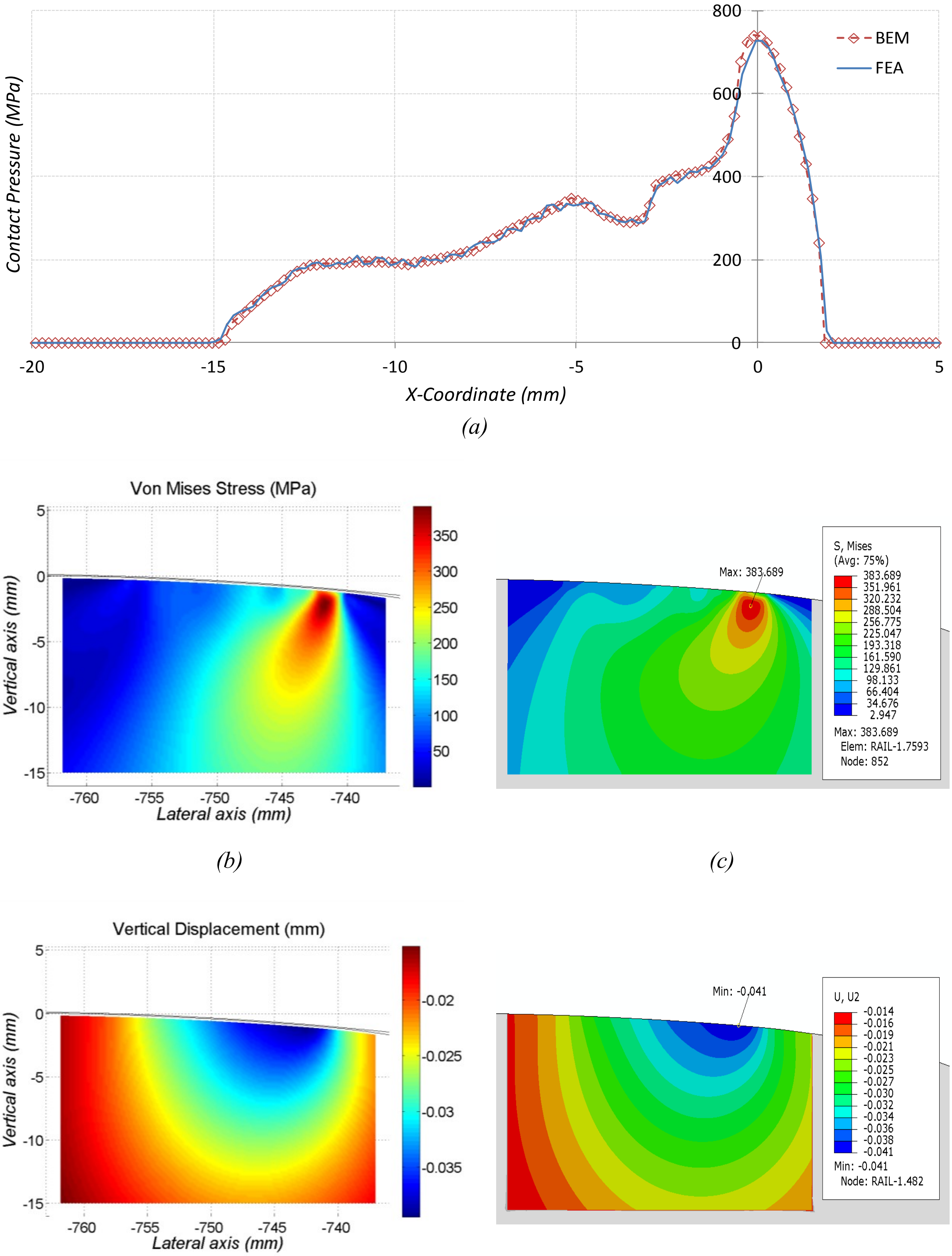

(a)

(b) (c)

(d) (e)

Figure 5-22: Case study 4 (P8 – BS113A contact) normal contact pressure (a), BEM internal von Mises stress (b), FEA internal von Mises stress (c), BEM internal domain vertical displacement (d), FEA internal domain vertical displacement (e)

5.5 Discussion / Summary

An indirect boundary element model has been adapted to enable automatic meshing and simulation of contact scenarios synonymous to those commonly found during wheel to rail interaction. Conformal, non-conformal and multi-point contact conditions were solved with comparable accuracy and superior computational efficiency when compared to a state-of-the-art finite element solution. Mesh convergence studies also demonstrated the importance of mesh size for achieving a suitable compromise between accuracy and computational efficiency. A boundary mesh of 0.2 mm combined with an internal domain mesh of 0.2 mm proved to be an optimal configuration and will be taken forward into *Chapter 6 – 2.5D BEM Modelling of Wheel-Rail Interaction*. Further computational improvements were also made through implementing a mesh coarsening procedure to remove nodes evenly from outside of the estimated contact region.

The major objectives for *Chapter 5*, as outlined within *section 5.1*, have all been successfully achieved. The results presented within Figure 5-22 and Table 5-5 should also present a significant improvement when compared to a purely elliptic, Hertzian solution. This will indeed be investigated during *Chapter 6*.

The ability to run detailed contact simulations without human intervention presents a much neater and sophisticated means of running detailed wheel-rail interaction and degradation studies. Applying the BEM model in this way also bridges some of the knowledge gaps and inefficiencies within current state-of-the-art wheel to rail degradation models where manual interventions are necessary between major simulation stages (*i.e.* local contact results manually fed into a more detailed FEA contact model as discussed within *Chapter 2, section 2.4*). To conclude, the 2D BEM application to wheel-rail interaction problems has proven to be a valuable alternative to existing simulation techniques.

The present example represents a solution of two dimensional wheel-rail contact problems. In reality, a three dimensional solution is required for the BEM results to be useful with regards to accurate damage prediction at geometrically complex switch and crossing profiles. *Chapter 6* will present further developments to convert the 2D lateral BEM model into a comprehensive 3D tool for non-Hertzian wheel-rail interaction studies.

Chapter 6 : Advanced BEM for Wheel-S&C Interaction

This chapter progresses the development of a combined tool for wheel-S&C interaction studies through further implementation of the boundary element solution. A novel 2.5D BEM modelling strategy is presented for three-dimensional contact patch predictions and is validated against detailed FE analysis. It is demonstrated that a single combined tool for wheel-rail contact detection, detailed contact stress analysis and wear damage approximation is indeed a feasible concept. The extension to the BEM model for including dynamic impact loading is presented along with some preliminary results. Further developments to include the prediction of plastic strain accumulation (i.e. plastic deformation) are also presented within this novel BEM application, demonstrating a general contact tool capable of complete S&C degradation analysis.

6.1 Introduction

Chapter 5 introduced a novel application of a two-dimensional, lateral boundary element model for wheel to rail interaction studies. Despite the obvious attraction of removing the wheel-rail contact point detection and force equilibrium stages from modelling process, a 2D representation does not fully capture the distribution of loads within a true contact patch. The contact stresses must be approximated in three-dimensional space to enable:

1. realistic normal contact pressures to be generated

2. the approximation of tangential tractions and slip / adhesion regions within the contact patch

3. accurate damage simulation

To achieve this, the 2D BEM solution has been implemented within a novel modelling process, which constructs a realistic 3D normal contact pressure distribution from multiple 2D BEM analyses. From here on in; the model will be referenced as the “2.5D BEM model”. The main purpose for implementing a 2.5D BEM technique is to improve both the normal and tangential traction approximations for geometrically complex rail profiles, as found within S&C. This in turn would improve the accuracy of wear approximations, making the tool more suited to longer-term damage accumulation modelling. The lateral BEM approach also brings a number of other significant and novel benefits to wheel-rail contact modelling, which include:

1. **Elasto-dynamic impact analysis** – The ability to model the effects of internal body inertia and hence stress wave propagation within the internal domain, enabling the material response due to impact loads to be investigated. Developments to include dynamic impact modelling are presented within *section 6.3.1*.

2. **Plastic deformation modelling** – The ability to obtaining solutions using influence functions for the entire rail domain enables gross plastic flow to be implemented within the lateral BEM solution. This is not currently possible within any existing wheel-rail contact models due to:

    a. only taking consideration of the contacting surfaces, and

    b. internal domain results only being calculated at the end of the simulation (*i.e.* not being part of the incremental loading process.

    The current implementation of plastic strain accumulation is presented within section 6.3.2 as a proof of concept, whilst further developments are given within *Appendix A2* and their full implementation has not been carried out as this was outside the scope of the work presented within this thesis.

3. **Crack analysis** – The lateral BEM approach also lends itself to modelling the effects of subsurface cracks within the rail. Crack analysis is not the focus of this investigation and has therefore been excluded from this study. Additional information can be found within the work of Zografos [118].

Before the above benefits can be included within a combined tool for S&C damage accumulation, it must first be proven that the 2.5D BEM methodology is indeed a feasible approach. *Chapter 6* therefore begins by discussing the novel integration of the lateral 2D BEM model into a scheme for generating realistic 3D contact pressures for wheel-rail interaction, the 2.5D BEM model.

6.2 2.5D lateral BEM model for Non-Hertzian Contacts

Figure 6-1 below illustrates the modelling strategy for obtaining a 2.5D BEM solution.

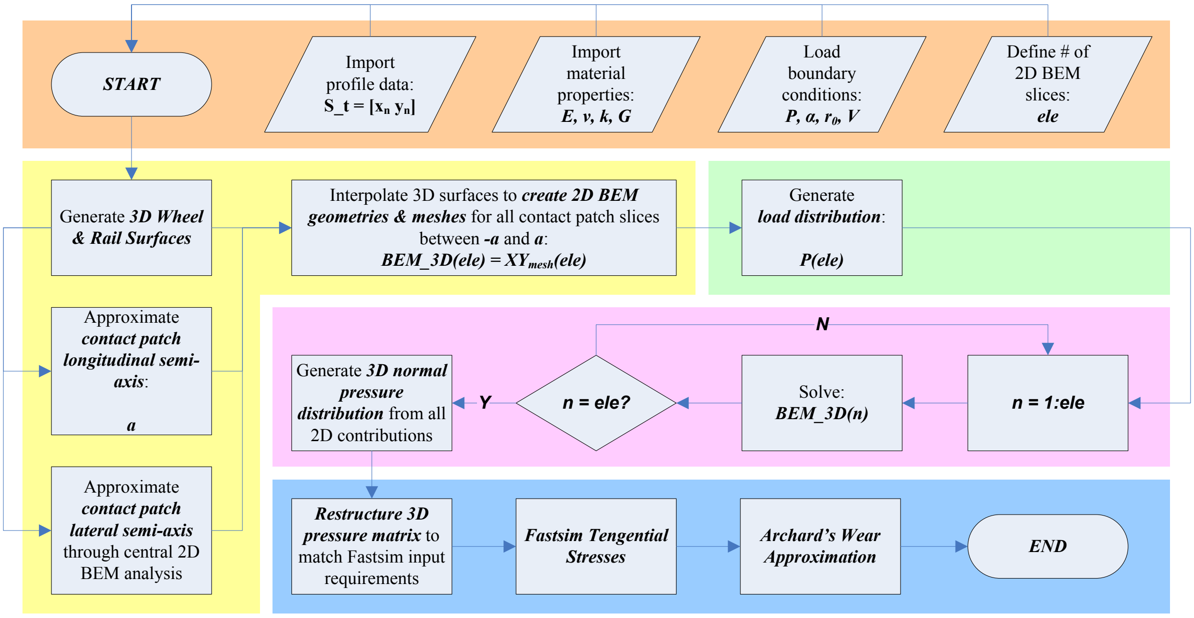

Figure 6-1: 2.5D BEM modelling strategy

Each of the key stages of the modelling process have been colour coded and are discussed within the remainder of *section 6.2*. The following sub-sections include:

1. Model setup (yellow)
2. Applied load distribution approximation (green)
3. 2.5D BEM contact tractions (purple = normal traction; blue = tangential traction)

6.2.1 Model setup

The BEM solution is based on applying both vertical and lateral loads to the contacting bodies then incrementally increasing the surface tractions, through assessment of the contact gap and surface deformation, until load equilibrium is achieved. As a direct result of this 'load balance' approach (as opposed to the alternative BEM technique of applying a 'body displacement'), the first step in generating a 2.5D representation of contact stresses is an initial approximation of the contact patch longitudinal semi-axis, a. This is achieved using the Hertzian approximation (*see section 4.3.1*). The maximum width (lateral semi-axis, b) and location of the contact patch is approximated by completing an initial 2D BEM analysis at the longitudinal centre of contact. The applied load is overestimated at *P/2* to ensure the entire contact patch width is captured. Figure 6-2 shows the 2D normal contact pressure obtained during the estimation process. To improve the computational efficiency, a coarse mesh of 0.5 mm is used, which provides a granular normal pressure distribution purely for approximating the contact patch width.

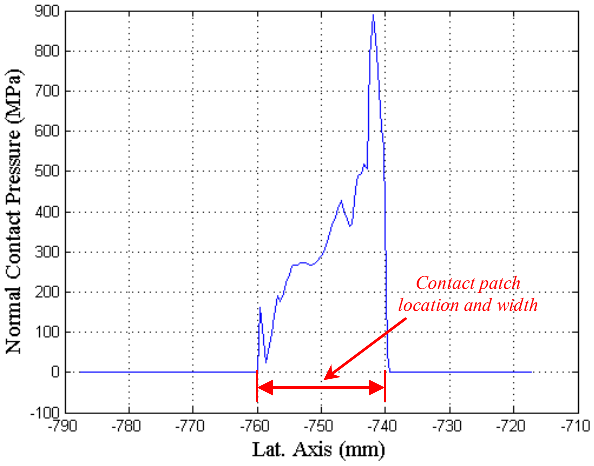

Figure 6-2: Normal contact pressure used to estimate lateral contact patch location and size.

Three-dimensional wheel and rail surface profiles are then automatically generated using the procedure identified within *Chapter 3*, *section 3.3*. For ease of development purposes and to continue the comparison work as per *Chapter 5*, a nominal P8 wheel profile on a generic BS113A rail profile has been used, although it is still possible to use complex switch or crossing profiles during the same procedure, as illustrated within Figure 6-3.

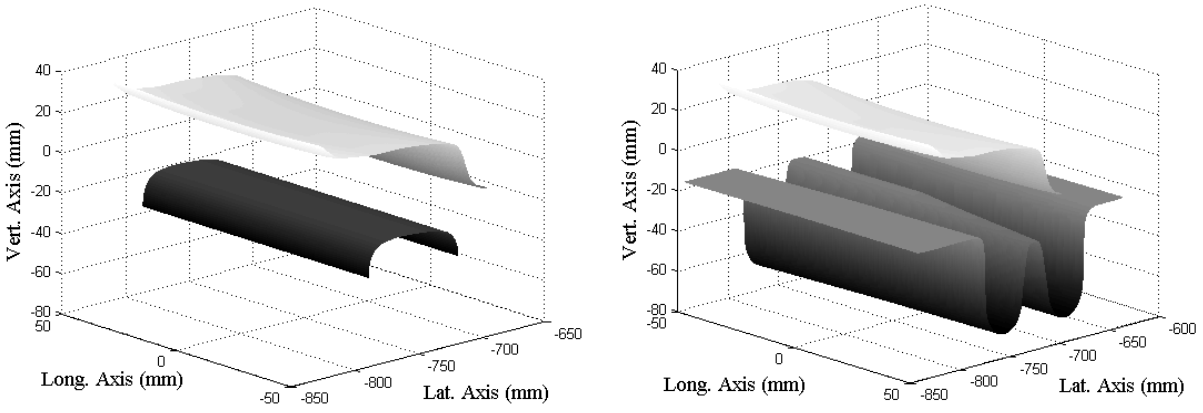

(a) *(b)*

Figure 6-3: A nominal P8 wheel contact surface plotted against a BS113A rail contact surface (a) and a complex crossing surface profile (b), generated during the 2.5D BEM process. Note: for ease of development, the BS113A rail surface profile has been used throughout the remainder of chapter 6.

Any number of 2D BEM slices can be defined for constructing a 2.5D BEM result depending on the desired resolution. The approximate contact patch longitudinal semi-axis, a, is used to define the longitudinal position of each 2D BEM slice (i.e. at intervals of 2a/number of slices) whilst the over-estimated contact patch width is used to define the lateral limits of the contact region. A lateral two-dimensional interpolation (yz-plane) of the three-dimensional wheel and rail surfaces is then performed at each longitudinal 2D slice location between the lateral limits. Figure 6-4 illustrates the estimated contact regions and the extracted 2D BEM surface profiles (slices) for use within the 2.5D BEM process. Figure 6-5 provides a not-to-scale magnification of the 50 x 2D BEM surface profiles.

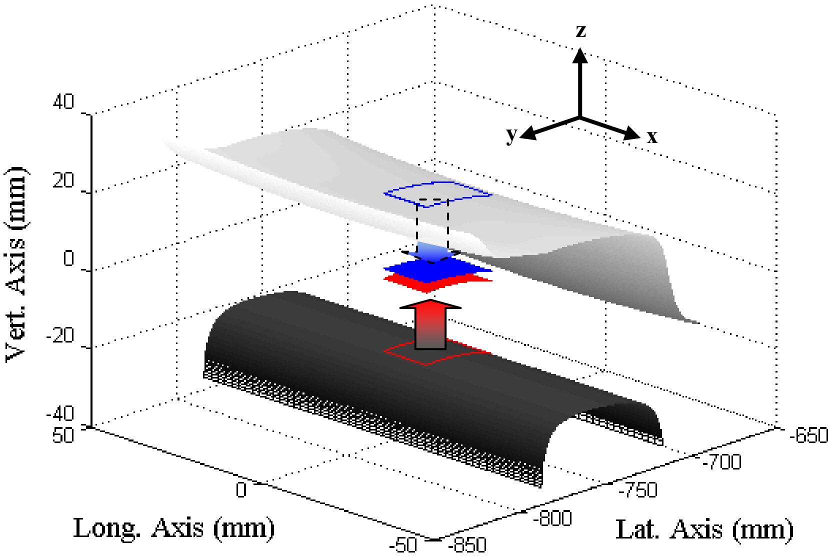

Figure 6-4: 3D wheel / rail contact surfaces and estimated contact regions for extracting the 2D BEM slices.

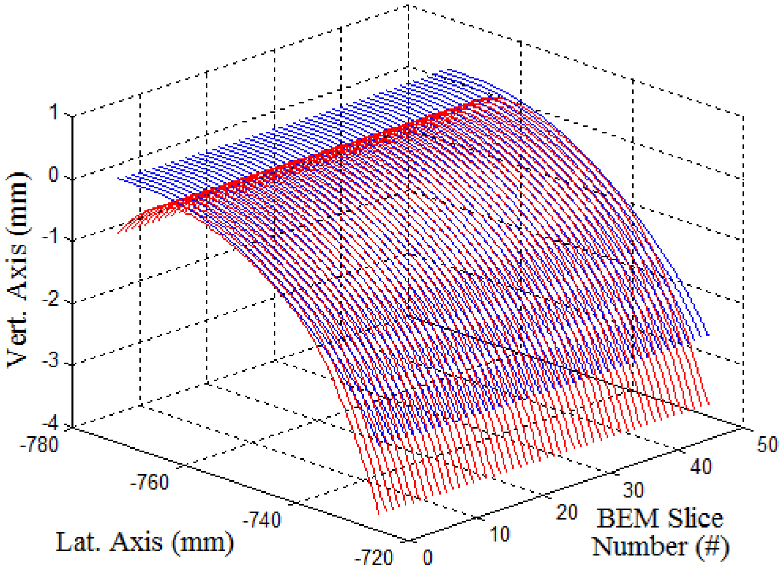

Figure 6-5: 2D BEM profiles (interpolated slices), extracted from the 3D surface profiles illustrated within Figure 6-4 (Note: axes not to scale for illustration purposes).

Elements	#	16	30	50	76	100
Solution Time	*mins*	9.23	17.27	28.81	43.80	57.43
Max. Normal Pressure (Parabolic)	*MPa*	718.02	752.03	755.66	762.69	764.97
Max. Normal Pressure (Elliptic)	*MPa*	634.14	702.61	707.56	708.82	712.23

Table 6-1: 2.5D BEM solution times and results for both parabolic and elliptic load distributions

Figure 6-6 presents results from a convergence study using the 2.5D BEM approach. It can clearly be seen that convergence is achieved between 30 and 50 BEM slices with less than 1% change in the maximum normal contact pressure. As the number of elements per BEM slice is kept constant, the solution time increases linearly with increasing 2.5D BEM resolution. This linear relationship is due to maintaining the same mesh size within each individual 2D BEM analysis (slice).

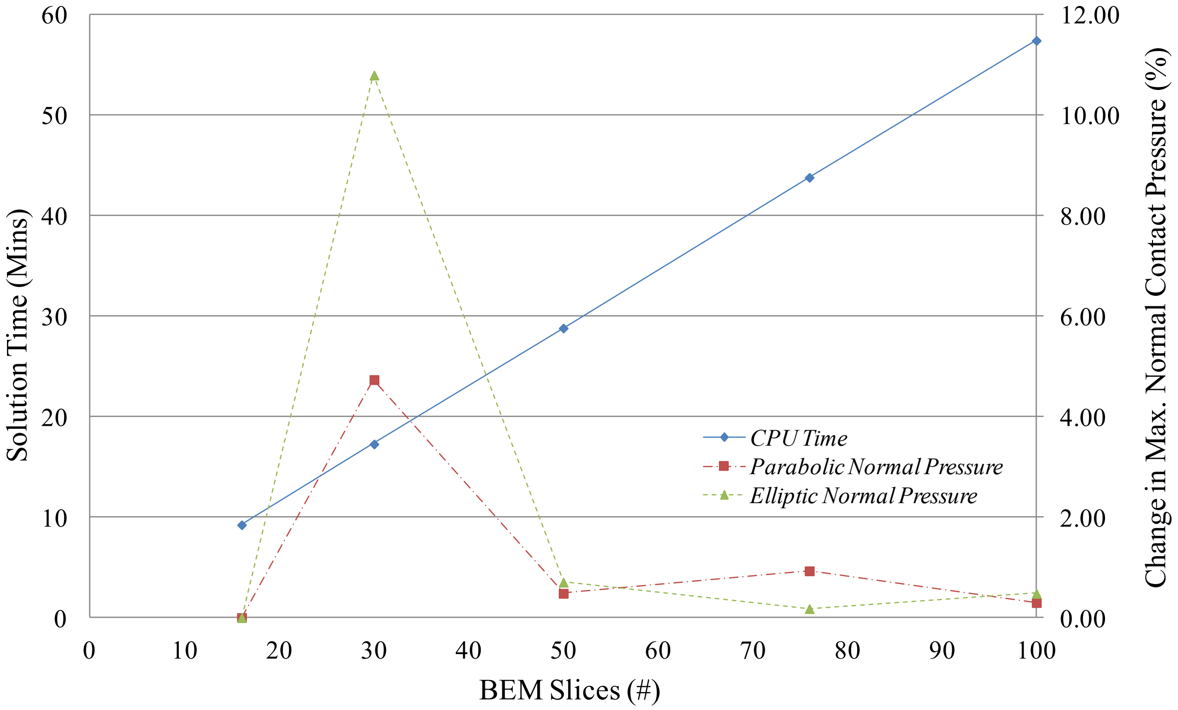

Figure 6-6: 2.5D BEM convergence chart

To determine the number of BEM slices to take forward for validation, the overall normal pressure distribution was compared with increasing number of slices. Figure 6-7 demonstrates the variation in normal pressure distribution for 5 case studies using between 16 and 100 slices. It can be observed that a coarse solution yields significant errors in the overall solution with regards to the general shape and width of the contact pressure distribution. On the other hand, the solution using 100 slices does not offer much benefit over that from 50 slices in terms of the contact pressure distribution.

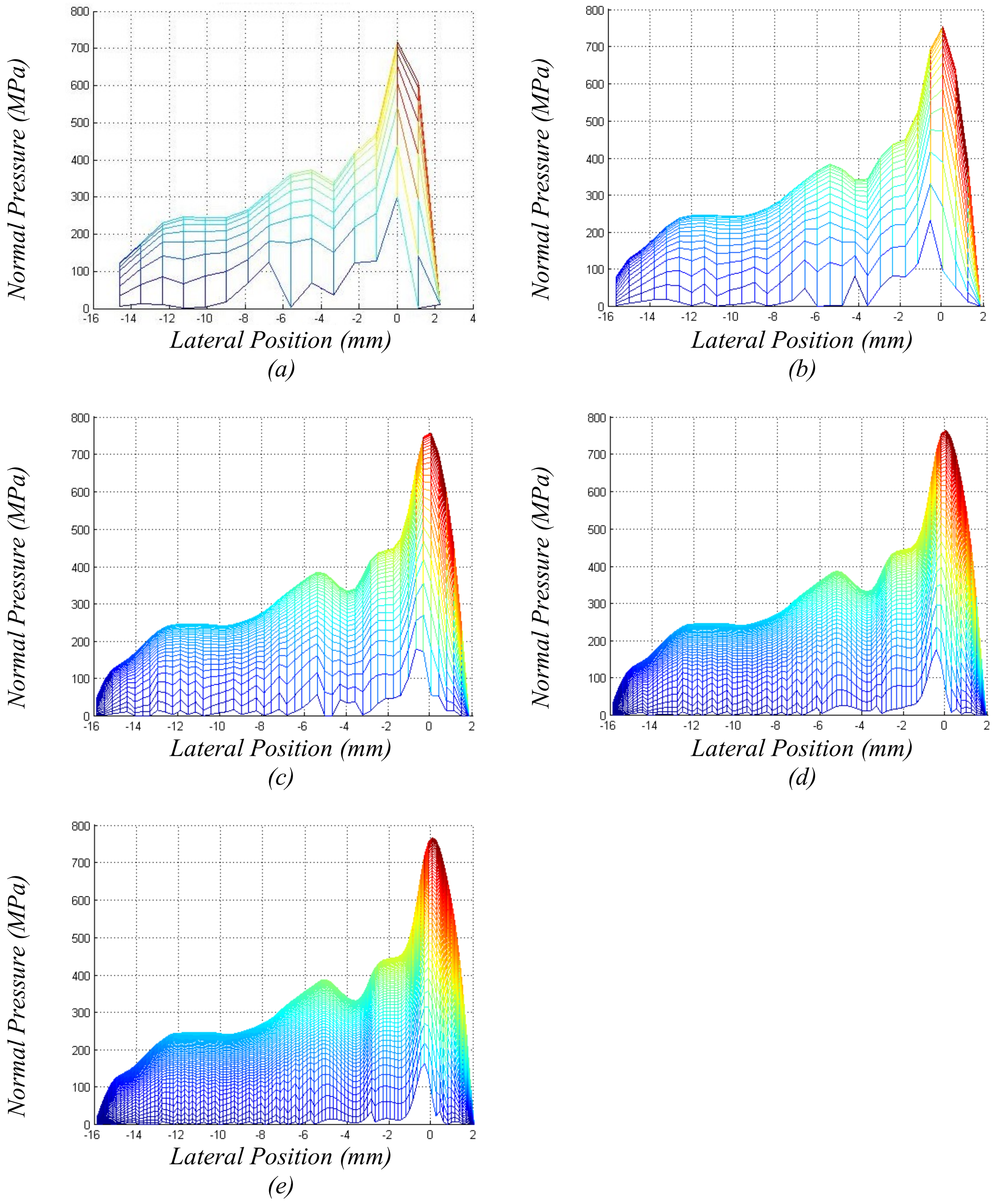

Figure 6-7: Normal contact pressure distributions for (a) 16 elements, (b) 30 elements, (c) 50 elements, (d) 76 elements and (e) 100 elements.

An acceptable compromise between computational efficiency and solution accuracy was achieved when using 50 BEM slices during the 2.5D BEM process. This also enabled a sufficiently detailed 3D FEA model to be used as a direct comparison for validation (see *section 6.2.4*).

6.2.2 Applied load approximation

Due to utilising a load application BEM model, a longitudinal distribution of discrete wheel loads per 2.5D BEM slice is required. Two distributions were trialled, elliptic and parabolic, from which the results were compared against an equivalent full 3D finite element analysis (validation results are presented within *section 6.2.4*). Equations 6-1 and 6-2 provide the elliptic and parabolic distributions, respectively, which are both illustrated in Figure 6-8. Within each equation, *x* is the discrete longitudinal distance along the contact patch, *a* is the longitudinal contact patch semi-axis and *P* is the total wheel load. A parabolic distribution provided the best fit with regards to FEA validation.

$$z_n^{Elliptic} = \sqrt{1 - \frac{x_n^2}{a^2} * P^2} \qquad 6\text{-}1$$

$$z_n^{Parabolic} = \sqrt{(x_n - a)(x_n + a) * P} \qquad 6\text{-}2$$

It can be seen that, in this case, the Hertzian assumption for the longitudinal semi-axis, *a*, over-estimates the length of the contact patch. A result of this is an under-estimation of the applied contact loads towards the centre of the contact patch. This is also evident within the results presented within *section 6.2.4*.

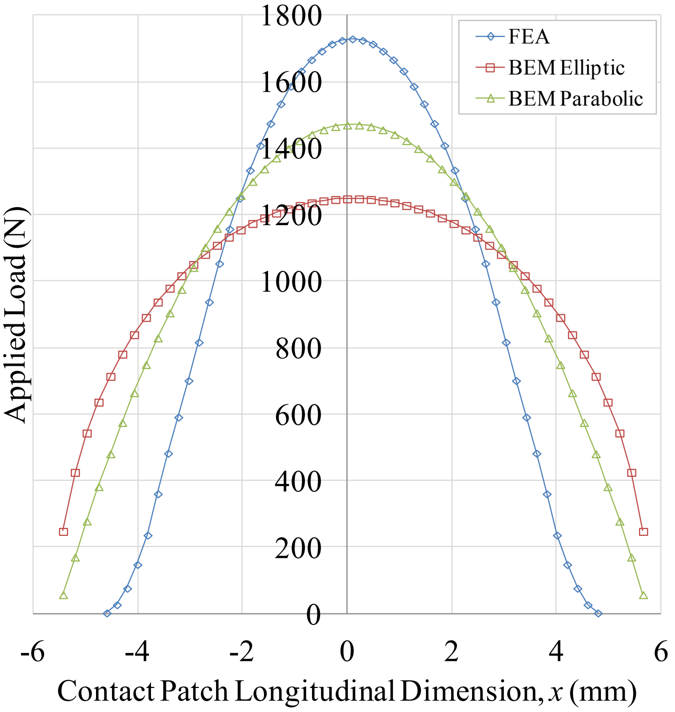

Figure 6-8: Proposed 2.5D BEM longitudinal load distributions compared against an equivalent 3D FEA result for a 10 tonne axle load.

6.2.3 2.5D BEM contact tractions

Once each of the discrete 2D BEM problems has been adequately defined, each slice of the contact patch can then be solved. A 3D, non-Hertzian matrix of results is constructed from each of the discrete 2D solutions. Post-processing of the 2.5D normal contact pressure matrix is then required to convert it into a format suitable for use within Fastsim (see *section 4.3.2* for a description of the Fastsim format). Figure 6-9 shows the initial 2D results from each contact patch slice constructed into an initial 2.5D plot *(a)* along with the post-processed data, which includes only results from within the contact patch *(b)*.

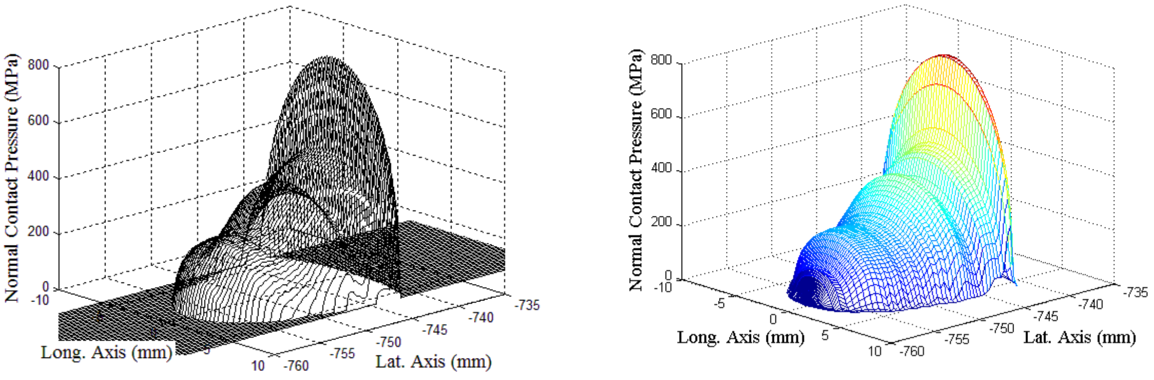

(a) *(b)*

Figure 6-9: Post-processing required when preparing the 2.5D pressure distribution ready for Fastsim; 2.5D normal pressure distribution generated from 50 x 2D pressure plots (a), results scoped to include only the contact patch (b).

The 2.5D BEM normal contact pressure matrix is now structured ready for use within the Fastsim algorithm. Before the tangential tractions can be solved, the longitudinal, lateral and spin creepages must first be approximated for the 2.5D contact patch. This is achieved through assessing the local contact parameters within the proximity of the contact origin. A reasonable assumption is made that the contact origin resides at the location of maximum contact pressure. Figure 6-10 provides an illustration of the 2.5D contact pressure distribution overlaid onto the original 2D wheel and rail profiles. Within this example, the contact origin exists at -741.91 mm from the track centre line. Local contact parameters, such as those identified within Table 6-2, are then automatically extracted using the wheel and rail geometries at the contact origin. Longitudinal (γ_1), lateral (γ_2) and spin (ω) creepage values are then estimated for subsequent use within the Fastsim algorithm.

Contact velocity	Rolling Radius	Contact Angle	Wheelset angular velocity	Lateral contact position	Creepages		
V_c	r_{x1}	δ	Ω	CP_{Lr1}	γ_1	γ_2	ω
m/s	*m*	*radians*	*1/s*	*m*	-	-	-
-14.9994	424.02	-0.0859	-35.37	0.7419	$3.7917\text{x}10^{-5}$	0.005	0.2023

Table 6-2: Local contact parameters required for Fastsim.

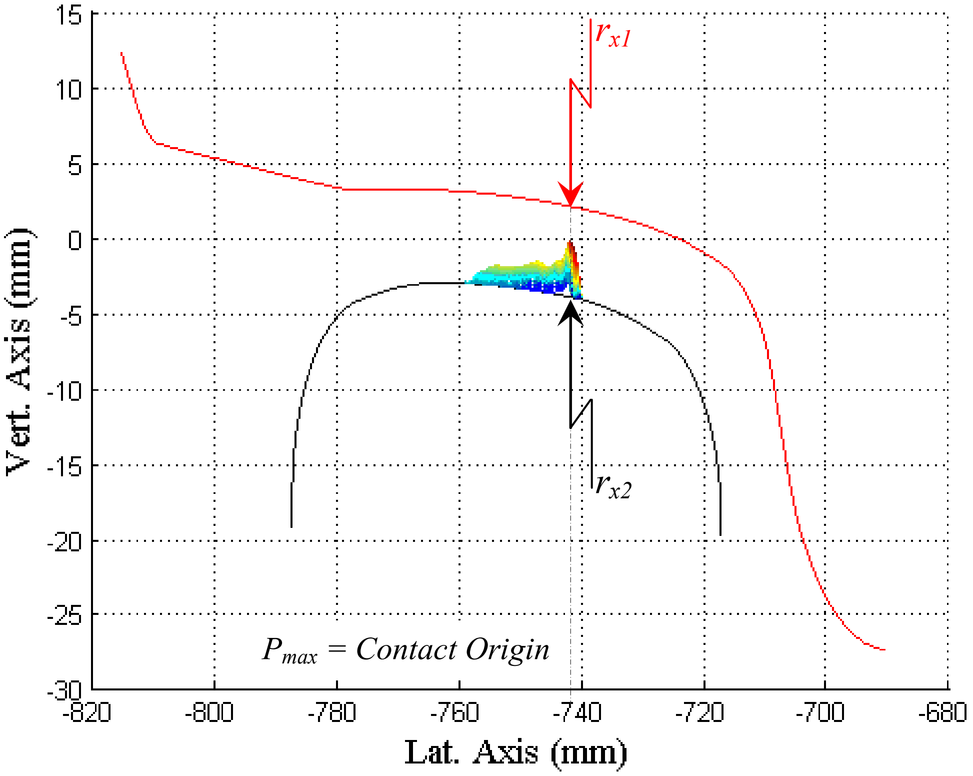

Figure 6-10: Location of contact origin used for creepage approximation (Note: profiles have been shifted by ±3 mm for illustration purposes).

The wear damage approximation process is then completed by utilising the wheel/rail slip calculation from Fastsim within the Archard wear model. The same procedure as described within *Chapter 4*, *section 4.4.1* is used during the contact patch wear depth simulation process.

6.2.4 Validation and Comparisons

The initial focus for developing the 2.5D BEM approach is to improve the normal contact pressure distribution in order to subsequently improve the accuracy of the damage simulation for non-Hertzian contact patches. To first demonstrate the feasibility of implementing the lateral 2.5D BEM approach, comparison is made with an identical model built within the established finite element (FE) software package Abaqus. Figure 6-11 illustrates the FE model and associated mesh. To ensure that the FE and

BEM geometries were identical, a manually defined script file was used to import the BEM mesh xy-coordinates into Abaqus. A longitudinal mesh size of 0.2 mm was used to replicate the modelled offsets between individual BEM slices. A Young's modulus of 201 GPa and a Poisson's ratio of 0.3 were assigned to the wheel and rail materials within both models. To replicate the boundary conditions used within the BEM procedure, the rail base is rigidly fixed whilst the wheel is only free to move vertically. A total wheel load of 49505 N has been used, which represents a static 10 tonne axle load (i.e. 10,000kg / 2 * 9.81 = 49505 N).

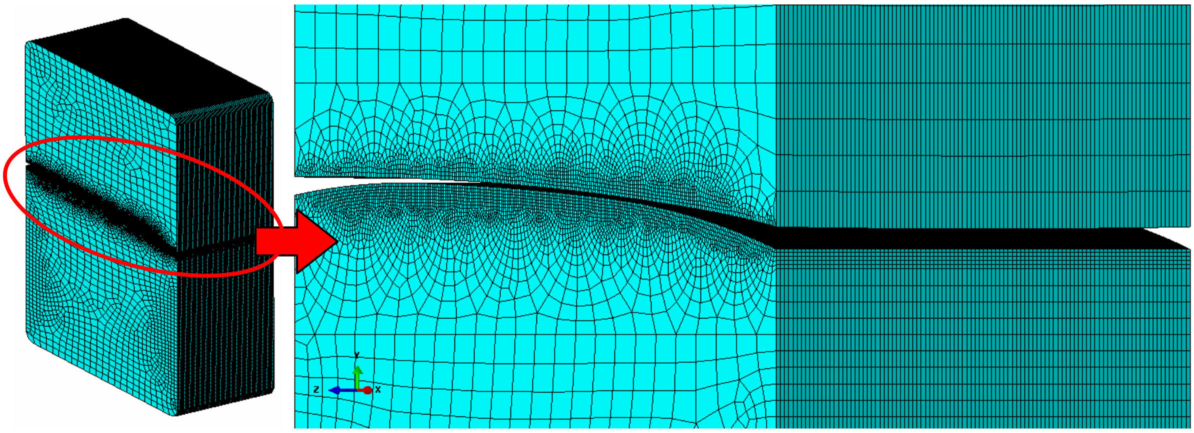

Figure 6-11: FEA mesh generated for 2.5D BEM comparison.

Figure 6-12 provides a comparison between the FEA and BEM solutions for the normal contact pressure distribution whilst Table 6-3 provides a summary of maximum results between simulation techniques. Very good comparison is achieved with regards to the general shape, size and overall distribution of contact pressure, although the normal pressure magnitude has been moderately under-estimated by the 2.5D BEM model. This is a direct result of approximating both the longitudinal semi-axis (a) and the shape of the applied load distribution. Within this case study, the contact patch longitudinal semi-axis has been overestimated using the Hertzian approximation, resulting in a larger contact area and hence reduced normal contact pressures. It is observed that the distribution of applied load seems to also be overestimated towards the front and rear of the contact patch, resulting in an underestimation of the applied loads as they approach the contact centre (refer to Figure 6-8). Figure 6-7, (a) to (e), also illustrates that the issue concerning load application and subsequent variation in 2.5D BEM normal pressure distribution is not related to the selected number of slices.

Improving the load application throughout the contact patch is an issue that can be easily overcome by converting the BEM model to one of displacement application as opposed to load. This was not done within the current PhD research project due to time constraints but will be suggested for further work. Additionally, the validation cases presented within *Chapter 5* confirm that a more realistic means of load application would indeed improve further the accuracy of the 2.5D BEM model.

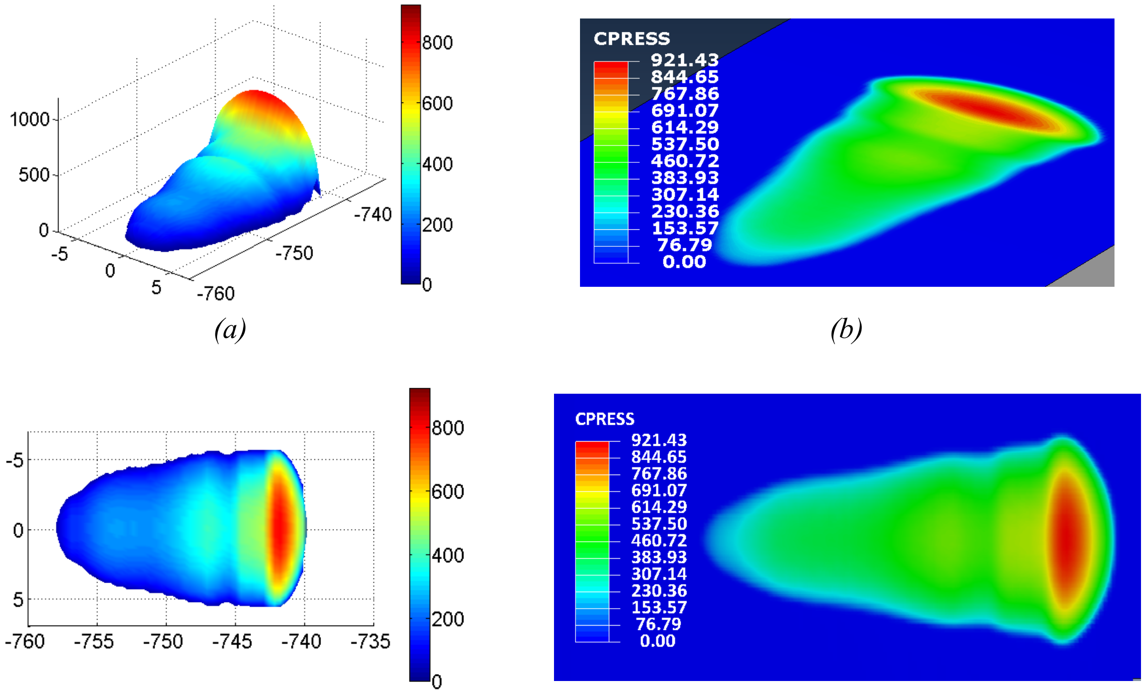

(a) *(b)*

(c) *(d)*

Figure 6-12: 2.5D BEM normal pressure distribution, (a) and (c), compared to the equivalent solution obtained using finite element analysis, (b) and (d).

6.2.4.1 Computational Efficiency

To demonstrate additional benefits of implementing a 2.5D BEM technique, a direct comparison of CPU (Central Processing Unit) times was made between the FE and BE approaches. The 2.5D BEM model with 50 x 2D BEM slices solved in 33.55 minutes on a standard desktop computer with 4 CPU's and 8.0Gb of physical memory. This compared to a total CPU time of 38.28 minutes for the equivalent 3D FEA model. It is very important to note that:

1. The 3D FEA model could not be solved on the same desktop computer as described for the 2.5D BEM solution due to the system running out of memory. To overcome this, the FE solution was solved using the Imperial College High Performance Computing (HPC) suite with 16 CPU's. The solution time of 38.28 minutes, when converted to equivalent CPU time, therefore equated to 37,164.17 seconds (10.32 hours). It should be noted that Abaqus is not perfectly parallelised when running over the HPC with efficiency dropping once more than 4 CPU's are requested. To make this a fairer comparison, we can divide the final solution time by 4, giving 2.58 hours. Even after adjustment it is obvious just how significant the computational benefits of implementing a 2.5D BEM approach really are.

2. The BEM model is also vastly un-optimised whilst the advance FE software has enjoyed many years of computational optimisation.

Further improvements in solution time are therefore expected after future code optimisation and the use of parallel processing, which is an ideal approach for solving multiple BEM slices at once. These areas of further work are also identified within *Chapter 8, Section 8.3 - Further work*.

6.2.5 Comparison with the Hertzian normal contact model

To illustrate the already significant improvements over simplified wheel-rail contact models, a comparison with the Hertzian solution is presented. Figure 6-13 compares the normal contact pressure distributions between the novel 2.5D BEM technique and the simplified Hertzian solution. The colour bar has been maintained between 0 - 1200 MPa to enable a direct comparison between normal pressure distributions to be made. The most significant advantage gained through developing the 2.5D BEM approach comes from accuracy of the shape, size and non-linear distribution of contact stresses within the contact patch. The location of maximum normal contact pressure, for both solutions, exists at approximately -742 mm. Within the Hertzian solution, this is then assumed to be the centre of contact, with the resulting contact patch being symmetrical about this origin. In reality, and as illustrated within Figure 6-12 and Figure 6-13, the location of maximum contact pressure does not always relate to the centre of the contact patch and the pressure distribution is rarely symmetrical about the contact origin. This is accurately captured by the 2.5D BEM model, which obtains a vastly improved solution for use within subsequent stages of the S&C degradation process.

Parameter	Units	FEA	BEM	%Error	Hertzian	%Error
Max. Normal Pressure	*MPa*	921.42	804.90	-12.64 %	1029.90	11.77 %
Longitudinal contact patch length (2a)	*mm*	9.59	11.32	18.04 %	11.32	18.04 %
Lateral contact patch width (2b)	*mm*	18.88	18.40	-2.54 %	8.04	57.42 %
CPU Time (50 x 50 elements)	*mins*	37,164.17	28.31	-	3.7278e-4	-

Table 6-3: Key results comparing FEA, BEM and Hertzian contact models.

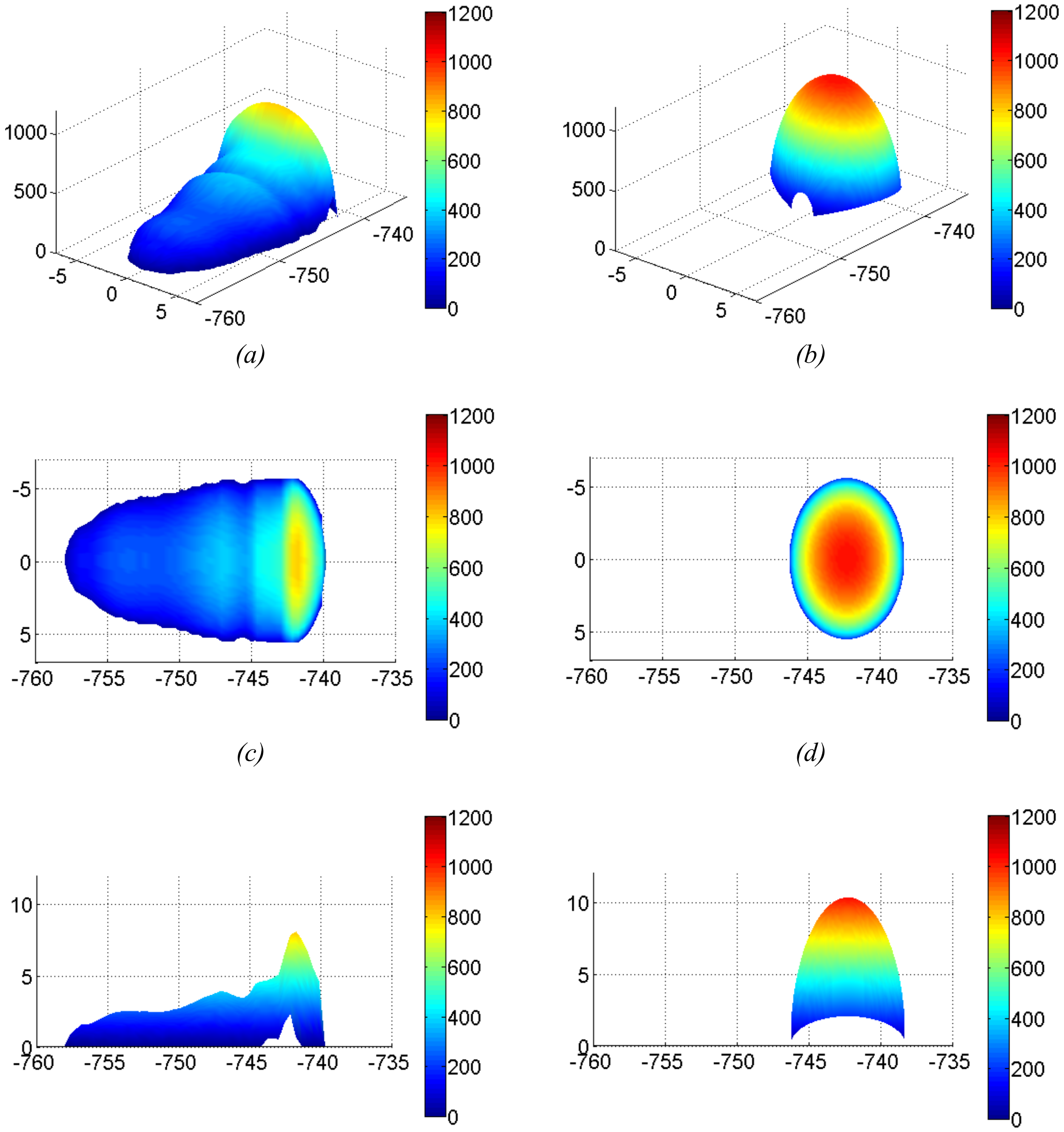

(a) *(b)*

(c) *(d)*

(e) *(f)*

Figure 6-13: 2.5D BEM normal pressure distribution, (a), (c) and (e), compared to the equivalent solution obtained using Hertzian contact theory, (b), (d) and (f). 2.5D BEM wear depth distribution (g) compared to the equivalent solution obtained using Hertzian contact theory (h).

To demonstrate further significant benefits of the 2.5D BEM approach, a comparison of slip velocity and wear depth prediction has been made. Figure 6-14 *(a)* and *(b)* compare the three-dimensional slip velocities. The vector arrows give an indication of both the direction and magnitude of slip. It is very evident that the more accurate, non-Hertzian normal contact solution leads to a vastly different prediction of the slip regions within the contact patch and hence significant differences in the subsequent wear depth distributions, as compared within Figure 6-15. The maximum wear depth is reduced by 81.46 %, from 3.66x10^{-4} μm to 6.79x10^{-5} μm. This significant reduction from the Hertzian to the 2.5D BEM approach is explained by lower normal contact pressures within the predicted slip region of the 2.5D BEM contact patch combined with lower overall slip velocities. The location of wear is also significantly different between approaches, with the 2.5D BEM solution predicting majority of the wear to the left of the contact origin whilst the simplified Hertzian approach distributes the wear symmetrically at the contact origin either side of the longitudinal axis.

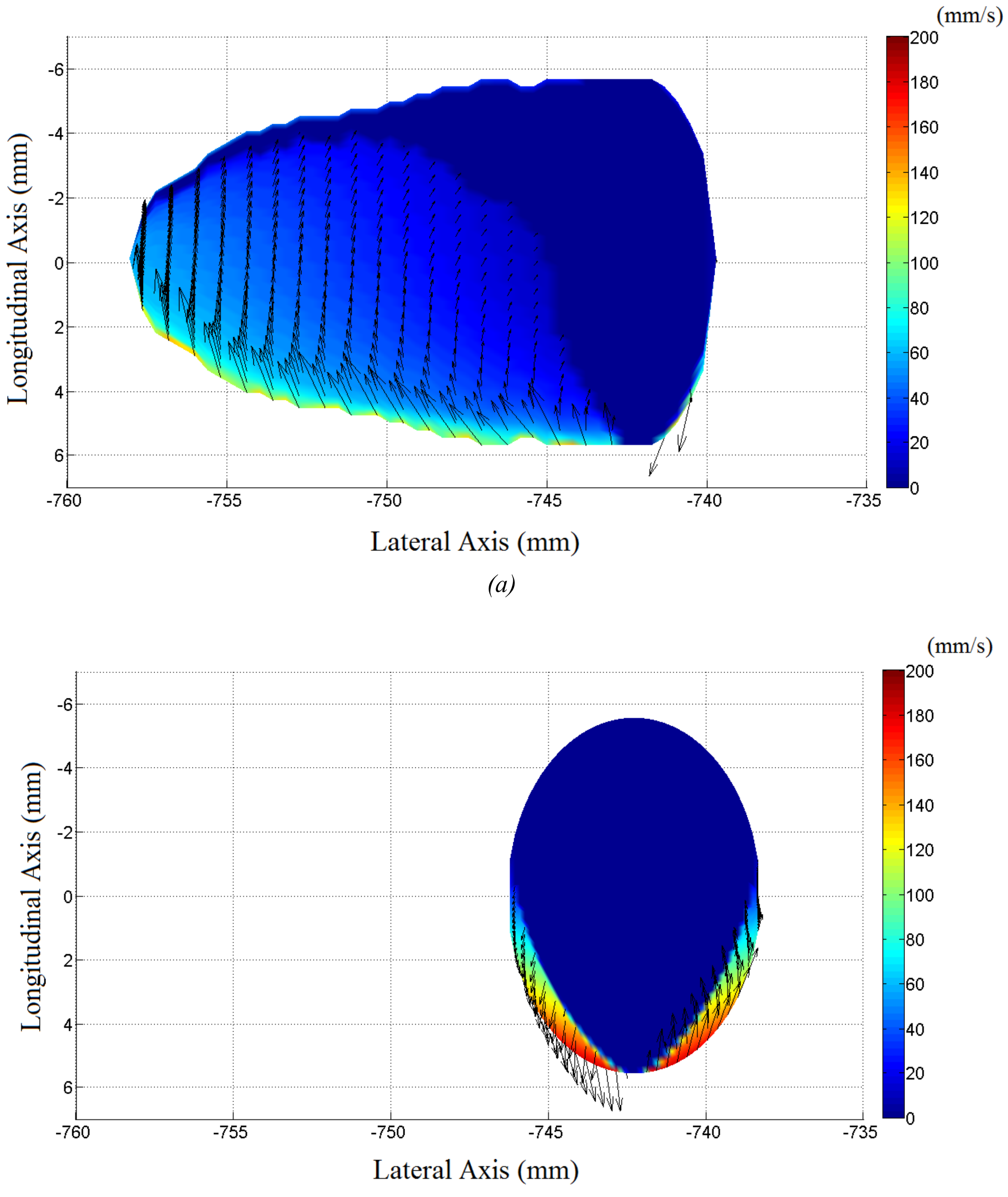

(a)

(b)

Figure 6-14: Slip velocities compared between the 2.5D BEM (a) and equivalent Hertzian (b) solutions.

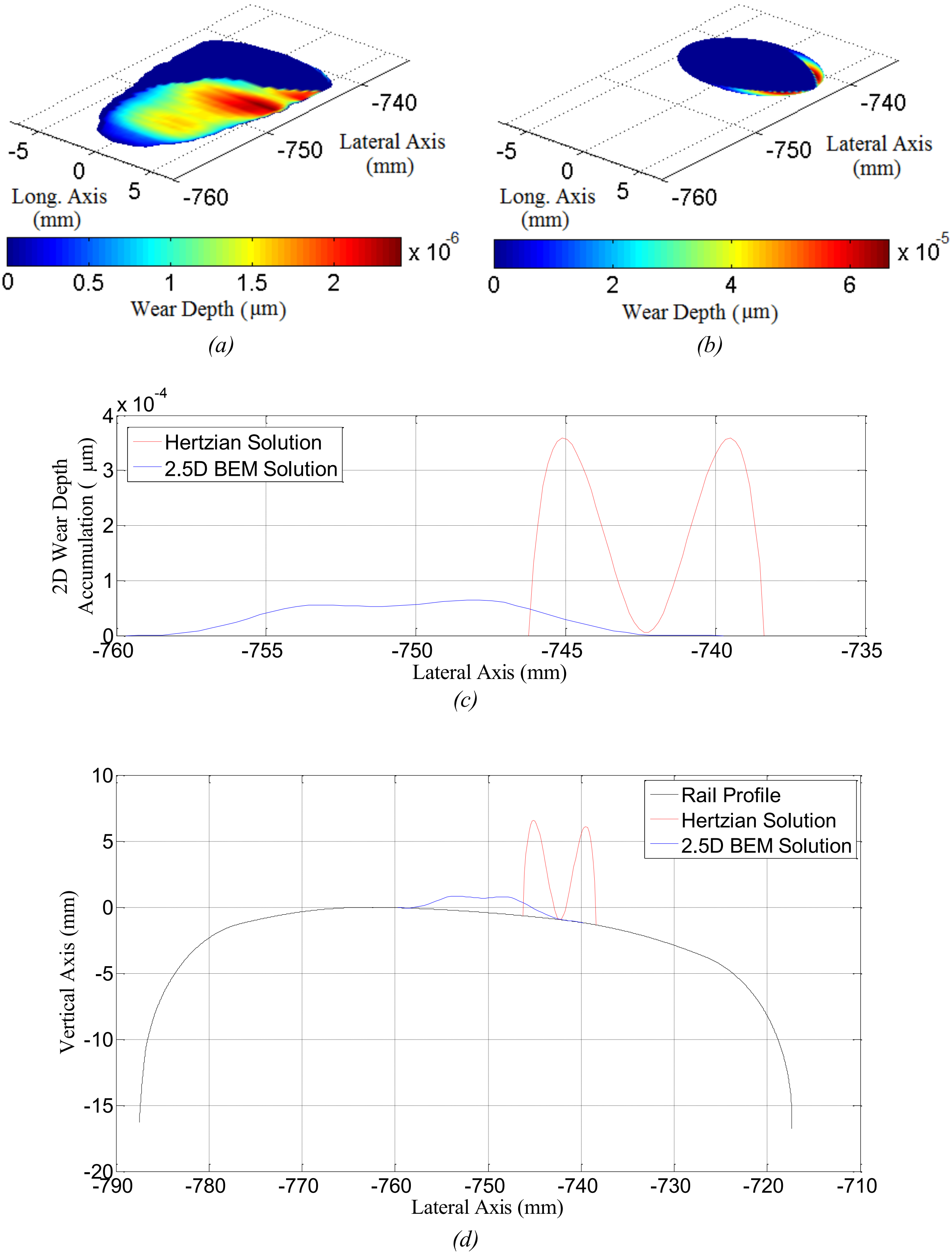

Figure 6-15: Comparison of 2.5D BEM (a) and Hertzian (b) wear depth distributions and the equivalent two-dimensional wear depth accumulation profiles (c). The predicted wear location across the rail profile is presented within (d) [Note: (d) is not to scale for illustration purposes].

]

This section of *Chapter 6* has identified some very significant benefits of implementing an advanced, novel 2.5D BEM solution for long-term S&C damage accumulation. The limiting assumptions that drive simplified contact theories lead to errors during the wheel-rail normal contact prediction stage of the damage simulation. These errors are then taken right through to the end of the modelling process, generating an inaccurate tangential solution and hence incorrect wear depth distributions within the contact patch. A major consequence of this would be the accumulation of error over many load cycles, which would lead to the incorrect evolution of the rail profile due to wear. Small errors at the onset of rail profile evolution would also introduce significant inaccuracies with regards to subsequent wheel-rail contact prediction as the entire process relies upon accurate wheel and rail contact geometries.

6.3 Internal domain influences

Other significant and novel benefits of implementing a lateral BE model for wheel-rail contact is the ability to include phenomena occurring within the internal domain of the contacting bodies. This section discusses initial developments for both dynamic impact and plastic deformation modelling and presents some preliminary results.

6.3.1 BEM extension for elasto-dynamics (impact)

As identified within *Chapter 2*, one of the current limitations of all existing wheel-rail contact models is the exclusion of material inertia terms and hence the inability to model the affects of impact loading on the contacting bodies. Although uncommon within normal wheel-rail rolling contact, impacts loads are a phenomenon that cannot be ignored when considering contact through S&C. In particular, wheel-rail transfer from the wing rail onto the crossing nose (and vice versa) generates a dynamic amplification of the rolling contact load. Short duration, high intensity impact loading generates stress waves that migrate through the rail. This phenomenon should not be ignored when considering a tool for long-term degradation of S&C rail profiles. There are also no existing publications that attempt to include inertial effects within the wheel-rail contact model.

The novel implementation of a lateral BE model investigates this issue by enabling an incremental calculation of nodal stresses and displacements within the internal domain of the contacting bodies. This is achieved by integrating the fundamental solutions (as discussed within *Chapter 5*) over the entire domain as opposed to just the problem boundaries. Internal body velocities and accelerations can then be obtained to generate a time incremental material response to impact loading scenarios. Although the elasto-dynamic formulation was already established within the adopted BE code, the architecture for enabling its application for wheel to rail interaction did not exist. This section, therefore, presents the additional developments required for wheel-rail implementation. A simple case study is also given, demonstrating the successful simulation of stress wave propagation due to vertical impact of a P8 wheel onto a BS113A rail with internal body inertia.

Figure 6-17 illustrates how the elasto-dynamic code has been structured for wheel to rail impact implementation. The process can be summarised by the following steps:

1. Load into memory the existing wheel and rail boundary element mesh and associated material properties (Young's modulus, Poisson's ratio, shear modulus, coefficient of friction and material density).

2. Define the wheel vertical impact speed, time-step and domain thickness.

3. Automatically generate the internal nodes and meshing parameters (*i.e.* nodal *x* and *y* coordinates, element half-width (*dx*) and height (*dy*) and the element type marker. It should be noted that, in comparison to the boundary mesh format presented within *Chapter 5*, *Table 5-2*, columns *4* and *5* become redundant for the internal mesh whilst column *7* is utilised for the vertical element height). Table 6-4 provide an extract of the internal mesh data whilst Figure 6-16 illustrates the final, automatically generated mesh for a BS113S rail section.

1	*2*	*3*	*4*	*5*	*6*	*7*
Nodal x-coordinates	*Nodal y-coordinates*	*Element half-width (dx)*	*Normal vector**	*Element radius**	*Element type marker*	*Element half-height (dy)*
-787.2356	-13.9564	0.7914	0	0	1000	0.3876
-785.6528	-7.9967	0.7914	0	0	1000	0.4821
-784.0700	-5.7163	0.7914	0	0	1000	0.5179
-782.4872	-4.1792	0.7914	0	0	1000	0.5383

** not used for internal elements*

Table 6-4: Example internal mesh data format (first 4 nodes of case study internal mesh)

Within an elasto-dynamic analysis, the internal mesh must cover the entire domain due to using the internal displacements and velocities for predicting subsequent material states. This differs to the internal mesh required for simply assessing the internal stress states as only the mesh within the region of interest is required.

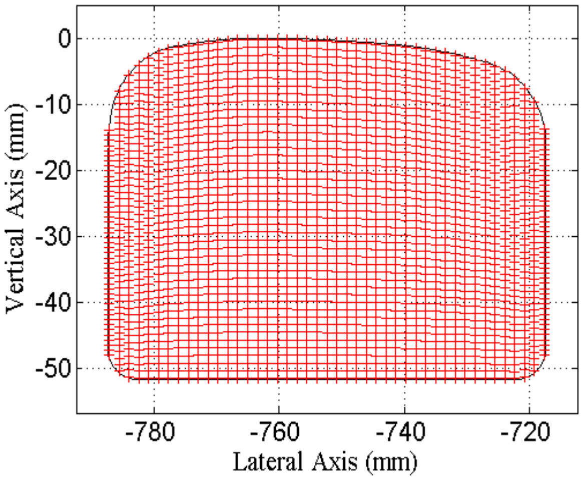

Figure 6-16: Example internal mesh automatically generated for a BS113A rail section.

4. Initialise influence function, solution and boundary condition matrices.

5. Define the problem boundary conditions and insert the influence due to body forces term (*dt^2/mass*) along all nodes *i* = *j*. This term defines the amount of body force for each node due to its own acceleration, which is generated by the elastic deformation taking place throughout the time step. *Equations 6-3* to *6-6* illustrate how the body force (BF) term is formulated and shows its location within the final displacement relationship, given here by *Equation 6-7*:

$$V_{(t)} = \frac{u_{(t)} - u_{(t-1)}}{\Delta t} \tag{6-3}$$

$$a_{(t)} = \frac{V_{(t)} - V_{(t-1)}}{\Delta t} = \left(\frac{u_{(t)}}{\Delta t^2} - \frac{u_{(t-1)}}{\Delta t^2} - \frac{V_{(t-1)}}{\Delta t}\right) \tag{6-4}$$

$$BF = m * a = m * \left(\frac{u_{(t)}}{\Delta t^2} - \frac{u_{(t-1)}}{\Delta t^2} - \frac{V_{(t-1)}}{\Delta t}\right) \tag{6-5}$$

$$u_{(t)} = \left(\frac{BF}{m} + \frac{u_{(t-1)}}{\Delta t^2} + \frac{V_{(t-1)}}{\Delta t}\right)\Delta t^2 \tag{6-6}$$

$$u_{(t)} = \frac{BF \cdot \Delta t^2}{m} + u_{(t-1)} + V_{(t-1)} \cdot \Delta t \tag{6-7}$$

Equation 6-5 links directly to the displacement influence function as discussed previously within *section 5.2.4*. This additional term is added to the displacement influence function as to include the displacement occurring due to inertia within the internal domain (*i.e.* displacement due to internal body forces). The components of *Equation 6-7* are highlighted yellow within *Figure 6-17.*

6. Generate the wheel to rail contact surface profile gap function using cubic spline curve arithmetic. This function is subsequently used to define rigid penetration of the wheel as it impacts upon the rail surface.

7. The current time increment is defined (*Time* = *Time* + *dt*) along with the initial conditions for both the surface and internal nodes. The internal conditions are set to the displacements experienced during the previous time-step (*i.e.* terms $u_{(t-1)} + V_{(t-1)}*dt$ from *Equation 6-7*).

8. The wheel vertical position is calculated using the vertical displacement and acceleration values calculated during the previous time-step. The contact duration is also estimated, using the contact patch longitudinal semi-axis and vehicle speed. If the current simulation time, T, exceeds the contact duration, T_{con}, the load (rail surface displacement) is removed (*i.e.* simulating that the wheel has now completely passed over the rail profile under analysis).

9. The boundary conditions are updated to reflect rigid penetration occurring during the current time-step. A deformation smoothing process has also been implemented to prevent sharp corners from forming at the edge of the contact region, leading to potential singularity issues.

10. The boundary element problem is then solved, providing displacements and stresses at each node. Internal domain velocities and accelerations are determined at every point within the contact domain.

11. Depending on the output frequency defined at the onset of the simulation, the results extraction process, illustrated within *Figure 6-18*, is initiated.

If the simulation has not reached the prescribed run duration, steps 7 – 11 are then repeated, using the previous set of results to determine the current wheel profile and rail domain displacement boundary conditions. A decelerated wheel velocity (V_t^{wheel}) is also calculated as a result of the opposing vertical contact force (F_y) acting upon the wheel mass (m^{wheel}) using the following equation:

$$V_t^{wheel} = V_{t-1}^{wheel} + 1000 * \left(F_y / m^{wheel} * dt\right) \qquad 6\text{-}8$$

Equation 6-8 is highlighted green within *Figure 6-17*.

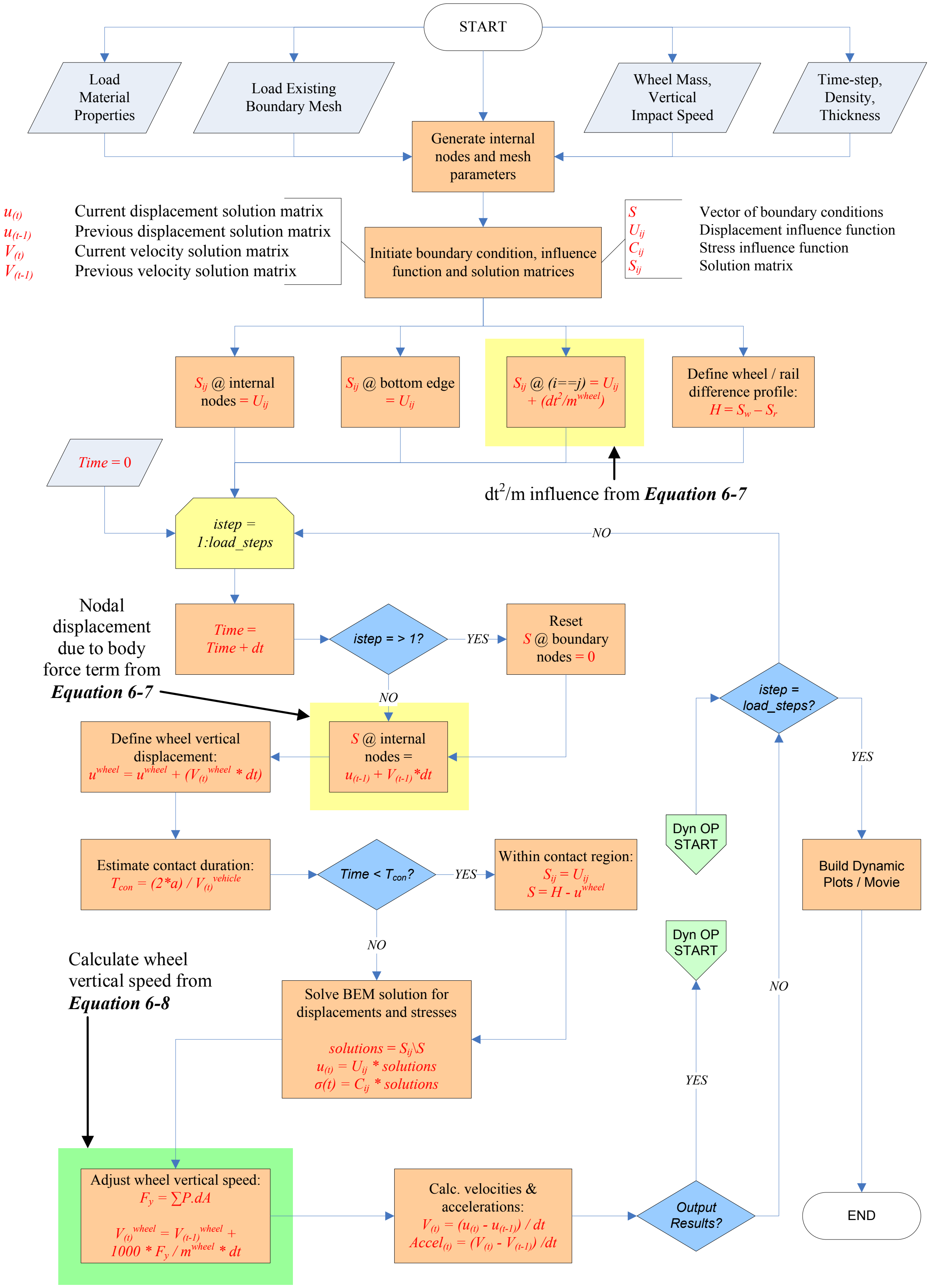

dt^2/m influence from ***Equation 6-7***

Nodal displacement due to body force term from ***Equation 6-7***

Calculate wheel vertical speed from ***Equation 6-8***

Figure 6-17: Dynamic BEM process flowchart.

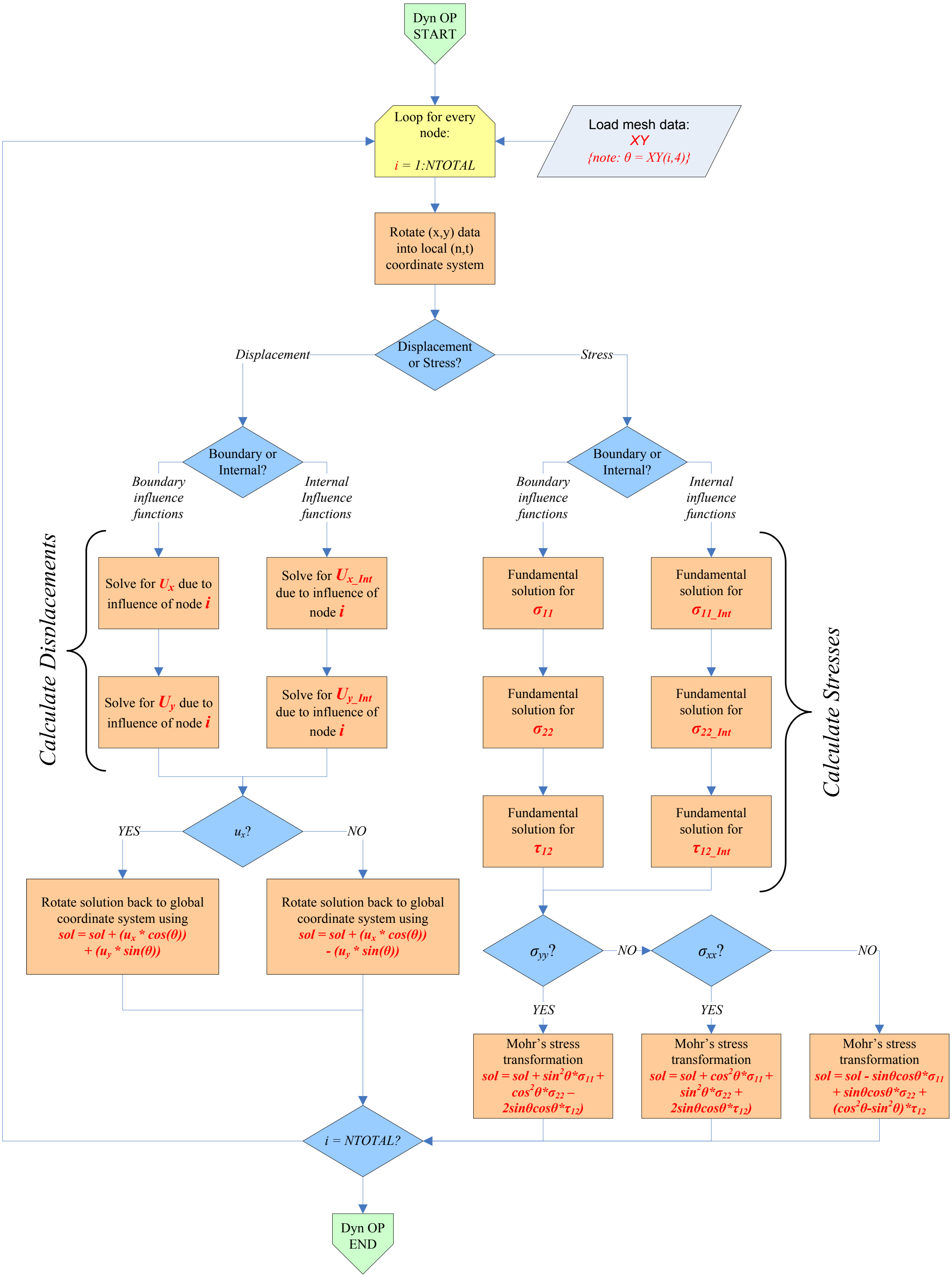

Figure 6-18: Dynamic BEM results extraction routine.

Figure 6-18 illustrates the extraction of internal displacement and stress results due to coordinate and Mohr's (see *Chapter 5 – section 5.2.4*) transformation. This step is essential for converting the solutions from their local (n, t) to the required global (x, y) coordinate system.

A dynamic impact analysis has been completed using a nominal P8 wheel profile impacting upon a generic BS113A rail profile. Assuming a longitudinal wheel velocity of 75 mph (33528 mm/s) and a contact patch longitudinal semi-axis of 5 mm, the contact duration was estimated to be 2.98e-4 s. A sufficiently small time step of 2.00e-5 s was therefore chosen to ensure that (1) enough load increments were achieved throughout the duration of contact and (2) the rapid relaxation of stress and stress wave propagation was captured upon removal of the contact load. A vertical wheel velocity of 100 mm/s was chosen to provide a realistic amount of wheel-rail penetration within the estimated contact duration. A total time of 1.90e-3 s was simulated over 95 load steps. Figure 6-19 illustrates the propagation of von Mises stress through the rail during the impact process. Outputs were extracted every 1.00e-4 s. The gradual build up of stress is observed throughout the contact duration and peaks at 615.20 MPa at approximately 5.00e-4 s despite the load being removed after 2.98e-4 s. This provides the first demonstration of how the internal body forces (inertial effects) lead to a dynamic amplification of results as the internal domain accelerations further increase the von Mises stress during initial unloading of the wheel. The maximum von Mises stress is also 45.58 % greater than the result obtained from an equivalent static analysis (422.59 MPa). It should be noted here that the process of load application between the static and dynamic analyses is very different. The static analysis always converges to steady-state equilibrium (*i.e.* relating to a wheel at rest) whereby the dynamic analysis relies upon a dynamic impact velocity and hence a varying application of load. Rapid relaxation of stress occurs over 3.00e-4 s, after which the stress waves reflect from the external boundaries of the rail geometry. Within the current process, stress propagation and relaxation within the rail domain can only occur laterally. In reality, the stress waves are also able to propagate along the rail. This technique may therefore be marginally overestimating the dynamic effects. It is, however, possible to use the BEM model for simulating longitudinal wheel-rail contact therefore further work is possible for investigating longitudinal stress waves.

These preliminary results show the importance of including body inertia terms and the dynamic application of load within the contact solution but should only be used where dynamic impact is a cause for concern. This is due to a significant increase in computational effort required to capture these very isolated dynamic events. A total solution time of 7.19 h was required to simulate the example within Figure 6-19, representing a significant increase over the 5.45 minutes required for a general static analysis with internal domain interrogation. The technique for load application should also be considered carefully. Rigid penetration of profiles has been implemented within this study. Further accuracy improvements can be made by modifying the BEM elastic contact model to operate using the dynamic load application. *Section 6.3.1* has therefore demonstrated the novel application of a lateral BEM model for including inertia effects within the wheel-rail contact model. Integrating an elasto-dynamic BEM code within the combined tool for S&C degradation studies and provides, for the very first time, a solid platform for modelling dynamic impacts within a wheel-rail contact model.

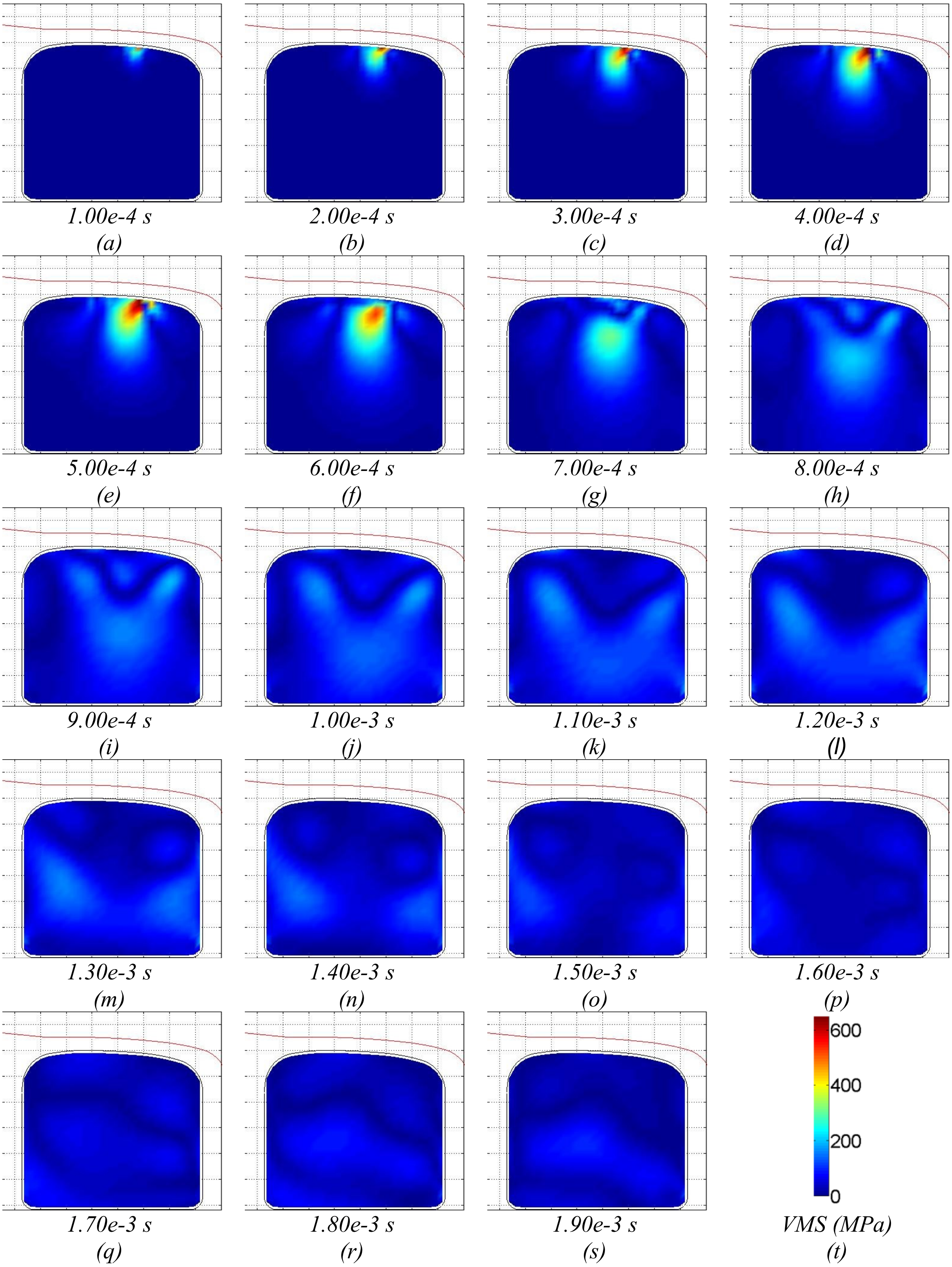

1.00e-4 s (a)
2.00e-4 s (b)
3.00e-4 s (c)
4.00e-4 s (d)
5.00e-4 s (e)
6.00e-4 s (f)
7.00e-4 s (g)
8.00e-4 s (h)
9.00e-4 s (i)
1.00e-3 s (j)
1.10e-3 s (k)
1.20e-3 s (l)
1.30e-3 s (m)
1.40e-3 s (n)
1.50e-3 s (o)
1.60e-3 s (p)
1.70e-3 s (q)
1.80e-3 s (r)
1.90e-3 s (s)
VMS (MPa) (t)

Figure 6-19: Preliminary dynamic impact results of von Mises stress from a P8 wheel profile impacting upon a BS113A rail. Plots (a) through to (s) represent results extracted every 0.0005s (i.e. total simulation time = 0.0095s). Figure (t) provides the stress scale used within Figures (a) through to (s).

6.3.2 BEM extension for plasticity

The second extension and novel aspect of the lateral BEM approach is the adaptation for plastic deformation modelling. Although not fully implemented within this thesis, an overview of the initial developments is provided.

BEM formulation for the solution of small strain elasto-plasticity, using the concept of the consistent tangent operator (CTO), was first introduced by Bonnet and Mukherjee [120]. The CTO was introduced by Simo and Taylor [121] and provides an elegant solution of the implicit approach by securing the exact derivative for the Newton-Raphson iteration, significantly improving the rate of convergence. Considering rate-independent elasto-plasticity, the radial return algorithm (RRA) was introduced by Simo and Taylor [121] and utilised the von Mises yield criterion with an associative flow rule. The method was suitable for both kinematic and isotropic hardening. Poon [122] demonstrated a BEM formulation including the RRA with CTO implementation for isotropic hardening and demonstrated the crucial role of the CTO upon application of Newton's method. Several different authors have tackled the elasto-plasticity problem using a boundary element formulation although none have applied the solution to wheel-rail interaction. Paulino [123] utilised the initial strain formulation whereby body forces are replaced by initial strains residing within the domain. Initial developments presented here are based on simple, non-hardening von Mises plasticity incorporating the RRA combined with CTO approach. The CTO is yet to be fully implemented within this study therefore this section will discuss initial developments to integrate of the RRA within the lateral BEM model. Some further developments associated with the CTO technique are provided within *Appendix A2*.

6.3.2.1 Von Mises plasticity – Radial return algorithm

Stress tensors can be divided into two independent components; the isotropic stress tensor and the deviatoric stress tensor. The isotropic component describes the volumetric change of the stressed body whilst the deviatoric component gives an indication of how the body is distorted under load. This is the fundamental principle behind the von Mises plasticity model, whereby the deviatoric component of stress is used within an iterative algorithm to predict the degree of deformation (plasticity). During yielding conditions, the algorithm brings the total stress tensor back down to a defined yield surface, which is defined by the material under analysis, by reducing the normal magnitude of the stress deviator tensor, hence the term radial return algorithm (RRA).

The von Mises yield criterion states that yielding occurs when the second deviatoric stress invariant (J_2) reaches a critical value. The technique is therefore often referred to as "J_2 plasticity" theory, where:

$$J_2 = \frac{1}{2} tr(\boldsymbol{s} \cdot \boldsymbol{s}) \tag{6-9}$$

$$\boldsymbol{s} \equiv \boldsymbol{\sigma} - \frac{1}{3}\big(tr(\boldsymbol{\sigma})\big)\boldsymbol{I} \tag{6-10}$$

Here, $\boldsymbol{s}$ represents the deviatoric part of the stress tensor $\boldsymbol{\sigma}$ and $\boldsymbol{I}$ is the identity matrix. Within *Equation 6-9*, *'tr'* denotes the trace of the tensor.

$$\boldsymbol{\sigma} = \begin{bmatrix} \sigma_{11} & \sigma_{12} & \sigma_{13} \\ \sigma_{21} & \sigma_{22} & \sigma_{23} \\ \sigma_{31} & \sigma_{32} & \sigma_{33} \end{bmatrix} \tag{6-11}$$

When expanded, the J_2 stress invariant can be expressed in terms of the principal stresses as:

$$J_2 = \frac{1}{6}[(\sigma_1 - \sigma_2)^2 + (\sigma_2 - \sigma_3)^2 + (\sigma_3 - \sigma_1)^2] \tag{6-12}$$

The von Mises stress criterion states that, at the onset of yield, the J_2 stress tensor equals a pre-defined material constant, k^2. This constant is very much dependent on the yielding conditions of the material under analysis. For uniaxial stress, the yield function reduced down to:

$$k^2 = \frac{{\sigma_Y}^2}{3} \tag{6-13}$$

Accumulated equivalent plastic strain rate is then obtained using the following procedure:

1. Assuming an elastic response, a trial prediction of the updated stress is obtained through assessing the individual components of strain rate:

$$\sigma_{t+\Delta t}^{trial} = \sigma_t + \Delta t \cdot [2G \cdot dev(\dot{\varepsilon}) + 3K \cdot iso(\dot{\varepsilon})] \tag{6-14}$$

2. The trial stress invariant, J_2^{trial}, is then obtained using *Equation 6-12* above.

3. J_2^{trial} is then tested against the yield condition:

    a. If $J_2^{trial} \leq k^2$, the elasticity assumption is correct and the trial stress can be maintained. The plastic strain rate $\left(\dot{\varepsilon}^p\right)$ can then be set to zero whilst the elastic strain rate $\left(\dot{\varepsilon}^e\right)$ equals the total strain rate $(\dot{\varepsilon})$.

$$\sigma_{t+\Delta t} = \sigma_{t+\Delta t}^{trial} \tag{6-15}$$

    b. If $J_2^{trial} > k^2$, the elasticity assumption is incorrect. In this scenario, the trial stress is updated to fall directly upon the yield surface through scaling of the deviatoric stress component:

$$\sigma_{t+\Delta t} = iso\left(\sigma_{t+\Delta t}^{trial}\right) + dev\left(\sigma_{t+\Delta t}^{trial}\right)/fac \tag{6-16}$$

where:

$$fac = \frac{J_2^{trial}}{k^2} \tag{6-17}$$

4. The consistent stress rate is then determined using the current and updated stress results:

$$\dot{\sigma} = \frac{\sigma_{t+\Delta t} - \sigma_t}{\Delta t} \tag{6-18}$$

5. Hooke's law is then applied to convert the stress rate into elastic strain rate:

$$\dot{\varepsilon}^e = \frac{iso(\dot{\sigma})}{3K} + \frac{dev(\dot{\sigma})}{2G} \tag{6-19}$$

6. Strain rate decomposition can then be used to determine the plastic strain rate:

$$\dot{\varepsilon}^p = \dot{\varepsilon} - \dot{\varepsilon}^e \tag{6-20}$$

7. From here, the plastic strain is determined for the time step using:

$$\varepsilon^p = \dot{\varepsilon}^p \cdot \Delta t \tag{6-21}$$

This process can then be used to accumulate plastic strain as the predicted stresses continuously exceed the yield stress of the material. Another layer of accuracy can also be implemented through the simulation of material hardening, which is achieved by modifying the yield surface to replicate an updated yield limit associated with a given material stress/strain curve.

A non-hardening plastic strain accumulation model using the radial return algorithm approach has been implemented within the current S&C contact and degradation model. An example using a BS113A rail profile and nominal P8 wheel profile is given. Within this example, 50 load steps have been used to apply a total of 6.36 kN, which provides a realistic normal contact pressure at the centre of the contact patch (see Figure 6-8, above). The optimised boundary mesh of 0.2 mm was used whilst the internal mesh was set to 0.5 mm to aid computational efficiency, as illustrated within Figure 6-20.

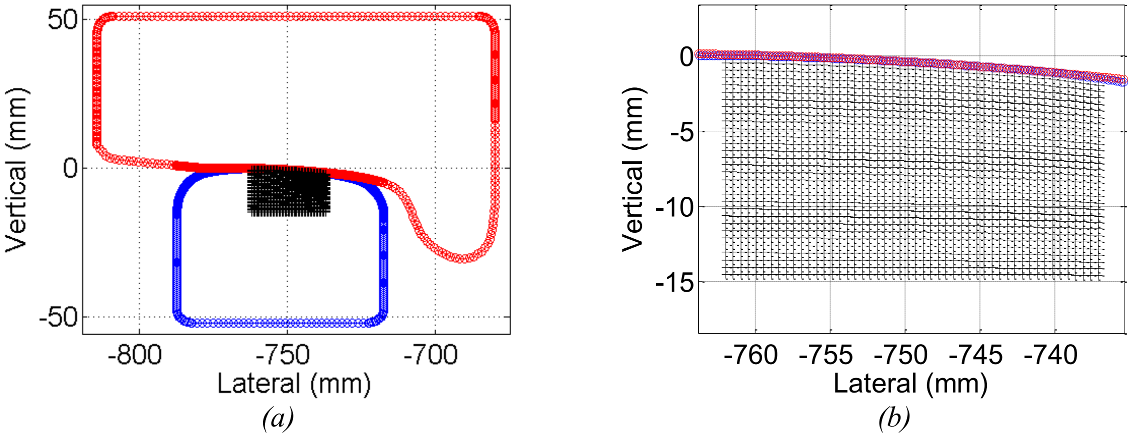

Figure 6-20: Complete BEM mesh (a) and a close-up of the internal domain mesh (b) used within the plastic strain accumulation case study.

Figure 6-21 presents the evolution of equivalent stress and associated plastic strains after every 10 load steps. It can be seen that the maximum equivalent stress is now limited by the yield condition defined within the RRA. Within this example, yield is defined by the maximum material shear stress (τ_y) of 173.21 MPa (*i.e.* $\tau_y = \sigma_y/\sqrt{3}$). Within the region of limited equivalent stress, it is shown that strain begins to accumulate up to a maximum of 5.54e-04.

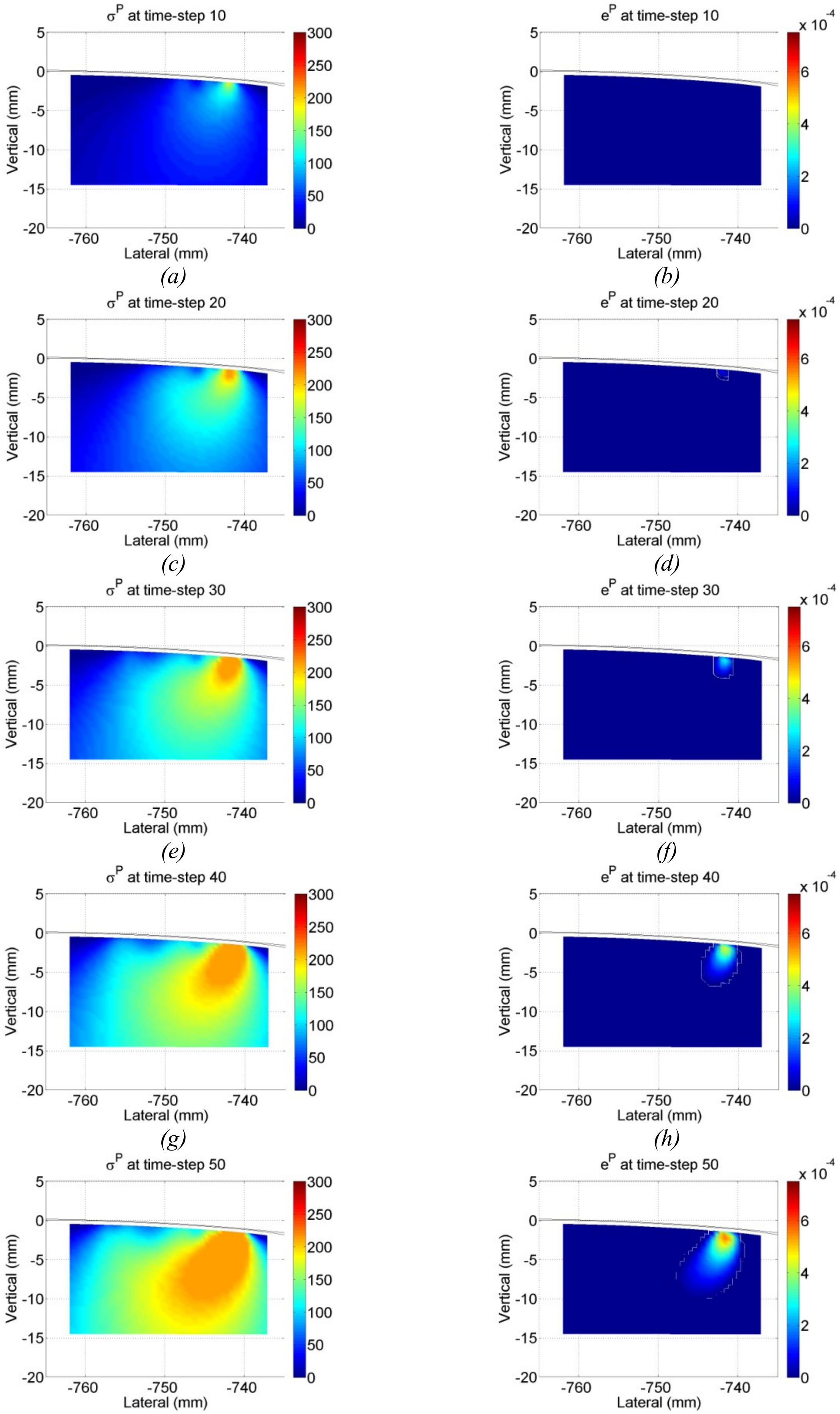

(a) (b)

(c) (d)

(e) (f)

(g) (h)

(i) (j)

Figure 6-21: Equivalent stress (left) and equivalent plastic strain (right) due to the radial return algorithm.

6.4 Conclusion

Chapter 6 has discussed the development of a novel approach for wheel to rail interaction modelling suitable for simulating all of the complex phenomena occurring at S&C. It has been demonstrated that a 2.5D BEM solution, as compared to simplified Hertzian contact, provides significant improvements with regards to the shape and size of the contact patch and also the distribution of normal contact stresses within it. Variation between tangential tractions is also vast, significantly altering the location and magnitude of predicted slip and adhesion within the contact patch. This is a very important characteristic with regards to developing a combined tool for long-term S&C damage accumulation. Combining material degradation models within a single tool requires inputs of an accuracy equivalent to those available from existing state-of-the-art techniques, such as the finite element method. This has been demonstrated with validation against an equivalent finite element model. Additional accuracy improvements are also possible by considering more realistic means of applying the boundary conditions within the discrete 2.5D BEM solutions.

The 2.5D BEM approach successfully combines all three critical stages of the wheel-rail contact problem, including:

1. the geometric problem of contact point detection
2. detailed stress analysis for non-Hertzian contact patches
3. accurate wear prediction

The 2.5D BEM model removes the manual interfaces as currently required within existing state-of-the-art wheel-rail damage simulations processes. In addition to this, the ability to model internal body inertia, plastic strain accumulation and sub-surface cracks (not considered as part of this thesis), all within the same contact model, leads to a versatile tool capable of simulating all of the major modes of degradation associated with S&C.

Due to the current development state of the 2.5D BEM code, it was decided at an early stage that a parallel model using an established FE code would be investigated to complement the research presented within Chapter 6. Chapter 7, therefore, illustrated a fully three-dimensional, dynamic, elastic-plastic finite element model of a railway wheel passing through a cast manganese crossing.

Cast crossings were also chosen due to real engineering problems, associated with asset degradation, being identified by senior Network Rail S&C engineers.

Further work is required to fully realise the benefits of the 2.5D BEM approach. It is therefore strongly advised that the suggestions presented within *Chapter 8* are considered.

Chapter 7 : Dynamic wheel to crossing interaction modelling

Chapters 3 to 6 demonstrate the development of a novel tool capable of modelling wheel-rail interaction at railway switches and crossings. Chapter 6 concludes by demonstrating the possibility of including plastic deformation modelling within the 2.5D BEM solution. In parallel with developing such an in-house tool, a secondary approach to predicting damage due to plastic deformation has been developing using the commercially available finite element package Abaqus. A wide range of parameters are studied to give an indication of how such variations affect both dynamic contact forces and material performance (plastic strain accumulation). A wide range of conclusions are drawn before presenting some recommendations for potential asset improvement.

7.1 Introduction

Crossings are critical track infrastructure assets that provide operational flexibility to the rail network by allowing the flange of the wheel to pass through an adjacent running rail. Wheel-rail interaction at crossings is very different to that of plain line rail. Discontinuities in the running rail, as illustrated within Figure 7-1, cause high impact forces as the wheel transfers from wing rail to crossing nose (facing move) and also from crossing nose to wing rail (trailing move).

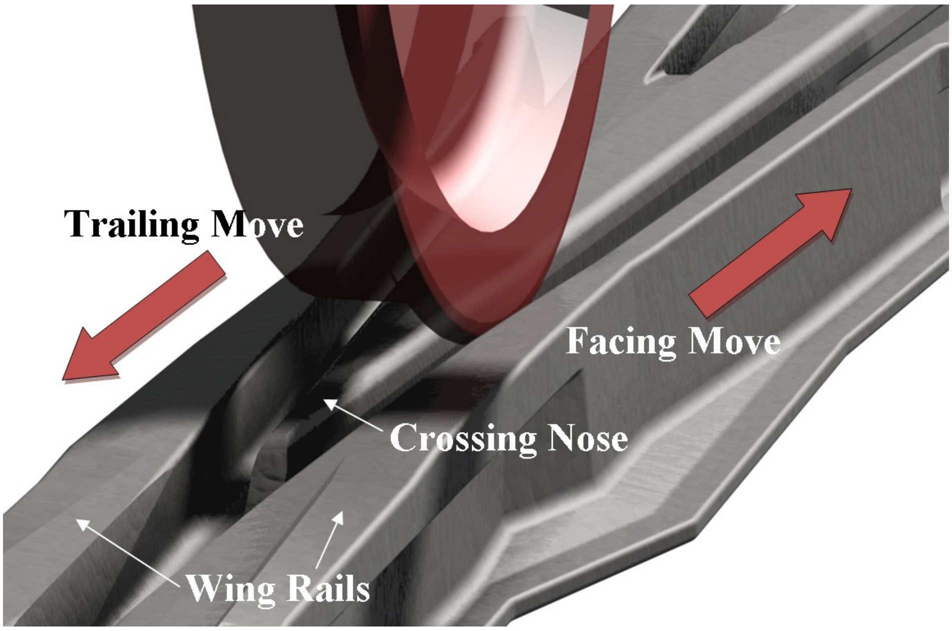

Figure 7-1: Picture of a railway wheel traversing a crossing

Such dynamic impacts generate amplified wheel-rail contact stresses and rapid onset of plastic deformation and work hardening of the contact surfaces. Multi-point contact also occurs within the wing rail / crossing nose transition region, which affects the rolling radius difference and hence slip and resulting wear damage at the rail surface. Over the last decade, the UK rail industry has also experience unprecedented rates of growth and hence an increasing demand on the infrastructure assets. Crossings, as with all other track assets, are experiencing higher axle loads, increased vehicle speeds and greater frequency of use. The combination of complex wheel-rail interaction and an ever increasing demand inevitably results in a negative impact on the maintenance requirements of cast crossings.

To date, the development of UK cast Manganese crossings has been one of design evolution and contact geometry optimisation with regards to providing a smooth transition between the wing rail and crossing nose. Early UK wheel-crossing nose trajectory and impact force studies were published by British Rail [124-126] where it was discussed that the dynamic effects observed were worse for vehicles with high unsprung mass. Despite these early studies, there have been no attempts to study UK crossing designs using explicit finite element techniques whereby the material response is also considered as a significant output. Kassa et al. [20,26,127,128] have presented the use of multi-body simulation (MBS) tools for assessing wheel-rail interaction and damage prediction. Most recently, Pletz presented a finite element model of a wheel passing through a standard Austrian design 1:15 crossing [85,86]. Although similar in nature to the model developed within this PhD research, there are some significant and noteworthy differences relating to the geometry, setup and key assumptions made. Pletz presented a model consisting of the wing to crossing nose transition region and assumed the vehicle was travelling along the diverging route, running with the opposite wheel hard up against the check rail. It was also assumed that the transition from plain line rail into the crossing had no or little affect on the dynamics of the system. The full effects of the vehicle's primary suspension were also neglected, with the entire wheel load being applied as unsprung mass (*i.e.* all mass below primary vehicle suspension) at the axle centre. It is reasonable to assume that the dynamic impact force would be somewhat affected by excluding the primary suspension due to the independent accelerations associated with the sprung and unsprung masses. UK track access charges are also related to the unsprung mass of the vehicle and hence it is deemed necessary to separate the sprung and unsprung masses within this study. Vehicle speed also influences the magnitude of vertical impact force; therefore, it was decided to study the through route within this PhD research. The operational speed on the diverging route of a UK crossing is limited by the maximum turnout speed, which for a 1:10.75 crossing is 40mph.

To complement the work already completed with regards to wheel-rail interaction and wear predictions using a novel BEM approach, *Chapter 7* demonstrates an explicit finite element model developed for studying dynamic wheel to crossing interactions and, in particular, the resulting impact loading and onset of plastic strain accumulation.

7.2 Finite Element Modelling

To assess in detail the complex interaction between a railway wheel and crossing, the contact patch must be adequately represented to provide a realistic non-Hertzian contact stress solution. Dynamic effects, such as impacts due to system inertia, are also essential if the simulation is to accurately obtain the forces generated during the wheels passage through the crossing. One such engineering tool that is readily available for such analyses is the Finite Element (FE) method.

There are two different approaches for solving FE problems based on the type of analysis being performed; Implicit or Explicit solution methods. The implicit method aims to solve linear simultaneous equations using a direct solution approach. Using a relatively large time increment, Δt, the implicit method seeks to satisfy dynamic equilibrium at time equal to $t + \Delta t$, solving for the nodal accelerations and hence displacements through integration. Being unconditionally stable, relatively large time increments can be used but computational costs of solving nonlinear problems can be high. When non-linearity is introduced, Newton iterations are used to solve displacement corrections for each incremental displacement. The solution of a set of simultaneous equations is required at each time step making the implicit method very expensive for large, complex models. A quadratic convergence rate is achieved for smooth, continuous nonlinear problems but is lost when discontinuous processes, such as elastic-plastic contacts, are present. Within such models, much iteration may be required, resulting in a necessary reduction in the time increment to achieve solution convergence.

In comparison, the explicit method solves for the nodal accelerations but does not rely upon solving complete sets of simultaneous equations. The equations of motion are solved explicitly through time using the previous time step kinematic conditions to directly obtain those at the next. The accelerations at each node are obtained through assessing directly its mass and the net force acting upon it. Accelerations are then integrated through time to obtain the change in nodal velocities and displacements, which are in turn added to the original, respective quantities from the previous time increment. By satisfying dynamic equilibrium at the beginning of the process, the accelerations, velocities and displacements can be progressed forward in time ‘explicitly’. The explicit method therefore also allows dynamic analysis of body inertias and hence assessment of impact, which becomes important when considering wheel to rail interaction, especially when dealing with railway crossings.

An explicit solver, within the software package Abaqus, was therefore chosen to study wheel to crossing interaction due to:

1. Contact and elastic-plastic material response representing significant system non-linearity
2. System velocity and inertia modelled, enabling impact analysis at crossing nose

To assess the performance of cast crossings with respect to dynamic wheel-rail interaction and material degradation, an explicit finite element (FE) model has been developed to enable the following major parameters to be studied:

1. Vehicle speed
2. Axle load (Sprung and unsprung mass)
3. Wheel profile
4. Direction of travel
5. Track foundation stiffness
6. Crossing material

7.2.1 Model Setup

The primary focus of *Chapter 7* is to investigate the performance of a UK cast Manganese crossing with respect to dynamic impact forces and plastic deformation. The following sections provide a detailed description of how the dynamic FE model has been built in order to achieve this goal.

7.2.1.1 Assumptions

The following assumptions have been taken when generating the dynamic wheel to crossing interaction model:

1. Steering effects are neglected and the lateral wheel trajectory remains fixed at the nominal position (*i.e.* wheelset and track centre-lines coincide). This assumes that the vehicle is travelling along the through route of the crossing and hence justifies simulation of velocities of up to 100mph.

2. The coefficient of friction remains constant and it is assumed that dry, clean contact conditions are present. This is due to modelling an 'as new' crossing (*i.e.* $\mu = 0.3$ [129]).

3. The track foundation stiffness remains constant beneath the entire crossing (i.e. no variation between individual crossing bearers).

4. The wheel is modelled using elastic material properties.

7.2.1.2 Geometry and Interactions

The geometry used within this study is that of a new UK 1:10.75 cast Manganese crossing, which was provided by the crossing manufacturer (Progress Rail) and is illustrated within Figure 7-2 *(b)*. The description '1:10.75' refers to the crossing angle, which can range from between 1:6 (tight crossing angle) down to 1:32 (shallow crossing angle) depending on the requirements of the track layout.

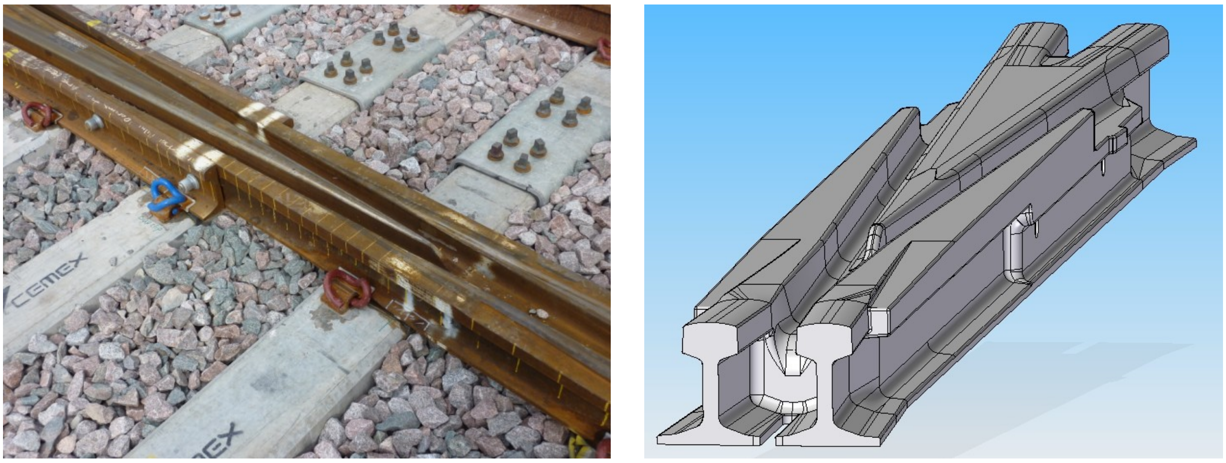
(a) *(b)*

Figure 7-2: A new 1:10.75 cast Manganese crossing (a) and an equivalent CAD model as provided by crossing manufacturer (b).

Both frictional rolling contact analysis and elastic-plastic material properties introduce significant non-linearity to the problem, therefore a number of model simplifications were first required to generate a realistic yet computationally efficient solution. The original CAD model has been adapted to provide only the contact surfaces and to also remove any complex features that would otherwise cause problems during FE mesh generation process. Figure 7-3 provides a complete system schematic *(a)* and the resulting FE geometry and interactions *(b)*. The final model consists of the crossing contact surfaces, the left wheel and the track foundation and the vehicle primary suspension spring/damper systems. The primary suspension has been included to enable the effect of both the sprung and unsprung mass on the performance of cast Manganese crossings to be investigated. To account for the loss of mass due to model simplification, additional mass nodes are also included for the crossing (additional crossing mass), the wheelset (unsprung mass) and vehicle (sprung mass). The additional damper node provides a temporary damping element to remove any unrealistic contact oscillations generated when bringing the wheel into initial contact with the rail.

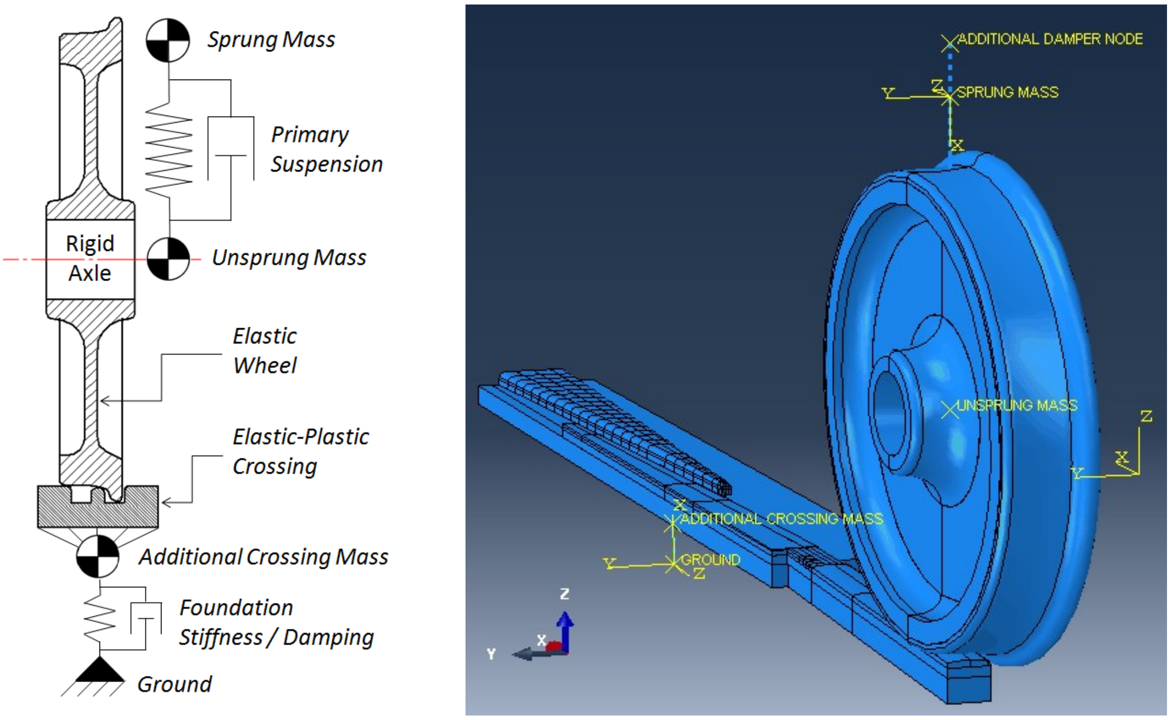

(a) (b)

Figure 7-3: Schematic diagram of dynamic wheel-crossing model and actual geometry.

7.2.1.3 Meshing

An important part of any FE model is the quality of the mesh used to adequately represent the problem geometry whilst providing the best compromise between solution accuracy and computational efficiency. A mesh convergence study was initially completed to determine an acceptable mesh size suitable for this study. Mesh convergence was checked for each of the significant outputs required from the model. Convergence results, presented within Figure 7-4, indicate that a sub-millimetre mesh size provides a good compromise between accuracy and computational efficiency. This is also reflected within the plastic strain accumulation results as they do not begin to settle (converge) until within the sub-millimetre mesh region.

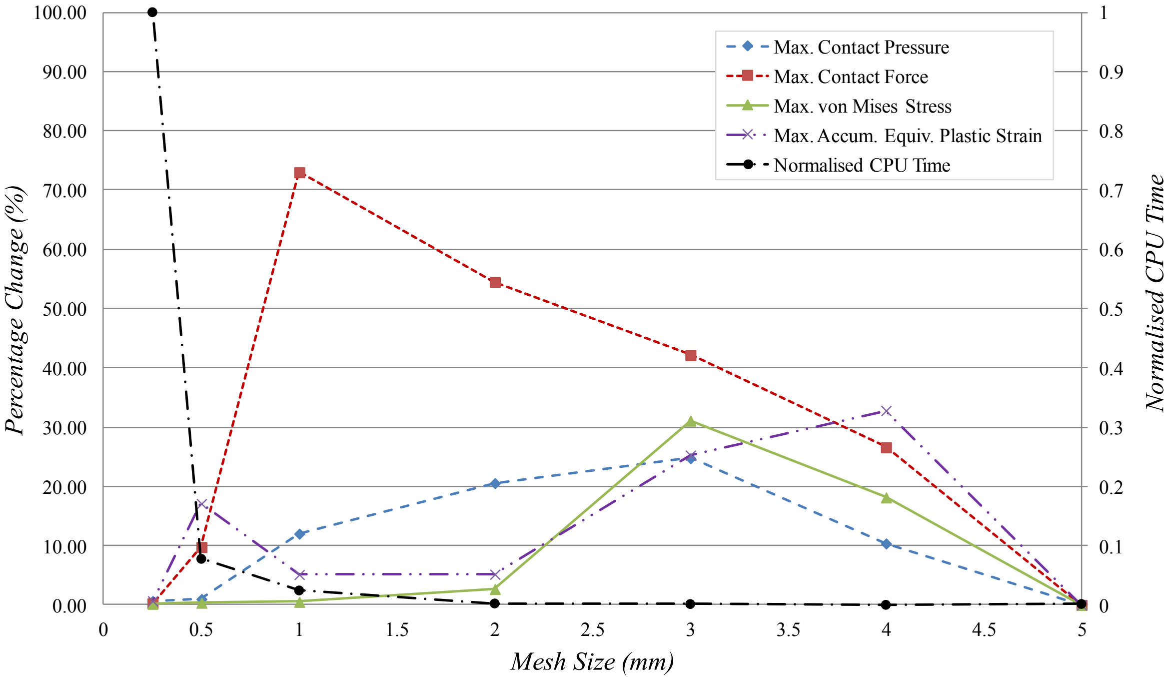

Figure 7-4: Wheel-rail mesh convergence chart.

Figure 7-5 *(a)* shows the entire domain mesh whilst *(b)* and *(c)* provide a magnified illustration of the refined mesh, approximately 0.5 mm in size, used within all of the geometrically complex crossings contact surface regions. The wheel geometry has also been generated from CAD and is modelled as a purely elastic body. To ensure that the general shape of the wheel profile is maintained, the tread surface has been modelled independently and contains a refined mesh of approximately 0.75 mm, illustrated within Figure 7-6 *(b)*. The mesh gradient here is fairly steep and would usually result in slight inaccuracies within the stress results. As the results within the wheel are of no importance within this study, the mesh gradient within the wheel was not considered to be important. To assist computational efficiency, element sizes within the remaining sections of the model are chosen to be as large as possible without invalidating the model geometry. A rigid axle is used to provide a location for assigning the linear and rotational velocity boundary conditions and loads and is coupled to the hub centre using tie constraints. The primary suspension is then modelled using a spring/damper connection between the sprung and unsprung mass nodes. A similar procedure is used to simulate the track foundation support conditions by assigning a spring/damper connection between the additional crossing mass node and the ground.

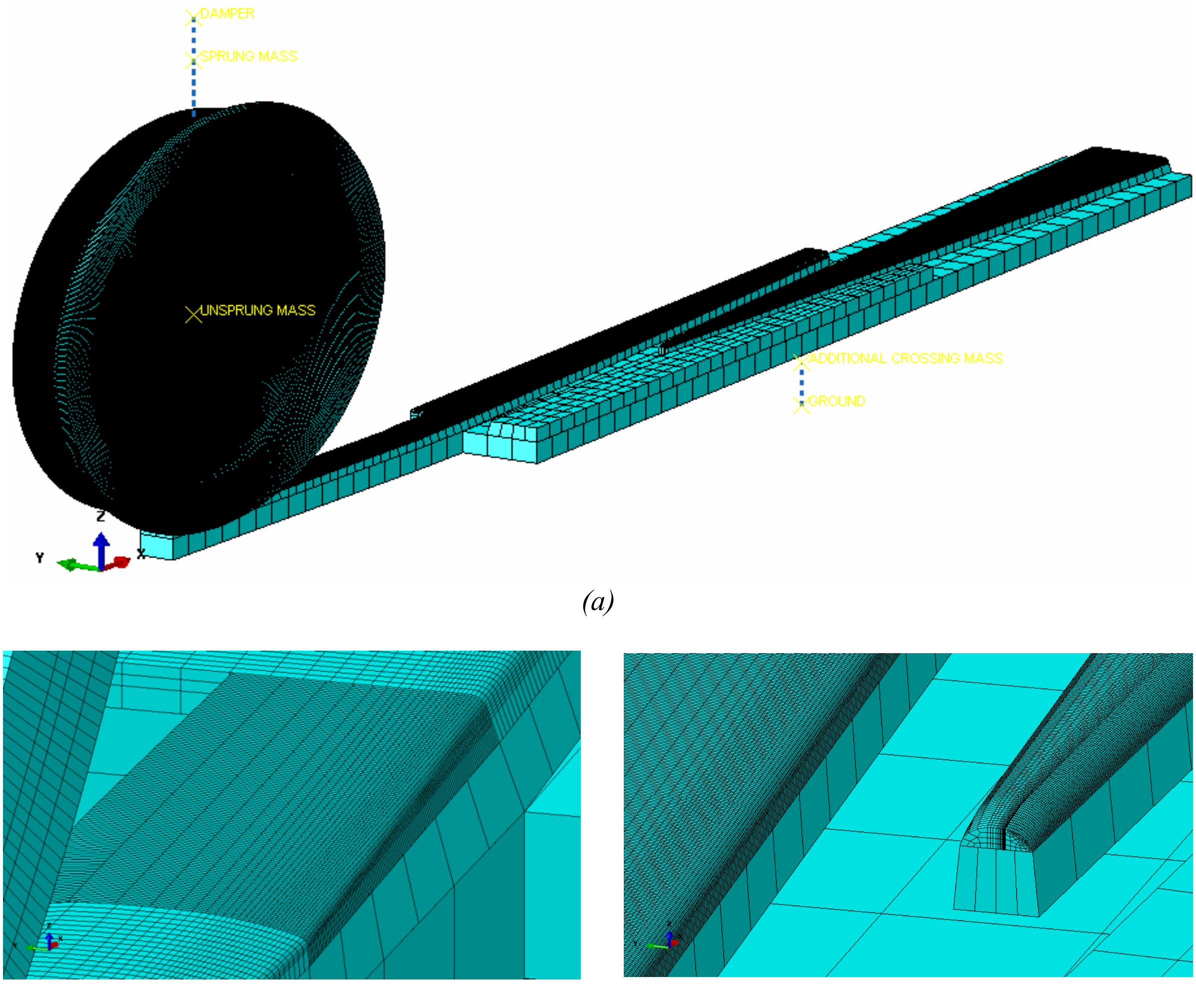

(a)

(b) (c)

Figure 7-5: Entire model mesh (a), plain line to wing rail transition region (b) and wing rail to crossing nose transition region (c)

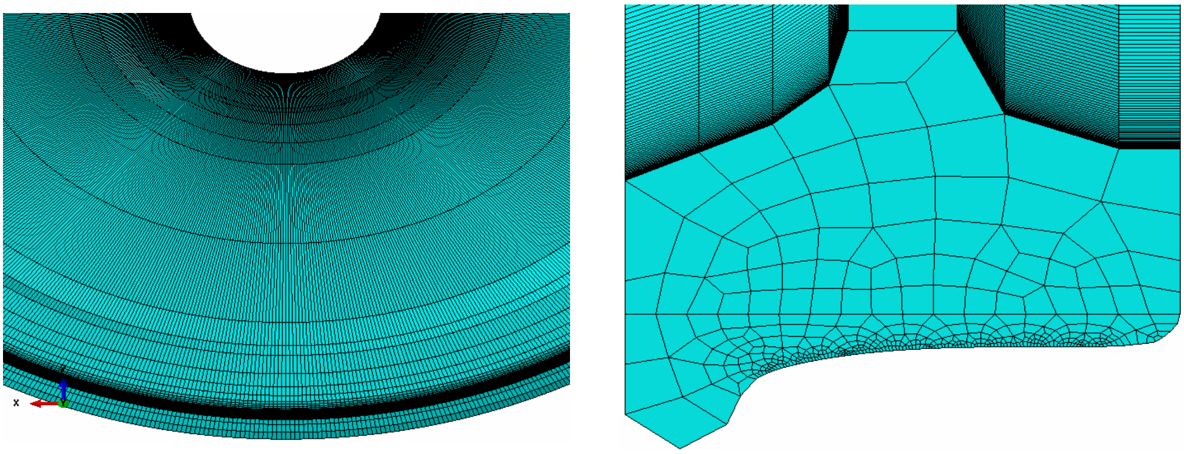

(a) (b)

Figure 7-6: Illustration of the circumferential (a) and internal (b) wheel mesh

7.3 Case studies

A total of 16 different case studies have been completed to provide a comprehensive investigation into parameters that may affect the performance of a UK 1:10.75 cast Manganese crossing. The variable parameters for each study are identified within Table 7-1.

#	**Velocity**	**Vehicle Sprung Mass**	**Wheelset Unsprung Mass**	**Direction of Travel**	**Wheel Profile**	**Foundation Stiffness**	**Crossing Material**
	(mph)	*(t)*	*(t)*	*Facing (F); Trailing (T)*	-	*N/mm*	-
1	100	66.25	1.00	F	Worn P8	160000	Mn13
2*	75	66.25	1.00	F	Worn P8	160000	Mn13
3	50	66.25	1.00	F	Worn P8	160000	Mn13
4	75	90.00	1.50	F	Worn P8	160000	Mn13
5	75	66.25	1.00	T	Worn P8	160000	Mn13
6	75	90.00	1.50	T	Worn P8	160000	Mn13
7	75	66.25	1.00	F	Nominal P8	160000	Mn13
8	75	66.25	1.00	F	Nominal P1	160000	Mn13
9	75	66.25	1.00	F	Hollow P8	160000	Mn13
10	75	66.25	1.00	F	Worn P8	100000	Mn13
11	75	66.25	1.00	F	Worn P8	200000	Mn13
12	75	66.25	1.00	F	Worn P8	160000	Mn13 + 200%
13	75	66.25	1.00	F	Worn P8	160000	Mn13 + 300%
14	75	66.25	1.00	F	Worn P8	160000	Mn13 + 400%
15	75	66.25	1.00	F	Worn P8	160000	Hybrid
16	75	66.25	1.00	T	Worn P8	160000	Hybrid

🟥 ** Reference state*
🟩 *Altered parameter with respect to reference state*

Table 7-1: Dynamic Wheel-Crossing FEA Case Studies.

Case study 2 has been chosen as the reference state for comparison with other case studies due to a vehicle speed of 75mph being a compromise between higher speed passenger and lower speed freight vehicles. In June 2012, a field investigation concerning wheel-rail interaction through UK cast manganese crossing, at 75mph, was completed by Hsu [130]. It was therefore considered that these results may also prove valuable for further validation of the dynamic FE model within this study. The FE solution time is also linked to vehicle speed; therefore, 75mph provides a compromise between the most (100mph) and least (50mph) efficient simulated scenarios.

Table 7-2 provides an overview of the 6 major parametric investigations covered by the 16 different case studies.

Case Studies	Parameter Investigation
1, 2 & 3	Vehicle Speed
4	Axle Load
5 & 6	Direction of Travel
7, 8 & 9	Wheel Profile
10 & 11	Track Foundation Stiffness
12, 13, 14, 15 & 16	Crossing Material Properties

Table 7-2: Summary of key parameter investigations.

7.3.1 Wheel profiles

To cover a range of wheel profiles that the 1:10.75 cast Manganese crossing is likely to see, four independent wheel models have been generated. The profiles used on each of these models are presented within Figure 7-7 and include:

1. Worn P8 profile measured from a vehicle having travelled 241,000 miles. This is representative of a typical passenger wheel profile.

2. Nominal P8 profile generated from engineering drawings provided by Network Rail. This will provide a comparison of new and old wheel profiles.

3. Nominal P1 profile generated from engineering drawings provided by Network Rail. This is a common freight wheel profile and will provide a comparison with the P8 profiles.

4. Hollow P8 profile measured from a heavily worn passenger wheel. Hollow wheels are not uncommon therefore it was deemed necessary to investigate their effect when compared with worn and nominal profiles.

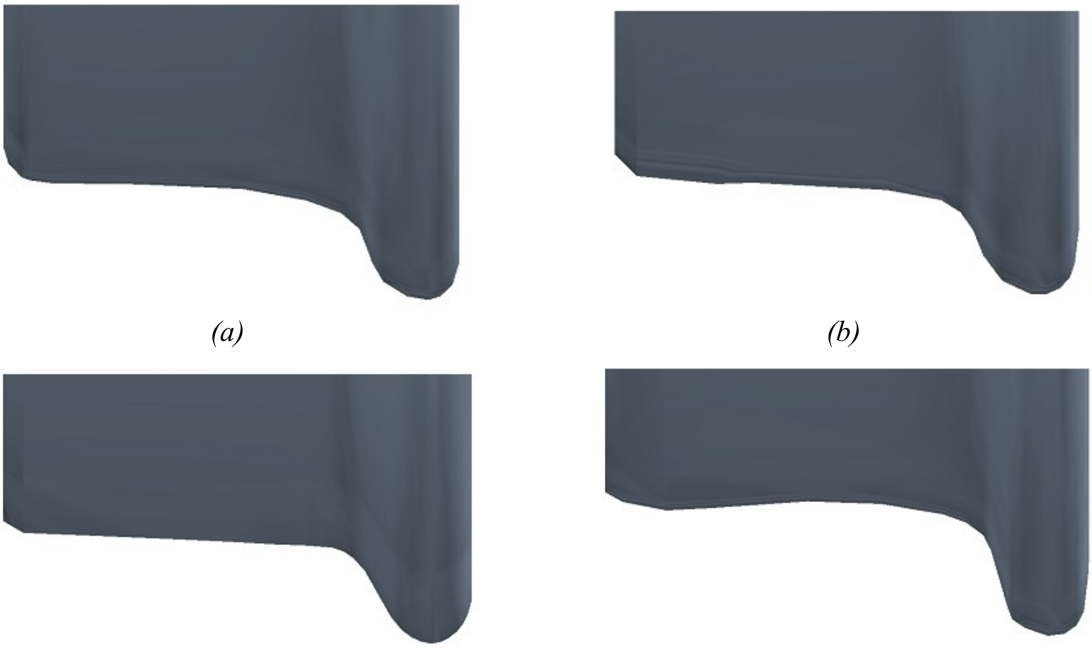

(a) (b)

(c) (d)

Figure 7-7: Worn P8 (a), Nominal P8 (b), Nominal P1 (c) and a Hollow P8 (d).

7.3.2 Material Properties

To model impact loading, contact stress distribution and plastic deformations throughout the crossing, accurate material properties of the cast Manganese steel (Mn13) were required. Results from a compression test of a Mn13 sample were provided by the crossing manufacturer and used to generate a realistic stress/strain curve for use within the FE model. The stress/strain relationship for Mn13 is shown in Figure 7-8 along with some modified curves used for investigating the influence of crossing material. These modified curves were manually generated due to the data for alternative crossing materials being unavailable. The hybrid material properties, as indicated within case studies 15 and 16, refer to using Mn13 for the wing rails and Mn13*400% for the crossing nose. This case study was generated due to recent advances in crossing design whereby the crossing nose is hardened, giving a yield strength of approximately 1200 - 1300MPa [131].

The general material properties used are presented within Table 7-3. The Young's modulus for Mn13 has been calculated using the data obtained from manufactures compression test data whereas the data for R8T wheel material was taken from [132]. It should be noted that the units presented are those consistent with the units used within the FE model (*i.e.* the length scale used to generate the FE geometry is in mm).

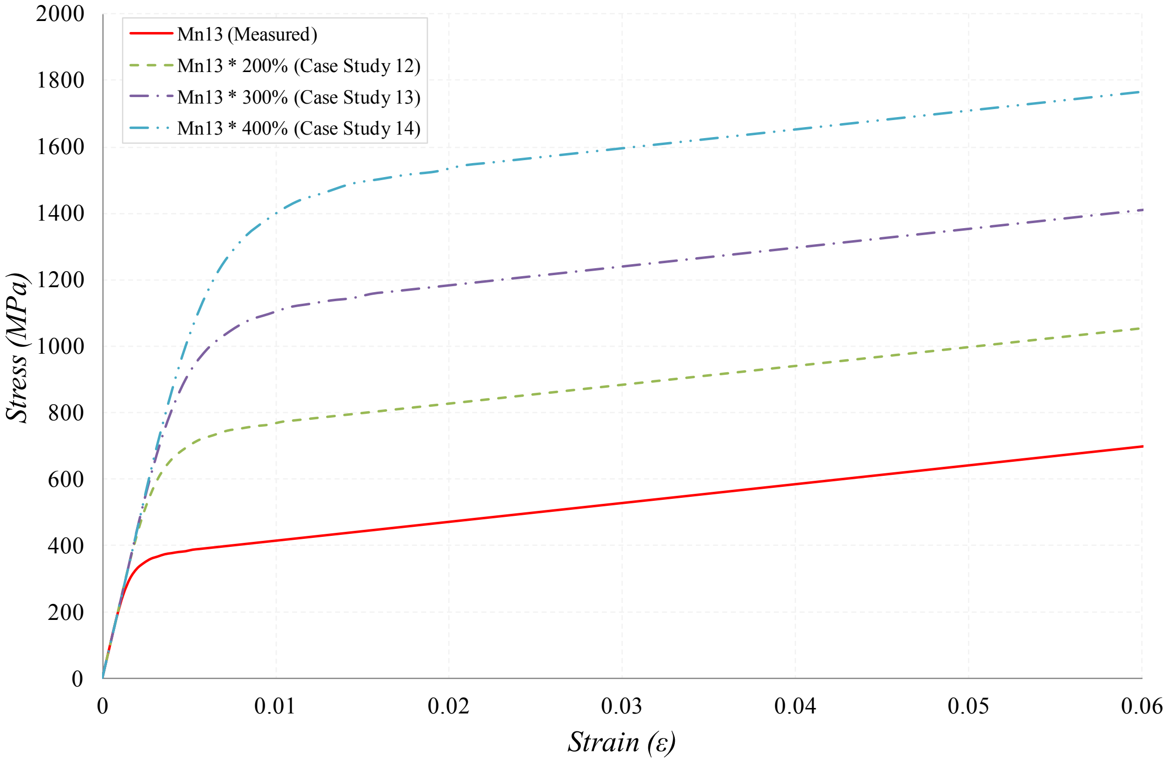

Figure 7-8: Stress/strain curves used for the crossing material properties.

Material	Component	Young’s Modulus	Poisson’s Ratio	Density	Yield Strength
Mn13	Crossing	1.90772e^5 MPa	0.3	7.433e-9 t/mm^3	310 MPa
R8T	Wheel	2.01000e^5 MPa	0.3	7.833e-9 t/mm^3	- *Elastic* -

Table 7-3: General material properties for within the dynamic FE model.

7.4 Comparison with railway vehicle dynamics multi-body simulation

Quantitative validation of dynamic wheel-rail contact models is a very difficult task. One common approach is to use a load measuring wheelset, which is instrumented with strain gauges to capture lateral, longitudinal and vertical contact forces at the wheel-rail interface. Unfortunately, this technology is yet to be introduced within the UK rail industry therefore an alternative approach to assessing the dynamic FE model was sought. Due to experimental validation being unavailable, a theoretical approach has been taken to compare the vertical contact forces with an already established railway vehicle dynamics multi-body simulation (MBS) software package, Vampire®. The MBS model shares the same basic parameters as discussed within section 7.2.1, above, and matches as closely as possible the load case parameters for the case study 2 within Table 7-1. Two-dimensional rail profiles were extracted from CAD drawings of the 1:10.75 cast manganese crossing model used within the dynamic FE study. Profiles were taken every 50 mm through the entire crossing.

Figure 7-9 demonstrates a good comparison between the dynamic FE model and MBS with regards to the location and magnitude of vertical contact forces through the crossing. Both techniques also simulate the loss of contact immediately after the plain line to wing rail transition region and then again after transitioning from the wing rail to crossing nose. The dynamic FE model predicts a somewhat larger impact prior to the first loss of contact. This is a direct result of Vampire linearly interpolating between longitudinal rail profiles (achieved by interpolating a pre-populated contact data table), simulating a smoother, less realistic transition. On the other hand, the dynamic FE model uses the exact crossing geometry throughout the entire simulation and hence models the correct contact conditions at all times. The non-linear geometry of the first transition region creates an artificial ramp, which the wheel first drops onto and then climbs after initial impact is made. Vampire does not fully capture this and hence predicts a smaller dynamic vertical contact force. This also explains the a shorter duration of contact loss and also a slightly reduced secondary impact as the wheel regains contact further down the wing rail. The location and magnitude of the maximum vertical contact force on the crossing nose is also comparable at 100 mm (188.18 kN) and 137 mm (171.42 kN) from the dynamic FE and MBS models, respectively. The MBS model also captures a higher frequency, short duration load, immediately after initial impact, at 142.50 mm (543.89 kN), which is not predicted by the dynamic FE model. These variations in contact results are attributed to both the differences in boundary conditions and limitations of each technique. Dynamically, the MBS model provides additional degrees of freedom by allowing the wheelset to move laterally but is limited by the accuracy of the contact geometry and the simple contact detection model (*i.e.* only capable of predicting one contact point). The dynamic FE model is capable of maintaining two-point contact during transition of the wheel from wing rail to crossing nose, which is evident between approximately 0.0 m and 0.1 m within Figure 7-9 *(a)*. In contrast, Vampire is only capable of maintaining a single point of contact, therefore transferring the entire dynamic load immediately onto the crossing nose. The transition of load between the wing rail and crossing nose cannot be easily identified using the vertical contact forces predicted by Vampire, illustrated within Figure 7-9 *(b)*. The static wheel load is clearly observed either side of the crossing geometry within both models and settles at approximately 1 m past the crossing nose. Vampire also simulates a rigid track foundation therefore the foundation elasticity modelled within the dynamic FE model would also contribute to explaining the minor variations between results. Another important difference between simulation techniques is the accuracy of the contact patch prediction. The dynamic FE model is capable of accurately simulating the shape, size and location of the contact patch (and indeed multiple contact points) whilst Vampire relies solely upon the simplified theory of Hertzian elliptic contact. This difference would also contribute to small variations between the results presented in Figure 7-9.

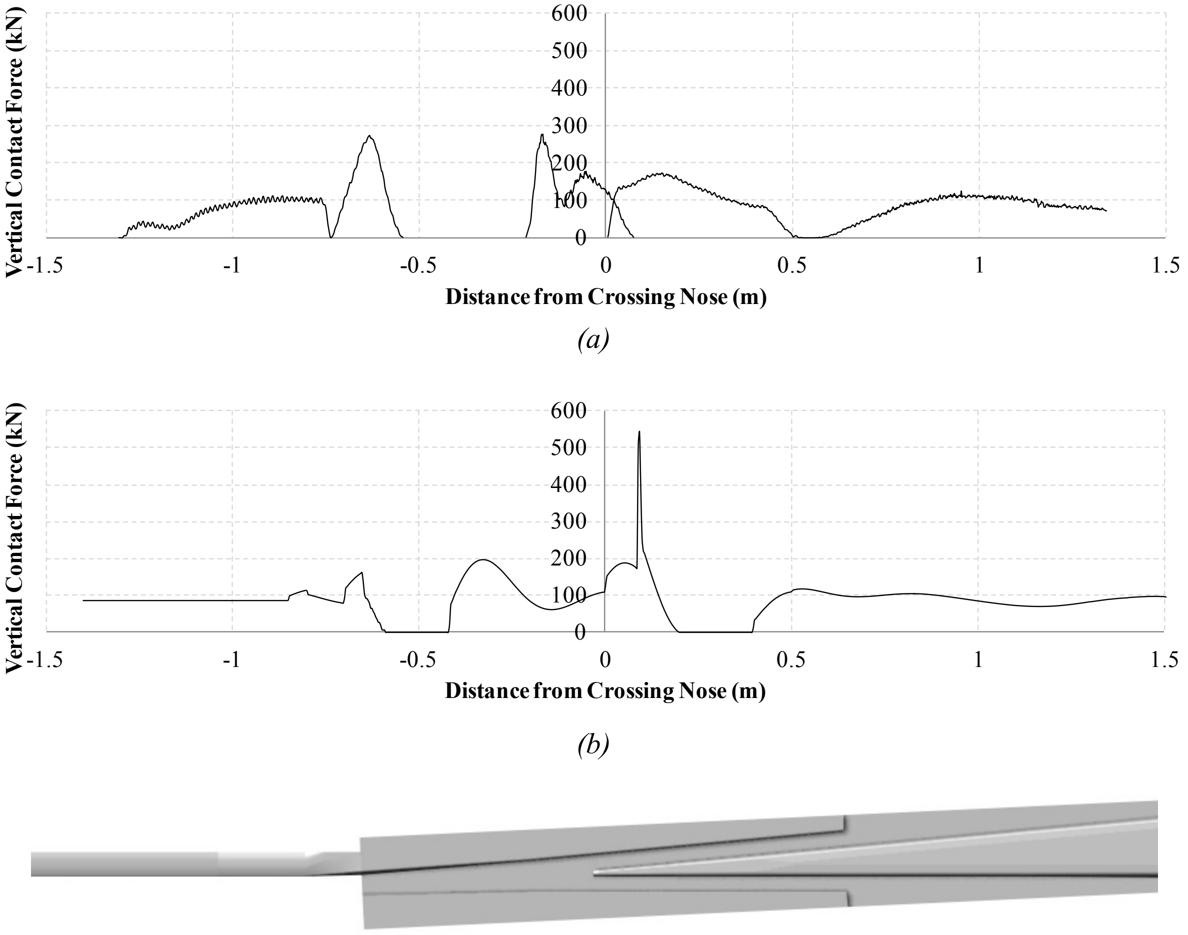

(a)

(b)

(c)

Figure 7-9: Vertical contact forces for a worn P8 wheel profile traversing a 1:10.75 cast manganese crossing. Results obtained from the dynamic FE model (a) and a VAMPIRE railway vehicle dynamics analysis (b).

To demonstrate that loss of contact through railway crossings is indeed an actual phenomenon, Figure 7-10 illustrates a similar occurrence observed by Network Rail S&C engineers on at 1:6 crossing at Shalford junction [130] with a vehicle speed of 70mph. The duration of contact loss experienced equated to $7\text{x}10^{-4}$ s over 22.00 mm, compared to $9\text{x}10^{-4}$ s over 28.49 mm as predicted by the dynamic FE model. This gives further confidence that, even with the imposed assumptions, the technique is indeed feasible with regards to accurately capturing complex contact phenomena during wheel to crossing interaction.

Figure 7-10: Loss of contact observed on a 1:6 crossing at Shalford Junction.

The dynamic FE model therefore compares well with existing modelling techniques and phenomena observed out in the field. In order to validate both the FE and MBS models, experimental measurements of wheel-rail contact forces through an as new 1:10.75 cast manganese crossing should be obtained. This will further improve both model validations whilst also enabling it to be calibrated against real contact conditions.

7.5 Results and Discussion

To visualise the significant results from each case study together, the maximum impact force and accumulated equivalent plastic strain (PEEQ) have been plotted in **Error! Reference source not found.**. Within this model, PEEQ values equate to the plastic strain accumulated during a single pass of the wheel (*i.e.* initial strain rate). Plastic deformation in the form of ratchetting (see *section 2.3.2*) is therefore not the focus of this study but should be considered as further work.

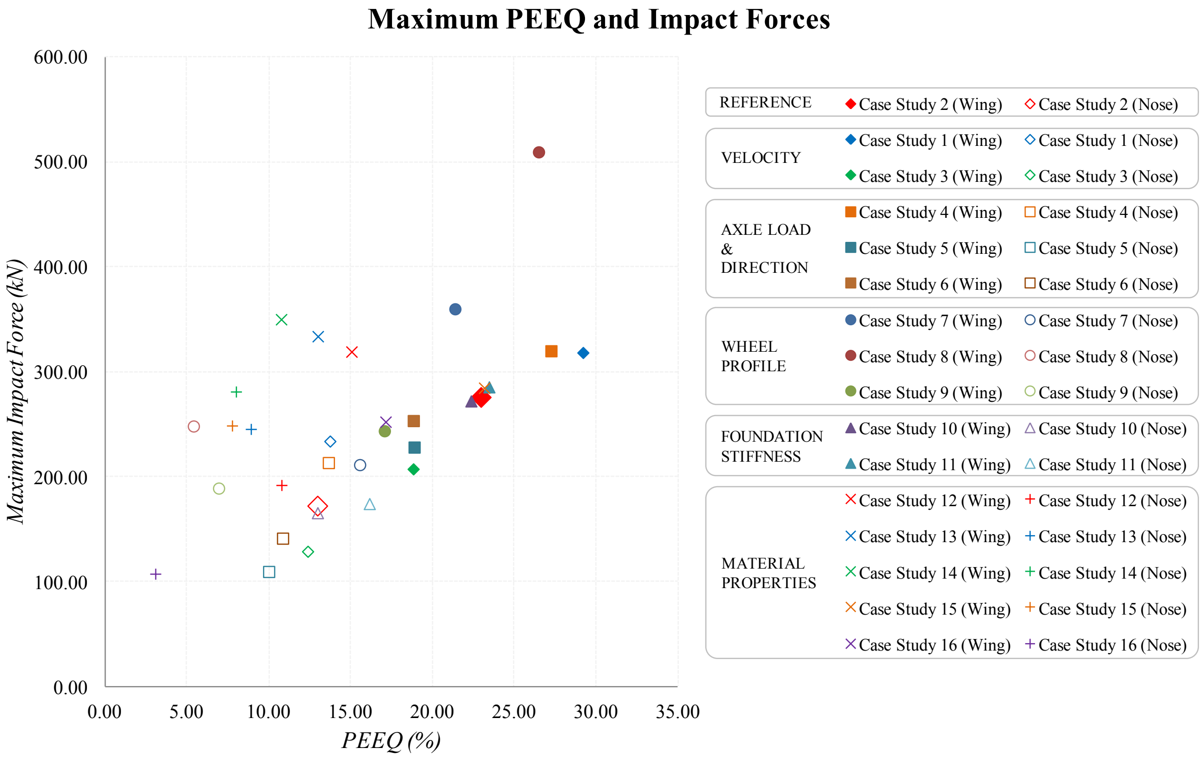

Figure 7-11: Summary of all case study maximum impact forces and accumulated equivalent plastic strains.

As a high level summary of results, the following conclusions are drawn:

1. The peak vertical forces obtained for each case study are those occurring at the transition from plain line rail into the wing rail of the crossing. This is against conventional thinking, whereby significant effort has gone into the optimisation of the wing rail to crossing nose geometry, possibly neglecting the plain line to wing rail transition region.
2. Peak vertical force and PEEQ are both directly related to vehicle speed.

3. Increased axle loads result in higher peak vertical forces and PEEQ.
4. The crossing performs favourably in the trailing direction with lower peak vertical forces and PEEQ values for both passenger and freight vehicle configurations.

5. The largest scatter of both peak vertical force and PEEQ arises from variations in wheel profile. A nominal P1 profile generates the most damaging results whilst a heavily worn, hollow P8 wheel profile significantly changes the contact trajectory through the crossing and results in much lower peak forces and PEEQ values.

6. Altering the crossing material increases the peak vertical forces whilst also reducing the amount of plastic deformation.

7.5.1 Dynamic FE vs. Analytical Vertical Peak Force (P_2)

The vertical contact force is an important parameter within the UK rail industry due to its use within numerous infrastructure standards. The UK standard for the cast austenitic manganese crossings, NR/SP/TRK/012 [133], stipulates a number of conditions that the crossing must comply with for use within the UK rail network. The two key requirements associated with this study include:

1. The dip angle associated with wheel transfer shall not exceed 10mrad for the case of a P8 wheel profile with the wheel centred on the approach rail for straight through running.

2. The sustained peak force (also known as P_2 force), occurring within the crossing transfer zone, to be used for fatigue analysis shall be estimated by:

    i. Simulating the wheel trajectory for new wheels with P8 wheel profiles.
    ii. Estimating the associated dip angle (2α), that is the acute angle between the tangents to the wheel trajectory at the point where it abruptly changes direction.
    iii. Calculating the dynamic forces using formula 7-1:

$$P_2 \approx (P_0 + 2\alpha . V\sqrt{(K_t M_u)} . \sqrt{(M_u/(M_u + M_t))}) * 1.2 \qquad \text{7-40}$$

where:

P_2 Peak dynamic force (N)
P_0 Static force (N)

2α	Dip angle (rad)
V	Vehicle speed (mm/s)
K_t	The stiffness of the track spring to be taken as 160MN/mm
M_u	Unsprung mass per wheel (kg)
M_t	Lumped track mass per rail to be taken as 750kg
1.2	Dynamic factor

The Network Rail cast manganese crossing standard also states maximum permissible P_2 forces for a range of vehicle types. There are two vehicle of interest for comparison within this study:

Vehicle type	**Maximum permissible P_2 force**
High-speed train (HST) power cars	266 kN
Modern freight locomotive	223 kN

Table 7-4: Max. permissible P2 forces used for cast manganese crossing fatigue assessment [133].

Figure 7-12 illustrates the process of assessing the dynamic vertical wheel trajectory and extracting the dip angle (2α) required for calculating the analytical peak force due to impact on the crossing nose. It should be noted that the displacements plotted within all subsequent displacement charts are measured, with reference to Figure 7-3 *(a)*, at the unsprung mass (axle centre line) of the wheel and at the additional crossing mass node of the crossing. A positive displacement therefore relates to a vertical lift (or bounce) from the vertical origin. Table 7-5 provides all of the dip angles calculated for each case study along with all other P_2 force calculation parameters. Within this initial study, every case study demonstrates a dip angle lower than the required 10mrad.

A variety of calculation cases are required by the standard therefore, due to simulating just two distinct vehicle types within this study, only the results of significant interest are discussed. The maximum dynamic vertical peak forces obtained from the FE model simulating freight vehicle conditions were both reduced values when compared to the analytical calculation. The one significant result comes from case study 14 where the maximum P2 force of 281.20 kN is 95.88% larger than predicted by the analytical calculation, which also exceeds the maximum permissible P_2 force from the standard. This suggests that the crossing is experiencing significantly larger dynamic loads than those otherwise estimated during the fatigue analysis procedure. Other case studies also predict P_2 forces of between -30.28% and 91.04% different to those obtained analytically, although these results remain within the maximum permissible values. This demonstrates that the contact condition not captured within equation 7-2, such as contact geometries and material properties, have a profound effect on the final contact forces experienced through the crossing. Figure 7-13 also shows that numerous peak vertical forces occur along the crossing as the wheel passes through it. These multiple impact forces would further reduce the fatigue life of such crossings due to increasing the frequency of loading twofold. It is therefore suggested that a comprehensive comparison with current UK crossing standards, using a full range of vehicle parameters and wheel profiles, travelling along both the through and diverging routes, would prove extremely beneficial with regards to supporting crossing design and future maintenance requirements. Further work is recommended and is discussed within section 7.6.

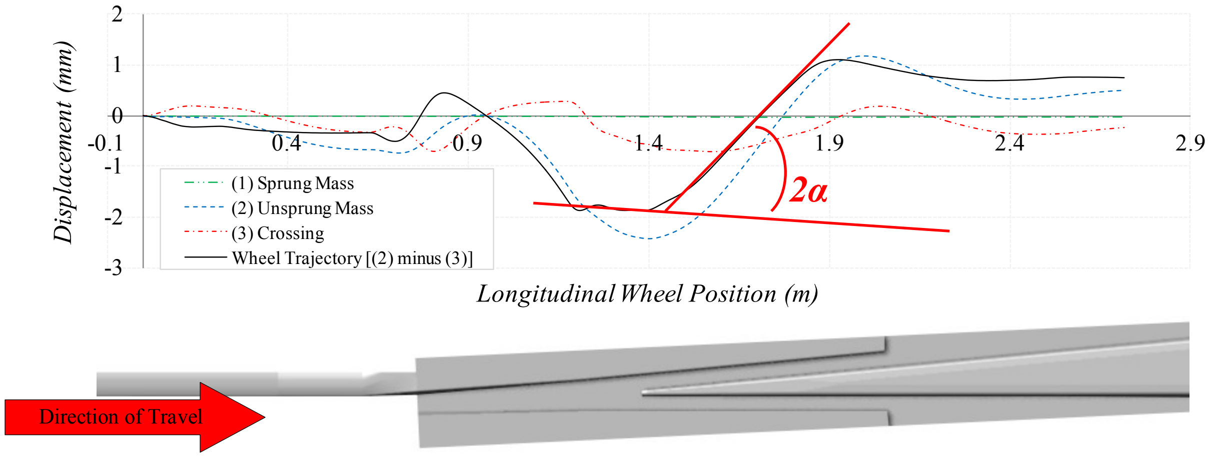

Figure 7-12: Reference case vertical displacements and associated dip angle (2α).

Case Study	Static Wheel Load	Dip Angle	Vehicle Speed	Unsprung Mass	Lumped Track Mass per Rail	Track Stiffness	P2 Force	Dynamic FE Peak Force	% Diff.
-	P_0	2α	V	M_u	M_t	K_t	P_2	P_{FEA}	-
#	*kN*	*mrads*	*mm/s*	*t*	*t*	*N/mm*	*kN*	*kN*	*%*
1	86.14	6.69	44704	1.00	0.75	$1.60e^8$	194.64	234.00	20.22
2	86.14	7.33	33528	1.00	0.75	$1.60e^8$	175.28	172.50	-1.59
3	86.14	5.74	22352	1.00	0.75	$1.60e^8$	132.67	129.00	-2.77
4	117.72	6.51	33528	1.50	0.75	$1.60e^8$	222.52	213.50	-4.05
5	86.14	5.35	33528	1.00	0.75	$1.60e^8$	151.20	109.75	-27.41
6	117.72	5.37	33528	1.50	0.75	$1.60e^8$	204.13	141.50	-30.68
7	86.14	2.02	33528	1.00	0.75	$1.60e^8$	110.74	211.55	91.04
8	86.14	6.25	33528	1.00	0.75	$1.60e^8$	162.12	248.35	53.19
9	86.14	7.11	33528	1.00	0.75	$1.60e^8$	172.62	189.20	9.60
10	86.14	6.83	33528	1.00	0.75	$1.00e^8$	151.85	165.75	9.16
11	86.14	7.57	33528	1.00	0.75	$2.00e^8$	189.14	174.44	-7.77
12	86.14	6.69	33528	1.00	0.75	$1.60e^8$	167.50	192.16	14.72
13	86.14	5.11	33528	1.00	0.75	$1.60e^8$	148.33	245.57	65.55
14	86.14	4.72	33528	1.00	0.75	$1.60e^8$	143.56	281.20	95.88
15	86.14	6.75	33528	1.00	0.75	$1.60e^8$	168.22	248.83	47.92
16	86.14	4.97	33528	1.00	0.75	$1.60e^8$	146.63	107.66	-26.58

Table 7-5: P_2 force calculation and associated parameters extracted from dynamic FE model.

7.5.2 Vehicle speed

Vehicle speed has a distinct effect on the magnitude of the dynamic peak forces observed as the wheel passes through the crossing. Figure 7-13 also demonstrates the significance of the plain line to wing rail transition region with regards to maximum vertical contact force, as also mentioned within *section 7.4*. Loss of contact is predicted immediately before and after the transition at approximately 0.65m and 0.8m respectively, which acts as a ramp by launching the wheel up off of the wing rail. The length of contact loss decreases with decreasing vehicle speed, after which a secondary impact then occurs as the wheel regains contact with the wing rail. This secondary vertical impact force is also consistently larger than those predicted within the wing rail to crossing nose transition, which is perceived to be the region of largest impact, although the crossing nose experiences more sustained loading durations. Further loss of contact is also predicted following initial impact on the crossing nose for vehicle speeds of 100mph and 75mph. No loss of contact is predicted on the crossing nose at 50mph.

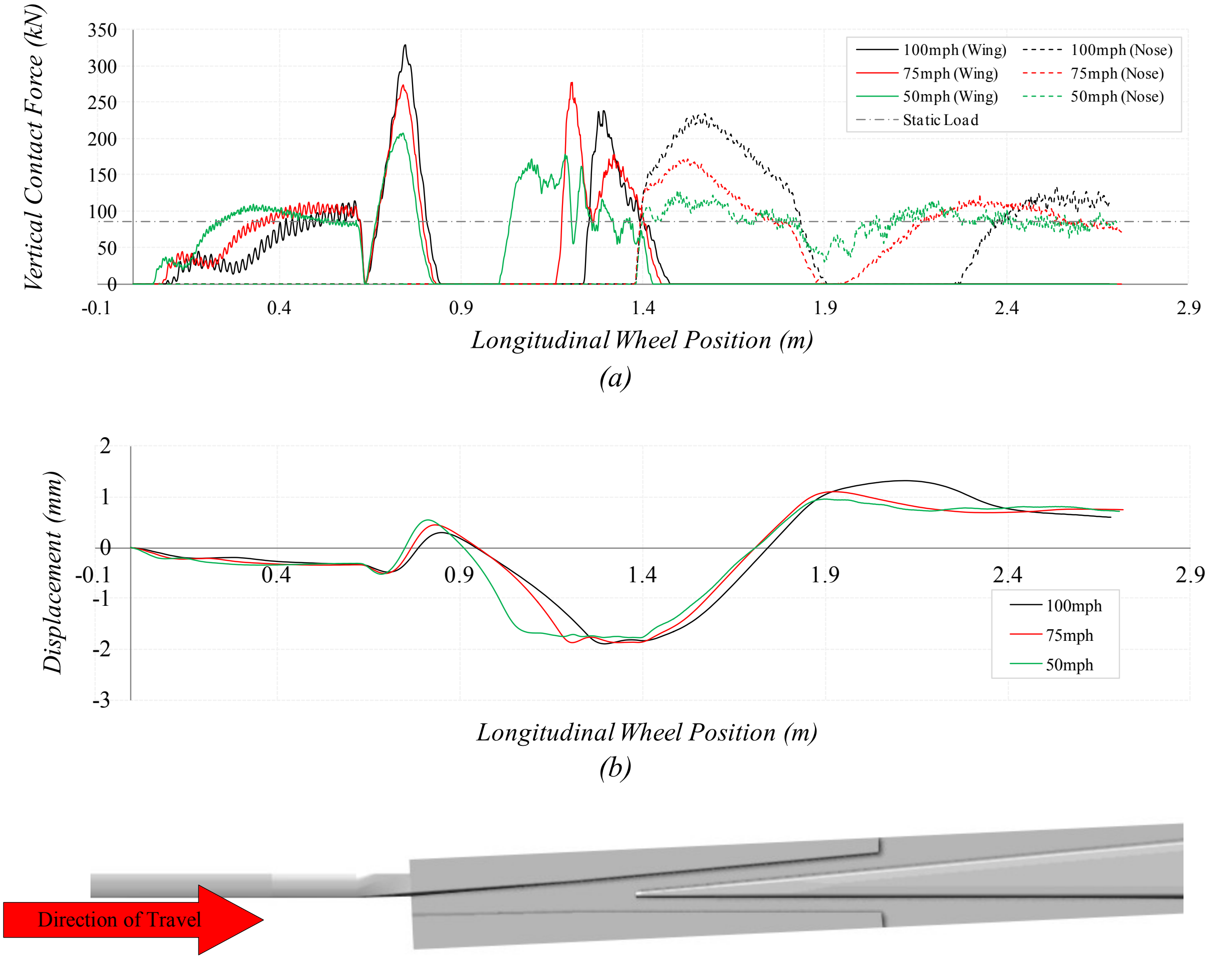

Figure 7-13: Case study 1, 2 & 3 - Vertical Contact Force (a) and Vertical Wheel Trajectory (b).

The onset of plastic deformation (PEEQ) for each load case is presented within Figure 7-14 *(a)* to *(c)*, which follows generally the same trend as observed for the maximum dynamic vertical contact forces. Highly localised PEEQ values, increasing with speed from 18.82 % for 50 mph, 22.95 % for 75 mph and 29.19 % for 100 mph running, are predicted at the end of the plain line to wing rail transition region. These values are significant and suggest that an initial and rapid geometric rail profile change occurs at this location for newly installed crossings. Cast manganese steel is a very soft material that rapidly work-hardens under repeated load. Simulating the ‘as new’ condition therefore represent an initial, worst case scenario whose severity, with regards to both contact forces and material degradation, reduces as the rail profile becomes more conformal to the wheel. Along the crossing nose, maximum PEEQ values reduce to 12.37 % for 50 mph, 12.96 % for 75 mph and 13.73 % for 100 mph.

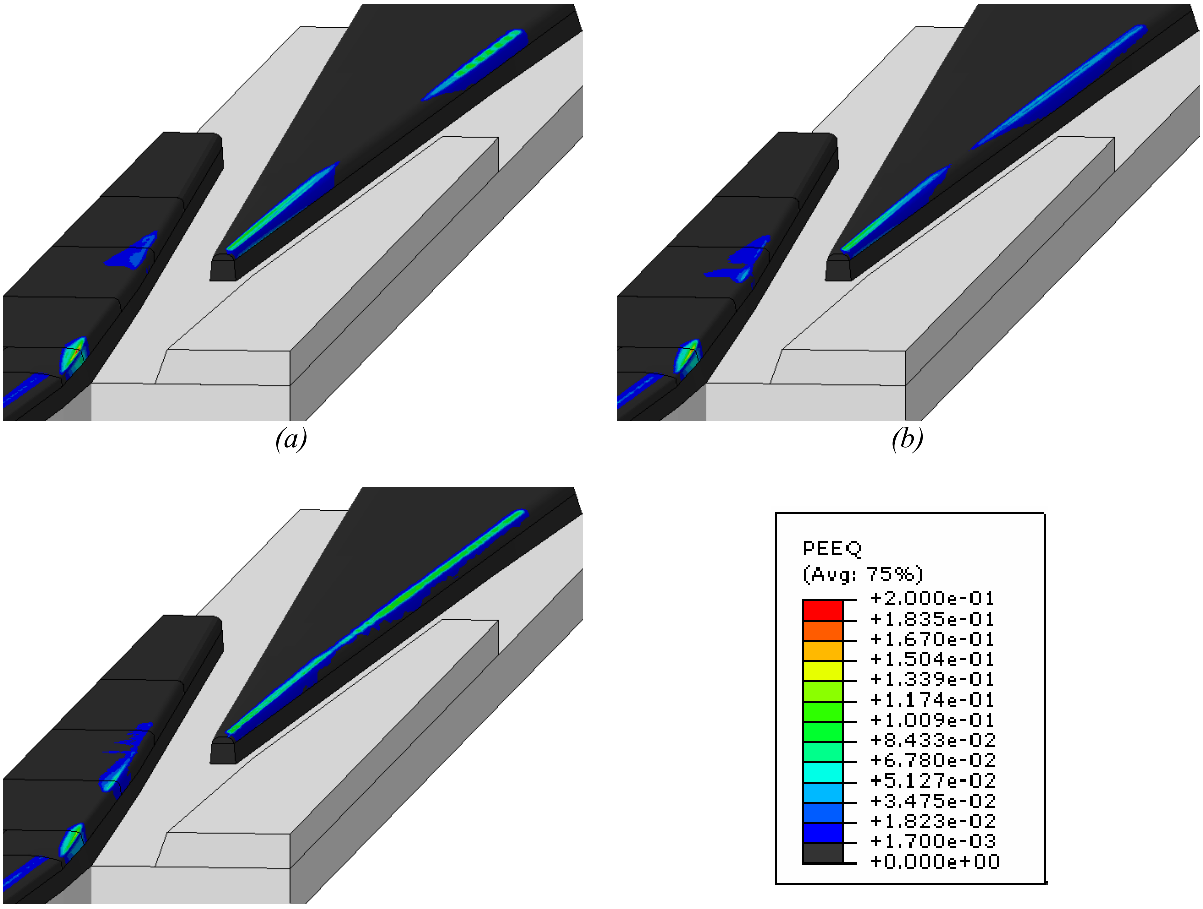

(a) *(b)*

(c) *(d)*

Figure 7-14: Accumulated equivalent plastic strain (PEEQ) for 100mph (a), 75mph (b) and 50mph (c). Legend presented in (d).

7.5.3 Axle load

Figure 7-15 *(a)* shows the relationship between axle load and vertical contact force. Here, the vertical contact force at the plain line transition increases with increasing axle load but decreases during the secondary wing rail impact. This is explained within both Figure 7-15 *(a)* and *(b)* by the freight wheel losing contact further along the plain line transition ‘ramp’ and regaining contact much sooner when compared to the lower axle load of the passenger vehicle. This indicates that for the same speed, a higher axle load results in a shorter ‘flight’ of the wheel, and hence reduced the vertical acceleration when regaining contact with the crossing. Despite a larger vertical impact force observed for the freight vehicle, no loss of contact is predicted on the crossing nose. This is due to the additional load holding the wheel down and in contact with the crossing nose. The inertia of the additional unsprung mass for the freight vehicle would also assist in reducing the vertical acceleration of the wheelset.

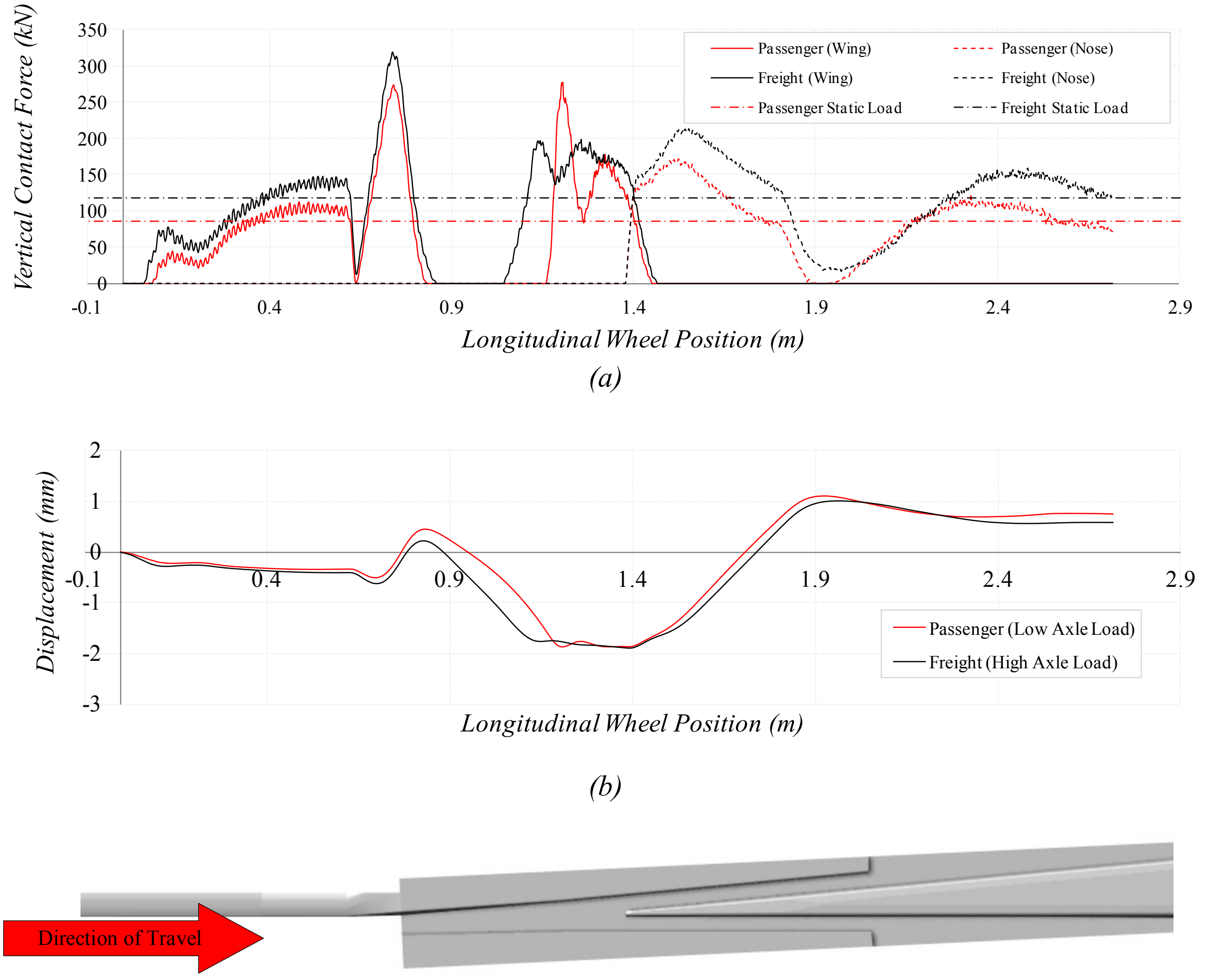

(a)

(b)

Figure 7-15: Case study 2 & 4 - Vertical Contact Force (a) and Vertical Wheel Trajectory (b).

Axle load has the anticipated effect of both increasing the maximum PEEQ at the wing rail transition region, increasing from 22.95 % for the passenger case to 27.24 % for the freight case, and extending the duration of sustained PEEQ along the crossing nose.

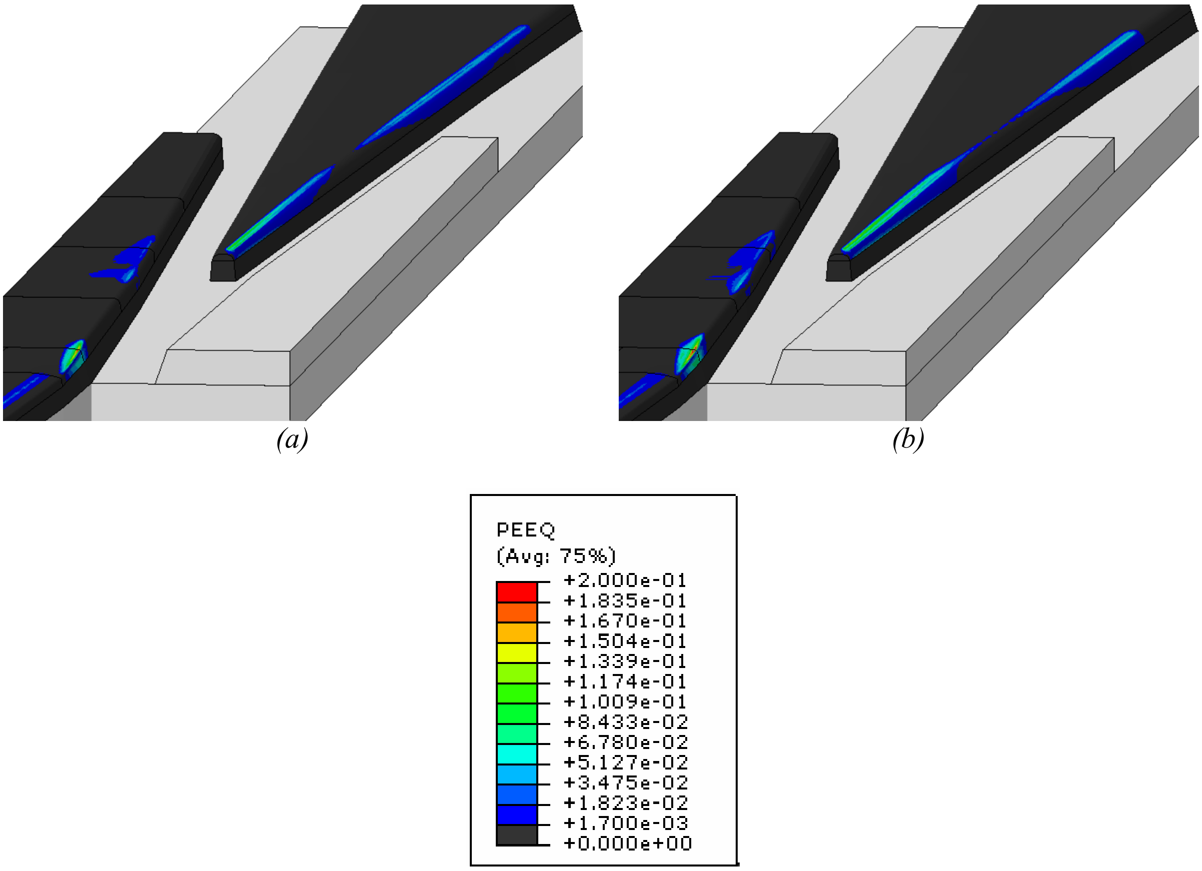

(a) *(b)*

(c)

Figure 7-16: Accumulated equivalent plastic strain for a facing passenger vehicle (a) and a facing freight vehicle (b). Common legend provided in (c).

7.5.4 Direction of travel

Travelling in the trailing direction significantly reduced the vertical contact forces on the crossing nose, as illustrated within Figure 7-17 *(a)*. The dynamic forces observed on the wing rail, after nose to wing rail transition, at approximately 1.4 m, are of a similar magnitude to those predicted for the facing direction. Loss of contact is again observed at the wing to plain line rail transition but this time the mechanism is due to the wheel dropping off the ‘ramp’ and back down onto the head of the plain line rail section at approximately 0.4 m. The freight vehicle regains contact earlier than the passenger vehicle due to the additional mass increasing the negative vertical acceleration of the wheel.

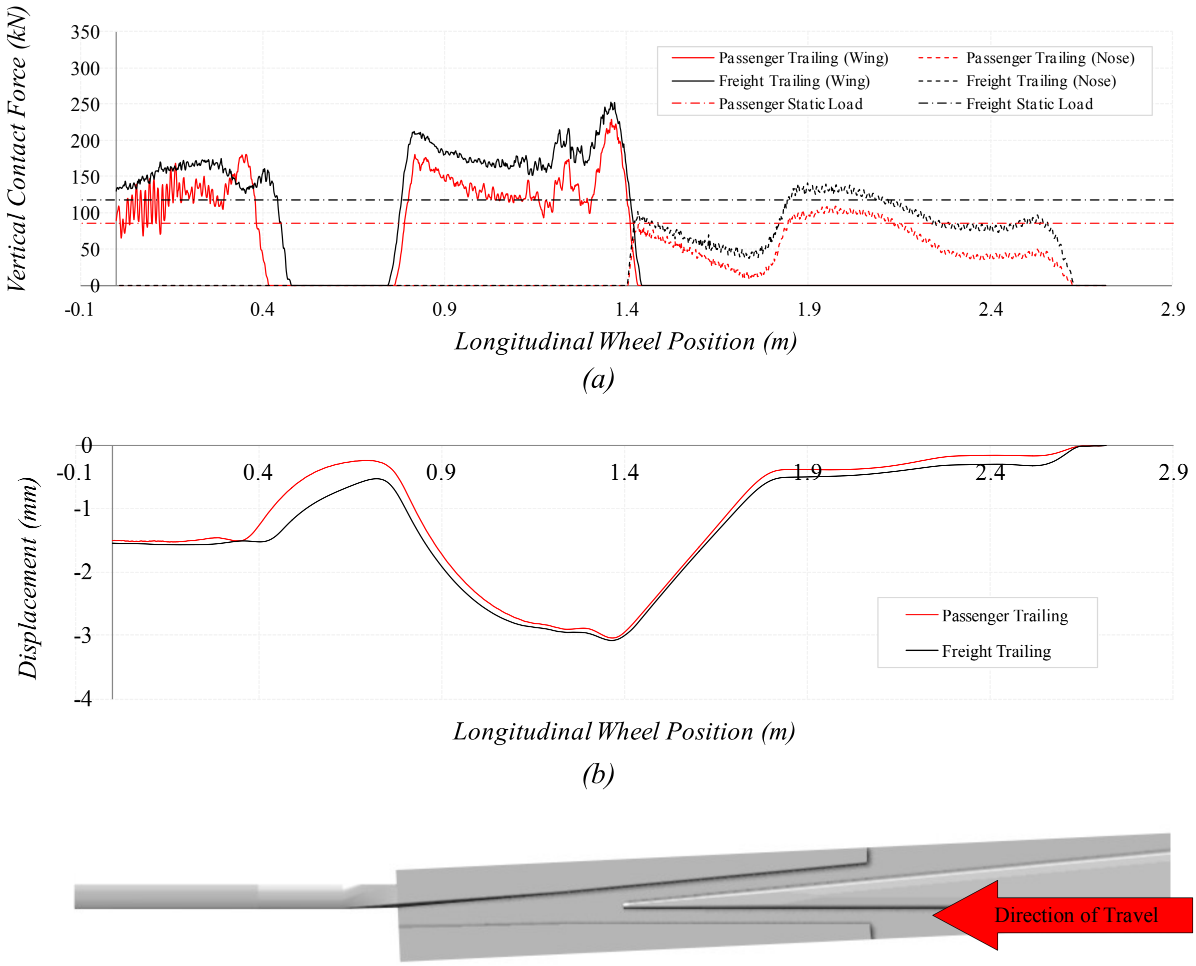

(a)

(b)

Figure 7-17: Case study 5 & 6 - Vertical contact force (a) and vertical trajectory of wheel centre (b).

Figure 7-18 is of a cracked leg end that was cut from a defective cast manganese crossing. The crack can be seen within the welded section, which is located at approximately 0.4 m on Figure 7-17. This exactly coincides with the increased dynamic loading experienced due to the rapid transition from the wing rail profile to that of the plain line rail section (*i.e.* where the wheel is dropping off of the transition and impacting back onto the plain line rail section). The direction of travel on the cracked specimen was trailing from the cast manganese crossing onto the standard grade plain line rail section (*i.e.* as modelled within case studies 5 and 6).

Figure 7-18: Cracked leg end weld and plastic deformation on a defective cast manganese crossing specimen

Figure 7-19 illustrates the severity of the issue concerning defective crossing leg ends. During financial year 2013/14 alone, a total of 94 defects were identified as cracked whilst 3 were found completely broken. Data from Network Rail's Rail Defect Management System (RDMS) [134] also indicates that a total of 25 crossing leg ends were found broken during CP4 (2009 – 2014).

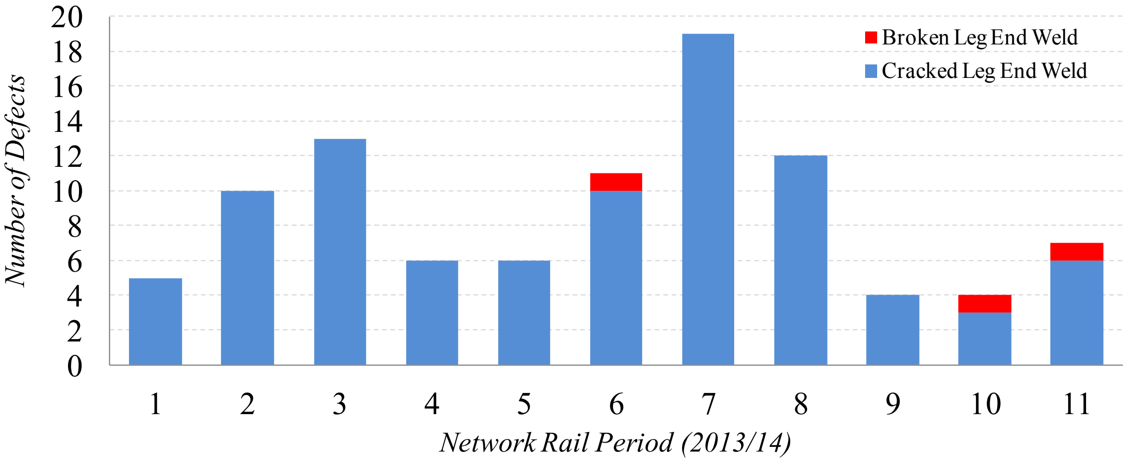

Figure 7-19: Defective cast crossing leg ends during year 2013/14 as reported by Network Rail [135]

When traversing the crossing in the trailing direction, the smoother transition from crossing nose to wing rail results in a more sustained contact along the edge of the wing rail. This in turn increased the amount of plastic strain accumulation simulated along the wing rail. Although occurring at the same concentrated point, the magnitude of PEEQ is also reduced within the wing rail to plain line transition region. In comparison to the facing direction, PEEQ values are reduced from 22.95 % to 18.88 %. The difference between maximum PEEQ values for passenger and freight vehicles in the trailing move is minimal with the freight vehicle achieving a marginally reduced value of 18.83 %. Evidence of plastic deformation is also observed on the specimen cut from the defective cast manganese crossing within Figure 7-18. This coincides with the predicted increase in dynamic vertical contact force and also the predicted PEEQ occurring on the plain line rail sections within Figure 7-20 (a) and (b).

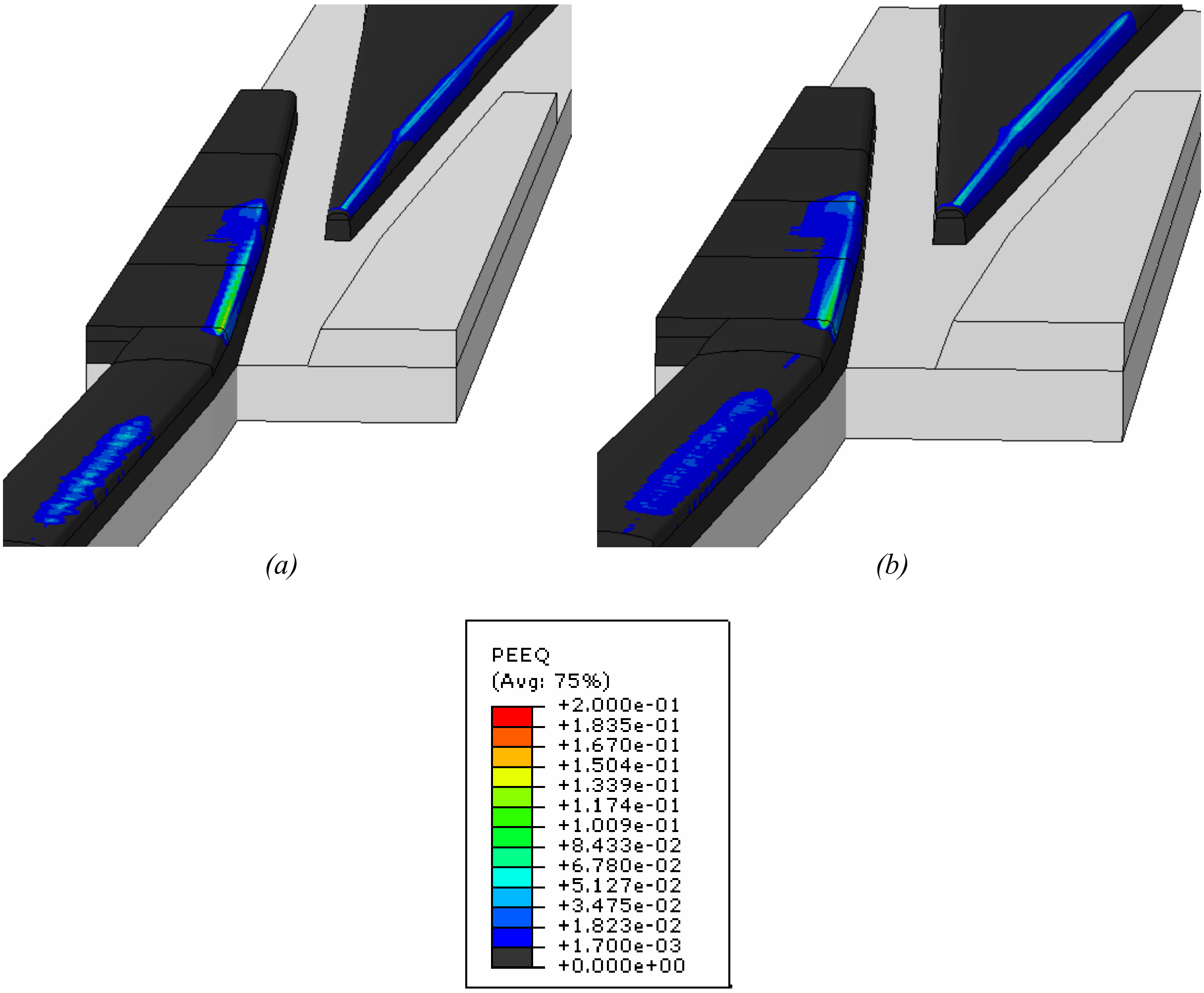

(a) *(b)*

(c)

Figure 7-20: Accumulated equivalent plastic strain for a trailing passenger vehicle (a) and a trailing freight vehicle (b). Common legend provided in (c).

7.5.5 Wheel Profile

Figure 7-21 *(a)*, *(b)* and *(c)* each show how variable and complex wheel to rail interactions can be as a result of introducing different wheel profiles. The vertical contact force varies significantly, with the nominal P1 profile generating the largest impact forces at both the plain line to wing rail and wing rail to crossing nose transition regions. At 0.65 m, the P1 wheel profile instantly loses contact due to the plain line transition geometry and, due to its profile, drops further down until contact is re-established at approximately 0.7 m. The worn P8 profile performs marginally better than the nominal P8 profile with respect to peak forces occurring within both transition regions, although the nominal P8 profile regains contact earlier than the worn P8. Figure 7-21 *(c)* gives a good visual representation of where and when the loss of contact occurs as well as providing the actual location of the vertical contact force on the crossing geometry. The hollow wheel is of particular interest as, although this wheel is severely worn, the contact forces within Figure 7-21 *(a)* seem to be favourable when compared to all other wheel profiles. The secondary crossing nose peak force at approximately 2.2 m is the result of the false flange at the field side of the wheel picking up contact with the crossing nose. This false flange 'pick up' is also observed on Figure 7-21 *(b)* and *(c)* with a large vertical lift of the wheel and lateral contact shift, respectively, at approximately 0.9m and 2.2m.

The largest variation of plastic strain accumulation is experienced when a variety of wheel profiles are introduced. Despite conventional thinking, the P1 wheel profiles resulted in one of the lowest PEEQ values of 5.39 % at the crossing nose. The largest came from the nominal P8 profile at 15.55 %. The hollow P8 profile gave the most significant result despite being the most heavily worn and perceived undesirable profile. When considering the transition regions, the hollow P8 profile resulted in significantly reduced dynamic contact forces. This is due to the false flange at the outside of the wheel profile lifting the wheel out of contact with the small radius gauge corner and running along the head of the wing rail. Load transfer therefore occurs much further down the crossing nose where there is substantially more material to support the wheel . Contact also picks up on the head of the crossing nose, again resulting in reduced PEEQ values compared to those observed along the gauge corner.

These results indicate that by shifting the contact trajectory to the head of both the wing rail and crossing nose, a clear reduction in material degradation is possible. This might be achieved through a further study looking at the geometry of both the crossing and wheel profiles. Although favourable in this situation, it is not recommended that hollow wheels are considered due to their negative effect on the vehicles steering ability and hence dynamic stability.

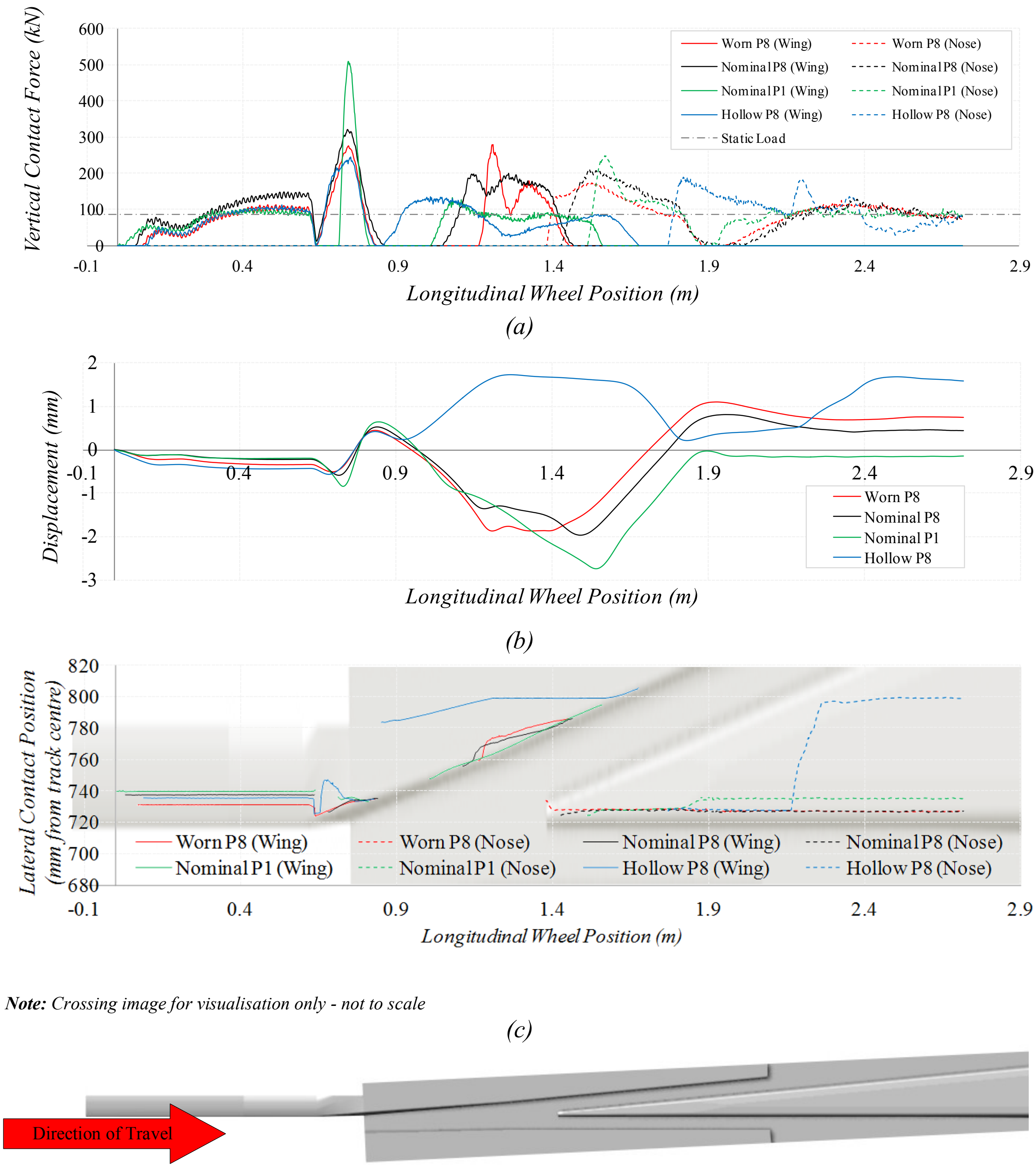

(a)

(b)

Note: *Crossing image for visualisation only - not to scale*

(c)

Figure 7-21: Case studies 2, 7, 8 & 9 - Vertical contact force (a), vertical wheel trajectory (b) and lateral contact positions for all wheel profiles (c).

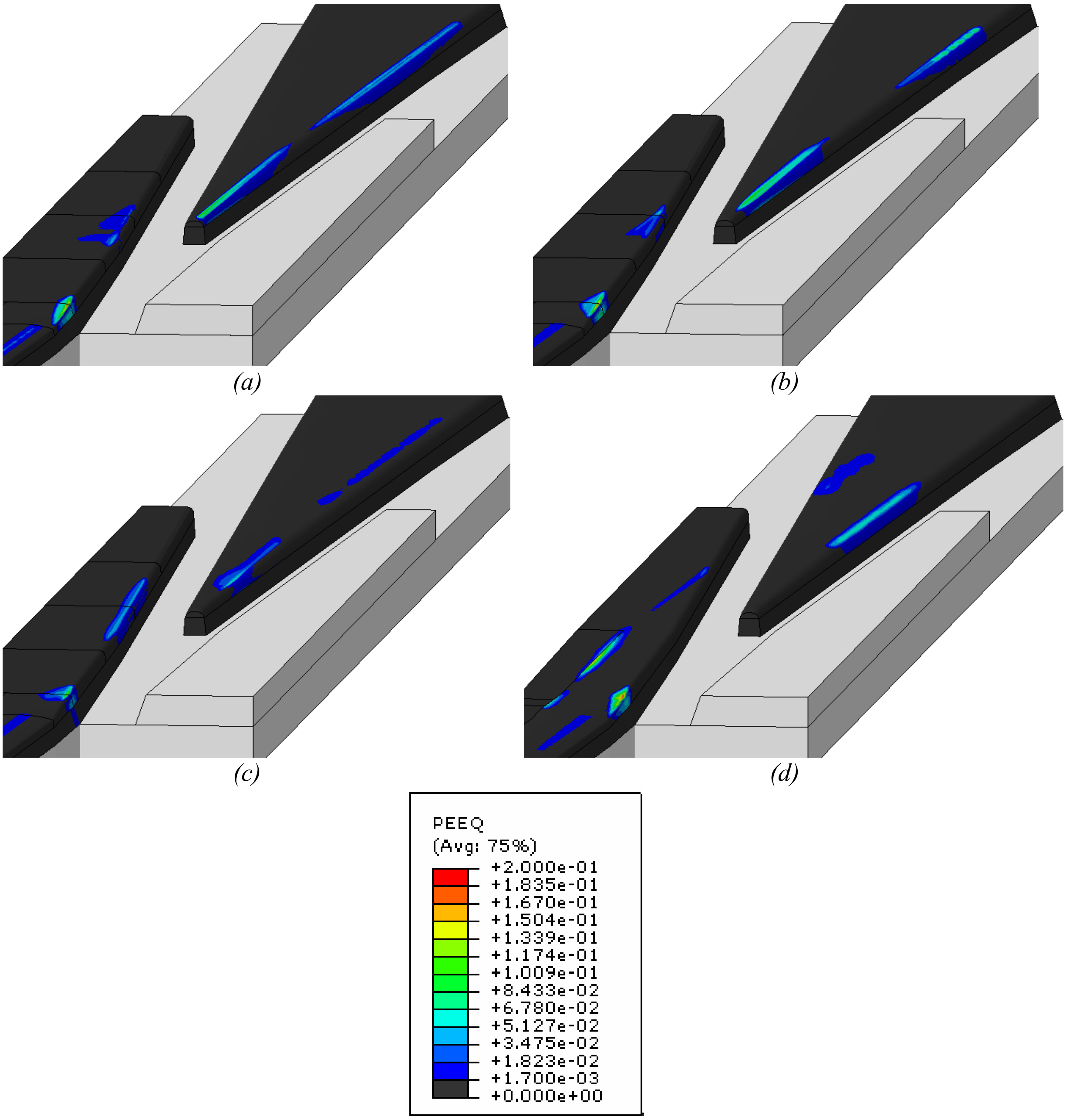

(a) (b) (c) (d) (e)

Figure 7-22: Accumulated equivalent plastic strain for a worn P8 (a), nominal P8 (b), nominal P1 (c) and hollow P8 (d) wheel profile. Common legend provided in (e).

7.5.6 Track Foundation Stiffness

To understand the effects of foundation stiffness on the dynamic forces through the crossing, three different stiffness values were modelled. It can be seen that the first impact occurring at the plain line to wing rail transition is unaffected by foundation stiffness due to the system being in a steady state. Immediately after impact, the crossing is displacement vertically down by between 0.63 - 0.78 mm, with displacement increasing with reducing foundation stiffness. It is from this point (at approximately 0.8 m) where the dynamics of the crossing motion begin to affect both the vertical contact forces and associated plastic strain accumulation. The lower foundation stiffness invokes an increased response from the crossing, reducing the duration on initial contact loss with the wheel. The reduced foundation stiffness then acts to cushion the wheel, reducing the magnitude of the secondary impact force along the wing rail by 22.41 %. Prior to transition onto the crossing nose, the dynamic vertical forces for both the reference case and the higher foundation stiffness converge to equivalent values of approximately 170 kN. At the same location, the dynamic vertical forces for the lower foundation stiffness increase to around 150 kN but quickly drop off to approximately 120 kN as a result of the foundation stiffness ‘cushioning’ effect. Wheel to crossing nose transfer seems to be completely unaffected by foundation stiffness, although the final dynamic response returns the vertical contact forces back to the static value much smoother within the low foundation stiffness case and without loss of contact on the crossing nose.

With regards to PEEQ, foundation stiffness has only has a noticeable effect at the crossing nose for the higher track foundation stiffness. Here, the maximum PEEQ value increases from 12.96 % (both reference state and low foundation stiffness) to 16.14 %, representing a 24.5 % increase.

Although presenting minimal differences in maximum vertical contact force and PEEQ values, the variation in track stiffness resulted in an amplified vertical displacement of the crossing. The maximum vertical displacement amplitude, measured as the amplitude between the displacement peak and trough either side of the crossing nose, increased by 0.55 mm between the high and low foundation stiffness. Amplified displacements of the crossing body, especially if localised around the crossing nose, would have a negative effect on other modes of known degradation, such as fatigue cracking at the base of the crossing. Foundation stiffness should therefore be considered in more detail during further work.

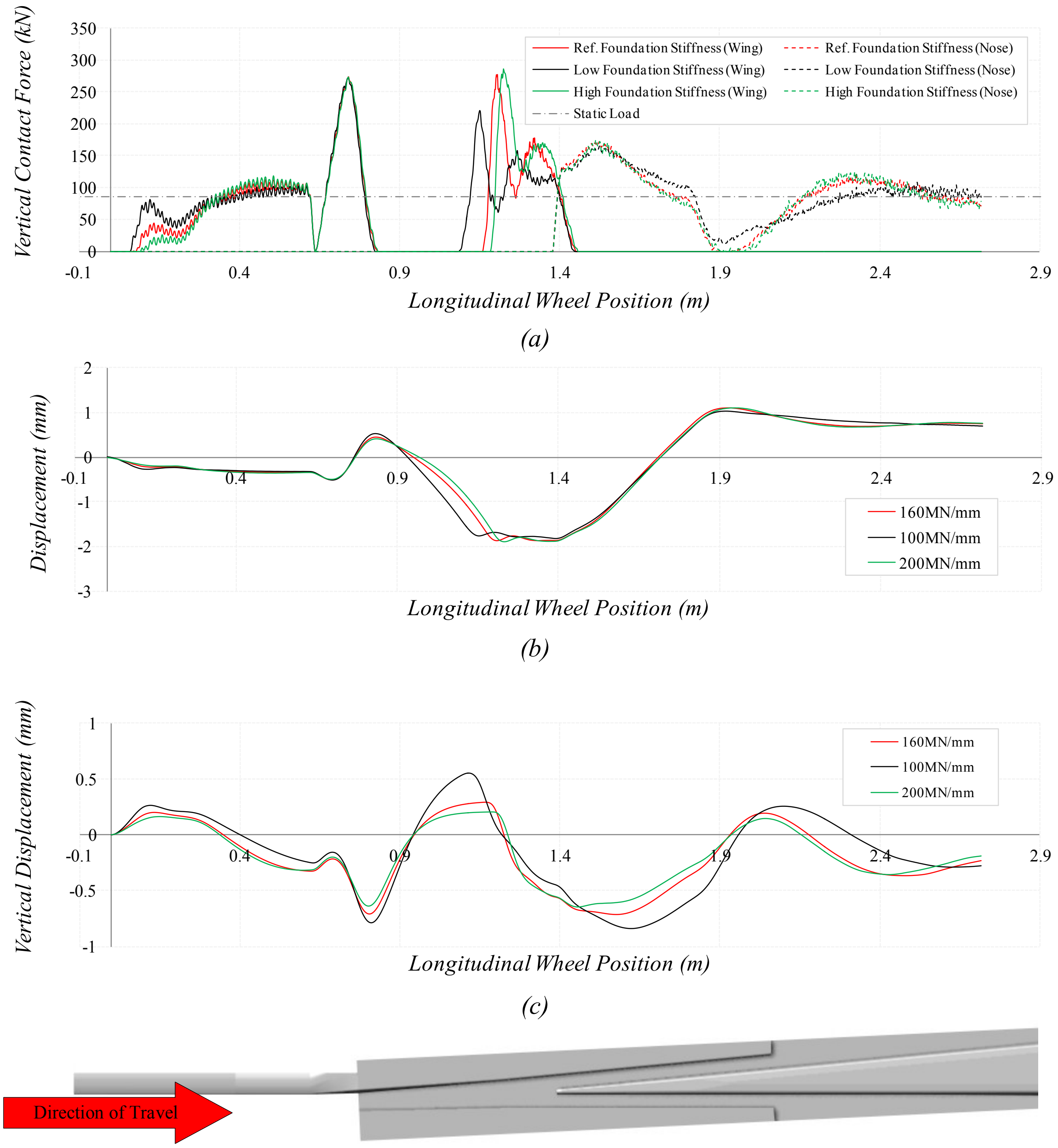

Figure 7-23: Case study 2, 10 & 11 - Vertical contact force (a), vertical wheel trajectory (b) and vertical crossing displacement (c).

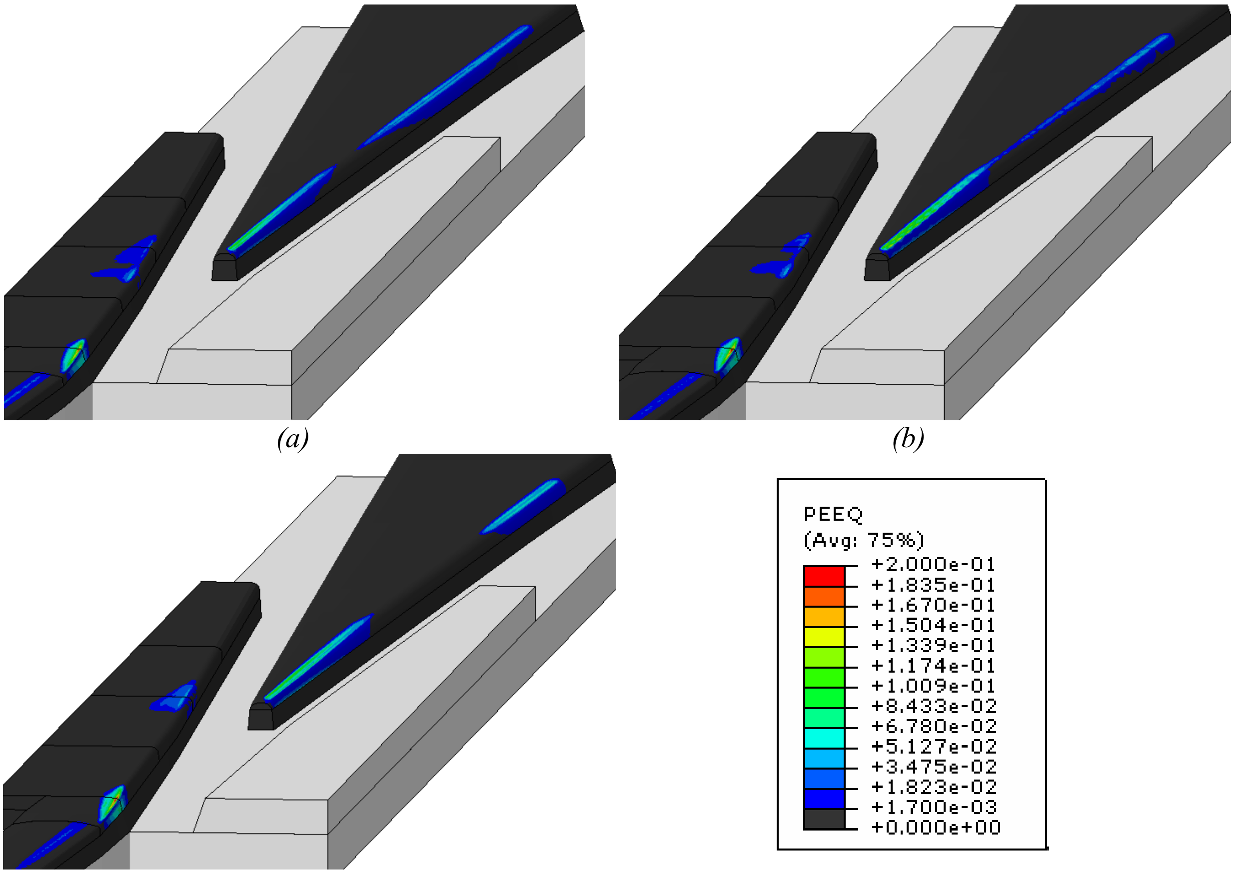

(a) *(b)*

(c) *(d)*

Figure 7-24: Accumulated equivalent plastic strain for a track foundation stiffness of 160MN/mm (a), 100 MN/mm (b) and 200 MN/mm (c). Common legend provided in (d).

7.5.7 Material Properties

The introduction of new crossing materials showed a very obvious trend with regards to initial impact loading on both the wing rail and crossing nose. By increasing the yield strength of the material, illustrated within Figure 7-8, the strains associated with the large contact stresses can be reduced significantly, therefore reducing the overall surface deformation experienced during contact. This in turn increases the dynamic contact forces, which is clearly observed within Figure 7-25 *(a)*. In contrast to the previous case studies, the increasing dynamic loads do not result in an increase in PEEQ. Increasing the yield strength enables the crossing surface to resist deformation, which reduced the dynamic contact force dampening effect experienced as the material begins to yield. This is also illustrated within Figure 7-25 *(a)* by an increase of vertical crossing displacement as the foundation stiffness works harder to resist the additional loads.

Outside of the identified issue surrounding impact at the plain line to wing rail transition region, all plastic strain accumulation is removed from the wing rail within case study 14, which presents a material yield strength of approximately 1200 MPa. Maximum PEEQ values on the crossing nose are also reduced to 7.99 %, down from 12.96 % as predicted when simulating the experimental cast manganese compression stress/strain curve.

These results present a quite obvious benefit to the crossing structure by introducing improved material properties but care should be taken to also consider the other parts of the crossing system. For example, it has been demonstrated that, by increasing the material yield strength, the degradation resistance of the crossing is improved whilst the dynamic impact loads actually increase. Within this model, the increased dynamic loads lead to increased vertical deflection of the crossing, as illustrated within Figure 7-25 (c). In reality, the loads would transfer through the crossing structure and into the adjoining components and supporting foundation. Through conversations with senior S&C engineers and from the authors own personal experience, it is common for the increased dynamic forces occurring within the wing rail to crossing nose transfer region to accelerate degradation of the supporting foundation (*i.e.* track ballast). This results in voiding (amplified vertical movement of the track due to reduced support) and eventually accelerated fatigue failure of the crossing.

The introduction of new crossing materials should therefore be accompanied by other initiatives to support reduction in the dynamic contact loads, such as improved wheel transition and transfer geometries or modifying the track foundation stiffness, as presented and discussed within sections 7.5.5 and 7.5.6, respectively.

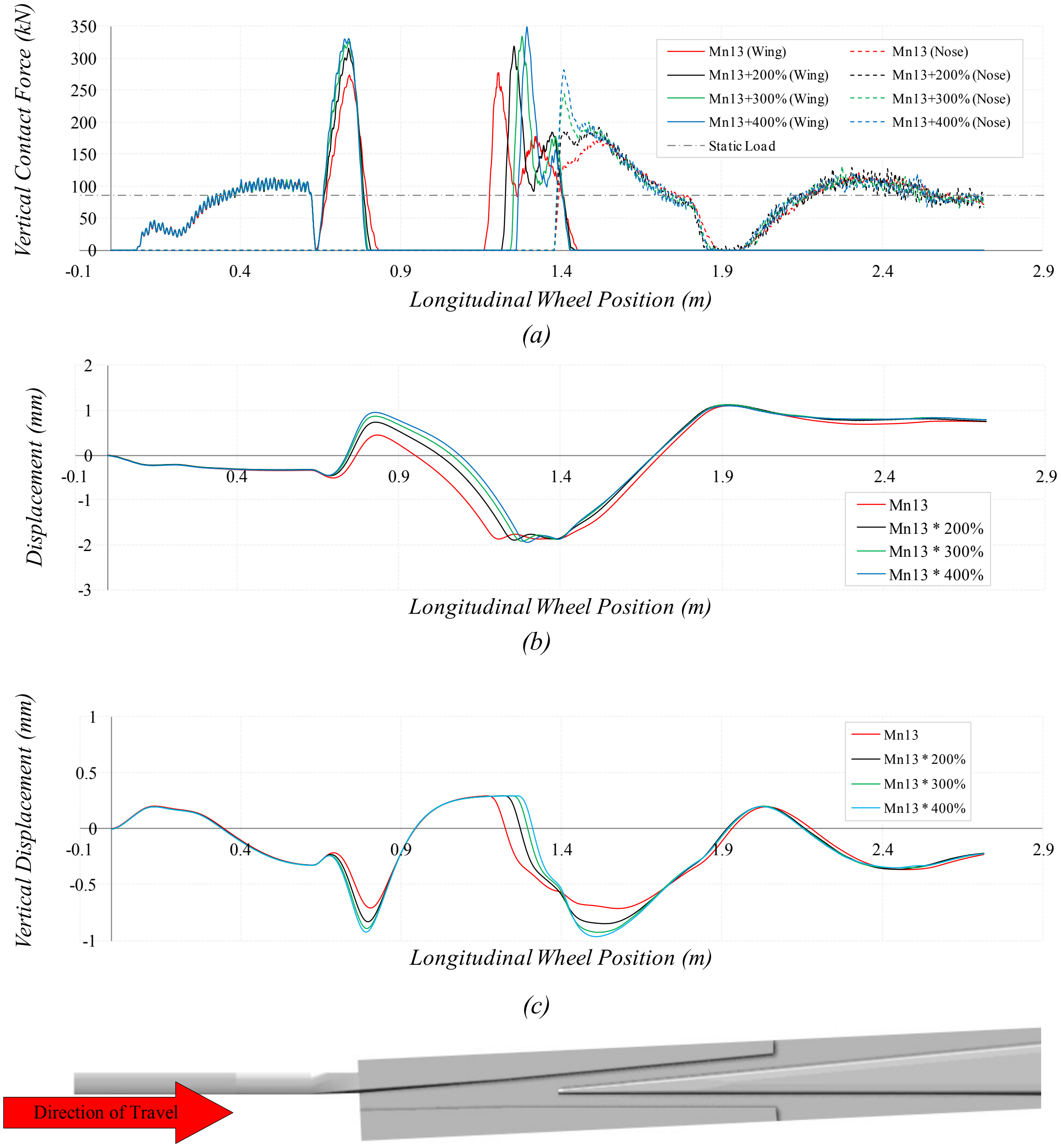

Figure 7-25: Case study 2, 12, 13 & 14 - Vertical dynamic contact force (a), vertical wheel trajectory (b) and vertical crossing displacement.

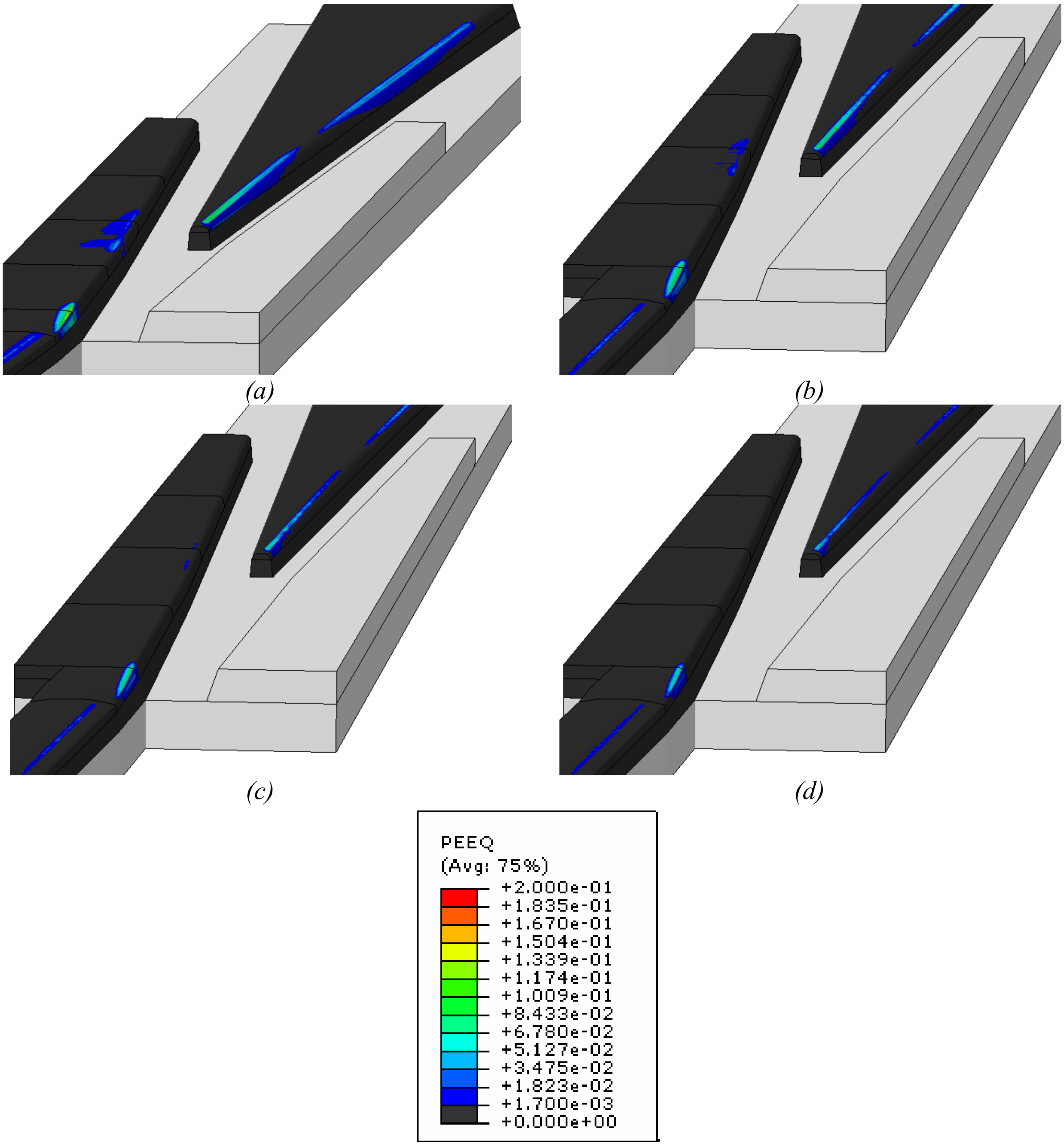
(a) (b) (c) (d) (e)

*Figure 7-26: Accumulated equivalent plastic strain for a different material models; Mn13 (a), Mn13*200% (b), Mn13*300% (c) and Mn13*400% (d). Common legend provided in (e).*

7.5.8 Hybrid Material Properties

A decision to investigate hybrid material properties was taken due to existing crossing designs that offer different materials for the wing rail and crossing nose, which are not currently adopted within the UK rail network. An example of such a crossing is given within Figure 7-27, which illustrates an existing built-up crossing design manufactured by a company called Voestalpine (VAE).

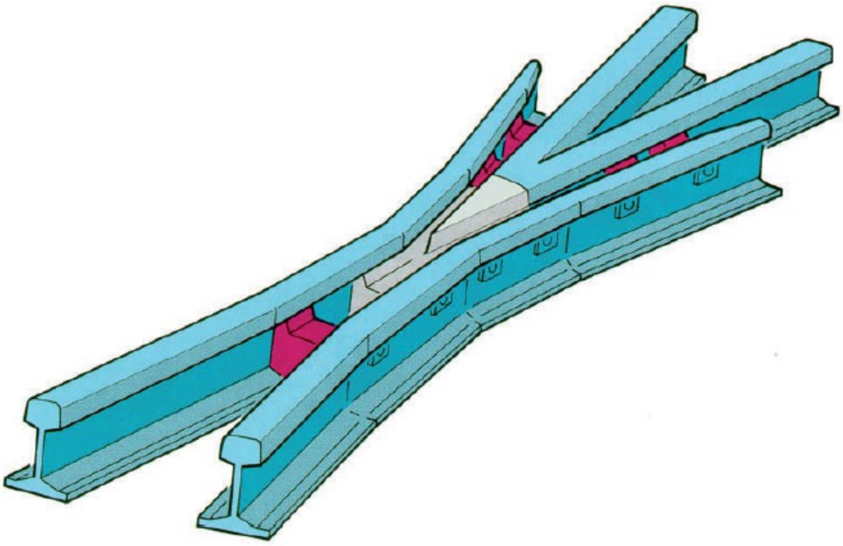

Figure 7-27: Voestalpine (VAE) built-up crossing (Perlit 1300) [131]

With regards to dynamic contact forces, introducing a hardened crossing nose does not seem to offer much benefit. Figure 7-28 (a) shows the simulated dynamic impact loads on the crossing nose. It can be seen that the hardened nose results in a 43.64% increase in vertical contact force from 165kN (Mn13) to 237kN (Mn13 * 400%). Despite this, the largest force simulated at the crossing nose for the hardened nose is of large amplitude and high frequency, which is more synonymous of a P1 load (not deemed to cause damage as discussed within [136]). The sustained peak force (P2) demonstrated minimal variation when compared to the standard Mn13 material. A slightly increased P2 force occurred when both wing rail and crossing nose materials were simulated in the hardened state. The most significant variation in dynamic contact forces occurs throughout the wing rail section with an increase of 25.7% (from 263.6kN to 331.35kN) at the plain line to wing rail transition region (0.65 m on Figure 7-28 *(a)*). This instantly puts the P2 force into a failure condition with regards to the Network Rail standard for cast manganese crossings (see Table 7-4). Although the plastic deformation (PEEQ) is notably reduced, introducing new, harder materials may therefore impact upon the current standards for crossing design.

In the trailing move, very little variation in dynamic contact force on the crossing nose is observed. It is however evident that the plastic deformation is marginally reduced. This study has not considered a hardened wing rail in the trailing move. Having studied the results for the facing move, it is likely that the dynamic loads on the wing rail would indeed increase. This should be considered as further work.

These results give an excellent indication of how the introduction of new materials might affect the performance of cast crossings but further validation should be made prior to committing to significant changes in material properties.

7.5.8.1 Facing Move

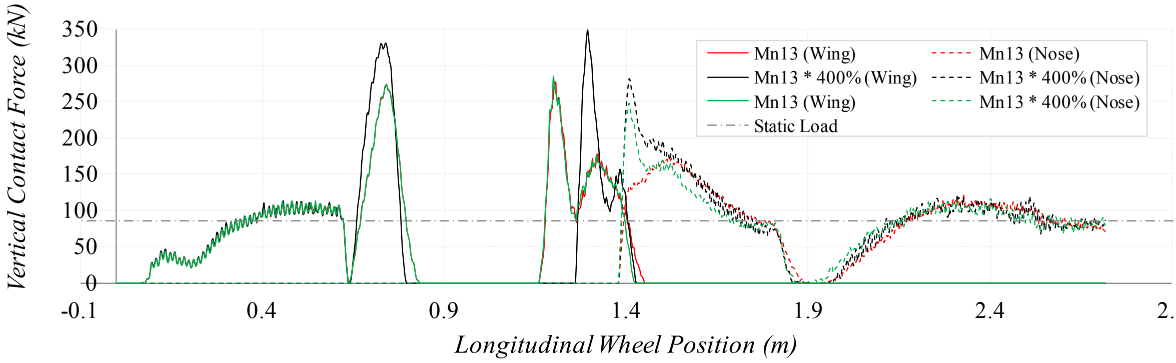

(a)

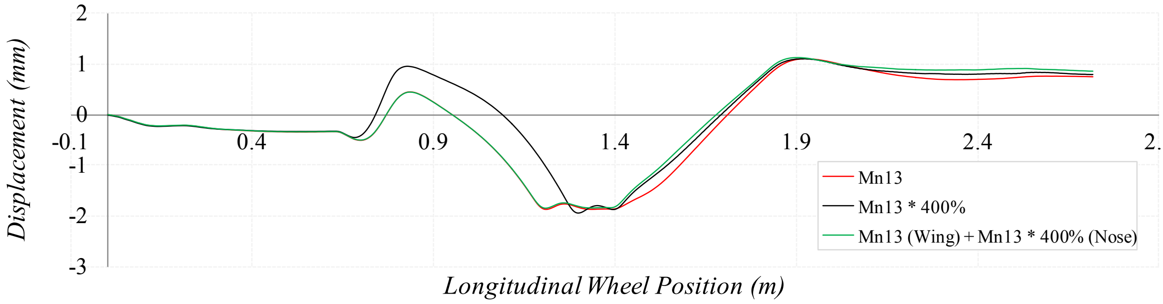

(b)

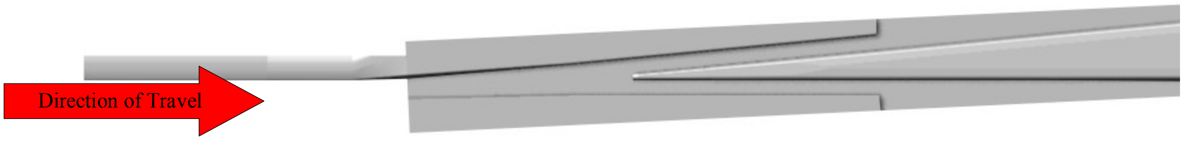

Note: The *red lines* are results from the standard material case, the ***black lines*** demonstrate results from the hardened crossing (Mn13 * 400%) whilst the *green lines* are those for the hybrid case (*i.e.* standard material on the wing rail (Mn13) and hardened on the crossing nose (Mn13 * 400%)).

Figure 7-28: Case study 2, 14 & 15 - Vertical Contact Force (a) and Vertical Wheel Trajectory (b).

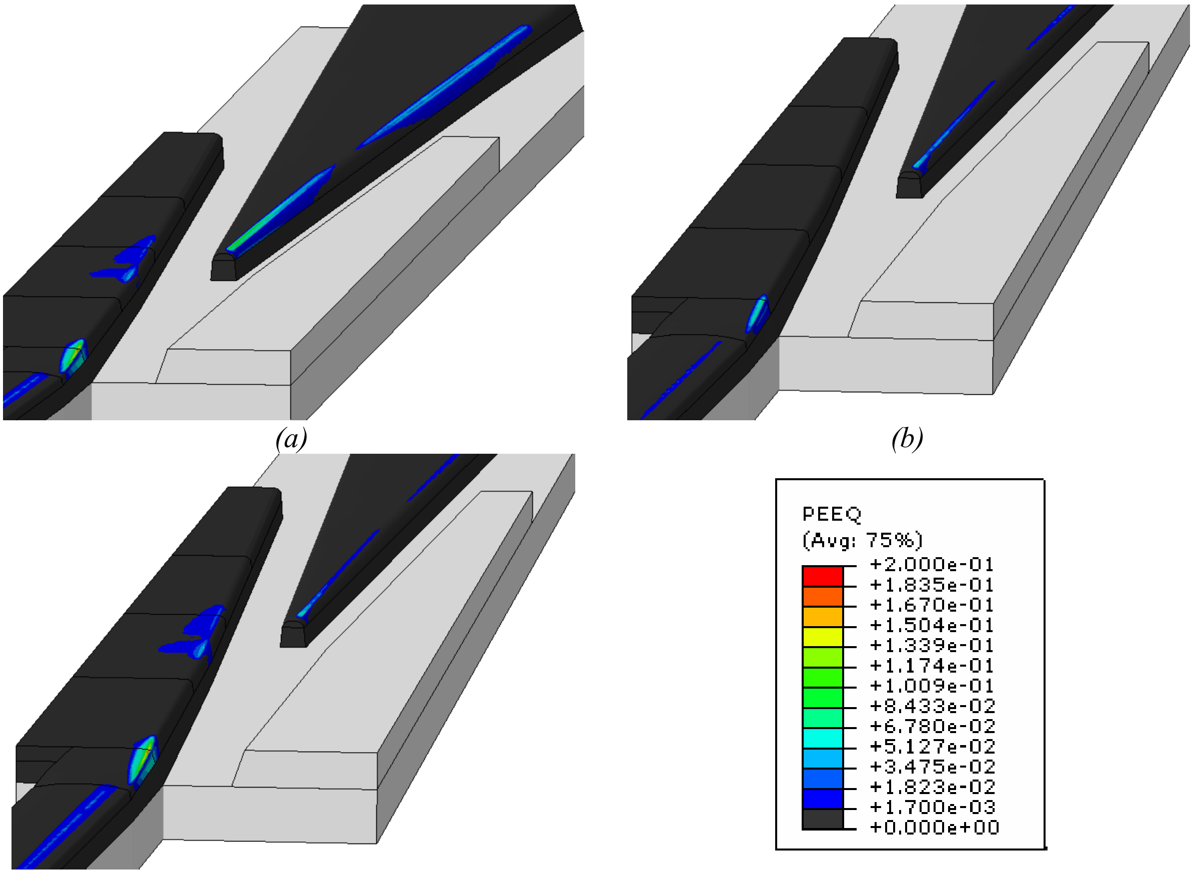

(a) (b)

(c) (d)

*Figure 7-29: Accumulated equivalent plastic strain for different material models running in the facing direction; Mn13 (a), Mn13*400% (b) and Hybrid Mn13 (Wing) / Mn13*400% (Nose) (c). Common legend provided in (d).*

7.5.8.2 Trailing Move

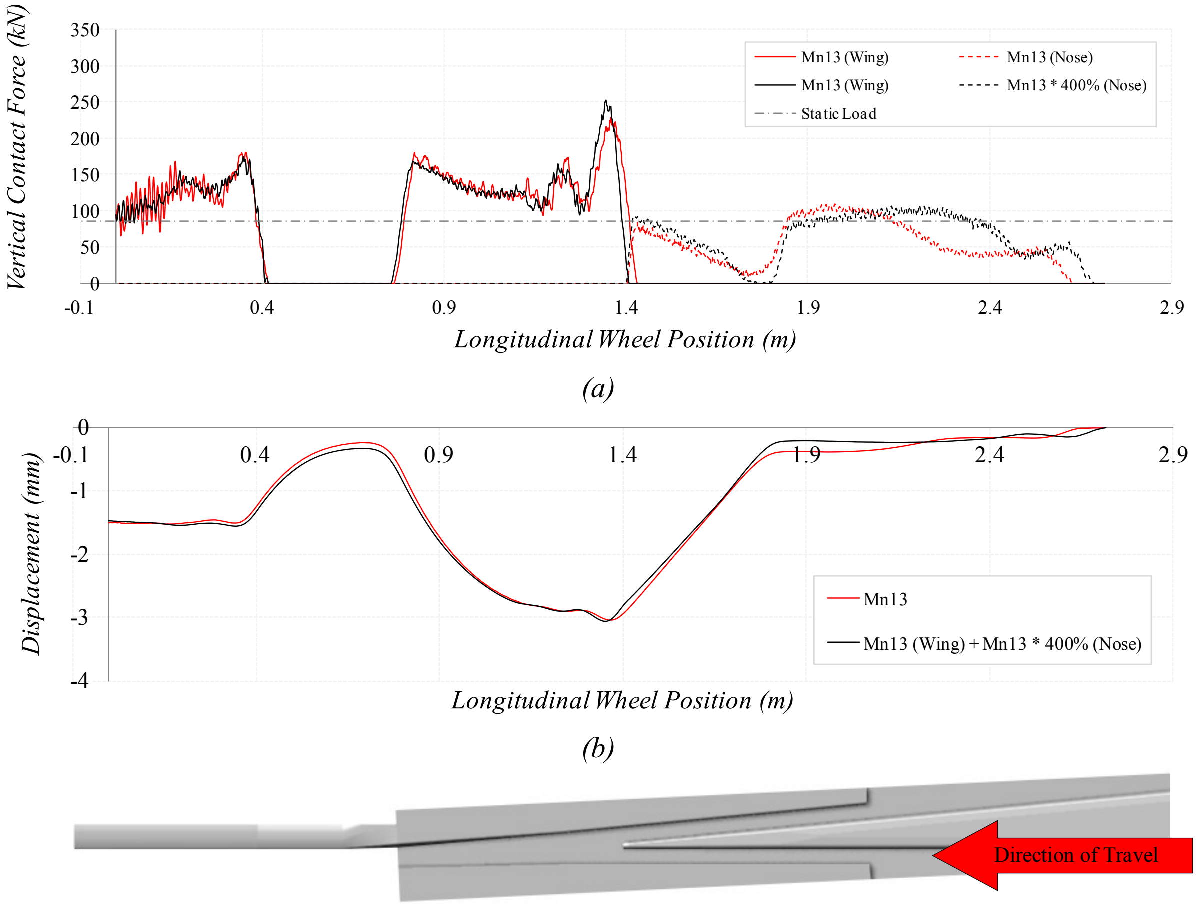

(a)

(b)

Figure 7-30: Case study 5 & 16 - Vertical Contact Force (a) and Vertical Wheel Trajectory (b).

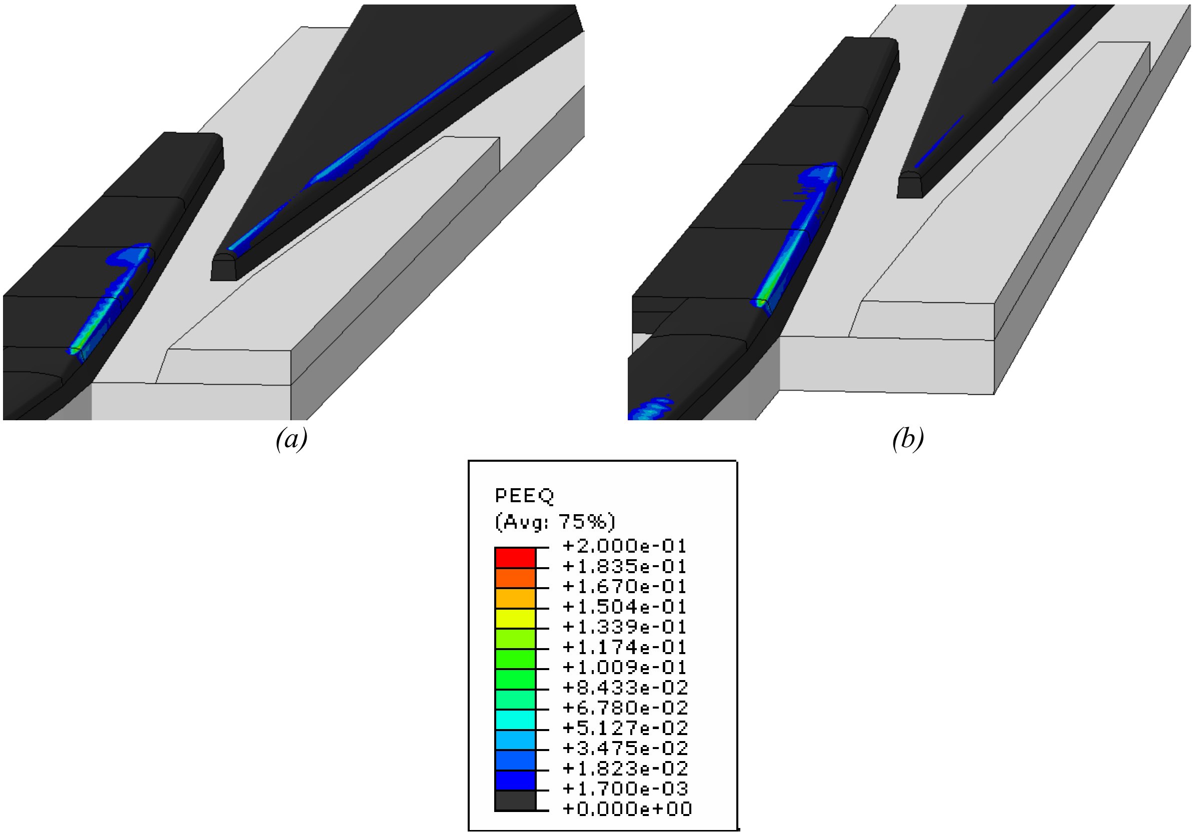

(a) (b)

(c)

*Figure 7-31: Accumulated equivalent plastic strain for a hybrid material model running in the trailing direction; Mn13 (a) and Hybrid Mn13 (Wing) / Mn13*400% (Nose) (b). Common legend provided in (c).*

7.6 Conclusion

This chapter has presented the novel development and application of a dynamic finite element (FE) model of a wheel passing through a UK 1:10.75 cast manganese crossing. It has been demonstrated that, although very different in the nature of computation, the dynamic wheel-rail contact forces simulated within the FE model very closely relate to those obtained from an equivalent model, which was built within the dedicated railway vehicle dynamics package Vampire. Results obtained using the new dynamic FE model also relate very closely to phenomenon observed out on the operational rail network. The simulated loss of contact within crossing transition and transfer zones also related to a recent site measurement at Shalford Junction, where the wheel was seen to either bounce upon or be 'launched' by the crossing nose. Simulation of the wheel passing through the crossing in the trailing move identified significant dynamic impact forces occurring at approximately 1 m back from the crossing nose. This corresponded exactly with the location of the welded leg end of the crossing, which has been reported by Network Rail to be an area of concern due to a significant number of cracked and broken welds within this region. The onset of plastic deformation within the leg region was also predicted by the FE analysis and related very well to a defective sample extracted from track. These initial observations provide not only validation of the phenomena simulated by the tool but also demonstrate the value of such a technique for analysing critical railway track assets.

A range of recommendations have been drawn from the case studies completed within this chapter. These include:

1. Complete further model validation using the load measuring wheelset once it becomes available on the UK rail infrastructure.

2. The plain line to wing rail transition zone acts as a ramp, causing significant loss of contact and subsequently amplified vertical dynamic contact forces as the wheel regains contact further along the wing rail. Large values of plastic strain accumulation are also simulated within this region, indicating that the 'ramping' effect may actually reduce as the rail section deforms, becoming more conformal to the passing wheels. Despite this, it is highly recommended that the contact geometry within this region is optimised to provide a smoother transition into the crossing.

3. A comparison between the analytical impact force (P2) and the dynamic FE results indicate some discrepancies with the current UK standard for cast crossings, NR/SP/TRK/012. With differences of up to 96%, which resulted in some cases not satisfying the requirements of the

standard, this study has demonstrated that the dynamic impact load is influenced by more than just the parameters used within the analytical equation. Both wheel profile and material properties had a significant influence on the maximum impact force experience by the crossing. It should also be noted here that there is more than one sustained vertical dynamic load occurring as the wheel passes through the crossing, whereas the standard only considers impact on the crossing nose. Both of these factors would amplify the cycles to failure during a fatigue analysis. It is therefore highly recommended that comprehensive study is made that considers all aspects of NR/SP/TRK/012.

4. The wheel trajectory as it negotiated the wing rail to crossing nose transfer zone has a profound effect on the peak dynamic impact forces experienced by the crossing. It is recommended that the contact geometry through this transition region is amended to enable lifting of the wheel away from the start of the crossing nose. This will allow wing to crossing nose transfer to occur further along the crossing nose and remove the tendency for the crossing to resist the forward motion of the wheelset.

5. Amend the wing rail geometry within the vicinity of the crossing nose transition to move the transfer zone further back along the crossing nose. The hollow wheel achieves this by lifting the wheel out of contact with the gauge corner due to the false flange. The same affect can be achieved by raising the wing rail, as is done on crossings with inclined wing rails.

6. Reducing the crossing support stiffness also assists in reducing the dynamic contact forces experience by the crossing. It is, however, unfavourable to introduce a weaker track formation beneath the crossing therefore it is recommended that the stiffness and damping properties at the interface between crossing and bearer (or bearer and track ballast) is investigated. This would provide the desired ‘cushioning’ effect and promote energy absorption during high impact wheel to rail contact conditions.

7. The use of improved materials can increase the degradation performance within cast crossings but should be accompanied by improvements in both the contact geometry and support stiffness to avoid amplifying the dynamic impact loads.

Results from this analysis can therefore be used to improve the design of the 1:10.75 cast manganese crossings. The most significant aspect of this work is that the technique can also be adopted for any other type of railway wheel to rail interface, including but not limited to simulating other crossing designs, switch rails and rail joints.

Chapter 8 : Conclusions

This chapter reviews the thesis before providing a summary of its main findings. Implications of the research presented within this thesis are then discussed. The significant contributions made towards advancing knowledge within the field of wheel-rail interaction modelling at railway switches and crossing are highlighted before concluding with recommendations for further work.

8.1 Thesis Review

As discussed within *Chapter 1*, the motivation behind this thesis was to investigate the complexity of wheel-rail interaction at railway switches and crossings (S&C), with the aim of advancing knowledge of the degradation process due to dynamic interaction with trains. In order to realise the aims of the thesis and to bridge the knowledge gaps identified within *Chapter 2*, a computational model for wheel-rail interaction, specifically suited to S&C, was developed. *Chapter 3* tackled the initial problem of contact point detection and accounted for the three-dimensional shapes of both the wheel and rail. Validation was made with an already established contact model used within the vehicle dynamics simulation package Vampire®. Benefits of the new S&C contact model developed within this thesis were then illustrated by means of a comparison of contact locations along a closed switch rail obtained using the newly developed model and the existing contact detection algorithms.

Chapter 4 introduced a complete modelling strategy for simulating wear accumulation at complex S&C profiles. Both Hertz's normal and Kalker's tangential contact stress solutions were integrated into the S&C multi-point contact detection model, enabling stick and slip regions within each identified contact patch to be solved. Discrete sliding distances and normal pressures were then obtained for use within the Archard's wear model. Wear depth predictions for up to 4 individual points of contact were made possible and then integrated within a damage accumulation routine, which enabled the rail profile to be updated by the magnitude of simulated wear.

In order to improve upon the results achieved throughout *Chapters 3* and *4*, a completely new approach for advanced wheel-rail interaction modelling was investigated. This was in the form of a two-dimensional, lateral boundary element model (BEM) and attempted to combine the contact detection, detailed stress analysis and material degradation stages of the damage prediction process. *Chapter 5* introduced the 2D BEM model and discussed in detail its integration into the overall wheel-rail damage simulation methodology. Three initial case studies were investigated, each representing typical contact condition expected during wheel-S&C interaction, including non-conformal, conformal and multi-point contact. Excellent validation was achieved against an established commercially available finite element software package, which gave initial confidence that the novel BEM model was indeed a feasible approach to tackling complex interactions at S&C.

Chapter 6 advanced the novel BEM approach by developing a technique for generating three-dimensional contact patches. Realistic contact patch shapes, sizes and normal contact pressure distributions were achieved, which significantly improved the inputs required for the subsequent tangential solution. The implementation of Kalker's Fastsim algorithm was then modified to accept non-Hertzian normal pressure distributions whilst also extracting local geometric parameters for approximating wheel-rail creepages. Comparisons with the simplified Hertzian solution were made. *Chapter 6* concluded by demonstrating some additional benefits associated with the lateral BEM model. Internal body inertia terms were included within the internal domain and used during the simulation process to model the effects of dynamic impact loading. This is the first time that such a technique has been implemented within a wheel-rail contact model and is a phenomenon of great interest within the subject of S&C. A case study demonstrating dynamic stress evolution within the rail was presented. Initial developments for integrating plastic deformation modelling within the combined tool for S&C degradation were also discussed. The ability to predict plastic strain accumulation using the lateral BEM model was also presented, giving further visibility to the very flexible nature of the proposed BEM approach. It was concluded that the lateral 2.5D BEM approach was indeed capable of integrating all of the critical modes of degradation within a single, combined tool for long-term S&C degradation. Above the benefits of incorporating physically sound models and the flexibility of the BEM approach, improved computational efficiency over existing state-of-the-art solutions was also demonstrated despite the current un-optimised implementation of the model. Further work in this area was recommended as improvements to the current tools are capable of providing a step change in the modelling approach used for S&C at Network Rail.

To complement the developments made throughout this thesis, *Chapter 7* took advantage of existing state-of-the-art modelling techniques by developing a dynamic finite element model for wheel to crossing interaction. The aim of this work was to provide Network Rail with an advanced understanding of the contact performance of cast manganese crossing with regards to contact trajectory, dynamic contact forces and the onset of plastic deformation. A wide range of case studies were investigated to give a good indication of the main parameters affecting wheel to crossing contact performance. Comparisons were also made with the existing UK standard for cast crossing design, resulting in a number of recommendations being made.

8.2 Summary of Findings

Within *Chapter 2*, a comprehensive review of existing literature identified that a tool capable of combining all of the modes of S&C degradation did not currently exist. Moreover, many of the existing wheel-rail interaction models contained simplifying assumption making them unsuitable for long-term degradation predictions at complex S&C.

8.2.1 Simplified wheel to S&C contact modelling

Chapter 3 discovered that incorrect contact locations were simulated at complex S&C rail profiles when using simplified detection routines as implemented within commercially available vehicle dynamics packages. This was a direct result of interpolating contact data tables for only one point of contact. Using a combined elastic deformation and three-dimensional rail profile approach, the detection of multiple points of contact for measured S&C profiles was made possible. The proposed model provides up to four independent points of contact (more than four is also possible with an extension of the code) and operates directly on the wheel and rail profiles. This ensures that the actual geometries are considered within the critical areas associated with S&C (*i.e.* wheel – rail transfer zones). An important outcome of the new approach also comes from the appropriate distribution of normal contact load across all points of contact. This is extremely important for long-term damage predictions as incorrect loading within the contact patch would result in errors during the damage assessment process.

8.2.2 Advanced wheel to S&C contact modelling

Chapter 4 demonstrated a complete solution for damage accumulation modelling but also discussed some of the significant limitations associated with the simplified models adopted. To overcome these issues, *Chapter 5* integrated an advanced boundary element model (BEM) into the overall solution. By doing so, it was found that the use of an independent contact detection routine could be completely avoided due to the potential use of the BEM to assess contact stresses across the entire measured contact surface. Errors of less than 2% were demonstrated when validated against equivalent finite element (FE) models. Another significant advantage was the ability to simulate different materials between the wheel and rail contact bodies. This is extremely important for long-term damage accumulation modelling at S&C due to different materials being used during the manufacture of switch rails and crossings noses. Differences of up to 22 MPa were found for a single case considering standard grade steel (*E = 201 GPa*) and cast manganese (*E = 190 GPa*). Although seemingly small, this discrepancy would eventually lead to accumulated errors over the duration of the damage assessment. The ability to model independent materials therefore offers a significant and essential benefit for long-term damage accumulation at the S&C interface.

8.2.3 Novel 2.5D BEM wheel to S&C contact modelling

It has been demonstrated that a 2.5D BEM solution provides a significant improvement over simplified models with regards to the shape and size of the contact patch and also the distribution of normal contact stresses within it. Within a case study concerning nominal contact between a P8 wheel profile and a BS113A rail profile, an 11.77 % over-estimation of the maximum contact pressure was observed when the simplified Hertzian model was compared to the exact finite element (FE) solution. In comparison, the 2.5D BEM technique indicated a 12.64 % under-estimation of the maximum normal contact pressure in comparison to the FE result. This discrepancy was found to be a direct result of the Hertzian approximation, used to estimate the contact length, and the assumed parabolic load distribution adopted to define individual “slice” loads. These assumptions constrained the BEM accuracy but are both easily overcome by introducing an improved approach to loading the contact surfaces (*i.e.* using a displacement boundary condition as opposed to load). It was also found that the Hertzian contact patch width was vastly incorrect with a 57.42 % deviation from the actual solution observed from FEA. In contrast, and despite the identified constraints, the BEM solution gave an excellent comparison with only a 2.54 % variation in contact width from FEA. The most important discovery came from the ability to realistically simulate the normal pressure distribution profile within the contact patch; again, a very good agreement between the FEA and 2.5D BEM pressure distributions was achieved.

A comparison of tangential tractions between the Hertzian / Fastsim and 2.5D BEM / Fastsim techniques also identified large variations in results. The location and magnitude of predicted slip and adhesion within the contact patch were significantly different. Although the contact origin occurred at approximately the same location, the realistic spread of normal contact pressure within the BEM solution dramatically shifted the slip area, with the bulk of the wear depth occurring outside of the contact patch originally identified within the simplified Hertzian approach. This is a very important characteristic as the location and severity of damage is therefore directly affected by the normal pressure predicted within the slip region.

One of the major goals of this thesis included the investigation into combining critical modes of degradation into a single contact model. *Chapter 6* concluded by demonstrating the unique capabilities of the lateral BEM approach by simulating phenomena occurring within the internal domain of the contacting bodies. General internal stress analysis was presented within *Chapter 6*, which was a post-processing capability that was already available within the widely accepted state-of-the-art solution for non-Hertzian contact, Kalker's Contact model. This thesis extended that capability by introducing a process for including internal body inertia, allowing the effects of dynamic impacts on the internal domain stresses to be investigated. Preliminary results indicated that a dynamic amplification of internal stresses occurred over a duration of $2.02\text{x}10^{-4}$ s immediately after the contact load was removed. This resulted in an increase in von Mises stress of 45.58 % within the internal domain when compared to an equivalent static analysis (*i.e.* from 422.59 MPa to 615.20 MPa). To accurately assess long-term S&C damage, internal body inertia effects must therefore be considered to fully capture the extent of stress distribution throughout the contact domain. Plastic strain accumulation has also been included in the BEM solver through integration of the radial return algorithm (RRA) within the BEM internal domain solution. Preliminary results demonstrated the ability to cap the internal stresses to within a predefined yield limit whilst subsequent load steps then began to accumulate plastic strain. A P8 wheel profile loaded to 6.36 kN onto a BS113A rail profile resulted in a plastic strain of $5.54\text{x}10^{-4}$. To the best knowledge of the author, no other wheel-rail BEM techniques have been demonstrated that are capable of assessing incremental internal domain effects as presented within this thesis.

Benefits in computational effort were also identified with a vast improvement over detailed 3D FEA models. The solution time for a full 2.5D BEM analysis, in its un-optimised state, was over 4.6 times faster in terms of individual CPU time. It was therefore found that a 2.5D BEM solution offered a detailed and efficient means of combining all of the major stages of the wheel-rail interaction process. In addition to this, the ability to model internal body inertia, plastic strain accumulation and sub-surface cracks leads to a versatile tool capable of simulating all of the major degradation modes associated with S&C.

8.2.4 Dynamic wheel to crossing interaction modelling

Chapter 7 gave some immediate benefits and recommendations for the rail infrastructure manager, Network Rail. Although historically concerned with impact loading on the crossing nose, it was found that significant dynamic contact forces also existed at the plain line to wing rail transition region. Background research identified that Network Rail were also suffering with defective crossing leg end welds, which reside close to this transition interface. Simulations in the trailing direction identified that amplified dynamic loads were occurring directly above the location of the leg end weld. It was concluded that contact geometry was acting as an artificial ‘ramp’ and should therefore be optimised to enable smoother entry and exit of the wheel into and out of the crossing. It is currently unknown whether or not this phenomenon is sustained throughout the life of the crossing. Large amounts of plastic strain accumulation (PEEQ = 22.95 % at the reference state) would indicate that this region progressively become more conformal to the wheel profile, which would in turn reduce the ramping effect.

Increasing the vehicle speed and axle load also increased both the dynamic wheel to rail contact forces and PEEQ. This aligns with the analytical equations as used within the cast crossing design standard and are parameters that are least influenced by Network Rail. A more in-depth analysis of these parameters might assist the calculation track access charges but this has not been studied within this thesis.

A comparison between the dynamic FE model and analytical P2 force identified discrepancies of up to 95 % variation in the predicted vertical contact force. With the P2 force being central to the fatigue analysis of existing cast manganese crossings, these results begin to provide an indication as to why the whole life of cast crossings is commonly much shorter than their design life. Variation in wheel profiles gave the largest discrepancy and it was initially surprising to see that the profile with the largest dip angle (7.11 mrad) actually resulted in the smallest dynamic peak force within the FE model. This was contrary to conventional thinking and indeed opposite to the results obtained using the existing analytical approach. Further analysis determined that, although the dip angle was indeed greatest for the hollow P8 wheel profile, its overall trajectory was profoundly different to all other wheel profile. Instead of accelerating into the crossing nose and being resisted by the longitudinal inertia of the crossing, the hollow wheel resulted in the wheelset lifting up onto the wing rail and then dropping back down onto the upper surface further along the crossing nose. The result of this is less resistance to the forward motion of the wheel and hence reduced dynamic loads (reactions forces) subsequent to wing rail to crossing nose transition. This is a significant discovery and one that should be carefully considered during the redesign of cast manganese crossings.

Reducing the crossing foundation stiffness resulted in a cushioning effect as the wheel transferred through the wing rail to crossing nose area. A reduction in peak impact force of 22.41 % was achieved at the secondary impact on the wing rail. At the crossing nose interface, minimal variation in dynamic peak force was simulated, although the softer foundation again resulted in a slight reduction in peak dynamic force (4.1 % reduction). This is due to the relative position of the wheel and rail reducing the dip angle and the softer foundation absorbing some of the impact through vertical deflection. Varying the support stiffness is an interesting concept as conventional thinking dictates that the foundation should be maintained to ensure consistent crossing support. It has been recommended that investigating the stiffness and damping properties at the interface between crossing and bearer (or indeed bearer and track ballast) would assist in reducing the overall dynamic impact experienced by crossings. An increase in track stiffness also increases the magnitude of PEEQ due to the material working harder to resist the dynamic contact forces. In this case, PEEQ increased from 12.96 % to 16.41 %.

Increasing the material yield strength has the desired effect of improving the material response to impact loading but also increases the dynamic impact forces experience by the crossing. This is due to the contact forces dissipating as the material begins to yield. The improved material properties provide additional resistance against material displacement and hence reacts more of the load, increasing the dynamic output within the model. Plastic deformation (PEEQ) reduces down to 7.99 % from the reference state of 12.96 %.

8.3 Novel tools for S&C Contact Modelling and their Implications

As identified across *chapters 3* to *8*, there are a variety of different initiatives for improving the contact modelling at the S&C interface. Introducing new tools, however, will have associated implications, which are discussed throughout this section.

8.3.1 Advanced contact detection modelling

The first improvement to existing, commercially available wheel – rail contact models was identified in *chapter 3* where a multi-point contact detection routine, suitable for S&C rail profiles, was developed. This new process considered the three-dimensional state of the wheel and rail and, as a direct result, required additional levels of computation when compared to the simplified approaches within existing software. A direct implication is the increase in computation time required to achieve the solution accuracy during a detailed S&C analysis. If fully implemented within railway vehicle dynamics, an increase in overall solution time is therefore to be expected. Despite this, the current models within this thesis are in the un-optimised state. Further work to optimise the computational efficiency would help to limit or indeed eliminate this potential limitation.

The use of a novel experimental technique for validating wheel-rail contact models has been introduced through use of thermal imaging. Currently, it is extremely difficult to validate contact models on the live rail network. This new approach provides, for the first time, a feasible means of directly measuring the location of contact from an in-service railway vehicle. An exciting opportunity is therefore presented for further validating a wide range of models, not only for detailed S&C degradation modelling but for general rail vehicle dynamics analysis. The implications of this could be huge due to data now being available for calibrating and improving all existing contact models.

8.3.2 Advanced 2.5D BEM Contact Modelling

One of the most significant achievements within this thesis is the development of a novel 2.5D BEM approach for advanced wheel-rail contact modelling. It has been demonstrated that the technique is indeed capable of combining all of the significant modes of degradation within a single tool. There is, however, a significant drawback to introducing such a tool for long-term degradation of S&C. This includes the time that would be required for simulating the degradation process throughout an entire railway turnout. Although benefits have been demonstrated against existing state-of-the-art solutions with regards to computational effort, the solution times demonstrated for a single contact location would need to be multiplied by hundreds of contact positions along the entirety of the S&C panel. This could be easily overcome by developing a strategy and algorithms for the solver to be implemented on multi-core and/or graphic processing units (GPUs). Furthermore, the implication of significant computation times is, however, not unique to this thesis as the current state-of-the-art solution also considers only a single contact location on a crossing nose.

8.3.3 Dynamic FE analysis of Cast Manganese Crossings

The use of advanced dynamic FE tools for complex wheel-rail interaction studies enables a more sophisticated approach to the design of cast crossings. Parameters such as contact geometry (crossing surface profile) and material properties are somewhat easier to implement as they are a direct result of the design process. Alternatively, other parameters are completely external to the design process, such as track support stiffness and wheel profile. Crossings are currently designed for ideal track quality conditions and therefore cannot be expected to perform favourably under degraded track and / or vehicle conditions. Despite this, an improved understanding of how these parameters are affecting crossing performance will undoubtedly assist future crossing designs, enabling them to be more resilient under degraded operating conditions.

This work will therefore have implications across the entire life cycle of the crossing, from design decisions made during the manufacturing process to defining maintenance prioritisations once the asset is installed in track.

8.4 Contributions to Knowledge

This thesis has contributed to knowledge in the area of wheel-rail contact at railway switches and crossings in the following ways:

- No existing wheel-rail contact model exists that has the capabilities of combining all of the major modes of degradation associated with S&C. In this thesis, a lateral boundary element solution has been developed, which is capable of not only solving complex three-dimensional contact patches but also considers internal body effects, such as dynamic response and plastic strain accumulation. Although not studied directly within this thesis, the adopted modelling technique is also capable of simulating the effects of internal flaws, such as cracks, and is therefore the first wheel-rail contact model to offer a combined solution to many different phenomena associated with S&C. The BEM solution within this thesis therefore offers a step change in the way in which degradation at the wheel-rail interface might be simulated.

- A novel experimental technique using thermal imaging for validating wheel-rail contact detection models has been demonstrated. The thermal imaging technology was originally used to assess the energy within the contact patch through assessing the heat trace. The existing data was therefore, for the first time, used in an alternative manner to directly assess the location of contact in comparison to simulated contact locations.

- For the first time, UK cast crossings have been assessed in detail for not only dynamic impact loading but also material response. The advanced, explicit FE model developed within this thesis has studied the entire contact geometry of an as cast crossing and also includes the primary suspension of the vehicle. This has not only allowed studying a wide range of parameters affecting the performance of UK cast crossings but has also identified potential root causes for existing failures commonly experienced within the UK rail network. A range of asset improvements have been recommended to Network Rail.

8.5 Further Work

There are two distinct areas of work within this thesis that are suitable for further work; 2.5D BEM modelling and dynamic FE wheel-rail interaction.

8.5.1 2.5D BEM modelling

Chapter 6 provides the basis of a versatile and adaptable tool capable of integrating and combining the analysis of many critical modes of S&C degradation. It is therefore highly recommended that the following areas of further work are investigated:

1. Complete the integration of plasticity within the BEM modelling strategy. This would require:
    a. Completing the integration of the consistent tangent operator (CTO) and radial return algorithm (RRA) within the BEM code.
    b. Implement a material hardening rule to introduce a further layer of accuracy.
    c. Understanding and developing a relationship between wear and plastic flow to allow the dominating failure mode to take place (*i.e.* plasticity is dominant during work-hardening of the crossing nose. Once the material has work-hardened, wear begins to take over as the dominant failure mode).
2. Investigate the effect of introducing discontinuities (cracks) and the effect of lubricants within the internal BEM mesh. Effective BEM crack analysis is demonstrated by Zografos [118] and strategies for including the presence of lubricants have been proposed by Balcombe et al. [89-92].
3. BEM code optimisation is essential to provide a solution more suitable for integration within a railway vehicle dynamics package.
4. Integrate the new BEM technique within a railway vehicle dynamics simulation process. This is a critical piece of work required to provide a complete solution for long-term wheel-S&C interaction and degradation modelling.

5. Use the 2.5D BEM model to investigate the interaction of two or more modes of degradation. (*i.e.* assessing how the dynamic response impacts upon strain accumulation and investigating the effects of interacting wear and plastic deformation).

8.5.2 Dynamic FEA of Wheel to Rail Interaction

An adaptable, dynamic FE model for wheel to rail interaction studies has been developed using the example of cast manganese crossings. Although a wide range of asset improvement initiatives have been identified, the true value in this piece of research actually sits within the modelling technique. The methodology developed for a dynamic wheel travelling along the track and through the crossing can now be transferred to any wheel to rail interaction problem. It is therefore also recommended that the FE modelling process is considered for use within other problems concerning wheel to rail damage.

The most significant piece of further work associated with the dynamic FE analysis for wheel to crossing interaction involves further validation of results. Conclusions drawn from within this thesis have been based predominantly upon assessing trends due to varying critical parameters. It is therefore recommended that a further level of model validation is completed through use of load measuring wheelset data.

References

[1] Network Rail (2013) *Annual Return 2013 - A technology-enabled future* [online] Available from: http://www.networkrail.co.uk/WorkArea/DownloadAsset.aspx?id=30064787839 [Accessed: February 18th 2012].

[2] Office of Rail Regulation (2006) *Train derailment at Hatfield: A Final Report by the Independent Investigation Board* [online] Available from: http://webarchive.nationalarchives.gov.uk/20131001175041/http://www.rail-reg.gov.uk/upload/pdf/297.pdf [Accessed: February 18th 2012].

[3] M. Burstow (2003) *Whole Life Rail Model application and development: Development of a rolling contact fatigue damage parameter.* RSSB. Report number: T115.

[4] Health & Safety Executive (2003) *Derailment at Potters Bar*. HSE.

[5] BBC News (special reports) (2007) *How Cumbria rail crash unfolded*. [online] Available at: http://news.bbc.co.uk/1/hi/in_depth/629/629/6393023.stm. [Accessed: November 21st 2013].

[6] Rail Accident and Investigation Branch (2009) *Derailment at Grayrigg.* RAIB. Report number: 20/2008 v5.

[7] Network Rail (2012) *A better railway for a better Britain* [online] Available from: http://www.networkrail.co.uk/WorkArea/DownloadAsset.aspx?id=30064784479 [Accessed: June 12th 2013].

[8] M.K. Sameni (2012) *Railway Track Capacity: Measuring and Managing*. PhD Thesis. University of Southampton.

[9] Office of Rail Regulation (ORR), National Rail Trends (NRT) Portal. [Accessed: March 5th 2013].

[10] T. McMahon (2013) Historical Inflation Rate [online] Accessible at: http://inflationdata.com/Inflation/Inflation_Rate/HistoricalInflation.aspx. [Accessed: December 2nd 2013].

[11] R. McNulty (2011) *Realising the Potential of GB Rail - Final Independent Report of the Rail Value for Money Study*.

[12] RailKonsult (2010) *Relative Infrastructure Managers' Efficiency*. Balfour Beatty Rail Technologies. Report number: BBRT-2229-RP-0002.

[13] A. Cornish, E. Kassa, R.A. Smith (2011) Investigation of failure statistics for switches and crossings in the UK. In: Ford M.C., (ed.) *Railway Engineering 2011, 11th International Conference and Exhibition, London, UK.*

[14] D.L. Cope & J.B. Ellis (2002) *Switch & Crossing Maintenance*, The Permanent Way Institution.

[15] Network Rail Company Standard (2009) NR/L2/TRK/001 *Inspection and Maintenance of Permanent Way - Inspection.*

[16] Railtrack Company Standard (1995) *Track Standards Manual - Section 1 : Basic Track Category Matrix.*

[17] Network Rail Company Standard (2009) NR/L2/TRK/001/D02 *Inspection and Maintenance of Permanent Way - Specific Requirement for Switches and Crossings.*

[18] R. Lewis, Basic Trobology of the wheel-rail contact (2009) In: R. Lewis, U. Olofsson (eds.), *Wheel-Rail Interface Handbook*, Woodhead Publishing, pp. 34-57.

[19] J. Auciello, E. Meli, S. Falomi & M. Malvezzi (2009) Dynamic simulation of railway vehicles: wheel/rail contact analysis. *Journal of Veh. Syst. Dyn.,* 47, pp.867-899.

[20] E. Kassa, C. Andersson & J.C.O. Nielsen (2006) Simulation of dynamic interaction between train and railway turnout. *Journal of Veh. Syst. Dyn.,* 44, pp. 247-258.

[21] D. Nicklisch, E. Kassa, J. Nielsen, M. Ekh & S. Iwnicki (2010) Geometry and stiffness optimization for switches and crossings, and simulation of material degradation. *Journal of Rail and Rapid Transit,* 224, 279-292.

[22] A. Ekberg & B. Paulsson (2010) *INNOTRACK - Concluding Technical Report : Switches & Crossings (Section 6)* [online] Available from: http://www.innotrack.net/IMG/pdf/innotrack_concl_20techn_report_lowres.pdf [Accessed: 12th January 2012] pp. 135-161.

[23] E. Kassa, C. Andersson & J.C.O. Nielsen (2006) Simulation of dynamic interaction between train and railway turnout. *Journal of Veh. Syst. Dyn.,* 44, pp. 247-258.

[24] E. Kassa & J.C.O. Nielsen (2008) Stochastic analysis of dynamic interaction between train and railway turnout. *Journal of Veh. Syst. Dyn.,* 46, pp. 429-449.

[25] E. Kassa & J.C.O. Nielsen (2008) Dynamic interaction between train and railway turnout: full-scale field test and validation of simulation models. *Journal of Veh. Syst. Dyn.,* 46, pp. 521-534.

[26] E. Kassa & J.C.O. Nielsen (2009) Dynamic train–turnout interaction in an extended frequency range using a detailed model of track dynamics. *Journal of Sound and Vibration*, 320, pp. 893-914.

[27] E. Kassa, J. Perez, S. Iwnicki & P. Allen (2009) Optimization of track stiffness and track gauge along a turnout using a multibody simulation tool. *Proceedings 21st international symposium: dynamics of vehicles on roads and tracks IAVSD, Stockholm, Sweden*. August 17-21, page 12 [available in CD].

[28] D. Nicklisch, E. Kassa, J. Nielsen, M. Ekh & S. Iwnicki (2010) Geometry and stiffness optimization for switches and crossings, and simulation of material degradation. *Journal of Rail and Rapid Transit,* 224, pp. 279-292.

[29] Y.Q. Sun, C. Cole & M. McClanachan (2010) The calculation of wheel impact force due to the interaction between vehicle and a turnout. *Journal of Rail and Rapid Transit*, 224, pp. 391-403.

[30] J.B. Ayasse & H. Chollet (2006) Wheel to Rail Contact. In: S. Iwnicki (ed.) *Handbook of Railway Vehicle Dynamics*, Taylor & Francis, London, pp. 86-120.

[31] Z. Ren, S. Sun & G. Xie (2010) A method to determine the two-point contact zone and transfer of wheel-rail forces in a turnout. *Journal of Veh. Syst. Dyn.,* 48 (10), pp. 1-19.

[32] R. Schmid, K.O. Endlicher & P. Lugner (1994) Computer-Simulation of the Dynamical Behavior of a Railway-Bogie Passing a Switch. *Journal of Veh. Syst. Dyn.,* 23, pp. 481-499.

[33] A.A. Shabana & C. Rathod (2007) Geometric coupling in the wheel/rail contact formulations: a comparative study. *Journal of Multi-Body Dynamics,* 22 (11), 47-160.

[34] J. Pombo, J. Ambrosio & M. Silva (2007) A new wheel-rail contact model for railway dynamics. *Journal of Veh. Syst. Dyn.,* 45 (1), pp. 65-189.

[35] H.R. Hertz (1882), Ueber die Beruehrung elastischer Koerper (On Contact Between Elastic Bodies). *Gesammelte Werke (Collected Works)*, Vol. 1.

[36] K.L. Johnson (1985) Contact Mechanics. Cambridge, Cambridge University Press.

[37] H.M. Wu & J.M. Wang (1995) Non-Hertzian Conformal Contact at Wheel Rail Interface. *Proceedings of the 1995 IEEE/ASME Joint Railroad Conference*, pp. 137-144.

[38] W. Yan & F.D. Fischer (2000) Applicability of the Hertz contact theory to rail-wheel contact problems. *Archive of Applied Mechanics*, 70, pp. 255-268.

[39] M. Wiest, E. Kassa, W. Daves, J.C.O. Nielsen & H. Ossberger (2008) Assessment of methods for calculating contact pressure in wheel-rail/switch contact. *Wear,* 265, pp. 1439-1445.

[40] J.J. Kalker (1982) A Fast Algorithm for the Simplified Theory of Rolling Contact. *Journal of Veh. Syst. Dyn.,* 11, pp. 1-13.

[41] J.J. Kalker (1990) *Three-Dimensional Elastic Bodies in Rolling Contact*. The Netherlands, Kluwer Academic Publishers.

[42] K. Knothe, R. Wille & B.W. Zastrau (2001) Advanced contact mechanics - Road and rail. *Journal of Veh. Syst. Dyn.,* 35, pp. 361-407.

[43] E.A.H. Vollebregt, C. Weidemann & A. Kienberger (2011) Use of "CONTACT" in multi-body vehicle dynamics and profile wear simulation: initial results. In: S. Iwnicki, R. Goodall & T. X. Mei (eds.) *22nd International Symposium on Dynamics of Vehicles on Roads and Tracks, IAVSD2011*. August 15 [Available in CD].

[44] M. Wiest, E. Kassa, W. Daves, J.C.O. Nielsen & H. Ossberger (2008) Assessment of methods for calculating contact pressure in wheel-rail/switch contact. *Wear*, 265, pp. 1439-1445.

[45] M. Wiest, W. Daves, F.D. Fischer & H. Ossberger (2008) Deformation and damage of a crossing nose due to wheel passages. *Wear,* 265, pp. 1431-1438.

[46] J.P. Pascal & G. Sauvage (1993) The Available Methods to Calculate the Wheel Rail Forces in Non-Hertzian Contact Patches and Rail Damaging. *Journal of Veh. Syst. Dyn.,* 22, pp. 263-275.

[47] J.P. Pascal (1993) About Multi-Hertzian-Contact Hypothesis and Equivalent Conicity in the Case of S1002 and UIC60 Analytical Wheel Rail Profiles. *Journal of Veh. Syst. Dyn.,* 22, pp. 57-78.

[48] J.B. Ayasse & H. Chollet (2005) Determination of the wheel rail contact patch in semi-Hertzian conditions. *Journal of Veh. Syst. Dyn.,* 43, pp. 161-172.

[49] P. Remington & J. Webb (1996) Estimation of wheel/rail interaction forces in the contact area due to roughness. *Journal of Sound and Vibration*, 193, pp. 83-102.

[50] R.A.J. Ford & D.J. Thompson (2006) Simplified contact filters in wheel/rail noise prediction. *Journal of Sound and Vibration*, 293, pp. 807-818.

[51] A. Pieringer, W. Kropp & D.J. Thompson (2011) Investigation of the dynamic contact filter effect in vertical wheel/rail interaction using a 2D and a 3D non-Hertzian contact model. *Wear,* 271, pp. 328-338.

[52] F.W. Carter (1916) The Electric Locomotive. *M. Inst. C.E.*, Paper Number: 4176, pp. 221-252.

[53] F.W. Carter (1926) On the action of a locomotive driving wheel. *Proceedings of the Royal Society of London, Series A*, 112, pp. 151-157.

[54] J.J. Kalker (1979) Survey of Wheel - Rail Rolling-Contact Theory. *Journal of Veh. Syst. Dyn.,* 8, pp. 317-358.

[55] JJ.J. Kalker (1991) Wheel Rail Rolling-Contact Theory. *Wear*, 144, pp. 243-261.

[56] O. Polach (1999) A fast wheel-rail forces calculation computer code. *Journal of Veh. Syst. Dyn.,* 33, pp. 728-739.

[57] R. Enblom (2009) Deterioration mechanisms in the wheel–rail interface with focus on wear prediction: a literature review. *Vehicle System Dynamics: International Journal of Vehicle Mechanics and Mobility*, 47, pp. 661-700.

[58] D.I. Fletcher & S. Lewis (2013) Creep curve measurement to support wear and adhesion modelling, using a continuously variable creep twin disc machine. *Wear*, 298, pp. 57-65.

[59] D.I. Fletcher & J.H. Beynon (2000) Development of a machine for closely controlled rolling contact fatigue and wear testing. *Journal of Testing and Evaluation*, 28, pp. 267-275.

[60] D.I. Fletcher (2013) A new two-dimensional model of rolling-sliding contact creep curves for a range of lubrication types. *Journal of Engineering Tribology*, 227, pp. 529-537.

[61] C. Tomberger, P. Dietmaier, W. Sextro & K. Six (2011) Friction in wheel-rail contact: A model comprising interfacial fluids, surface roughness and temperature. *Wear*, 271, pp. 2-12.

[62] K. Sawley (2010) Wheel-Rail Deterioration and its Impact and Mitigation. In: F. Schmid, M. Burstow, S. Clark, B. Eickhoff, M. Hiensch, S. Hsu & S. Kent (eds.) *Wheel-Rail Best Practice Handbook*, University of Birmingham Press.

[63] H.C. Meng & K.C. Ludema (1995) Wear Models and Predictive Equations - their Form and Content. *Wear*, 181, pp. 443-457.

[64] S.K. Rhee (1970) Wear Equation for Polymers Sliding Against Metal Surfaces. *Wear,* 16 (6), pp. 431-445.

[65] J.F. Archard & W. Hirst (1956) The Wear of Metals under Unlubricated Conditions. *Proceedings of the Royal Society of London, Series A, Mathematical and Physical Sciences,* 236, pp. 397-410.

[66] J.F. Archard (1957) Elastic Deformation and the Laws of Friction. *Proceedings of the Royal Society of London.Series A, Mathematical and Physical Sciences,* 243, pp. 190-205.

[67] S. Fouvry, P. Kapsa, H. Zahouani & L. Vincent (1997) Wear analysis in fretting of hard coatings through a dissipated energy concept. *Wear*, 203, pp. 393-403.

[68] T.G. Pearce, N.D. Sherratt (1991) Prediction of Wheel Profile Wear. *Wear,* 144, pp. 343-351.

[69] F. Braghin, R. Lewis, R.S. Dwyer-Joyce & S. Bruni (2006) A mathematical model to predict railway wheel profile evolution due to wear. *Wear*, 261, pp. 1253-1264.

[70] R.H. Fries & C.G. Davila (1988) Analytical Methods for Wheel and Rail Wear Prediction. *International Association of Vehicle System Dynamics, IAVSD*, 10, pp. 112-125.

[71] Z. Li (2002) *Wheel-rail rolling contact and its application to wear simulation*, PhD Thesis. T U Delft.

[72] Z.L. Li & J.J. Kalker (1998) *Proceedings of the 6th International Conference on Computer Aided Design, Manufacture and Operation in the Railway and other Mass Transit systems, 2-4 September, Lisbon.* Portugal, Computational Mechanics Publications, pp. 393-402.

[73] T. Telliskivi (2004) Simulation of wear in a rolling-sliding contact by a semi-Winkler model and the Archard's wear law. *Wear,* 256, pp. 817-831.

[74] T. Telliskivi & U. Olofsson (2004) Wheel-rail wear simulation. *Wear*, 257, pp. 1145-1153.

[75] A.F. Bower & K.L. Johnson (1991) Plastic-Flow and Shakedown of the Rail Surface in Repeated Wheel Rail Contact. *Wear,* 144, pp. 1-18.

[76] A. Mazzu (2009) Surface plastic strain in contact problems: prediction by a simplified non-linear kinematic hardening model. *J. Strain Anal. Eng. Des.* 44, pp. 187-199.

[77] J.W. Ringsberg & B.L. Josefson (2001) Finite element analyses of rolling contact fatigue crack initiation in railheads. *Journal of Rail and Rapid Transit,* 215, pp. 243-259.

[78] J.W. Ringsberg & T. Lindback (2003) Rolling contact fatigue analysis of rails including numerical simulations of the rail manufacturing process and repeated wheel-rail contact loads. *Int. Journal of Fatigue*, 25, pp. 547-558.

[79] A. Kapoor, J.H. Beynon, D.I. Fletcher & M. Loo-Morrey (2004) Computer simulation of strain accumulation and hardening for pearlitic rail steel undergoing repeated contact. *J. Strain Anal. Eng. Des.*, 39, pp. 383-396.

[80] M. Busquet, L. Baillet, C. Bordreuil & Y. Berthier (2005) 3D finite element investigation on the plastic flows of rolling contacts - correlation with railhead microstructural observations. *Wear,* 258, pp. 1071-1080.

[81] M. Busquet, H. Chollet, L. Baillet, C. Dagorn, J.B. Ayasse & Y. Berthier (2006) From railway dynamics to wheel/rail contact mechanics, an approach for the modelling of the wheel/rail contact: elasto-plastic response of the railhead. *Journal of Rail & Rapid Transit,* 220, pp. 189-200.

[82] Z. Wen, L. Wu, W. Li, X. Jin & M. Zhu (2011) Three-dimensional elastic-plastic stress analysis of wheel-rail rolling contact. *Wear*, 271, pp. 426-436.

[83] J. Brouzoulis, P.T. Torstensson, R. Stock & M. Ekh (2011) Prediction of wear and plastic flow in rails-Test rig results, model calibration and numerical prediction. *Wear,* 271, pp. 92-99.

[84] S. Foletti, S. Beretta & G. Bucca (2010) A numerical 3D model to study ratcheting damage of a tramcar line. *Wear,* 268, pp. 737-746.

[85] M. Wiest, W. Daves, F.D. Fischer & H. Ossberger (2005) Plastification and Damage in Wheel-Rail Rolling Contact - Case Study on a Crossing. *PAMM,* 5, 67-70.

[86] M. Pletz, W. Daves & H. Ossberger (2012) A wheel passing a crossing nose: Dynamic analysis under high axle loads using finite element modelling. *Journal of Rail and Rapid Transit*, 226, pp. 603-611.

[87] M. Pletz, W. Daves & H. Ossberger (2012) A wheel set/crossing model regarding impact, sliding and deformation-Explicit finite element approach. *Wear*, 294, pp. 446-456.

[88] J.R. Evans & M.C. Burstow (2006) Vehicle/track interaction and rolling contact fatigue in rails inthe UK. *Veh. Syst. Dyn.,* 44, pp. 708-717.

[89] D.I. Fletcher, F.J. Franklin & A. Kapoor (2009) Rail surface fatigue and wear. In: R. Lewis & U. Olofsson (eds.) *Wheel-Rail Interface Handbook*, pp. 280-310.

[90] R. Balcombe, M.T. Fowell & D. Dini (2009) Modelling rolling contact fatigue cracks in the hydrodynamic lubrication regime: a coupled approach. *Mesomechanics,* 1, pp. 245-248.

[91] R. Balcombe, M.T. Fowell, A.V. Olver & D. Dini (2010) A Coupled Approach for Modelling Rolling Contact Fatigue Cracks Under Elastohydrodyanmic Lubrication. In: ASME/STLE 2009 International Joint Tribology Conference, pp. 269-271.

[92] R. Balcombe, M.T. Fowell, A.V. Olver, S. Loannides & D. Dini (2011) A coupled approach for rolling contact fatigue cracks in the hydrodynamic lubrication regime: The importance of fluid/solid interactions. *Wear*, 271, pp. 720-733.

[93] R. Balcombe (2012) *A study of rolling contact fatigue cracks in lubricated contacts*. ImperialCollege London Report.

[94] D.I. Fletcher & J.H. Beynon (1999) A simple method of stress intensity factor calculation for inclined fluid-filled surface-breaking cracks under contact loading. *Journal of Engineering Tribology*, 213, pp. 299-304.

[95] D.I. Fletcher & J.H. Beynon (2000) The effect of contact load reduction on the fatigue life of pearlitic rail steel in lubricated rolling-sliding contact. *Fatigue & Fracture of Engineering Materials & Structures,* 23, pp. 639-650.

[96] D.I. Fletcher & J.H. Beynon (2000) Equilibrium of crack growth and wear rates during unlubricated rolling-sliding contact of pearlitic rail steel. *Journal of Rail and Rapid Transit,* 214, pp. 93-105.

[97] D.I. Fletcher & J.H. Beynon (2000) The effect of intermittent lubrication on the fatigue life of pearlitic rail steel in rolling-sliding contact. *Journal of Rail and Rapid Transit*, 214, pp. 145-158.

[98] M.F. Frolish, D.I. Fletcher & J.H. Beynon (2002) A quantitative model for predicting the morphology of surface initiated rolling contact fatigue cracks in back-up roll steels. *Fatigue & Fracture of Engineering Materials & Structures*, 25, pp. 1073-1086.

[99] A. Kapoor & F.J. Franklin (2000) Tribological layers and the wear of ductile materials. *Wear,* 245, pp. 204-215.

[100] F.J. Franklin, T. Chung & A. Kapoor, Ratcheting and fatigue-led wear in rail-wheel contact. *Fatigue & Fracture of Engineering Materials & Structures*, 26, pp. 949-955.

[101] D.I. Fletcher, F.J. Franklin & A. Kapoor, Image analysis to reveal crack development using a computer simulation of wear and rolling contact fatigue. *Fatigue & Fracture of Engineering Materials & Structures*, 26, pp. 957-967.

[102] D.I. Fletcher & A. Kapoor (2006) Rapid method of stress intensity factor calculation for semi-elliptical surface breaking cracks under three-dimensional contact loading. *Journal of Rail and Rapid Transit,* 220, pp. 219-234.

[103] D.I. Fletcher, A. Kapoor, F.J. Franklin, L. Smith & P. Hyde (2006) *Comparison of the Hatfieldand alternative UK rails using models to assess the effect of residual stress on crack growth from rolling contact fatigue*, Health & Safety Executive, Report number: 461.

[104] A. Kapoor, D.I. Fletcher, F.J. Franklin, G. Vasic & L. Smith (2005) Rail-wheel contact research at the University of Newcastle. *Proceedings of the 11th International Conference on Fracture (ICF XI), Turin Italy, 20-25 March 2006.*

[105] D.I. Fletcher, P. Hyde & A. Kapoor (2004) Growth of multiple rolling contact fatigue cracks driven by rail bending modelled using a boundary element technique. *Journal of Rail and Rapid Transit,* 218, pp. 243-253.

[106] A. Ekberg & B. Paulsson (2010) *INNOTRACK - Concluding Technical Report : Switches & Crossings (Section 6)* [online] Available from: http://www.innotrack.net/IMG/pdf/innotrack_concl_20techn_report_lowres.pdf [Accessed: 12th January 2012] pp. 135-161.

[107] D. Nicklisch, J.C.O. Nielsen, M. Ekh, A. Johansson, B. Palsson, J.M. Reinecke & A. Zoll, Simulation of Wheel-Rail Contact Forces and Subsequent Material Degradation in Switches & Crossings. pp. 1-14.

[108] MathWorks (2011) MATLAB (Version R2011b (7.13.0.564) 64-bit (win64)) [software] Available from: http://www.mathworks.co.uk

[109] A. Wickens (2005) *Fundamentals of Rail Vehicle Dynamics*, Swets & Zeitlinger Publishers.

[110] M. Burstow, M. Podesta & J. Pearce (2011) Understanding wheel/rail interaction with thermographic imaging. In: S. Iwnicki, R. Goodall & T. X. Mei (eds.) *22nd International Symposium on Dynamics of Vehicles on Roads and Tracks, IAVSD2011*, *August 15* [Available in CD].

[111] I.J. Coleman, E. Kassa & R.A. Smith (2012) Wheel-Rail Contact Modelling within Switches and Crossings. The International Journal of Railway Technology, *International Journal of Railway Technology*, 1 (2), pp. 45-66.

[112] C. Chongyi (2010) Study on numerical method to predict wheel/rail profile evolution due to wear. *Wear*, 269, pp. 167-173.

[113] G. Xie & S.D. Iwnicki (2008) Calculation of wear on a corrugated rail using a three-dimensional contact model. *Wear,* 265, pp. 1238-1248.

[114] G. Lundberg & H. Sjovall (1958) Stress and Deformation in Elastic Contacts. Chalmers University of Technology, Gothenburg, Sweden.

[115] T. Jendel (2002) Prediction of wheel profile wear-comparisons with field measurements. *Wear*, 253, pp. 89-99.

[116] R. Lewis & U. Olofsson (2004) Mapping rail wear regimes and transitions. *Wear*, 257 pp. 721-729.

[117] NAFEMS (2003) *NAFEMS A Finite Element Primer*.

[118] C.A. Brebbia (1980) *The Boundary Element Method for Engineers*, Pentech Press.

[119] A. Zografos (2011) *Numerical and Experimental Investigation of Fretting in Wheel-Hub Type Bolted Joints*, PhD Thesis, Imperial College London.

[120] S.G. Mogilevskaya & A.M. Linkov (1998) Complex fundamental solutions and complex variables boundary element method in elasticity. *Comput. Mech.,* 22, pp. 88-92.

[121] M. Bonnet & S. Mukherjee (1996) Implicit BEM formulations for usual and sensitivity problems in elasto-plasticity using the consistent tangent operator concept. *Int. J. Solids Structures*, 33, pp.

[122] J.C. Simo & R.L. Taylor, Consistent Tangent Operators for Rate-Independent Elastoplasticity. *Comput. Methods Appl. Mech. Eng.*, 48, pp. 101-118.

[123] H. Poon, S. Mukherjee & M. Bonnet (1998) Numerical implementation of a CTO-based implicit approach for the BEM solution of usual and sensitivity problems in elasto-plasticity. *Eng. Anal. Boundary Elements*, 22, pp. 257-269.

[124] G.H. Paulino & Y. Liu (2001) Implicit consistent and continuum tangent operators in elastoplastic boundary element formulations. *Comput. Methods Appl. Mech. Eng.,* 190, pp. 2157-2179.

[125] P.R. Cheesewright (1977) *The paths of wheelsets through a cast manganese crossing - report 2 - the effects of crossing geometry*,

[126] P.R. Cheesewright (1977) *Wheel rail forces measured at crossings of cast manganese and built-up types*. British Rail Board Research & Development Division, Report number: 263-191-24.

[127] R.A. Clark (1981) *Measurement of wheel-rail contact forces at a selection of switches & crossings using HSFV1 equipped with load measuring wheelsets*. British Rail Board Research & Development Division, Report number: 263-370-39.

[128] E. Kassa & J.C.O. Nielsen (2008) Dynamic interaction between train and railway turnout: full-scale field test and validation of simulation models. *Veh. Syst. Dyn.*, 46, pp. 521-534.

[129] E. Kassa & J.C.O. Nielsen (2008) Stochastic analysis of dynamic interaction between train and railway turnout. *Veh. Syst. Dyn.*, 46, pp. 429-449.

[130] U. Olofsson (2009) Adhesion and friction modification, In: R. Lewis, U. Olofsson (eds.), *Wheel-Rail Interface Handbook*, Woodhead Publishing Ltd., Oxford, pp. 510-528.

[131] S. Hsu (2012) *Shalford Junction - Vehicle Dynamics Simulations,* Network Rail Presentation.

[132] Voestalpine (2007) *Bulit-up Crossings*.

[133] Railway Safety and Standards Board Limited (2010) GMRT2466 Iss 3. *Railway Wheelsets*.

[134] Network Rail Company Standard (2002) NR/SP/TRK/012. *Cast Austenitic Manganese Steel Crossings*. Milton Keynes, Network Rail Infrastructure Ltd.

[135] Network Rail (2014) Rail Defect Management System (RDMS) [Accessed 06/03/2014].

[136] Network Rail (2014) *S&C System Report*, [online] Network Rail Intranet.

[137] H.H. Jenkins, J.E. Stephenson, G.A. Clayton, G.W. Morland, D. Lyon (1974) The Effect of Track and Vehicle Parameters on Wheel/Rail Vertical Dynamic Forces. *Railway Engineering Journal*, pp. 2-16.

[138] G. Beer (2001) *Programming the Boundary Element Method - an Introduction for Engineers*, John Wiley & Sons, Ltd, Chichester.

Appendix A1: BEM Influence Functions

The analytical expressions for the displacement and stress influence functions, $u_{(x,y)}^{tri}$ and $\sigma_{(x,y)}^{tri}$ respectively, were generated using the MATLAB symbolic toolbox.

Input variables

(x,y)	Coordinate of field point within source point coordinate systems
Y	Vertical coordinate of source point within source point coordinate system (Note: Y=0 due to source point residing on the boundary surface).
P	Magnitude of applied normal traction
Q	Magnitude of applied tangential traction
a	Triangular element semi-length
p	π (pi)
k	Kolosov's constant
m	Material shear modulus

Displacement in x-direction, $\boldsymbol{U_x}$

$\boldsymbol{U_x}(x, y, P, Q, a, p)$ =

```
(1/(8*a*(1 + k)*m*pi()))*((-a^2)*(1 + k)*Q + 2*a*(a*(Q + 2*k*Q) - k*Q*x +
2*P*y) - 4*y*(a*(1 + k)*Q - (1 + k)*Q*x + P*y)*atan((a - x)/(0 + y)) -
4*y*(a*(1 + k)*Q - (1 + k)*Q*x + P*y)*atan(x/(0 + y)) - a^2*k*Q*log((a -
x)^2 + y^2) - (2*a*(k*Q*x - P*y) + 2*y*(P*x + Q*y) + k*Q*(-x^2 +
y^2))*log(x^2 + y^2) + (2*a*(k*Q*x - P*y) + 2*y*(P*x + Q*y) + k*Q*(-x^2 +
y^2))*log(a^2 - 2*a*x + x^2 + y^2)) - (1/(8*a*(1 + k)*m*pi()))*(a^2*(1 +
k)*Q - 2*a*(a*(Q + 2*k*Q) + k*Q*x - 2*P*y)-4*y*(a*(1 + k)*Q + (1 + k)*Q*x -
P*y)*atan(x/(0 + y)) + 4*y*(a*(1 + k)*Q + (1 + k)*Q*x - P*y)*atan((a +
x)/(0 + y))-(2*a*(k*Q*x - P*y) - 2*y*(P*x + Q*y) + k*Q*(x^2 - y^2))*log(x^2
+ y^2) + (2*a*(k*Q*x - P*y) - 2*y*(P*x + Q*y) + k*Q*(x^2 - y^2))*log(a^2 +
2*a*x + x^2 + y^2) + a^2*k*Q*log((a + x)^2 + y^2))
```

Displacement in y-direction, $\boldsymbol{U_y}$

$\boldsymbol{U_y}(x, y, P, Q, a, p, m)$ =

```
(1/(8*a*(1 + k)*m*pi()))*((-a^2)*(-1 + k)*P - 2*a*(a*(P - 2*k*P) + k*P*x -
2*Q*y) - 4*y*(a*(-1 + k)*P - (-1 + k)*P*x + Q*y)*atan((a - x)/(0 + y)) -
4*y*(a*(-1 + k)*P - (-1 + k)*P*x + Q*y)*atan(x/(0 + y)) - a^2*k*P*log((a -
x)^2 + y^2)+(2*y*((-Q)*x + P*y) + a*(-2*k*P*x + 2*Q*y) + k*P*(x^2 -
y^2))*log(x^2 + y^2)-(2*y*((-Q)*x + P*y) + a*(-2*k*P*x + 2*Q*y) + k*P*(x^2
- y^2))*log(a^2 - 2*a*x + x^2 + y^2))-(1/(8*a*(1 + k)*m*pi()))*(a^2*(-1 +
k)*P - 2*a*(a*(-1 + 2*k)*P + k*P*x - 2*Q*y) + 4*y*(a*(P - k*P) - (-1 +
k)*P*x + Q*y)*atan(x/(0 + y)) - 4*y*(a*(P - k*P) - (-1 + k)*P*x +
Q*y)*atan((a + x)/(0 + y)) +(-2*y*((-Q)*x + P*y) + a*(-2*k*P*x + 2*Q*y) +
k*P*(-x^2 + y^2))*log(x^2 + y^2)-(-2*y*((-Q)*x + P*y) + a*(-2*k*P*x +
2*Q*y) + k*P*(-x^2 + y^2))*log(a^2 + 2*a*x + x^2 + y^2) + a^2*k*P*log((a +
x)^2 + y^2))
```

Stress tensor component, $\boldsymbol{\sigma_{xx}}$

$\boldsymbol{\sigma_{xx}}(x, y, Y, P, Q, a, p)$ =

```
(log(Y^2 - 2*Y*x + x^2 + y^2)*(3*Q*a - 3*Q*Y - 5*P*y + 3*Q*x - Q*Y*k +
Q*a*k + P*k*y + Q*k*x))/(4*a*p*(k + 1)) - (atan((Y - x)/y)*(3*P*a - 3*P*Y +
3*P*x + 5*Q*y + P*Y*k - P*a*k - P*k*x + Q*k*y))/(2*a*p*(k + 1)) - (atan((Y
- x)/y)*(3*P*x - 3*P*a - 3*P*Y + 5*Q*y + P*Y*k + P*a*k - P*k*x +
Q*k*y))/(2*a*p*(k + 1)) - (log(Y^2 - 2*Y*x + x^2 + y^2)*(3*Q*Y + 3*Q*a +
5*P*y - 3*Q*x + Q*Y*k + Q*a*k - P*k*y - Q*k*x))/(4*a*p*(k + 1)) + (atan((Y
+ a - x)/y)*(3*P*x - 3*P*a - 3*P*Y + 5*Q*y + P*Y*k + P*a*k - P*k*x +
Q*k*y))/(2*a*p*(k + 1)) - (atan((a - Y + x)/y)*(3*P*a - 3*P*Y + 3*P*x +
5*Q*y + P*Y*k - P*a*k - P*k*x + Q*k*y))/(2*a*p*(k + 1)) - (log(x^2 - 2*x*(Y
- a) + (Y - a)^2 + y^2)*(3*Q*a - 3*Q*Y - 5*P*y + 3*Q*x - Q*Y*k + Q*a*k +
P*k*y + Q*k*x))/(4*a*p*(k + 1)) + (log((Y + a)^2 + x^2 + y^2 - 2*x*(Y +
a))*(3*Q*Y + 3*Q*a + 5*P*y - 3*Q*x + Q*Y*k + Q*a*k - P*k*y -
Q*k*x))/(4*a*p*(k + 1)) - (Q*(Y + a)*(k + 3))/(2*a*p*(k + 1)) + (Q*Y*(k +
3))/(a*p*(k + 1)) - (Q*(Y - a)*(k + 3))/(2*a*p*(k + 1)) - (y*(P*Y^2 -
2*P*Y*x + P*a*Y + P*x^2 - P*a*x + P*y^2 + Q*a*y))/(a*p*(k + 1)*(Y^2 - 2*Y*x
+ x^2 + y^2)) - (y*(P*Y^2 - 2*P*Y*x - P*a*Y + P*x^2 + P*a*x + P*y^2 -
Q*a*y))/(a*p*(k + 1)*(Y^2 - 2*Y*x + x^2 + y^2)) + (y*(P*x^2 + P*y^2 +
P*Y*(Y + a) + P*a*(Y + a) - P*x*(Y + a) - Q*y*(Y + a) - P*Y*x + Q*Y*y -
P*a*x + Q*a*y))/(a*p*(k + 1)*((Y + a)^2 + x^2 + y^2 - 2*x*(Y + a))) +
(y*(P*x^2 + P*y^2 - P*Y*x + P*Y*(Y - a) + Q*Y*y + P*a*x - P*a*(Y - a) -
Q*a*y - P*x*(Y - a) - Q*y*(Y - a)))/(a*p*(k + 1)*(x^2 - 2*x*(Y - a) + (Y -
a)^2 + y^2))
```

Stress tensor component, σ_{yy}

$\sigma_{yy}(x, y, Y, P, Q, a, p)$ =

```
(atan((a - Y + x)/y)*(P*Y - P*a - P*x + Q*y))/(2*a*p) - (atan((Y + a -
x)/y)*(P*Y + P*a - P*x + Q*y))/(2*a*p) + (atan((Y - x)/y)*(P*Y + P*a - P*x
+ Q*y))/(2*a*p) + (atan((Y - x)/y)*(P*Y - P*a - P*x + Q*y))/(2*a*p) + (Q*(Y
+ a)*(k - 1))/(2*a*p*(k + 1)) - (log(Y^2 - 2*Y*x + x^2 + y^2)*(k^2 -
1)*(Q*a - Q*Y + P*y + Q*x))/(4*a*p*(k + 1)^2) + (log(Y^2 - 2*Y*x + x^2 +
y^2)*(k^2 - 1)*(Q*Y + Q*a - P*y - Q*x))/(4*a*p*(k + 1)^2) - (Q*Y*(k -
1))/(a*p*(k + 1)) + (Q*(Y - a)*(k - 1))/(2*a*p*(k + 1)) + (log(x^2 - 2*x*(Y
- a) + (Y - a)^2 + y^2)*(k^2 - 1)*(Q*a - Q*Y + P*y + Q*x))/(4*a*p*(k +
1)^2) + (y*(P*Y^2 - 2*P*Y*x + P*a*Y + P*x^2 - P*a*x + P*y^2 +
Q*a*y))/(a*p*(k + 1)*(Y^2 - 2*Y*x + x^2 + y^2)) + (y*(P*Y^2 - 2*P*Y*x -
P*a*Y + P*x^2 + P*a*x + P*y^2 - Q*a*y))/(a*p*(k + 1)*(Y^2 - 2*Y*x + x^2 +
y^2)) - (y*(P*x^2 + P*y^2 + P*Y*(Y + a) + P*a*(Y + a) - P*x*(Y + a) -
Q*y*(Y + a) - P*Y*x + Q*Y*y - P*a*x + Q*a*y))/(a*p*(k + 1)*((Y + a)^2 + x^2
+ y^2 - 2*x*(Y + a))) - (log((Y + a)^2 + x^2 + y^2 - 2*x*(Y + a))*(k^2 -
1)*(Q*Y + Q*a - P*y - Q*x))/(4*a*p*(k + 1)^2) - (y*(P*x^2 + P*y^2 - P*Y*x +
P*Y*(Y - a) + Q*Y*y + P*a*x - P*a*(Y - a) - Q*a*y - P*x*(Y - a) - Q*y*(Y -
a)))/(a*p*(k + 1)*(x^2 - 2*x*(Y - a) + (Y - a)^2 + y^2))
```

Stress tensor component, τ_{xy}

$\tau_{xy}(x, y, Y, P, Q, a, p)$ =

```
(atan((Y - x)/y)*(Q*Y + Q*a + 3*P*y - Q*x + Q*Y*k + Q*a*k - P*k*y -
Q*k*x))/(2*a*p*(k + 1)) - (atan((Y - x)/y)*(Q*a - Q*Y - 3*P*y + Q*x - Q*Y*k
+ Q*a*k + P*k*y + Q*k*x))/(2*a*p*(k + 1)) - (log(Y^2 - 2*Y*x + x^2 +
y^2)*(P*a - P*Y + P*x + 3*Q*y + P*Y*k - P*a*k - P*k*x + Q*k*y))/(4*a*p*(k +
1)) - (log(Y^2 - 2*Y*x + x^2 + y^2)*(P*x - P*a - P*Y + 3*Q*y + P*Y*k +
P*a*k - P*k*x + Q*k*y))/(4*a*p*(k + 1)) - (atan((a - Y + x)/y)*(Q*a - Q*Y -
3*P*y + Q*x - Q*Y*k + Q*a*k + P*k*y + Q*k*x))/(2*a*p*(k + 1)) - (atan((Y +
a - x)/y)*(Q*Y + Q*a + 3*P*y - Q*x + Q*Y*k + Q*a*k - P*k*y -
Q*k*x))/(2*a*p*(k + 1)) + (log(x^2 - 2*x*(Y - a) + (Y - a)^2 + y^2)*(P*a -
P*Y + P*x + 3*Q*y + P*Y*k - P*a*k - P*k*x + Q*k*y))/(4*a*p*(k + 1)) +
(log((Y + a)^2 + x^2 + y^2 - 2*x*(Y + a))*(P*x - P*a - P*Y + 3*Q*y + P*Y*k
+ P*a*k - P*k*x + Q*k*y))/(4*a*p*(k + 1)) - (P*(Y + a)*(k - 1))/(2*a*p*(k +
1)) + (P*Y*(k - 1))/(a*p*(k + 1)) - (P*(Y - a)*(k - 1))/(2*a*p*(k + 1)) -
(y*(Q*Y^2 - 2*Q*Y*x - Q*a*Y + Q*x^2 + Q*a*x + Q*y^2 + P*a*y))/(a*p*(k +
1)*(Y^2 - 2*Y*x + x^2 + y^2)) - (y*(Q*Y^2 - 2*Q*Y*x + Q*a*Y + Q*x^2 - Q*a*x
+ Q*y^2 - P*a*y))/(a*p*(k + 1)*(Y^2 - 2*Y*x + x^2 + y^2)) + (y*(Q*x^2 +
Q*y^2 + Q*Y*(Y + a) + Q*a*(Y + a) + P*y*(Y + a) - Q*x*(Y + a) - P*Y*y -
Q*Y*x - P*a*y - Q*a*x))/(a*p*(k + 1)*((Y + a)^2 + x^2 + y^2 - 2*x*(Y + a)))
+ (y*(Q*x^2 + Q*y^2 - P*Y*y - Q*Y*x + Q*Y*(Y - a) + P*a*y + Q*a*x - Q*a*(Y
- a) + P*y*(Y - a) - Q*x*(Y - a)))/(a*p*(k + 1)*(x^2 - 2*x*(Y - a) + (Y -
a)^2+y^2))
```

Appendix A2: BEM Plasticity Developments

A2.1 Interim BEM plasticity theory

The boundary integral equation (BIE) below considers the external loading and accumulation of internal body strains on the overall stress analysis of the boundary element problem:

$$\int_{\partial\Omega} [u_i(z) - u_i(x)] P_{ki}(x,z)\, dS_z - \int_{\partial\Omega} p_i(z) U_{ki}(x,z) dS_z = \int_{\Omega} U_{ki,j}(x,z) C_{ijab} \varepsilon_{ab}^{p}(z)\, dV_z$$

Here, x denotes any fixed source point on the boundary ($\partial\Omega$) and z represents the variable field point within the domain (Ω). The influence functions (or Kevin kernels) are given for the displacements and tractions by U_{ki} and P_{ki} respectively. These are singular functions providing a reaction at the field point due to unit loading at the source point. This formulation is represented in matrix form by:

$$[\boldsymbol{H}]\{\boldsymbol{u}\} - [\boldsymbol{G}]\{\boldsymbol{p}\} = [\boldsymbol{Q}]\{\boldsymbol{C}:\boldsymbol{\varepsilon}^{p}\}$$

After collecting the boundary unknowns ($\{\boldsymbol{u}\}$ and $\{\boldsymbol{p}\}$) into $\{\boldsymbol{y}\}$ and the displacement and traction influences into $[\boldsymbol{A}]$, this formulation can be rewritten in the form:

$$[\boldsymbol{A}]\{\boldsymbol{y}\} = \{\boldsymbol{f}\} + [\boldsymbol{Q}]\{\boldsymbol{C}:\boldsymbol{\varepsilon}^{p}\}$$

where $\{\boldsymbol{f}\}$ represents the contribution of known boundary variables. By rearranging equation 1, the displacement at an internal point can be given by:

$$u_k(x) = \int_{\partial\Omega} p_i(z) U_{ki}(x,z) dS_z - \int_{\partial\Omega} u_i(z) P_{ki}(x,z)\, dS_z + \int_{\Omega} U_{ki,j}(x,z) C_{ijab} \varepsilon_{ab}^{p}(z)\, dV_z$$

Bonnet et al. [122] demonstrated that the displacement gradient could be obtained through differentiation with respect to x_l (displacement into the domain), yielding the formulation:

$$u_{k,l}(x) = \int_{\partial\Omega} u_i(z)P_{ki,l}(x,z)\,dS_z - \int_{\partial\Omega} p_i(z)U_{ki,l}(x,z)dS_z$$

$$- C_{ijab}\varepsilon_{ij}^{p}(x)\int_{\partial\Omega} n_l(z)U_{ka,b}(x,z)dS_z - \int_{\partial\Omega} U_{ki,jl}(x,z)\,C_{ijab}\left[\varepsilon_{ab}^{p}(z) - \varepsilon_{ab}^{p}(x)\right]dV_z$$

Converting this into symbolic matrix form, it was shown that the total strain at x could be obtained using:

$$\{\boldsymbol{\varepsilon}\} = [\boldsymbol{G}']\{\boldsymbol{p}\} - [\boldsymbol{H}']\{\boldsymbol{u}\} + [\boldsymbol{Q}']\{\boldsymbol{C}{:}\,\boldsymbol{\varepsilon}^{\boldsymbol{p}}\} = -[\boldsymbol{A}']\{\boldsymbol{y}\} + \{\boldsymbol{f}'\} + [\boldsymbol{Q}']\{\boldsymbol{C}{:}\,\boldsymbol{\varepsilon}^{\boldsymbol{p}}\}$$

Substituting for $\{\boldsymbol{y}\}$ we get:

$$\{\boldsymbol{\varepsilon}\} = \{\boldsymbol{n}\} + [\boldsymbol{S}]\{\boldsymbol{C}{:}\,\boldsymbol{\varepsilon}^{\boldsymbol{p}}\}$$

where

$$\{\boldsymbol{n}\} = \{\boldsymbol{f}'\} - [\boldsymbol{A}'][A]^{-1}\{\boldsymbol{f}\}$$

$$[\boldsymbol{S}] = [\boldsymbol{Q}'] - [\boldsymbol{A}'][A]^{-1}[\boldsymbol{Q}]$$

A2.2 Fundamental Solutions for Initial Strains

Within the existing BEM model, $[\boldsymbol{G}]$ and $[\boldsymbol{H}]$ are available from the elasto-dynamic solution therefore influence function $[\boldsymbol{Q}]$ must first be generated. This function was found in computational form within [137]. Considering a 2-D problem, matrix $[\boldsymbol{Q}]$ is given by:

$$[\boldsymbol{Q}] = \begin{bmatrix} Q_{xx} & Q_{xy} \\ Q_{yx} & Q_{yy} \end{bmatrix}$$

where

$$Q_{kk} = \frac{C_2}{r^n}\left(C_3 r_k + C_4 r_k^3\right)$$

and

$$Q_{kj} = \frac{C_2}{r^n}\left(-C_3 r_k + C_4 r_k^3 r_j\right)$$

for

$$k, j = x, y, z$$

Constants n and $C_{2,3,4}$ are provided within the table below.

	Plain strain problems
n	1
C_2	$1/4\pi(1-\nu)$
C_3	$1-2\nu$
C_4	2